UNIVERSITY of TASMANIA

3D medical image analysis using knee MRI

by

Isshaa Aarya

M.Sc Biomedical Engineering, University of Dundee, 2011

B.E Biomedical Engineering, University of Mumbai, 2009

A thesis submitted in fulfillment of the requirements for the degree of Doctor of Philosophy in Engineering

in the

School of Engineering & ICT

December 2016

Declaration & Statements

Declaration of Originality This thesis contains no material which has been accepted for a degree or diploma by the University or any other institution, except by way of background information and duly acknowledged in the thesis, and to the best of my knowledge and belief no material previously published or written by another person except where due acknowledgment is made in the text of the thesis, nor does the thesis contain any material that infringes copyright.

Authority of access This thesis may be made available for loan and limited copying and communication in accordance with the Australian *Copyright Act 1968.*

Declaration of the Copyrights for the Published Chapters The publishers of the papers comprising Chapters 2 & 3 hold the copyright for that content, and access to the material should be sought from the respective journals. The remaining non published content of the thesis may be available for loan and limited copying and communication in accordance with the Australian *Copyright Act 1968.*

Statement of Ethical Conduct The research associated with this thesis abides by the international and Australian codes on human and animal experimentation, the guidelines by the Australian Government's Office of the Gene Technology Regulator and the rulings of the Safety, Ethics and Institutional Biosafety Committees of the University.

Signatures:

Candidate

Statement of Co-authorship

Papers arising from this study are based on the research work carried out during this PhD project. I. Aarya is the primary author of all the papers, primary supervisor Dr. Jiang has contributed as an advisor and technical guide towards the development of the papers. Dr. Gale has assisted in refinement and presentation of the papers. The following people and institutions contributed to the publication of work undertaken as part of this thesis

Candidate : **I. Aarya**, School of Engineering & ICT, University of Tasmania
Co-author 1 : **Dr. D. Jiang**, School of Engineering & ICT, University of Tasmania
Co-author 2 : **Dr. T. Gale**, School of Engineering & ICT, University of Tasmania

We the undersigned agree with the above stated contributions for the published peer-reviewed manuscripts contributing to this thesis.

Signatures:

Dr. Danchi Jiang
Supervisor
School of Engineering & ICT
University of Tasmania

5/5/2016
Date

Dr. Andrew Chan
Head of School
School of Engineering & ICT
University of Tasmania

6. 5. 2016
Date

Dr Leonie Ellis
Acting Head
School of Engineering & ICT

"Alice: Where should I go?.
Cheshire Cat: That depends on where you want to end up"

Lewis Carroll, Alice's Adventures in Wonderland & Through the Looking Glass

UNIVERSITY of TASMANIA

Abstract

School of Engineering & ICT

Doctor of Philosophy

by Isshaa Aarya

This thesis works on 3D image analysis for efficient cartilage detection, Rician noise removal, visualization and shape analysis of the articular cartilage of the knee using MRI images.

Due to the renewed focus on Osteoarthritis, emphasis is now laid on early detection of cartilage degeneration and the use of MRI imaging modality for imaging and visualization of the cartilage tissue. MRI offers superior contrast resolution which helps in visualization of soft tissues such as cartilage and can offer non-invasive diagnostic procedure for OA. Despite these improvements in imaging and quantitative analysis of the cartilage tissue, it is still faced with multiple challenges due to poor resolution, noise and imaging artifacts present in these images.

This thesis addresses some of the key issues of noise and limited contrast in knee cartilage analysis for OA commonly observed when using MRI images. It specifically addresses Rician noise observed in single coil magnitude MRI images which is an inherent noise and affects both image quality and contrast. This noise is both non-linear and signal dependent. This thesis investigates the presence of Rician noise on MRI signal and proposes new imaging techniques to efficiently reduce the effect of noise while retaining crucial edge information in addition to improving the overall signal content which will enable in improved cartilage detection and quantification.

This thesis also offers an improvement in cartilage detection technique despite its poor resolution. For this purpose it incorporates use of 3D un-decimated wavelets and their multiresolution capabilities to achieve better cartilage detection. A novel imaging technique is developed using wavelets multiresolution edge detection and optimization. Local and multiscale edge detection is attained with help of wavelet singularity and better time-scale localization. Role of Rician noise in presence of edge and its localization has also been addressed. Subsequently a 3D model of the cartilage tissue is reconstructed using the volume rendering function. This cartilage volume is also used for a quantitative assessment of the tissue for analysis of OA.

In addition this thesis also considers geometric analysis of the cartilage shape as a smooth 2D Riemannian manifold. The variation in cartilage shape amongst individuals and during different stages of OA adds to the complexity of prediction of OA. Due to our assumption of cartilage as Riemannian manifold it can be used for shape analysis and feature extraction of the cartilage by making use of the intrinsic information of the manifold as a global feature. The Riemannian geometry enables us to compute the global nature of the cartilage shape and also its extrinsic variations in the form of Gauss and mean curvatures.

As a final part of this study, we have included all the imaging algorithms to form the basis of a new software prototype for OA analyses. This software prototype incorporates wavelet multiresolution GUI for visualization of cartilage surface at higher wavelet resolutions and enables cartilage tissue analysis at these resolutions. The performance of the above imaging algorithms is assessed by their ability to improve the signal to noise ratio, computational efficiency and improvement in cartilage analysis inconsideration with respect to other methods.

The contributions of this thesis include efficient Rician noise removal and improvement in signal information and contrast ratio of the image, 3D cartilage detection using wavelets and multiresolution addressing the limited resolution information which primarily comprise chapters 2 & 3 of this thesis and have resulted in subsequent journal publications. In addition we address the role of cartilage curvature as Riemannian manifold to account for shape variations and curvature computation using the Riemannian manifold which may be implemented as a MRI imaging biomarker which comprises chapter 4. Finally we introduce a software prototype tool for OA analysis using MRI images in chapter 5 with final conclusions in chapter 6.

Acknowledgements

I would like to thank my supervisors, Dr. Jiang and Dr. Gale for their constant support and guidance during this research project. Dr. Jiang has been a good mentor, providing a stimulating environment and technical insights wherever necessary. I thank both my supervisors for providing encouragement and assistance during this project.

I would also like to thank Changai Ding and Menzies Institute of Research, Tasmania, Australia for providing us with the MRI images used in this study. The images have primarily been used for the study of imaging algorithms which may help contribute towards efficient and early analysis of Osteoarthritis using MRI.

Last but not the least I would like to thank my family and friends for their love and encouragement during my study. They have been a constant source of motivation during my PhD study.

Contents

List of Figures

List of Tables

Publications

Journal:

- Aarya I., Jiang D., and Gale T., "Adaptive Rician Denoising with edge preservation for MR images of the articular cartilage". Computer Methods in Biomechanics and Biomedical Engineering: Imaging & Visualization, 2014, pp 1-10

- Aarya I., Jiang D. and Gale T., "Signal Dependent Rician noise denoising using nonlinear filter". Lecture Notes on Software Engineering, 2013, 1(4) 344-349.

- Aarya I., Jiang D., "Automated and optimal detection of 3D articular cartilage using undecimated wavelets in MRI". Signal, Image and video processing, 2015, 9(1), pp 305-314

- Aarya I., Jiang D., and Gale T., "Edge localisation in MRI for images with signal dependent noise". Electronic Letters, 2015, 51(15), pp 1151-1153.

- Aarya I., Jiang D., "Articular cartilage diagnosis for Osteoarthritis using wavelet multiresolution GUI". Draft

Conference:

- Aarya. I, Jiang D. and Gale T., "Adaptive SNR Filtering Technique for Rician Noise Denoising in MRI". Biomedical Engineering International Conference (BMEiCON), 2013 6th IEEE conference, pg. 1- 5.

Abbreviations

OA	**O**steo**A**rthritis
MRI	**M**agnetic **R**esonance **I**maging
ACR	**A**merican **C**ollege of **R**heumatology
KL	**K**ellgren **L**aw
CT	**C**omputed **T**omography
μ-CT	**M**icro **C**omputed **T**omography
WORMS	**W**hole **OR**gan **M**ri **S**coring
WOMAC	**W**estern **O**ntario and **McM**aster Universities Osteoarthritis Index
KOSS	**K**nee **O**steoarthritis **S**coring **S**ystem
BLOKS	**B**oston **L**eeds **O**steoarthritis **K**nee **S**coring
SNR	**S**ignal to **N**oise **R**atio
PSNR	**P**ower **S**ignal **N**oise **R**atio
CNR	**C**ontrast **N**oise **R**atio
MRA	**M**ulti **R**esolution **A**nalysis
MLE	**M**aximum **L**ikelihood **E**stimation
PDE	**P**artial **D**ifferential **E**quation
LMMSE	**L**inear **M**inimum **M**ean **S**quare **E**stimation
TE	**T**ime **E**cho
TR	**T**ime **R**epetition
RMSE	**R**oot **M**ean **S**quare **E**rror
MSE	**M**ean **S**quare **E**rror
MSSIM	**M**ean **S**tructural **SIM**ilarity indes
SSIM	**S**tructural **SIM**imilarity index
QILV	**Q**uality **I**ndex based on **L**ocal **V**ariance
BF	**B**rown **F**orsythe

ANOVA	**An**alysis **o**f **Va**riance
MAE	**M**ean **A**bsolute **E**rror
FT	**F**ourier **T**ransform
WT	**W**avelet **T**ransform
STFT	**S**hort **T**ime **Fourier T**ransform
UWT	**U**ndecimated **W**avelet **T**ransform
DWT	**D**iscrete **W**avelet **T**ransform
CWT	**C**ontinous **W**avelet **T**ransform
WTMM	**W**avelet **T**ransform **M**odulus **M**axima
WTMS	**W**avelet **T**ransform **M**odulus **S**um
COI	**C**one **O**f **I**nfluence
FIR	**F**inite **R**esponse **F**ilter
FOM	**F**igure **O**f **M**erit
CoC	**Co**rrelation **C**oefficient
QMF	**Q**uadrature **M**irror **F**ilter
HKS	**H**eat **K**ernel **S**ignatures
VKS	**V**olume **K**ernel **S**ignatures

Symbols

M	Magnitude image function	μ_{VI}	mean of true image
A	True image function	μ_{VJ}	mean of denoised image
n_r	noise real component	σ_{VI}	standard deviation of true
n_i	noise imaginary component	σ_{VJ}	standard deviation of denoised
P	Probability distribution function	μ_1	mean of high intensity region
σ_n	standard deviation of Rician noise	μ_2	mean of low intensity region
I_0	Zero order Bessel function	r	observed signal
$\bar{M}$	Estimated image function	s	true signal
$\tilde{A}$	Estimated true signal function	n	noise
$\sigma_{i,j}$	Regional standard deviation	k	multiplicative factor
H_0	Proposition 1	f_s	signal function
H_a	Proposition 2	$\hat{\sigma_n}$	estimate variance noise
$z_{i,j}$	group variable after absolute deviation	$\dot{M}$	observed data
$y_{i,j}$	group variable	y	observed noisy image
$\tilde{y_j}$	group median	$\hat{x}$	desired signal
W	BF statistic value	e	error
N	total number of observations within group	R_{xx}	desired signal autocorrelation
k	total number of groups	r_{xy}	cross correlation
N_i	total number of variables in individual group	R_{yy}	observed signal autocorrelation
Z_i	group mean	W	Wiener filter
$Z..$	overall mean	W_{opt}	Optimal wiener output

F_α	F-table value for selected alpha	$W_{u,v}$	Wiener filter coordinates
$d_{i,j}$	Euclidean distance	$\hat{H}$	complex conjugate of H
h	smoothing parameter	P_{xx}	power spectral density signal
NL	nonlocal estimate	P_{nn}	power spectral density noise
v	noisy image	Y	signal
$E\{\}$	moments	$\hat{M}$	observed signal estimate
$A_{i,j}$	true signal intensity	$\hat{A}$	true signal estimate
$K_{i,j}$	correction factor for LMMSE	c_{j+1}	scaling coefficients
$N_{i,j}$	Neighbourhood	n	signal
I_{ref}	true reference image	h_j	forward low pass filter
I_{test}	test image	g_j	forward high pass filter
I	true image	k	filter length
J	denoised image	w_j	wavelet coefficients
g_i	high pass filter	$\tilde{h_j}$	inverse low pass filter
$\tilde{g_j}$	inverse high pass filter	P_R	Rayleigh distribution
c_ψ	wavelet coefficients	μ_R	Rayleigh sample mean
σ_R	estimated variance Rayleigh distribution	$c_{\hat{\psi}_R}$	estimated Rayleigh mean
t_1	t-distribution value	$\frac{\alpha}{2}$	alpha t-table
S_R	sample variance Rayleigh distribution	N_P	degrees of freedom
$c_{\hat{\psi}_G}$	estimated Gaussian mean	t	t-distribution
t_l	local threshold	i_{RH}	Rayleigh intensity
i_{GL}	Gaussian intensity	b_{RH}	Rayleigh pixel data
b_{GL}	Gaussian pixel data	$L^2(R)$	square integrable space
V_j	scale space	W_j	wavelet space
W	wavelet function	$f(u,s)$	signal function wavelet domain
A	constant	s	wavelet scale
N_s	WTMS	W_s	wavelet function at s
$\grave{A}$	modified constant	W_r	wavelet inter-scale ratio
$\grave{\gamma}$	proposed global threshold	γ	wavelet inter-scale difference
$E[]$	expectation operation	y_s	edge response
y_n	noise response	δ	MSE

$\hat{l}$	detected position	l	true position
$E_0[]$	final edge	k	principal curvatures
K	Gaussian Curvature	H	Mean curvature
$T_p(S)$	Tangent space for surface S	S	parametrized shape surface
N	Normal for surface S	$g_{i,j}$	Riemannian metric
E, F, G	First Fundamental coefficient	e, f, g	Second Fundamental coefficient
W_p	Wavelet Fundamental form	M, R	Riemannian manifold
P	position vector	ϕ_t	level-set curvature function
$\xi_{i,j}$	local shape coordinates		

Dedicated to Shagun, Nikhitta & Yash

Chapter 1

Introduction: Osteoarthritis Diagnosis & MR image processing

This chapter is an insight to the PhD research topic and provides an introduction to Osteoarthritis (OA), physiology and current clinical diagnostic procedures with MRI. In addition it also discusses the motivation of this project, research objectives and the overall layout of this thesis.

1.1 Introduction

Osteoarthritis (OA) is a disease of the musculo-skeletal joint characterized by loss of the articular cartilage tissue (Vincent and Watt, 2010). It is predominantly classified under the group of arthritic diseases and is usually considered as an age related occurrence. But there has been increasing evidence that it may take place much earlier in life depending on individual circumstances. Australia alone has observed 1.9 million cases with an expenditure of $3.75 billion in 2012 (Elsternwick, 2013). This number is estimated to increase by 1.1 million by 2032 with an expected growth rate of 58% (Elsternwick, 2013). This medical condition not only incurs direct medical expenditure but also affects the productivity and quality of life of the individual suffering from the disease. Recent attention to this ailment has been directed towards early detection of Osteoarthritis with a possibility of better treatment procedures.

The primary challenge often found is the nature of the disease and its various definitions across different radiographic, clinical and pathological groups. Articular cartilage tissue assessment differs across these different study groups and may also include the different

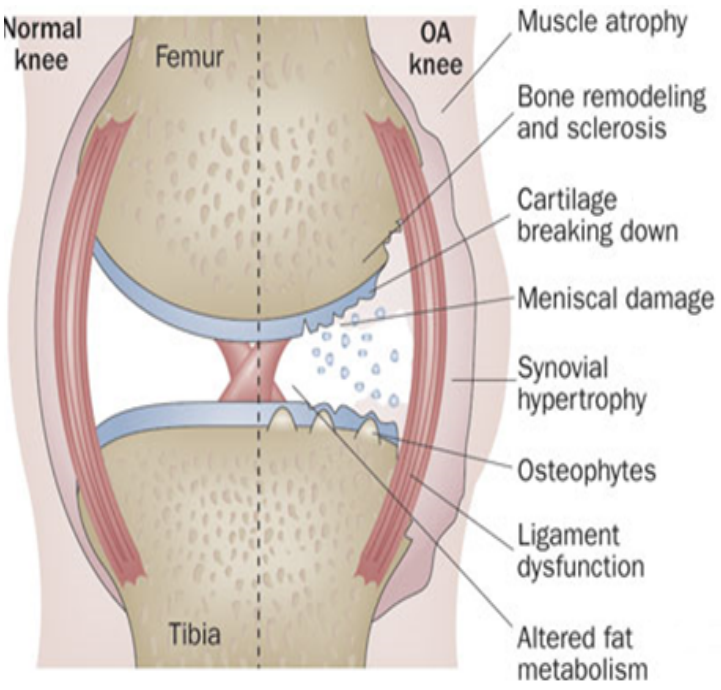

FIGURE 1.1: Comparison between normal and osteoarthritic knee (Hunter, 2011)

selection and grading criteria and hence lacks a unified universal assessment of OA (Adams and Wallace, 1991). The clinical definition as proposed by the American College of Rheumatology (ACR) committee encompasses osteophytosis, age, crepitus and other evidence in addition to pain and cartilage loss. While other groups may also consider peripheral joint disturbance in addition to above mentioned symptoms some may also include loss of cartilage and osteophyte formation for its pathological assessment (Adams and Wallace, 1991). As a result there exists a huge spectrum of assessment criteria including physical, chemical, physiological and metabolic factors which increases the complexity of the nature of disease. The following subsections briefly describe the OA pathology, causative factors, diagnostic procedures and treatment methods.

1.1.1 OA pathology

Articular cartilage is present mostly in the synovial joints of the human body. It is a smooth and a fibrous connective tissue which enables frictionless gliding movements of the bones. A healthy cartilage is bluish-white with a shiny appearance and is composed of bio-molecules such as proteoglycans, water and collagen matrix (Kumar et al., 2011; Crema et al., 2011). Collagen provides the necessary shear and tensile strength to the cartilage tissue while proteoglycans provide it with the compressive strength (Crema et al., 2011). Chondrocytes present in the cartilage tissue, are primarily responsible for

maintaining a healthy extracellular matrix without which the tissue is unable to withstand mechanical stress within the joint (Adams and Wallace, 1991).

It is suspected by most of the research groups, that during the presence of OA the proteoglycan content of the tissue may be reduced which results in less retention of water molecules (Kumar et al., 2011; Crema et al., 2011). Absence of this proteoglycan content makes cartilage tissue susceptible to degradation and causes it to wear out thus exposing the underlying bone (Crema et al., 2011). Research also indicates that study of these biomolecules may provide an insight towards early stages of OA (Kumar et al., 2011; Theiler et al., 1994).

Since cartilage tissue is devoid of any blood vessels and pain receptors it is unable to heal itself in case of any structural damage. It is also one of the reasons why early stage cartilage tissue damage goes unnoticed. In addition damage and/or mechanical stress to the surrounding muscle group may also be one of the causative factors for knee OA (Vincent and Watt, 2010; Adams and Wallace, 1991). Loss of cartilage tissue further results in bone on bone friction due to the exposed area of the bone surface. And while cartilage tissue itself may be devoid of any pain receptors, there exists a large amount of blood vessels and nerve endings within the bone tissue resulting in excruciating pain, inflammation and swelling with loss of joint mobility.

During the early stages of OA the cartilage often displays fibrillation of the surface followed by fissures and thinning of the tissue as also demonstrated by Fig. (1.1) (Vincent and Watt, 2010; Adams and Wallace, 1991). As the disease progresses, there might be presence of bone spurs or osteophytes in the synovial fluid surrounding the joint which may eventually lead to loss of the cartilage tissue in the final stages of OA. Although OA commonly affects large weight bearing joints such as hip and knee it is also observed in the joints of hand, feet and spine (Vincent and Watt, 2010; Adams and Wallace, 1991).

Pain has been a primary indicator of OA, caused as a result of joint pain. It may often be misleading as early stage OA may be asymptomatic; while cartilage damage progresses silently within the tissue (Theiler et al., 1994). Patients may also experience joint stiffness, loss of movement, joint locking and crepitus during joint movement. And while OA may be a non-inflammatory condition some patients do experience inflammation. Joint deformities and joint re-modelling may also be observed during the later stages of OA (Bijlsma et al.,2011).

1.1.2 Causative Factors

OA can be caused by a wide range of multiple factors, it affects all population and is prevalent worldwide (Ding et al., 2007). Generally most of the epidemiological studies indicate an exponential trend with respect to age, usually after 40 years (Elsternwick, 2013). The reason though unknown is largely suspected to be due to fatigue failure of the cartilage. OA is also known to have a higher prevalence amongst females as compared to men with a conflicting evidence indicating role of oestrogen in pathogenesis (Vincent and Watt, 2010). Recent evidence may also indicate obesity as the cause of the disease while genetic evidence points towards type-II procollagen gene to be associated with genetically related OA (Vincent and Watt, 2010).

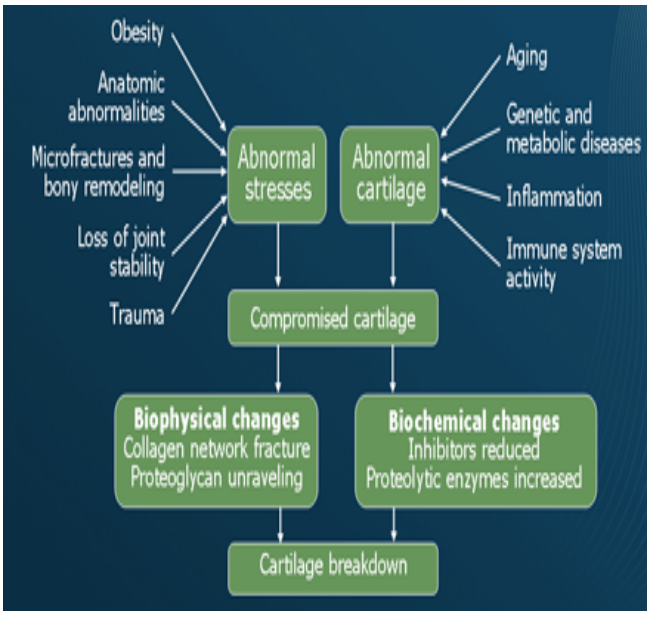

FIGURE 1.2: Various factors responsible for OA (Spitzer)

Premature OA may also be caused due to direct or secondary injury to knee joint, metabolic condition and joint abnormality. And while some research groups have observed OA in patients with joint hyper-mobility and high mechanical loading it is also found to be present in patients with severe paralysis. OA may be considered as primary where cartilage loss and damage is the prime factor of the disease such as those observed in ageing. But in cases where cartilage modification is a subsequent occurrence caused due to compromise within the knee joint OA is considered as secondary. The wide spectrum of causative factors, slow development of disease and a high variance in the nature of disease has added to the complexity of diagnosis and a relative cure for it.

1.1.3 Current Diagnostic Procedures

Traditional diagnostic procedures for OA include visual inspection of the joint and further corroboration of evidence using medical images such as X-rays as demonstrated by Tab. 1.1 (Adams and Wallace, 1991). Clinical inspections along with image information are together used to confirm presence of OA and to grade the cartilage according to degree of disease progression.

TABLE 1.1: Pathological features of OA appearing in imaging (Theiler et al.,1994)

Anatomy	Pathological Changes
Cartilage Degeneration	Fibrillation
	Fissuring
	Erosions
	Loss/joint space narrowing
Bone reaction	Increased Vascularity
	Trabecular remodeling
	Subchondral sclerosis
	Eburnation
	Cyst formation
	Osteophyte formation
	Osteonecrosis
Synovial reaction	Synovial effusions
	Capsular fibrosis
Other Features	meniscal/ligament tears
	Pathological calcification
	angular deformities

X-rays are the common choice of imaging modality used for knee OA diagnosis due to its high spatial resolution and cost efficiency; and are currently considered as the gold standard for OA evaluation (Bijlsma et al., 2011). Kellengren-Law (KL) as also indicated by Tab. 1.2 is the benchmark grading system which utilizes radiographic images and is a universally accepted standard (Eckstein et al., 2006). Although X-rays cannot detect changes in the cartilage tissue itself, they can monitor changes in the joint space narrowing and look for presence of osteophytes as demonstrated in Fig.(1.3). As a result

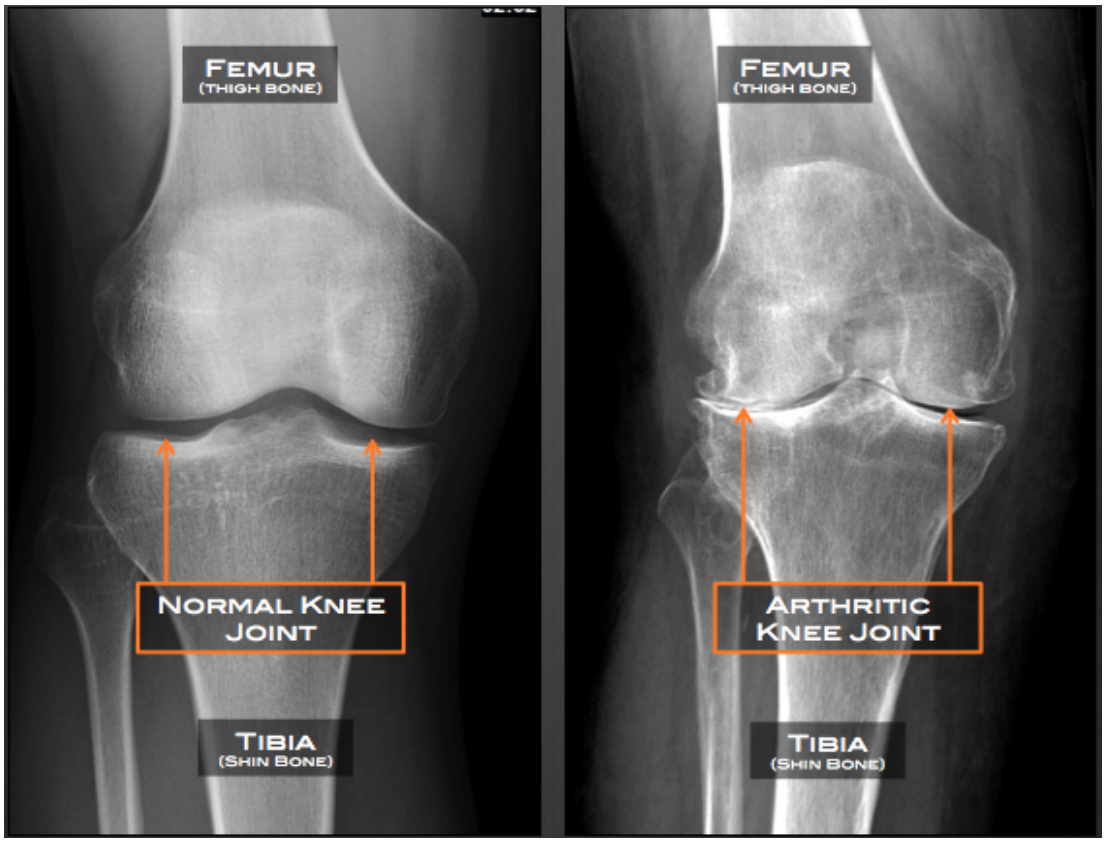

FIGURE 1.3: Joint space narrowing using X-rays (Driscoll)

X-ray performance has been restricted to detection of late stage OA commonly affecting the bone tissue (Bijlsma et al., 2011).

Other imaging modalities for OA include computed tomography (CT) and micro-CT (u-CT) which offer a higher resolution imaging, thus enabling detection of fibrillation of the cartilage surface; despite X-rays and CT exposing patient to harmful ionizing radiation (Kumar et al., 2011; Bijlsma et al., 2011). Ultrasound (US) has also been proposed for OA diagnosis and makes use of sound waves to image the cartilage tissue. The potential of this imaging modality is limited by its poor resolution and inability to image deep tissues due to absorption of US waves. Although it should be noted that both US and MRI are capable of offering a safer and a non-invasive diagnostic procedure for OA (Kumar et al., 2011; Adams and Wallace, 1991; Bijlsma et al., 2011).

Due to high Tesla MRI machines and advanced imaging sequences, we are now able to provide a better visualization of the articular cartilage tissue. MRI offers improved cartilage visualization due to its better contrast resolution. A study of the cartilage biomolecules such as the proteoglycans and water content is now possible with the help of different image sequences. This may be attained by utilizing MR imaging sequences

such as delayed gadolinium enhanced MR imaging (dGEMRIC), T1ρ imaging, sodium and diffusion weighted sequences which highlight the specific tissue by changing the contrast within the region of interest as indicated by Tab. 1.3. Other imaging sequences such as standard spin-echo (SE), fast spin-echo (FSE), and gradient recall echo (GRE) may also be employed (Crema et al., 2011). And although higher Tesla field improves the SNR, image quality and relative spatial resolution of the image with reduced acquisition time; a low magnetic field strength of 1T may still be adequate enough for imaging of the articular cartilage tissue if required (Bijlsma et al., 2011).

In addition to visualization, a morphologic assessment of the cartilage tissue with MRI is also possible. It may include assessment of the knee and the surrounding joint structure using either a quantitative or semi-quantitative method (Eckstein et al., 2006; Gold et al., 2009).

These modifications in the cartilage structure and its chemical properties may also be observed and quantified for the purposes of grading. OA grading systems with help of WORMS and WOMAC have already been proposed to categorize disease progression with help of MR images (Theiler et al., 1994; Bijlsma et al., 2011). These grading systems may also be used to provide knee joint evaluation after surgery and drug treatment (Bijlsma et al., 2011). Hence MRI is obtaining a wide popularity among clinicians for early stage diagnosis of Osteoarthritis.

TABLE 1.2: Kellgren-Lawrence radiographical grading system for OA (Theiler et al.,1994)

Grade	0	None	No features of OA
	1	Doubtful	Minute Osteophyte, doubtful significance
	2	Minimal	Definite osteophyte, unimpaired joint space
	3	Moderate	Moderate diminution of joint space
	4	Severe	Joint space greatly impaired with sclerosis of subchondral bone.

TABLE 1.3: MRI Imaging techniques for assessment of tissue-structure damage in OA (Bijlsma et al., 2011)

Sequence	**Study**	**Advantage**	**Disadvantage**
Standard SPGR	cartilage morphology	3D quantitative	Time consuming
T2 MRI	Collagen distribution	Semi-quantitative, provides information on cartilage quality, validated, does not require contrast agent	complex interpretation
T1 ρ	Proteoglycan distribution	Semiquantitative with information on cartilage quality, high sensitivity to early degeneration, does not require contrast agent	requires special pulse sequences, not yet validated
Na MRI	FCD/Proteoglycan content	Semiquantitative, does not require contrast agent	Field strength $\geq$ 3T, not yet validates
dGEMRIC	FCD/Proteoglycan content	Semiquantitative, information on early changes, well validated	contrast agent required with time delay

1.1.4 OA grading systems

OA grading systems often rely on the use of imaging modality and biomarkers to assess and grade the degree of arthritis within the cartilage tissue. In addition to cartilage assessment they may also help in improving the understanding of OA progression and its natural propensity under mechanical loading within the joint. Some of the pathological changes mentioned in Tab. 1.1 are the most commonly used criteria for OA assessment.

Pain still remains the most prevalent and common indicator for OA although it is quite subjective and is an unreliable biomarker.

The Kellgren-Law (KL) grading system indicated in Tab. 1.2 was developed in 1957; it is a universally accepted gold standard and primarily works in conjunction with X-ray imaging modality (Theiler et al., 1994; Bijlsma et al., 2011). X-rays with their high spatial resolution, predominantly provide information with respect to the denser bone tissue but lack tissue analysis as compared to the other synovial and cartilage soft tissue.

As a result the grading system is designed to take into account the osteophyte formation, joint space narrowing (JSN) and bone sclerosis as an additional criteria for grading of cartilage. Any 3D or soft tissue information is not available with X-rays which is a considerable drawback (Bijlsma et al., 2011). In addition any significant changes in the clinical biomarkers indicated in Tab. 1.2, may take at least 1-2 years for a smallest detectable change such as of 0.20 mm in joint space width (JSW) (Ding et al., 2007). As a result articular cartilage grading with X-rays is restricted to extremely severe stages of OA, usually of clinical grade 3 and grade 4.

In contrast MRI may be able to provide a quantitative assessment of the cartilage tissue by predominantly monitoring changes within the tissue itself (Gold et al., 2009; Guermazi et al., 2011). A wide variety of imaging sequences can now help in visualization of both cartilage and the periarticular tissues despite limitations in spatial resolution. The semi-quantitative scoring systems in MRI may also take into consideration the size and location of lesion, subchondral and cartilaginous bone and other aberrations within the joint in addition to tissue information (Theiler et al., 1994; Eckstein et al., 2006). Whole organ scoring systems such as knee osteoarthritis scoring system (KOSS), whole organ MR scoring (WORMS) and Boston-Leeds OA knee scoring (BLOKS) look at complete cartilage structure with focus on tissue quality. WORMS and BLOKS both divide the cartilage surface into several medial and lateral regions within the femoral and tibial cartilage surface (Hunter et al., 2011; Hunter et al., 2008). The thickness and area are used as biomarkers to define the interrelation between these sub-regions for OA grading. Both WORMS and BLOKS are at par with results for several conditions of the cartilage tissue. Although the assessment is necessitated by an accurate and reliable detection of the cartilage and is dependent on the evaluator of the scoring system.

The scoring systems are often complex and time consuming process with reduced reproducibility due to lack of standardization in imaging and acquisition protocol. There may exist an inter-observer and intra-observer variability in the grading process depending on the observer reliability (Bijlsma et al., 2011). As a result it is thus desirable to offer a more robust scoring system with reduced observer dependence. In addition as OA progresses slowly, the grading system and biomarkers should be able to account for changes during these relative transitions.

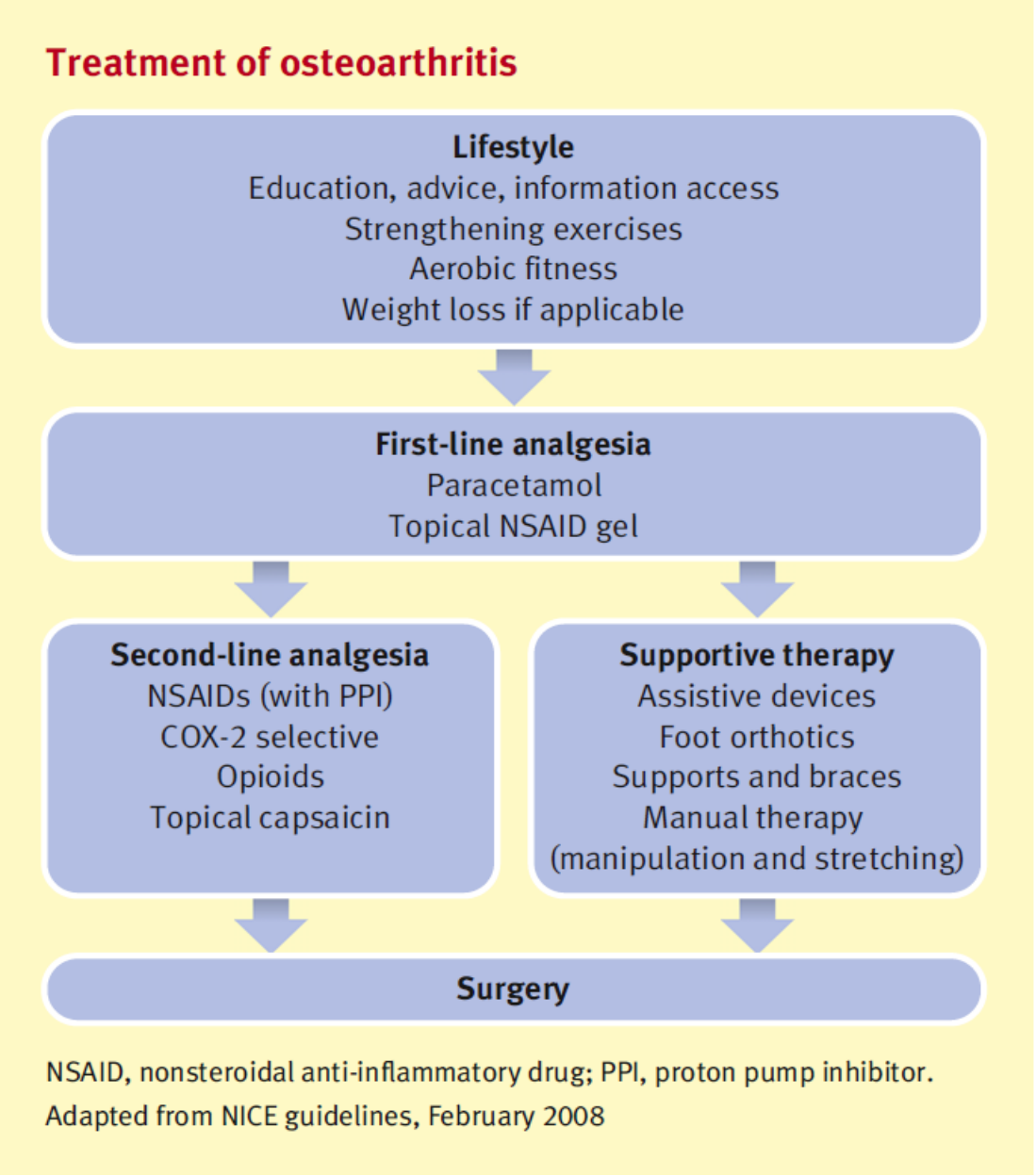

FIGURE 1.4: treatment procedures for OA (Bijlsma et al., 2011)

1.1.5 Treatment

Currently there exists no cure for OA. It can only be treated for pain and joint immobility. Current treatment methods may include intervention to slow down cartilage loss and relief from pain. These procedures include exercise, change in lifestyle and diet, use of analgesics and NSAIDS as indicated by Fig. (1.4) (Bijlsma et al., 2011). Assistive devices such as foot orthotics and braces may also be provided. If pain becomes debilitating with complete restriction of movement, the patient may then be offered a joint replacement surgery upon the discretion of their orthopaedic surgeon and patient history. New treatment procedures are focussing on slowing and if possible reversal of

cartilage loss but are constricted due to lack of knowledge of physiology of early stage of OA, cartilage changes and joint biomechanics for OA. They are also limited by lack of accurate assessment of cartilage tissue with help of imaging techniques.

1.2 Project Motivation

This project considers 3D image processing and modelling of MRI images, for an efficient analysis of the articular cartilage of the knee for OA, as also demonstrated in Fig. (1.5). As new MRI imaging sequences are being developed for better soft tissue visualization there is a huge potential to work with pre-processing and post-processing of MRI data. The project aims to develop new and novel 3D image processing algorithms, using MRI image data that enables efficient cartilage detection which will subsequently be utilized for developing 3D model and assessment of cartilage tissue. The articular cartilage tissue often suffers from artefacts and limited contrast resolution that can affect the accuracy of any cartilage detection process and its subsequent quantitative assessment for OA prognosis. Also the current clinical cartilage detection procedures are usually manual in nature and may introduce an operator induced error.

This project will address the issues of noise and cartilage detection in MRI. It will also try to achieve 3D modelling for cartilage visualization. For this purpose it will specifically address Rician noise present in single coil magnitude MRI image and try to reduce the effect of noise with an overall improvement in image quality by using the proposed denoising technique. An investigation of incorporating multiresolution analysis using wavelets for a more efficient cartilage diagnosis and visualization will also be carried out. In addition this thesis also looks at the possibility of developing a more robust MRI image biomarker for cartilage shape analysis that may be able to address cartilage shape variations.

1.2.1 Research Objectives

The primary objectives of this research include,

- Rician noise removal for the cartilage image to improve the signal content and contrast ratio.
- Automated and efficient 3D cartilage detection with multiresolution analysis.
- Structural descriptor for cartilage shape.

- GUI development for assessment for cartilage tissue using imaging parameters.

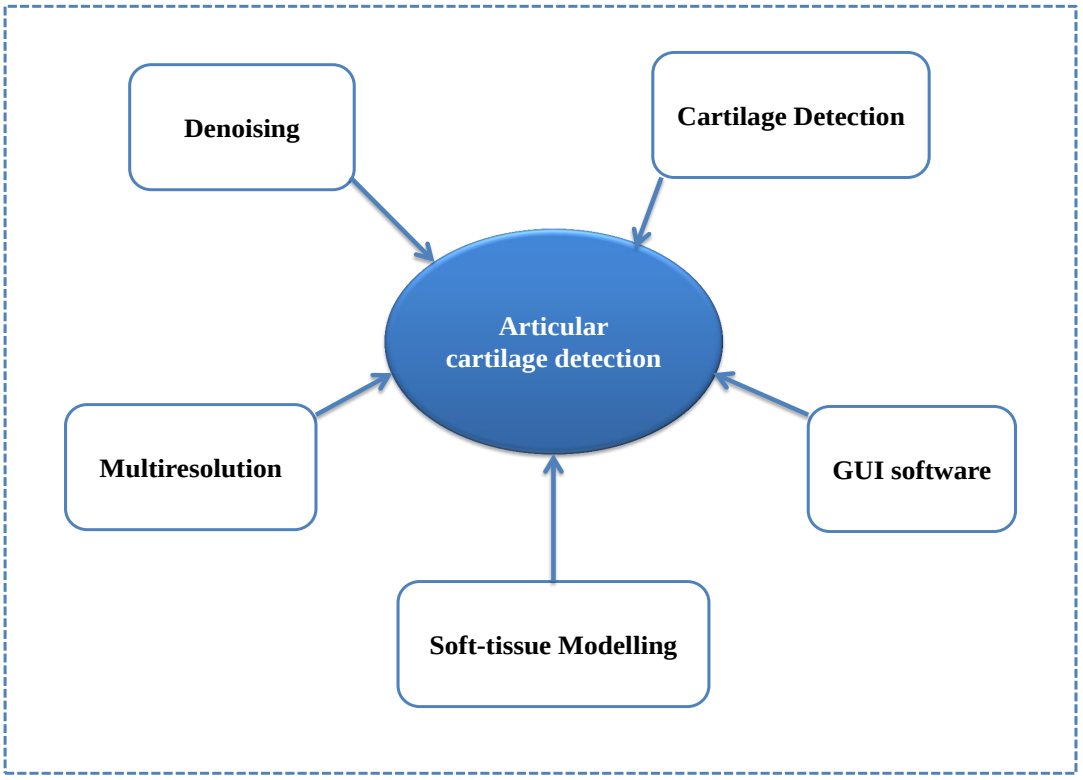

FIGURE 1.5: Research Overview

1.2.2 Rician Denoising

This thesis addresses the key issues of Rician noise present in a knee MRI image and its effect on the signal quality. Due to improved contrast resolution offered by MRI images, they are currently in focus for cartilage imaging and visualization. Observing changes in the cartilage shape, its boundaries and the surrounding joint structure may enable us to analyse cartilage shape for OA and propose necessary interventional therapies to delay the onset of complete OA.

But similar to other imaging modalities, MRI too suffers from noise and imaging artefacts due to their longer acquisition time. Recent studies have indicated that this noise in a single coil MRI image may be a non-linear signal dependent Rician noise, as against the previously assumed Gaussian noise. There has been evidence, that although noise present in raw k-space data may be Gaussian; restructuring of this data into a magnitude image causes this noise to follow a non-linear Rician distribution (Sijbers et al., 1998). This noise is signal dependent and affects contrast and the overall signal quality of an image. As a result, presence of noise may reduce the sensitivity of any cartilage

detection methods and their efficiency in diagnosis of OA with help of cartilage tissue information. In addition cartilage being a thin tissue with a thickness of only few pixels, is further degraded due to loss of tissue during OA. This added complexity increases the demand on the image processing task to provide adequate denoising with a better preservation of all the image details while achieving an overall improvement in the image quality.

This thesis focuses on providing sufficient Rician denoising for single coil magnitude MRI images while still retaining the crucial image details. The existing denoising methods for Rician noise focus more towards an accurate estimation of the variance of Rician noise in order to improve the efficiency of the noise removal techniques. This thesis, in addition to Rician denosing tries to achieve edge preservation in the image while doing so. Such an operation will retain all necessary image details which may help in more efficient cartilage detection for OA diagnosis. In order to do this it proposes a new adaptive Rician denoising method which selects edge as a non-homogeneous region with the help of local statistics and Brown-Forsythe hypothesis. A modified nonlocal weight is attributed to this non-homogeneous region to preserve edge information, followed by a LMMSE signal estimation to reduce the effect of noise. As a result the proposed method is able to offer improved Rician denosing with edge preserving ability.

In addition this thesis also investigates the non-linear influence of Rician noise on MRI signal. It has tried to capture this attribute of Rician noise on a MRI signal and propose a non-linear filter design for Rician denoising. Two different studies addressing SNR and signal dependent characteristics of Rician noise with help of local statistics in the image data have been addressed.

1.2.3 Multiresolution cartilage detection

An efficient and robust diagnosis of OA relies on an accurate detection and segmentation of the cartilage tissue. Current clinical practices depend on the expertise of an experienced operator who manually segments the cartilage tissue. This process is a time consuming, operator dependent and may suffer from inaccuracies and reliability. In addition the cartilage detection task is carried out in spatial domain and relies on the intensity information in the image as interpreted by the observer (Eckstein et al., 2006). Cartilage detection is performed slice by slice on 2D MRI image data which may lose resolution information along the third dimension; which also contributes towards the thickness estimation of the tissue (Eckstein et al., 2006; Pham et al., 2000, Folkesson

et al., 2007). Furthermore the contrast of the cartilage tissue is poor with respect to the surrounding fluid within the joint structure, which may make it a challenging task to segregate cartilage tissue especially in presence of noise or other inflammatory conditions of the knee joint. In these situations it is desirable to offer an automated and robust cartilage detection method that can address some of these issues if not all.

In this thesis we approach the cartilage detection task using multiresolution analysis. A wavelet based cartilage detection method which can perform 3D cartilage detection and optimization, with either limited or zero input from the operator is investigated. As wavelets are known to offer better event localization in a signal and can offer multiresolution analysis they have been selected for the 3D cartilage detection method. This thesis will try to obtain a 3D cartilage detection method with help of un-decimated wavelets which may help in observing the resolution information along all three axial directions. The proposed cartilage detection method is designed for an enhanced detection in presence of both poor contrast and noise. It also takes into consideration the modification of true signal content by Rician noise while achieving cartilage detection. The proposed method performs cartilage detection in wavelet domain using both local and global wavelet resolutions with help of a 3D wavelet histogram. In addition, due to a 3D cartilage detection approach, we obtain cartilage detection along a MRI volume instead of 2D slices. As a result the proposed method is able to capture a more global information of the cartilage boundaries. The use of multiple wavelet resolutions will enable us to capture and optimize edges in the cartilage image that may enable in a more efficient and robust cartilage detection method. The final processed volume obtained with 3D cartilage detection method is later used for volume rendering for the 3D visualization of the cartilage surface. The proposed cartilage detection method reduces the need of an operator to perform cartilage detection and can also address the reduced image quality of MRI image due to noise. It also provides the clinician with an opportunity to observe the cartilage surface at multiple wavelet resolutions for a closer inspection of the tissue.

In addition the thesis also investigates the influence of Rician noise on a step edge in an image. Based on the study carried out, this thesis has proposed a new edge localization factor for step edges in a MRI image subjected to signal dependent Rician noise. The proposed localization factor is implemented using the first order edge detection filter.

1.2.4 Cartilage shape analysis

This thesis considers geometric shape analysis of the cartilage structure as a smooth 2D Riemannian manifold. While cartilage shape is universally considered as curvilinear, it still displays variations in its shape from person to person and also during different stages of OA. These shape variations may be used to study and predict cartilage tissue changes during different stages of OA. Recent studies have revealed the possibility of using the curvature information of the cartilage tissue as a MRI imaging biomarker for OA analysis (Folkesson et al., 2008; Tummala and Dam, 2010). Variations in curvature values of cartilage tissue may provide insight into early signs of tissue deformation and prediction of OA. Also curvature information provides an easy to compare structural parameter for changes in the cartilage tissue.

This thesis investigates computation of a geometric based cartilage shape descriptor using Riemannian geometry. It proposes use of new wavelet based Riemannian metric for computation of the Gaussian and mean curvature values as the geometric descriptor for cartilage structure. This descriptor will account for the global cartilage shape and the extrinsic information that may differ as the shape is deformed over time. For this purpose we will try to address the cartilage shape as a smooth continuous 2D Riemannian manifold and the use of extrinsic and intrinsic curvature information for the shape analysis. The intrinsic Gaussian curvature information is based on a global shape topology and is less susceptible to variations that may occur across different patient groups, while extrinsic mean curvature is a local information and takes into account the shape variations and may be used to observe regional cartilage shape variations. The gradients obtained with help of undecimated wavelet transform on the MRI volume are used as the partial differential equations of the cartilage surface in order to compute the Riemannian metric and reduce the necessity of obtaining a parametrized representation of the cartilage surface.

This curvature information is obtained using the cartilage data and may enable to capture early signs of cartilage deformation, unlike X-rays which look at only the bone tissue. Also unlike WORMS and BLOKS it does not require the user to classify and allocate regional surfaces on the cartilage surface for OA analysis, as the proposed curvature can predict both the global and local cartilage conditions. This geometric shape descriptor for cartilage tissue may also be used as a MRI imaging biomarker for OA analysis.

1.2.5 Software prototype and MRA GUI development

The image processing algorithms developed during this project will be assembled under a single software prototype framework as an OA assessment tool. In addition to the above imaging techniques developed for cartilage detection and analysis; we will also implement a new multiresolution widget that enables the user to visualize the cartilage surface at different wavelet resolutions and offer surface analysis of the cartilage tissue. The proposed widget was developed using 3D undecimated Haar wavelets and incorporated with the above mentioned imaging techniques for a closer inspection of the cartilage surface. This software prototype implements the proposed 3D cartilage detection method for MRI volume and enables the user, if they choose to do so, to be able to compute the surface information for different wavelet resolutions.

1.3 Thesis organization

The organization of this thesis and its individual chapters are explained in the following sections

1.3.1 Chapter 1

The first chapter provides a detailed introduction to Osteoarthritis, which encompasses clinical definition, pathogenesis, current clinical diagnostic procedures and the grading systems used for assessment. The several challenges in medical image analysis with MRI images for clinical diagnosis of OA have been identified. It also outlines the motivation of this project, its research objectives and methods.

1.3.2 Chapter 2

The second chapter addresses Rician noise observed in single coil magnitude MRI images. The chapter provides an introduction to Rician noise in MRI and its effect on image quality, related work and the proposed imaging algorithms. Rician noise can not only affect image quality but also contrast in the image which may inadvertently affect the cartilage detection process. In this chapter we propose a new denoising technique for Rician noise removal with edge preservation. The chapter is also part of the publication 'Adaptive Rician Denoising with edge preservation for MR images of the articular cartilage' in Computer Methods in Biomechanics and Biomedical Engineering: Imaging

& Visualization. The advantages of the proposed denoising technique include significant reduction in noise with an overall improvement in image quality and preservation of image details. It also conducts a further study on the signal dependent and non-linear characteristic of Rician noise in MRI image and investigates a new nonlinear denoising filter for the same. The proposed method and its results were published in 'Signal Dependent Rician noise denoising using nonlinear filter' for Lecture Notes in Software Engineering and 'Adaptive SNR Filtering Technique for Rician Noise Denoising in MRI' for BMEiCON 2013.

1.3.3 Chapter 3

Cartilage detection is the most crucial part of OA assessment and relies on effective segmentation of the tissue. In this chapter we propose a new cartilage detection method with wavelet multiresolution detection. This chapter is also part of the publication of 'Automated and optimal detection of 3D articular cartilage using undecimated wavelets in MRI' for Signal, Image and Video processing; using undecimated wavelets. In addition the chapter tries to give a detailed but brief introduction of undecimated wavelets for better cartilage detection and a few of its properties. Furthermore a separate study on presence of Rician noise on edges in MRI images has also been conducted. A new edge localization factor for signal with nonlinear dependent noise has been proposed and published as a letter, 'Edge localisation in MRI for images with signal dependent noise' for Electronic Letters.

1.3.4 Chapter 4

The focus of this chapter is a shape based geometric descriptor for articular cartilage surface. It investigates the use of Riemannian curvature as a possible metric for shape analysis for cartilage tissue. As a result it proposes use of a new wavelet based Riemannian metric for computation of the Gaussian and Mean curvature values as a geometric descriptor for cartilage structure. The descriptor is designed to investigate cartilage shape changes as an intrinsic curvature function with the help of Riemannian manifold and wavelets. The descriptor may help try to account for cartilage deformation and provide intrinsic and extrinsic shape parameters. Gaussian and mean curvatures have also been computed for the cartilage surface for different MRI datasets.

1.3.5 Chapter 5

This chapter focuses on the development of a software prototype system for OA diagnosis, using MRI and undecimated wavelet system. It implements the proposed cartilage detection method mentioned in Chapter 3, for 3D cartilage detection and multiresolution visualization. The proposed CAD system is designed for analysis and diagnosis of OA using knee MRI images. This chapter explains in detail the structure of the proposed CAD system and the architecture of the new 3D wavelet GUI. The wavelet GUI is a novel user interactive (UI) widget incorporating 3D wavelet multiresolution analysis. This widget uses the cartilage models obtained with the help of wavelet analysis for UI assessment of the tissue and computation of cartilage parameters. Wavelet multiresolution is used for visualization and zooming of cartilage details at different scales without distortion of information content. The prototype framework has been designed as a portable and independent unit.

1.3.6 Chapter 6

This chapter concludes the research project and highlights the new contributions of this work. It discusses the possible areas of future work for this project and the challenges that were addressed during the implementation of this project for OA. It also mentions the areas in the field of OA diagnosis that have yet to be addressed and the possible challenges and limitation faced by existing methods. It points towards the possible areas that may be undertaken for early stage OA diagnosis and in improving the accuracy and reliability of these methods.

Chapter 2

Rician Denoising for Articular Cartilage in MRI

This chapter is an introduction to Rician noise and its effect on MRI images. Several disadvantages in cartilage detection due to presence of Rician noise have also been identified. In this study we have specifically tried to address better denoising for cartilage, using an adaptive filter with edge preservation for MRI images affected by Rician noise. Also as Rician noise is nonlinear and signal dependent, we have conducted another study to address this dependence of noise on signal, while the third study implements a non-linear signal dependent filter to address Rician noise.

The results of this study have been published in the following

- Aarya I., Jiang D., and Gale T., "Adaptive Rician Denoising with Edge Preservation for MR Images of the Articular Cartilage". J. Computer Methods in Biomechanics and Biomedical Engineering: Imaging & Visualization. 2014, pp 1-10 (Aarya et al., 2014)
- Aarya. I, Jiang D. and Gale T., "Adaptive SNR Filtering Technique for Rician Noise Denoising in MRI". Biomedical Engineering International Conference (BMEiCON), 2013 6th IEEE conference, pg. 1- 5 (Aarya et al., 2013)
- Aarya I., Jiang D. and Gale T., "Signal Dependent Rician Noise Denoising using Nonlinear Filter". Lecture Notes on Software Engineering, 2013, 1(4) 344-349 (Aarya et al., 2013)

2.1 Rician noise and MRI

Osteoarthritis is a chronic joint disease affecting a large percentage of the world's population (Eckstein et al., 2006). It is mainly characterized by degradation of the cartilage tissue, with loss in volume of the cartilage as the disease progresses (Eckstein et al., 2006). Articular cartilage in healthy patients is 1.3 - 2.5 mm thick and less in patients suffering from Osteoarthritis (Eckstein et al., 2006). Due to its superior soft tissue contrast, MRI offers better visualization of the cartilage which enables to identify changes in the cartilage thickness and morphology (Adams and Wallace, 1991; Eckstein et al., 2006). These changes in the cartilage tissue may be used to predict various stages of disease progression in Osteoarthritis. MRI can therefore provide a non-invasive method for diagnosis of Osteoarthritis and help quantify the articular cartilage data (Kumar et al., 2011; Ding et al., 2007). To help in diagnosis one should be able to correctly identify the cartilage tissue and accurately isolate it from its surrounding joint structure for a quantitative analysis (Eckstein et al., 2006; Ding et al., 2007). A common problem faced for cartilage study, is the similarity in tissue contrast of the cartilage with the surrounding joint tissues (Cashman et al., 2002). This task is made even more difficult due to the reduced contrast ratio of the image in presence of noise. This reduced contrast ratio makes it difficult to differentiate between cartilage boundaries and the surrounding fluid, causing error in diagnosis (Cashman et al., 2002). Hence it is essential to reduce the effect of noise and improve image contrast to properly identify the cartilage tissue within the joint structure without any loss of cartilage information.

Noise is introduced in the MRI image due to limitations in the data acquisition time (Rajan et al., 2012). This noise in the k-space data is considered to be uncorrelated zero-mean Gaussian (Rajan et al., 2012). A magnitude image is obtained by computing the magnitude of the real and imaginary k-space data (Nowak, 1999; Gudbjartsson and Patz, 2005). MRI images are converted to magnitude images to avoid phase artefacts (Gudbjartsson and Patz, 2005). Due to this nonlinear operation noise follows a Rician distribution and is known as Rician noise. This noise is nonlinear and signal dependent and may significantly affect the image quality and contrast thus making it difficult to perform cartilage diagnosis (Adams and Wallace, 1991; Rajan et al., 2012). For single coil MRI data, the noise affects SNR and the overall contrast of the image (Sijbers et al., 1998). Rician noise displays a varying distribution depending on the SNR of the image (Sijbers et al., 1998; Nowak, 1999). Images exhibiting low SNR tend to follow a Rayleigh distribution while those with a higher SNR approximately follow a Gaussian distribution (Nowak, 1999). The magnitude image equation for MRI is given by Eq. (2.1) and its Rice

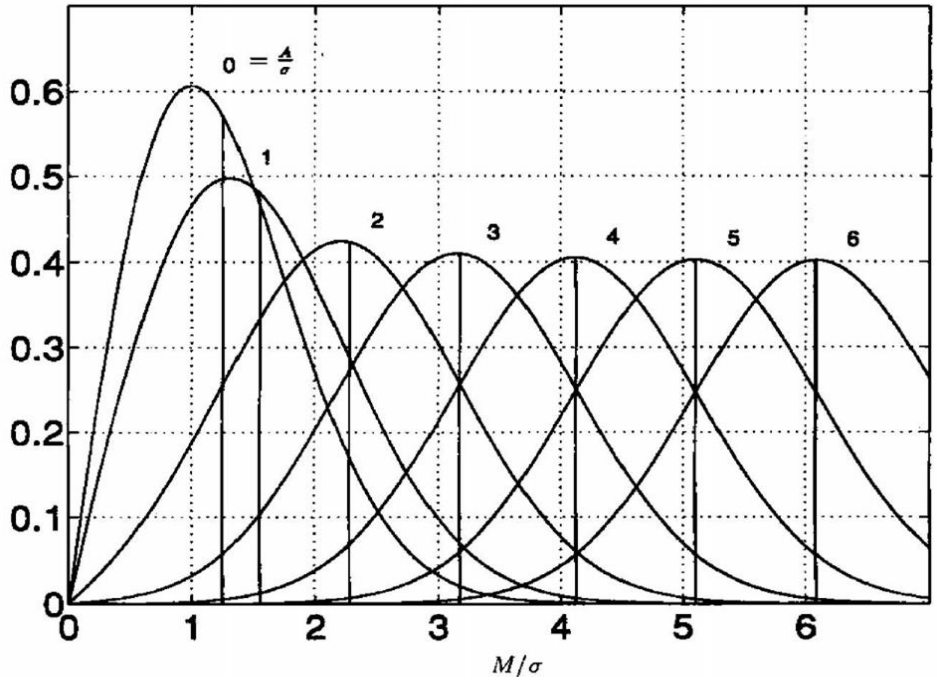

FIGURE 2.1: Rician probability distribution function for different standard deviations of noise and intensities Gudbjartsson and Patz, 2005

distribution function is given by Eq. (2.2) (Nowak, 1999; Gudbjartsson and Patz, 2005).

$$M = \sqrt{(A + n_r)^2 + n_i^2} \tag{2.1}$$

$$P(M|A, \sigma_n) = \frac{M}{\sigma_n^2} \exp(-\frac{M^2 + A^2}{2\sigma_n^2})\ I_0(\frac{A\ M}{\sigma_n^2}) \tag{2.2}$$

Where M represents the observed pixel intensity affected by noise, A represents true signal intensity, n_r represents real component of noise and n_i represents the imaginary component of noise. P is the Rician distribution function of noise in magnitude image and requires prior information of true signal intensity A. The variance of noise is given by σ_n and I_0 is the zero-order modified Bessel function (Gudbjartsson and Patz, 2005). As noise affects the original pixel intensity, it is essential that the denoising procedure helps to restore this original image information. This might be a difficult task, as the original nature of the signal is unknown to the user and actual variance of noise is seldom known. Adequate denoising can be achieved if one can correctly determine the value of variance of noise and its distribution within the image. This information about the noise may then be used to restore the image.

In the background of the MRI image where intensity of the signal function is zero, Rician noise follows a Rayleigh distribution (Gudbjartsson and Patz, 2005). This characteristic feature of Rician noise is often used to estimate the variance of noise in the image. The probability distribution function of Rayleigh noise is given by Eq. (2.3) and its mean is given by Eq. (2.4) (Gudbjartsson and Patz, 2005).

$$P(M) = \frac{M}{\sigma^2} exp(\frac{-M^2}{2\sigma^2}) \tag{2.3}$$

$$\bar{M} = \sigma\sqrt{\frac{\pi}{2}} \tag{2.4}$$

The noise in the magnitude MRI image can thus be obtained from the background of the image, where the signal function intensity is zero (Tran and Jiang, 2012). This estimation of noise is also used to carry out the denoising process. For higher SNR regions the Rician distribution function can be given by Eq. (2.5) and is very similar to the Gaussian distribution function (Gudbjartsson and Patz, 2005).

$$P(M) \approx \frac{1}{\sqrt{2\pi\sigma^2}} exp \frac{-(M - \sqrt{A^2 + \sigma^2})^2}{2\sigma^2} \tag{2.5}$$

The observed mean for the above distribution is very close to the actual mean of the signal function but may contain some bias due to the presence of noise (Gudbjartsson and Patz, 2005; Tran and Jiang, 2012). The bias can be corrected by using Eq. (2.6) (Gudbjartsson and Patz, 2005).

$$\tilde{A} = \sqrt{|M^2 - \sigma^2|} \tag{2.6}$$

While noise may be Rician for single coil systems it may no longer be Rician for multi-coil systems (Rajan et al., 2012). In MR images acquired with the parallel imaging techniques using multiple coil system, noise is highly inhomogeneous. Assuming that the noise components are still independent and identically distributed (IID); the envelope of the magnitude signal $M_L(x)$ will follow a non-central chi distribution with probability distribution function

$$P_{M_L}(M_L|A_L, \sigma_n, L) = \frac{A_L^{1-L}}{\sigma_n^2} M_L^L e^{\frac{-M_L^2 + A_L^2}{2\sigma_n^2}} I_{L-1}(\frac{A_L M_L}{\sigma_n^2}) \mu(M_L) \tag{2.7}$$

Where L is the number of coils and reduces to $L = 1$ for single coil systems. In the background this probability distribution function (PDF) reduces to central chi-distribution with PDF as (Rajan et al., 2012),

$$P_{M_L}(M_L|\sigma_n, L) = \frac{2^{1-L}}{\Gamma(L)} \frac{M_L^{2L-1}}{\sigma_n^{2L}} e^{\frac{-M_L^2}{2\sigma_n^2}} \mu(M_L) \tag{2.8}$$

above equation will become Rayleigh when $L = 1$. In such systems noise is still non-linear function but with a chi-square distribution function.

2.2 Related Work

Several denoising methods have been previously proposed for Rician noise removal in literature. Traditional denoising techniques using Gaussian filtering often cause blurring of the image boundaries and fail to improve image contrast as the noise in the image is assumed to follow a Gaussian distribution (Sijbers et al., 1998). Other methods involve use of Wiener filters, averaging filters, nonlocal means filtering, anisotropic filtering and parameter estimation techniques to determine true signal function using single and multiple images (Sijbers et al., 1998; Buades et al., 2005; Perona and Malik, 1990; Krissian and Aja-Fernandez, 2009). The efficiency of most of these procedures relies on accurate estimation of the noise in the image (Aja-Fernandez et al., 2008; Coupe et al., 2009).

Parameter estimation process, such as the 'Maximum-likelihood method' (MLE) are able to achieve considerable denoising for Rician noise as compared to traditional approaches; but they often rely on the accuracy of the noise variance σ_n selected in the estimation process (Sijbers et al., 1998). In addition these methods also rely on a prior knowledge of true signal intensity A (Sijbers et al., 1998). A conventional estimation approach for Rician noise may be given as follows,

$$\hat{A}_c = \sqrt{max(\langle M^2 \rangle - 2\sigma_n^2, 0)} \tag{2.9}$$

where $\langle M^2 \rangle$ is the sample second order moment. And the sample estimator is defined as,

$$\langle I \rangle = \frac{1}{\eta} \sum_{p \epsilon \eta} I_p \tag{2.10}$$

where η is a square neighbourhood. Whereas, the MLE of Rice distribution function results in,

$$\hat{A}_{ML} = argmax_A(logL) \tag{2.11}$$

with

$$logL = \sum_{i=1}^{N} log(I_0(\frac{AM_i}{\sigma_n^2})) - \frac{NA^2}{2\sigma_n^2} - \sum_{i=1}^{N} \frac{M_i^2}{2\sigma_n^2} \tag{2.12}$$

From the above equation it is quite clear that for parameter estimation methods one requires a-priori information to obtain adequate estimator for denoising. This phenomenon is also repeated with an estimator obtained using Expectation-maximization method given below,

$$\hat{A}_{k+1} = \frac{1}{N} \sum_{i=1}^{N} \frac{I_1(\frac{\hat{A}_k M_i}{\hat{\sigma}_k^2})}{I_0(\frac{\hat{A}_k M_i}{\hat{\sigma}_k^2})} M_i \tag{2.13}$$

where initial values are computed as $\hat{A}_0 = (2(\frac{1}{N}\sum_{i=1}^{N} M_i^2)^2 - \frac{1}{N}\sum_{i=1}^{N} M_i^4)^{1/4}$ and $\hat{\sigma}_0^2 = \frac{1}{2}(\frac{1}{N}\sum_{i=1}^{N} M_i^2 - \hat{A}_0)$. This estimator too is based on prior computation of signal and variance, which it uses to also compute the estimator for signal function. Other estimation techniques such as SureShrink and Bayesian estimation methods too face a similar problem and can be attributed to the nature of Rice distribution function (Van De Ville and Kocher, 2009; Lauwers et al., 2009).

As compared to previous methods, nonlocal means filtering uses image self-similarity for the noise removal process (Buades et al., 2005). But it may result in over smoothing of the image if the filtering parameter is not properly set (Buades et al., 2005). On the other hand, anisotropic filtering is a nonlinear filtering technique which preserves edge information in the image. Anisotropic filter make use of directional filters which searches for edge in the image (Perona and Malik, 1990; Krissian and Aja-Fernandez, 2009). This filtering technique follows the behaviour of partial density equation (PDE) of heat for the noise removal process (Perona and Malik, 1990). Anisotropic diffusion filters proposed by Perona and Malik are nonlinear filters and work by using local intensity within the homogeneous regions for smoothing (Perona and Malik, 1990). The smoothing operation is controlled by a diffusion process, obtained from partial differential equation of heat and stops in the presence of an edge, thus preserving edge details

(Perona and Malik, 1990). Median filters too are nonlinear filters and make use of local statistics for noise removal, but are found to be more suitable for suppressing impulsive noise (Perona and Malik, 1990). Median filters and anisotropic diffusion filters are both nonlinear filters with good edge preserving capabilities. Rician noise removal has also been addressed using TV filters. Total variation (TV) filters work with changes in the variation of the image due to presence of noise (Rudin et al., 1992 ; Tran and Jiang, 2012). Images with noise are considered to have a higher total variation as compared to noise free images (Rudin et al., 1992; Varghees et al., 2012).

Other filtering techniques using linear minimum mean square estimation (LMMSE) have recently been proposed to estimate true signal intensity using higher order moments of the Rice distribution function and are found to offer reliable denoising in presence of noise if the variance of noise is correctly estimated (Aja-Fernandez et al., 2008). LMMSE tries to determine the underlying true signal intensity with the help of expectation function of the true signal intensity and noise covariance matrix in the image (Aja-Fernandez et al., 2008). These higher order moments of Rice distribution function have also been used to determine the variance of noise. The general moment of the Rice distribution function is given as,

$$\acute{\mu} = \sigma^k 2^{k/2} \Gamma(1 + k/2) L_{k/2}(-\nu^2/2\sigma^2) \tag{2.14}$$

where $L_q(x)$ denotes Laguerre polynomial $L_q(x) = M(-q, 1, x) =_1 F_1(-q; 1; x)$ and $M(a, b, z) =_1 F_1(a; b; z)$ is the confluent hyper-geometric function of the first kind. When k is even the raw moments become simple polynomials in σ and ν given as,

$$\acute{\mu}_2 = 2\sigma^2 + \nu^2 \tag{2.15}$$

$$\acute{\mu}_4 = 8\sigma^4 + 8\sigma^2\nu^2 + \nu^4 \tag{2.16}$$

These higher order moments of Rice distribution function given by Eq. (2.15) and Eq. (2.16) are polynomial functions which can be used to determine the variance of noise (Aja-Fernandez et al., 2008).

Other Rician denoising procedures include use of histogram to determine variance of noise, wavelets, bilateral filters and Koay estimation technique using SNR of the image (Sijbers and Den Dekker, 2004; Nowak, 1999; Koay and Basser, 2006; Coupe et al., 2009;

Jiang and Yang, 2003). The Koay estimation techniques looks at generating analytical solution for a fixed point SNR which is subsequently used to estimate signal intensity. The analytical solution proposed by Koay et. al for a fixed point SNR is given as,

$$\theta = \sqrt{\xi(\theta)[1 + \frac{\langle M \rangle^2}{\sigma}] - 2} \tag{2.17}$$

where $\xi(\theta)$ is the correction factor and is given below

$$\xi(\theta) = 2 + \theta^2 - \frac{\pi}{8} e^{-\frac{\theta^2}{2}} [(2 + \theta^2) I_0(\frac{\theta^2}{4}) + \theta^2 I_1(\frac{\theta^2}{4})]^2 \tag{2.18}$$

which enables to determine signal intensity with help of following expressions,

$$\eta^2 = \langle M^2 \rangle + (1 - \frac{2}{\xi(\theta)})\sigma^2 \tag{2.19}$$

where η^2 is desired signal intensity to be estimated.

Similarly noise estimation techniques include mean absolute deviation (MAD) of the image using wavelets to estimate noise (Coupe et al., 2012). In addition, equation below demonstrates noise estimation using MAD and wavelets where w_j is wavelet coefficients of higher order sub-band (Bartušek et al., 2011; Nasri and Nezamabadi-pour, 2009; Li et al., 2008). The procedure involves use of statistics of the pixels obtained by wavelet domain transformation to determine deviation of pixels from the true values and as a result estimate the value of variance of noise (Coupe et al., 2012; Nowak, 1999; Jiang and Yang, 2003).

$$\sigma_{est} = \frac{MAD(w_j)}{0.6745} \tag{2.20}$$

As can be observed, most of the above methods are able to predict the value of noise variance and can be used for the denoising process. The choice of noise estimation can significantly impact the denoising process. In addition most of the above mentioned procedures do not consider the effect of dependent noise on the signal while filtering. Hence even though these procedures offer sufficient denoising they are not able to isolate noise from the true MR signal and may face limitation while estimating true signal intensity, when denoising. We know that Rice noise due to their signal dependent nature modifies the true intensity of the signal and changes contrast levels in the image. As a result, most of the above mentioned denoising procedures offer a trade-off between

either adequate denoising or loss of edge information and seldom offer improvement in the image contrast ratio.

2.3 Materials

Images used to perform the denoising study include two MRI data-sets, a phantom cartilage and brain MRI images. The image acquisition technique used for the first MRI dataset, was "TE 13 RF Fast FatSat" with TR=43, TE=13, flip angle of 50, number of averages is 1 and comprises of 62 slices. Dataset 2 was obtained using 'GR' scanning sequence with a series description of 'SAG Volume'. The number of averages is 1, with TR=31, TE=6, and flip angle of 30. The samples per pixel for both datasets was 1. All MR images were 512 x 512 pixels in resolution with a slice thickness of 1.5 mm and acquired with a magnetic field strength of 1.5 T. A Rician noise distribution was assumed for the MRI data-sets as the details of the original MRI scanner coil configurations were not available. Rician noise was chosen for illustrative purposes as typical of MRI noise and for simplicity of analysis.

As the MR images are already corrupted by noise due to the image acquisition process, they were used directly in the simulation study. A phantom cartilage image and brain MRI image were also used in the simulation study, as true noise free images. The phantom image was prepared in MATLAB and is 256 x 256 pixels, while the brain image of 128 x 128 pixels was obtained from the MATLAB image processing toolbox, from the 'imdemos' directory. Since these images were noise free they were artificially corrupted with Rician noise prior to the denoising procedure. The program code for the denoising study was written in MATLAB version R2012A in windows 7.

2.4 Proposed Methods

2.4.1 Adaptive edge detection

In this study we propose a novel Rician denoising procedure with edge preservation capability. Regions containing edges are identified by use of an adaptive circular mask and a localized smoothing of the region is performed. The proposed adaptive filter implements a Brown-Forsythe statistical criterion to avoid excessive filtering near the edges. Denoising is further achieved using LMMSE estimate of the regional sample, obtained using a modified nonlocal means estimate within the neighbourhood of the image. The

proposed filter was implemented on MRI images of the knee, synthetic and a phantom image. The efficiency of the denoising procedure was determined using SNR, RMSE, QILV and CNR ratios between true and denoised images of the cartilage. The method was also compared with other existing Rician denoising procedures and showed improved image contrast with edge preservation ability.

The proposed denoising method, is an adaptive filtering technique designed to preserve edge information while performing noise removal. In order to do this the method performs filtering by implementing a rotating circular mask to identify regions with and without edges and accordingly select sample regions within the neighbourhood to perform localized denoising. Based on the region selection criteria and orientation of an edge in the neighbourhood, nonlocal weights $w(i,j)$ are determined to compute the mean $NL[v]$ of the sample regions. To preserve edge information we implement modified nonlocal weights $w(i,j)$ where higher weights are imparted to pixels containing edge details.

The sample mean, $NL[v]$ thus computed is further used to implement a linear minimum mean square estimate (LMMSE) of the regions to determine the underlying signal intensity $A_{i,j}$. Such a denoising procedure avoids excessive smoothing of the edge information and at the same time performs localized noise removal. The variance of noise σ_n^2 used for the denoising procedure is determined using Eq. (2.21) (Aja-Fernandez et al., 2008).

$$\sigma_n^2 = \frac{1}{2N} \sum_{i,j=1}^{N} M_{i,j}^2 \tag{2.21}$$

Where, σ_n^2 is the variance of noise estimated from the background of the image, N is the total number of pixels within the mask, i and j indicate pixel positions and M is the observed signal information. This variance is determined from the background of the MRI image where noise follows a Rayleigh distribution due to zero intensity MR signal function (Sijbers et al., 1998; Aja-Fernandez et al., 2008). The flowchart for the denoising procedure is as shown in Fig. (2.2)

2.4.1.1 Adaptive Mask

An adaptive mask is used to achieve filtering, edge detection and region selection for denoising by the proposed method. A circular mask is used for this purpose, as it is found to provide a more dynamic approach in the edge detection process as compared to the traditional rectangular and square masks (Davies, 1984; Dongxiang et al., 2004;

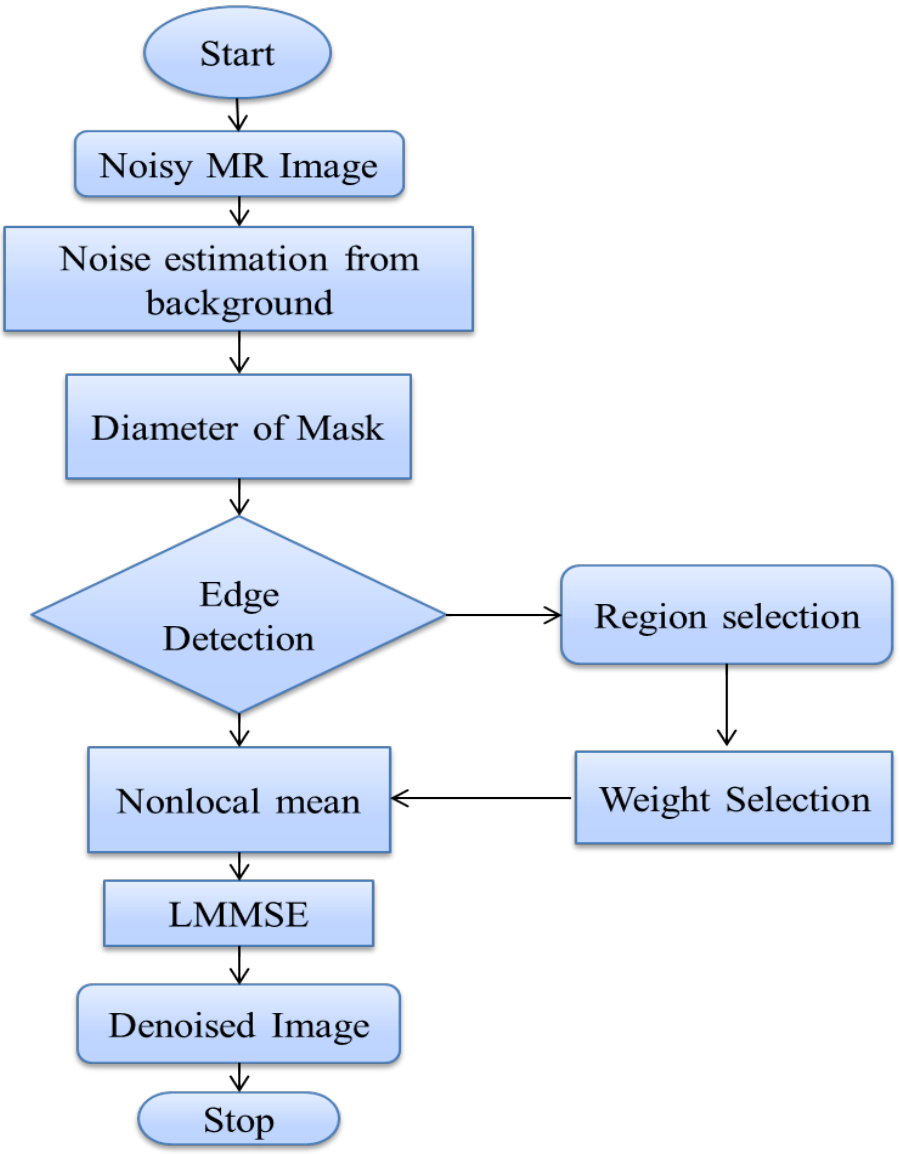

FIGURE 2.2: Flowchart of the proposed denoising procedure

Liu et al., 2007). The role of this mask is to identify edges and their orientation and accordingly performs region selection for the denoising process. In this study, an edge is characterized by dissimilarity in variance σ_n^2 for the two regions across the diagonal. Regions with absence of edge information are considered as homogeneous while those with edge information are considered as non-homogeneous (Perona and Malik, 1990). Identification of a non-homogeneous region results in further sub-division of the neighbourhood into smaller sample regions across the edge to perform true signal estimation.

$$\sigma_{i,j}^2 = \frac{1}{N_{i,j} - 1} \sum_{p \in N_{i,j}} (I_p - \mu_{i,j})^2 \tag{2.22}$$

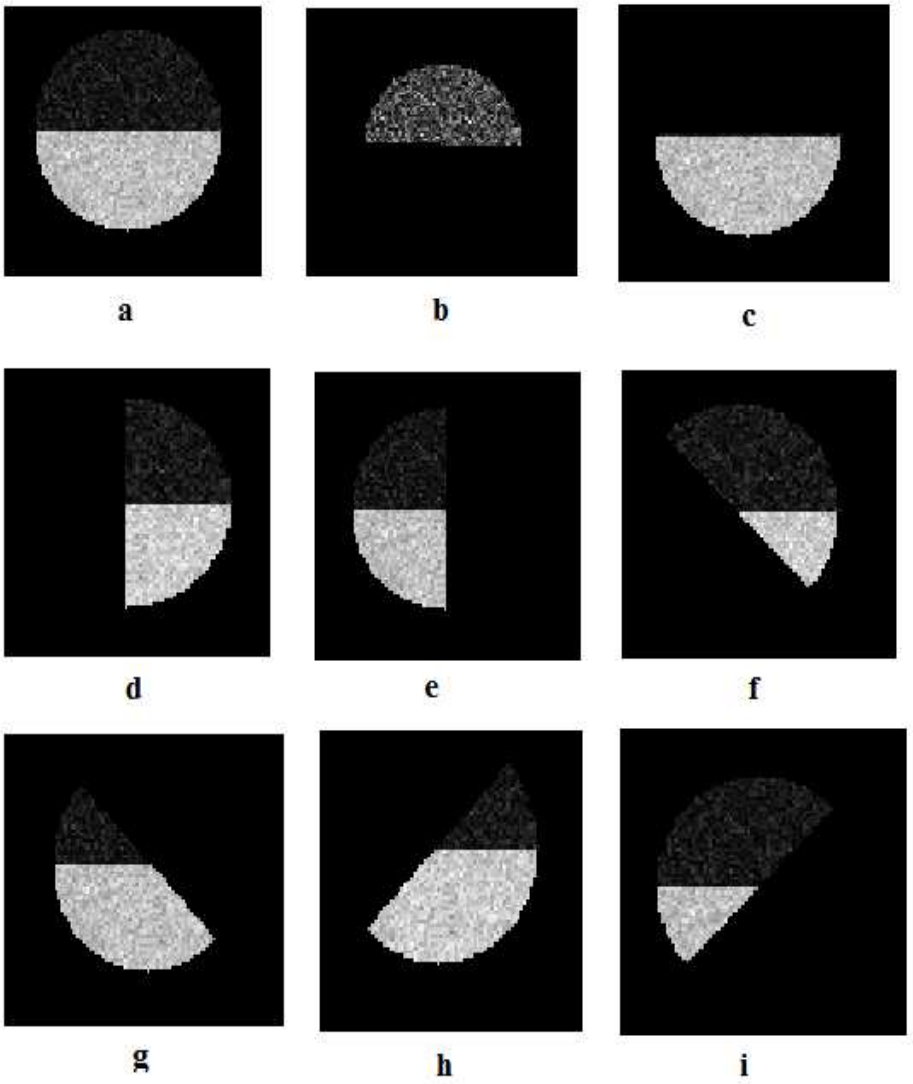

FIGURE 2.3: a) neighbourhood within a circular mask, b) region 1 for diagonal at 0˚, c) region 2 for diagonal at 0˚, d) region 3 for diagonal at 90˚, e)region 4 for diagonal at 90˚, f) region 5 for diagonal at 135˚, g) region 6 for diagonal at 135˚, h) region 7 for diagonal at 45˚, i) region 8 for diagonal at 45˚

Hence, as the circular mask rotates along its diagonal it computes for variance σ_n^2 for the two regions across the diagonal using Eq. (2.22) (Aja-Fernandez et al., 2008). Where, $\sigma_{i,j}$ is the local sample variance of noise, $N_{i,j}$ is the total number of pixels in the sample, I_p is the observed signal intensity, $\mu_{i,j}$ is the sample mean of the neighbourhood and i and j are indicators of the pixel position in the given neighbourhood (Aja-Fernandez et al., 2008). Ideally the rotation should be continuous and stop only when the diagonal of the mask aligns with the edge present within the neighbourhood of the mask. But for the purposes of simulation and to reduce the computation time, this rotation is kept discrete with a step size of 45 °. The rotation starts from 0 °and halts at 180 °. An example of the sample regions selected by the mask as it is rotated along its diagonal for

a given neighbourhood is shown in Fig. (2.3). An additional criterion W to determine presence of an edge between the two regions has also been implemented, as explained in Section (2.4.1.2). As homogeneous regions do not contain any edge information and one can perform filtering over the entire neighbourhood. But for a non-homogeneous region, smaller sample regions depending on the orientation of the edge are used to perform selective denoising. This operation thus enables the mask to adapt and perform region selection around the edges in an image for the denoising process.

2.4.1.2 Edge Detection Criteria

An additional criteria W using Brown-Forsythe test (BF-test) has been implemented as part of the edge detection process. BF-test has been proposed to avoid any false positive or true negative edge detection by the mask. The output of this test is also used to determine the orientation of an edge. BF-test is also known as the modified Levene's test and determines the equality of variances of two groups with a non-normal distribution using one way ANOVA F-test (Brown and Forsythe, 1974). Since Rician noise follows a non-normal distribution, a BF-test can be implemented to verify the equality of variances σ_n^2 and to avoid false positives. The test begins with a null hypothesis H_0 and alternate hypothesis H_a as shown in Eq. (2.23) and Eq. (2.24) respectively (Brown and Forsythe, 1974). The null hypothesis H_0 states that the variances for the two groups is the same while the alternate hypothesis H_a states that the variances for the two groups is different. The alternate hypothesis H_a is considered to be true only if the null hypothesis is found to be false (Brown and Forsythe, 1974). For a homogeneous region the null hypothesis should remain true as the variances across the sample regions should remain the same.

$$H_0 : \sigma_1^2 = \sigma_2^2 \tag{2.23}$$

$$H_a : \sigma_1^2 \neq \sigma_2^2 \tag{2.24}$$

The two regions across the diagonal are considered as independent random groups for whom the equality of variance is to be determined. The test requires absolute deviation of the group variables y_{ij} from its median value using Eq. (2.25). Where $\widetilde{y_j}$ is the median value of each individual group and Z_{ij} are the new variables for the two groups obtained after taking the absolute deviation for individual variables in each group (Brown and Forsythe, 1974). A selection of the median value $\widetilde{y_j}$ offers more robustness to the test for a non-normal distribution (Brown and Forsythe, 1974).

$$Z_{ij} = |y_{ij} - \widetilde{y_j}| \tag{2.25}$$

$$W = \frac{(N-k)}{(k-1)} \frac{\sum_{i=1}^{k}(N_i\ (\bar{Z}_i.\ - \bar{Z}..)^2)}{\sum_{i=1}^{k}\sum_{j=1}^{N_i}(Z_{ij} - \bar{Z}_i.)^2} \tag{2.26}$$

An F-value for the two groups is then computed using Eq. (2.26). Where N is the total number of observations within the two groups, k is the total number of groups used to perform the F-test, N_i is the total number of variables in each individual group, i is the number of groups, j represents the variables within each individual group, $\bar{Z}_i.$ represents group means of Z_{ij} and $\bar{Z}..$ is the overall mean of Z_{ij}. $N-k$ is the degree of freedom between the groups and $k-1$ is the degree of freedom within each individual groups (Brown and Forsythe, 1974). The BF-test can thus be said to compute the ratio of variances between and within each group to determine the equality of variances between two independent groups (Brown and Forsythe, 1974). This computed statistic value is then compared with the F-value within a distribution table for a significant alpha level as shown in Eq. (2.27).

$$W > F_{\alpha,k-1,N-k} \tag{2.27}$$

where W is the calculated value obtained using statistics of the two groups and F is the value obtained from the F-distribution table of a particular α level using the two degrees of freedom (Brown and Forsythe, 1974). If the computed test statistic W is found to be larger than the tabulated value $F_{\alpha,k-1,N-k}$, then the null hypothesis H_0 is rejected and the alternated hypothesis is accepted H_a.

As the null hypothesis H_0 of the BF-test will hold true only for regions with similar variance values σ_n^2 an index value of zero is attributed to these regions. But the null hypothesis will fail for regions with dissimilar variances σ_n^2 and the sample pair are attributed with an index value equivalent to their F-value $F_{\alpha,k-1,N-k}$. This operation generates a set of index values indicating similarity between regions for various orientations of the diagonal in the neighbourhood. This is also used as an indicator to determine the orientation of an edge in the neighbourhood. If the maximum value within the set is zero the region is considered as homogeneous, but if the maximum value in the set is more than zero, then the region is considered as non-homogeneous and the position of the index value is used to determine the orientation of the edge. A maximum index value at position 1 in the set indicates a horizontal edge in the neighbourhood. Similarly

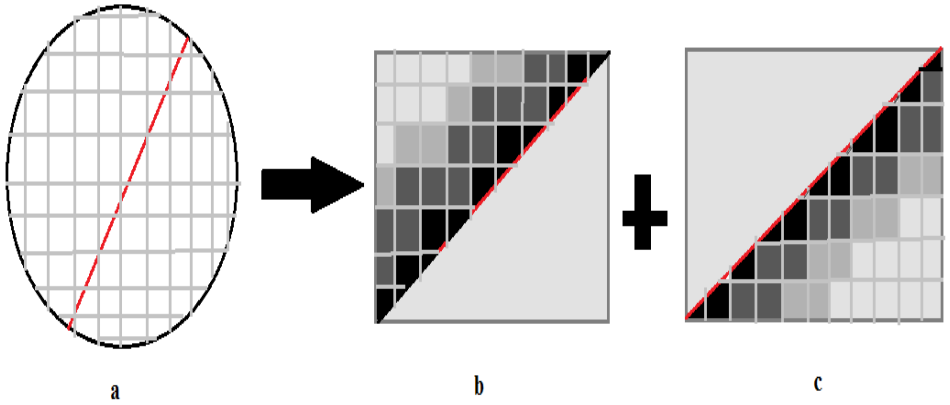

FIGURE 2.4: a) edge located with help of circular mask, b) nonlocal weights for region 1 indicated by top diagonal and c) nonlocal weights for region 2 indicated by bottom diagonal, where darker regions represent highest weights in the region

a maximum index value at position 2 indicates presence of a vertical image, while maximum index value at position 3 and 4 indicates a 45 °and 135 °orientation respectively. In this manner the proposed method detects and determines the orientation of an edge within the neighbourhood of an image.

2.4.1.3 Denoised Signal Estimation

The final step of the proposed method is to determine the denoised signal intensity $A_{i,j}$ of the neighbourhood using the local statistical information. In order to do this a modified nonlocal mean estimation $NL[v]$ of the sample regions followed with their linear minimum mean square estimate has been implemented $E[M_{i,j}]$.

A non-local means filter determines the mean sample intensity $NL[v]$ by using weights between neighbourhoods. These weights $w(i,j)$ are computed by using the Euclidean distance between surrounding neighbourhood regions as shown by Eq. (2.28) and Eq. (2.29) (Rajan et al., 2012; Buades et al., 2005; Manjon-Herra, 2006).

$$d_{i,j} = E[\|N_i - N_j\|]^2_{2,\sigma_n} \tag{2.28}$$

$$w(i,j) = \frac{1}{Z(i)} \exp(\frac{d_{i,j}}{h^2}) \tag{2.29}$$

where $d_{i,j}$ is the Euclidean distance between two neighbourhoods, N_i is the neighbourhood of pixel i, N_j is the neighbourhood of pixel j, $w(i,j)$ is the weight and h is the

smoothing parameter and is dependent on variance of noise (Buades et al., 2005). Neighbourhoods with similar intensity $NL[v]$ are assigned higher weights $w(i,j)$ as compared to non-similar regions and the sum of weights $w(i,j)$ is always equal to one (Buades et al., 2005; Perona and Malik, 1990; Manjon-Herra, 2006). Eq. (2.30) computes the nonlocal mean of the image, where $'NL'$ is the nonlocal estimate of i for a noisy image v (Buades et al., 2005).

$$NL[v](i) = \sum_{j \in J} w(i,j)\ v(j) \tag{2.30}$$

The proposed method uses a modified non-local mean filter to determine mean sample intensity $NL[v]$. Since we work with smaller regions to perform nonlocal means filtering, we use similarity information between the pixels rather than surrounding neighbourhoods to determine mean intensity of the sample. Also the knowledge about the orientation of an edge in a neighbourhood is included to assign the distribution of weights $w(i,j)$ within the sample using Eq. (2.29). This distribution of weights $w(i,j)$ is such that the pixels containing diagonal information are imparted with higher weights as compared to the rest of sample pixels. Such an operation preserves edge information during the denoising process. A similar example of nonlocal weight distribution by the proposed method for a neighbourhood containing a 45 °edge is shown in Fig. (2.4). In Fig. (2.4) darker regions indicate pixels with higher weights along the diagonal, while lighter regions indicate pixels with lower nonlocal weights. A nonlocal mean for the sample is then computed using Eq. (2.30).

The modified sample regions further undergo a linear minimum mean square estimate to determine the underlying signal intensity. The LMMSE method uses even order moments $E\{M_{i,j}^n\}$ where n is an even integer of the Rice distribution function for determining true signal intensity (Aja-Fernandez et al., 2008). The higher order moments of the Rice distribution function are given by Eq. (2.31) and Eq. (2.32) (Sijbers et al., 1998; Aja-Fernandez et al., 2008; Aja-Fernandez, 2012).

$$E\{M_{i,j}^2\} = E\{A_{i,j}^2\} + 2\sigma_n^2 \tag{2.31}$$

$$E\{M_{i,j}^4\} = E\{A_{i,j}^4\} + 8\sigma_n^2\ E\{A_{i,j}^2\} + 8\sigma_n^4 \tag{2.32}$$

where M is the observed magnitude, A is the true magnitude, E is the expectation operator, i and j are indicators of pixel position and σ_n is the variance of noise

(Aja-Fernandez et al., 2008). These higher order moments along with information of noise variance are used to obtain a linear minimum mean square estimate of true signal function and are given by Eq. (2.33) and Eq. (2.34) (Aja-Fernandez et al., 2008).

$$A_{i,j}^2 = \langle M_{i,j}^2 \rangle - \ 2\sigma_n^2 + K_{i,j} \ (M_{i,j}^2 - \langle M_{i,j}^2 \rangle) \tag{2.33}$$

$$K_{i,j} = 1 - \frac{4\sigma_n^2(\langle M_{i,j}^2 \rangle - \sigma_n^2)}{\langle M_{i,j}^4 \rangle - \langle M_{i,j}^2 \rangle^2} \tag{2.34}$$

The true signal intensity $A_{i,j}$ is thus estimated by computing the mean square estimation between a set of observed and estimated pixels within a region to undermine the effect of noise (Aja-Fernandez et al., 2008; Jiang and Yang, 2003). The denoised signal intensity is computed for each region, using the modified nonlocal means filter and a linear minimum mean square estimate. This process is repeated till the signal intensity for all the pixels are computed for the given MR image to complete the denoising process.

2.4.1.4 Results and Simulation Study-I

The simulation study for the proposed method has been conducted on the phantom cartilage, brain and MRI images of the articular cartilage. In the first part of this study, we have subjected the phantom image with increasing levels of standard deviation of noise σ to better understand the behaviour of Rician noise in the image. A plot of signal to noise ratio (SNR) and mean square error (MSE) for these values of noise was observed. Also changes in the contrast to noise ratio (CNR) with respect to signal to noise ratio (SNR) was observed for the phantom image. It was observed that the signal to noise ratio (SNR) for the phantom image significantly dropped after subjecting it to a noise of standard deviation greater than 10 while its mean square error (MSE) considerably increased as can be seen from Fig. (2.5). The plots of these image parameters were further used as an indicator to understand the effect of Rician noise on the phantom datasets.

The proposed method was then implemented on the phantom image. Variance of noise was estimated from the background of this image using Eq. (2.21). A circular mask of diameter 9 was selected to perform region selection and denoising. This mask was moved from top left to bottom right within the image and rotated in discrete step size of 45 °within the neighbourhood to search for presence of edge. Edge detection was performed using Eq. (2.22) and Eq. (2.27). The F-distribution table for significant alpha of

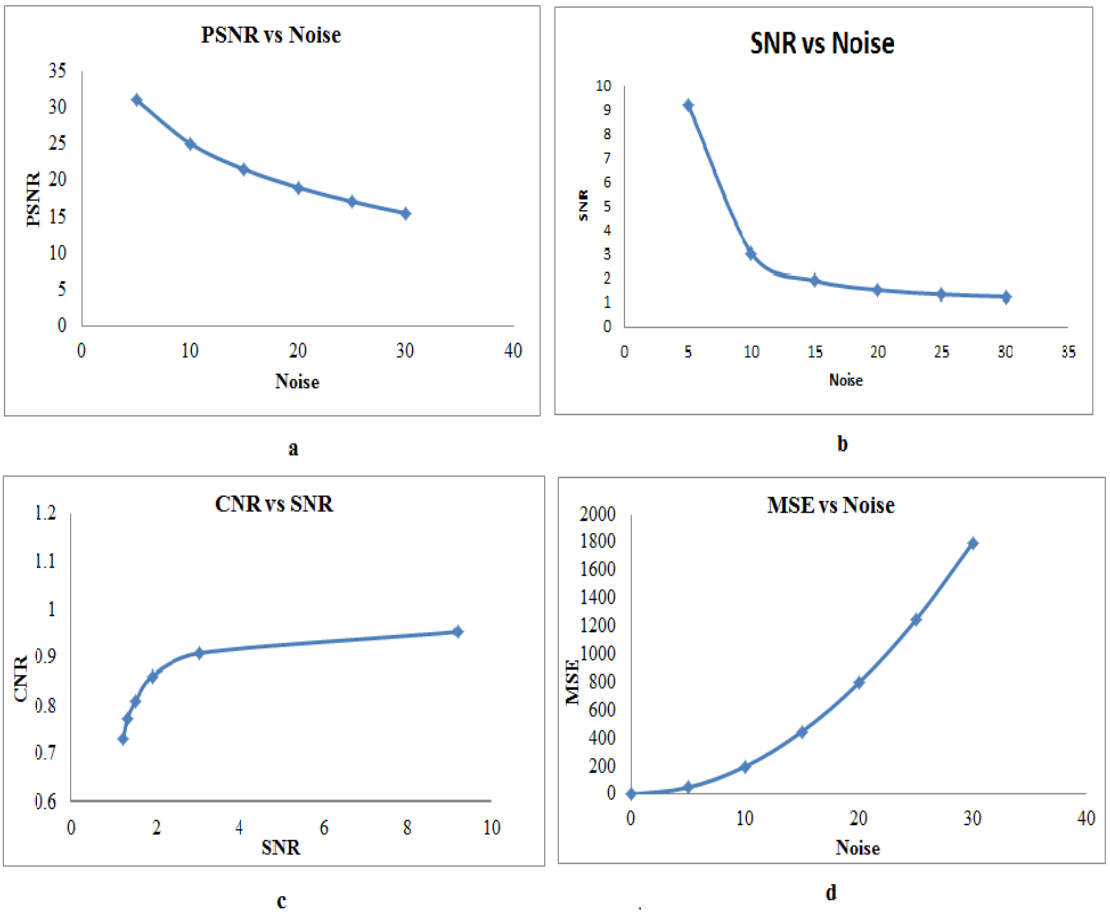

FIGURE 2.5: Characteristics of the phantom image for various values of noise

0.01 for a two tailed test evaluation was used to compute the index values (Montgomery and Runger, 2006). A denoised signal estimation of the sample region was performed using the modified nonlocal means filter and a LMMSE of the neighbourhood as part of the denoising process using Eq. (2.30), Eq. (2.33) and Eq. (2.34) (Aja-Fernandez, 2012).

To quantify the performance of the proposed method, root mean square error (RMSE), power signal to noise ratio (PSNR), and quality index based on local variance (QILV) ratios of the true and denoised image, as given by Eq. (2.36), Eq. (2.37) and Eq. (2.38) respectively were used (P. et al., 2012; Lopez-Rubio and Florentin-Nunez, 2011; Hore and Ziou, 2010; Aja-Fernandez et al., 2006; Aja-Fernandez et al., 2008).

$$MSE = \frac{1}{MN}\sum_{i=1}^{M}\sum_{j=1}^{N}[I_{ref(i,j)} - I_{test(i,j)}]^2 \tag{2.35}$$

$$RMSE = \sqrt{MSE} \tag{2.36}$$

$$PSNR = 10\log_{10}\frac{255^2}{MSE} \tag{2.37}$$

$$QILV(I,J) = \frac{2\mu_{V_I}\mu_{V_J}}{\mu_{V_I}^2+\mu_{V_J}^2}\frac{2\sigma_{V_I}\sigma_{V_J}}{\sigma_{V_I}^2+\sigma_{V_J}^2}\frac{\sigma_{V_IV_J}}{\sigma_{V_I}\sigma_{V_J}} \tag{2.38}$$

where I_{ref} in Eq. (2.35) represents the reference true noise free image used to compare with the denoised test image given by I_{test}. M and N represent total number of pixels in an image. Pixel positions were given by i and j. A QILV index was selected as it can better handle the non-stationarity of the image due to presence of various structures within the image (Aja-Fernandez et al., 2006). V_I and V_J in Eq. (2.38) were true and denoised images, μ_{V_I} and μ_{V_J} represent the mean of the local variances of the two images, σ_{V_I} and σ_{V_J} represent the standard deviation of the local variances of the two images and the final term compares the spatial coherence of the two images (Aja-Fernandez et al., 2006). CNR ratio of the denoised image was computed using Eq. (2.39) (Nowak, 1999).

$$CNR = \frac{\mu_1-\mu_2}{\mu_1+\mu_2} \tag{2.39}$$

where, μ_1 was the mean intensity of brighter region and μ_2 was the mean intensity of the darker region (Nowak, 1999). For the CNR assessment, the brighter region intensity was obtained from the cartilage while μ_2 represents intensity of the background in the MR image.

In the second part of the simulation study a comparative analysis of the proposed method with anisotropic diffusion filter, nonlocal means filter and LMMSE method was undertaken. For this study we included use of both phantom and brain image, where the true noise free images were available and variance of noise could be controlled. To maintain uniformity in this study, all the denoising methods used similar images subjected to the same standard deviation of noise. The noise in all the methods was estimated from the background of the MR image using Eq. (2.21) except for anisotropic diffusion filter. Also the window size utilized for all the methods was 9 x 9 except for the anisotropic diffusion filter where directional convolution masks of size 3 x 3 were used. Fig. (2.6) displays the noisy and denoised images with their corresponding histogram for all the methods used in the comparative study. The quantitative analysis for this comparison study is shown in Tab.2.1, where results for the denoising procedures for standard deviation of noise of 5 and 10 are displayed.

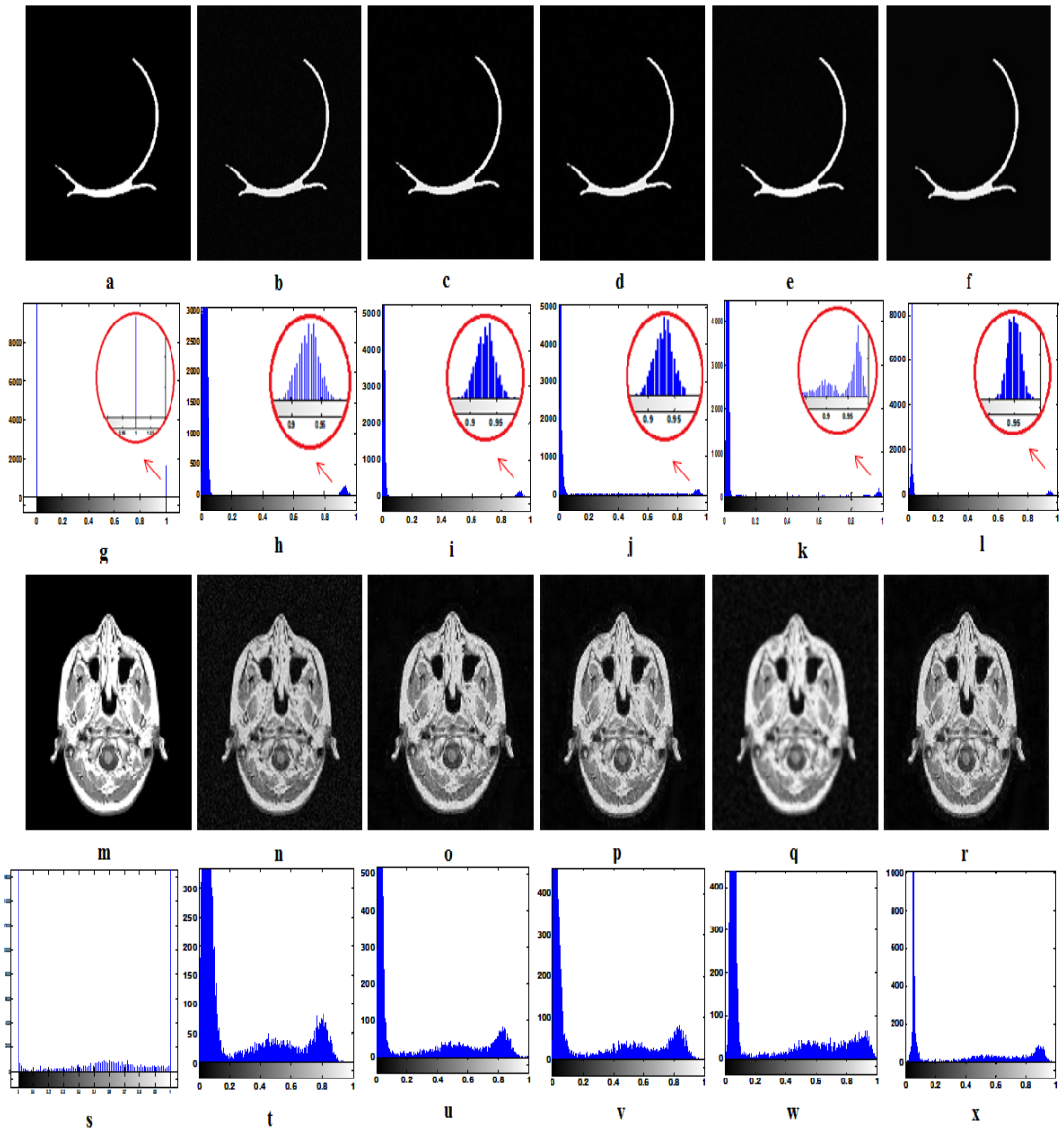

FIGURE 2.6: a) True phantom image, b) phantom image with noise of 5, c) denoised image with proposed method, d) denoised image with LMMSE method, e) denoised image with Anisotropic diffusion filtering, f) denoised image with nonlocal means filtering, g) histogram of True phantom image, h) histogram of phantom image with noise of 5, i) histogram of denoised image with proposed method, j) histogram of denoised image with LMMSE method, k) histogram of denoised image with Anisotropic diffusion filtering, l) histogram of denoised image with nonlocal means filtering, m) True brain image, n) brain image with noise of 5, o) denoised image with proposed method, p) denoised image with LMMSE method, q) denoised image with Anisotropic diffusion filtering, r) denoised image with nonlocal means filtering, s) histogram of true brain image, t) histogram of brain image with noise of 5, u) histogram of denoised image with proposed method, v) histogram of denoised image with LMMSE method, w) histogram of denoised image with Anisotropic diffusion filtering, x) histogram of denoised image with nonlocal means filtering

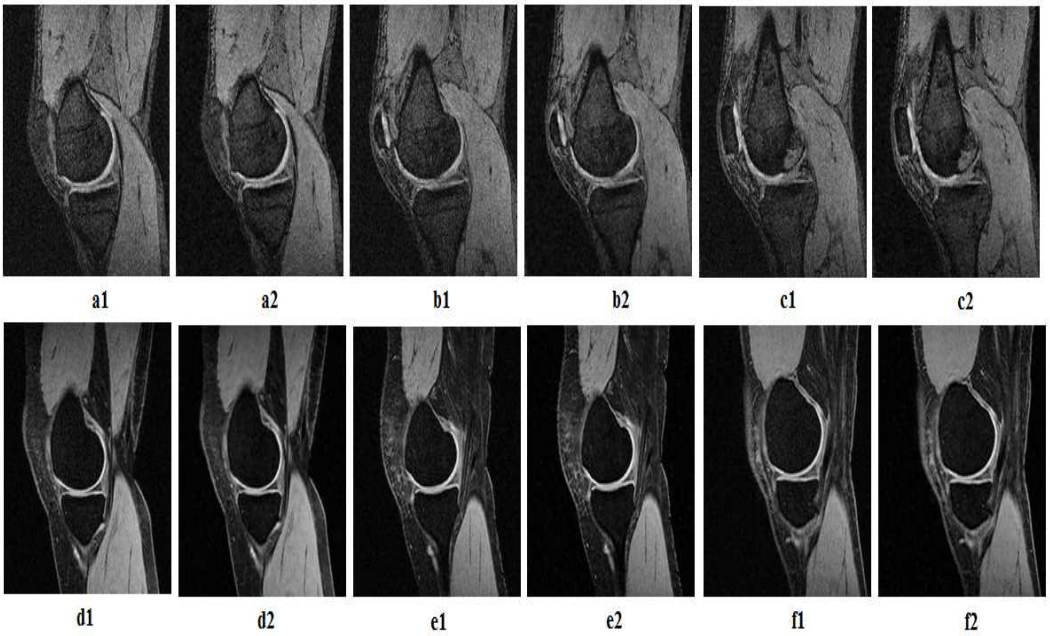

FIGURE 2.7: a1) Dataset 1 observed slice MRIM0016 , a2) dataset 1 denoised slice MRIM0016, b1) dataset 1 observed slice MRIM0020 b2) dataset 1 denoised slice MRIM0020, c1) dataset 1 observed slice MRIM0023 c2) dataset 1 denoised slice MRIM0023 d1) dataset 2 observed slice MRIM0080 d2) dataset 2 denoised slice MRIM0080 e1) dataset 2 observed slice MRIM0385 e2) dataset 2 denoised slice MRIM0385 f1) dataset 2 observed slice MRIM0690 f2) dataset 2 denoised slice MRIM0690

The proposed method has further been implemented on the two MRI datasets of the articular cartilage. Fig. (2.7) shows the result of the proposed denoising procedure for several slices of both the MRI dataset. We have used a circular mask of diameter 9 for denoising of the MRI images.

2.4.2 Adaptive SNR filtering technique for Rician noised denoising in MRI

Rician noise displays signal dependent behaviour with a varying probability distribution function depending on the SNR of the image. As a result the study investigated the possibility of using this anomaly to design a more efficient denoising filter. Rician noise approximately follows a Gaussian distribution for higher SNR values and may follow a Rayleigh distribution for a lower SNR.

In this study we propose an adaptive filtering technique for Rician noise, addressing this characteristic distribution behaviour. Based on the probability distribution function of noise $P(M)$ and SNR information obtained from the image, the proposed filter uses local

TABLE 2.1: Image Quality Assessment of the Denoising Methods

Noise	**Image**	**Quality**	**Proposed Method**	**Anisotropic**	**NLM**	**LMMSE**
$\sigma = 5$	Brain	SNR	**107.635**	26.474	35.4715	91.7894
		RMSE	**3.8529**	7.6746	6.7443	4.1877
		CNR	**0.938**	0.8307	0.8306	0.903
		QILV	**0.9884**	0.7224	0.9335	0.978
		PSNR	**36.4151**	30.4297	31.5537	35.6913
$\sigma = 5$	Cartilage	SNR	**212.90**	29.5395	32.9111	178.290
		RMSE	**2.775**	7.2983	7.1044	3.034
		CNR	**0.9768**	0.9493	0.9493	0.9674
		QILV	**0.9983**	0.9448	0.9448	0.9969
		PSNR	**39.2654**	30.8663	31.1002	38.490
$\sigma = 10$	Brain	SNR	**26.3567**	11.6099	11.928	24.9555
		RMSE	**7.7507**	12.0087	11.8361	8.0484
		CNR	**0.8711**	0.6884	0.6804	0.8136
		QILV	**0.9412**	0.6573	0.7146	0.8873
		PSNR	**30.344**	26.5409	26.6667	30.0166
$\sigma = 10$	Cartilage	SNR	**46.1251**	9.5793	10.6862	45.1685
		RMSE	**5.9961**	13.3073	12.8828	6.0611
		CNR	**0.9498**	0.9015	0.9025	0.936
		QILV	**0.9922**	0.9185	0.98	0.9875
		PSNR	**32.5735**	25.649	25.9306	32.4798

statistics of the neighbourhood within the mask to perform denoising. The filter thus performs an adaptive denoising based on the regional SNR of the neighbourhood. The proposed filtering technique has been implemented on synthetic image and T2 weighted magnitude MRI images. The efficiency of the proposed filtering technique is verified with a study of the PSNR, MSSIM and RMSE characteristic of the denoised and noisy image with respect to the true image. The proposed denoising technique shows an improvement in the contrast ratio and PSNR of the noisy image.

2.4.2.1 Proposed technique for Adaptive SNR filtering

An adaptive SNR filtering technique is proposed for denoising of Rician noise. The proposed method uses the local SNR of the neighbourhoods in the image to perform

denoising. Such an operation allows the filter to adapt itself to the distribution characteristic of noise within the neighbourhood for efficient denoising. Fig. (2.8) shows the flowchart of the noise removal process. The initial step of the denoising process is to estimate the variance of noise σ_n in the image. In order to do this we use the background of the image to estimate value of noise using Eq. (2.21) (Aja-Fernandez et al., 2008).

This variance σ_n is further used to estimate the regional SNR and the mean intensity μ of the neighbourhood. The regional SNR of the neighbourhood is given by Eq. (2.40) where μ indicates the mean intensity of the neighbourhood (Sijbers et al., 1998).

$$SNR_{reg} = \frac{\mu}{\sigma_n} \tag{2.40}$$

For regions with higher SNR, usually greater than 3 dB the distribution in the neighbourhood is assumed to be Gaussian. In addition the observed signal intensity μ should be similar to the true signal intensity $\bar{A}$ along with the bias σ introduced due to the noise. This bias in the mean intensity μ value can be corrected using Eq. (2.6) (Gudbjartsson and Patz, 2005). The filter thus uses Eq. (2.6) to correct the pixel intensity M for bias introduced due to noise. Instead of using the mean intensity μ of the local region we can make use of the median intensity value as it is more robust towards outliers such as noise (Aysal and Barner, 2007).

For regions with a lower SNR, noise tends to follow a Rayleigh distribution in that neighbourhood. The bias σ introduced due to presence of noise, as shown in Eq. (2.6) can no longer be ignored (Sijbers et al., 1998). One can now perform Rayleigh filtering on these neighbourhoods using a wide variety filters designed for Rayleigh noise filtering. These filters include use of median filter, Lee filter, Frost filter etc. (Yin et al., 1996). In the proposed method, such a low SNR neighbourhood is further classified into regions with zero intensity and regions with absence of zero mean intensity. Such an approach is used to perform denoising of the zero intensity background using mean estimation μ for Rayleigh distribution using Eq. (2.4). This approach can help us to significantly clean up the background and other regions with absence of any signal function. Also note that the estimation provide by Eq. (2.4) does not take into consideration the mean intensity μ information of the region. This mean intensity information μ is still used for low SNR regions with mean intensity of the neighbourhood greater than one. In such regions filtering is achieved using geometric mean filter as it offers better denoising capability for signal dependent noise (Arsenault and Denis, 1983; Pitas and Venetsanopoulos, 1986).

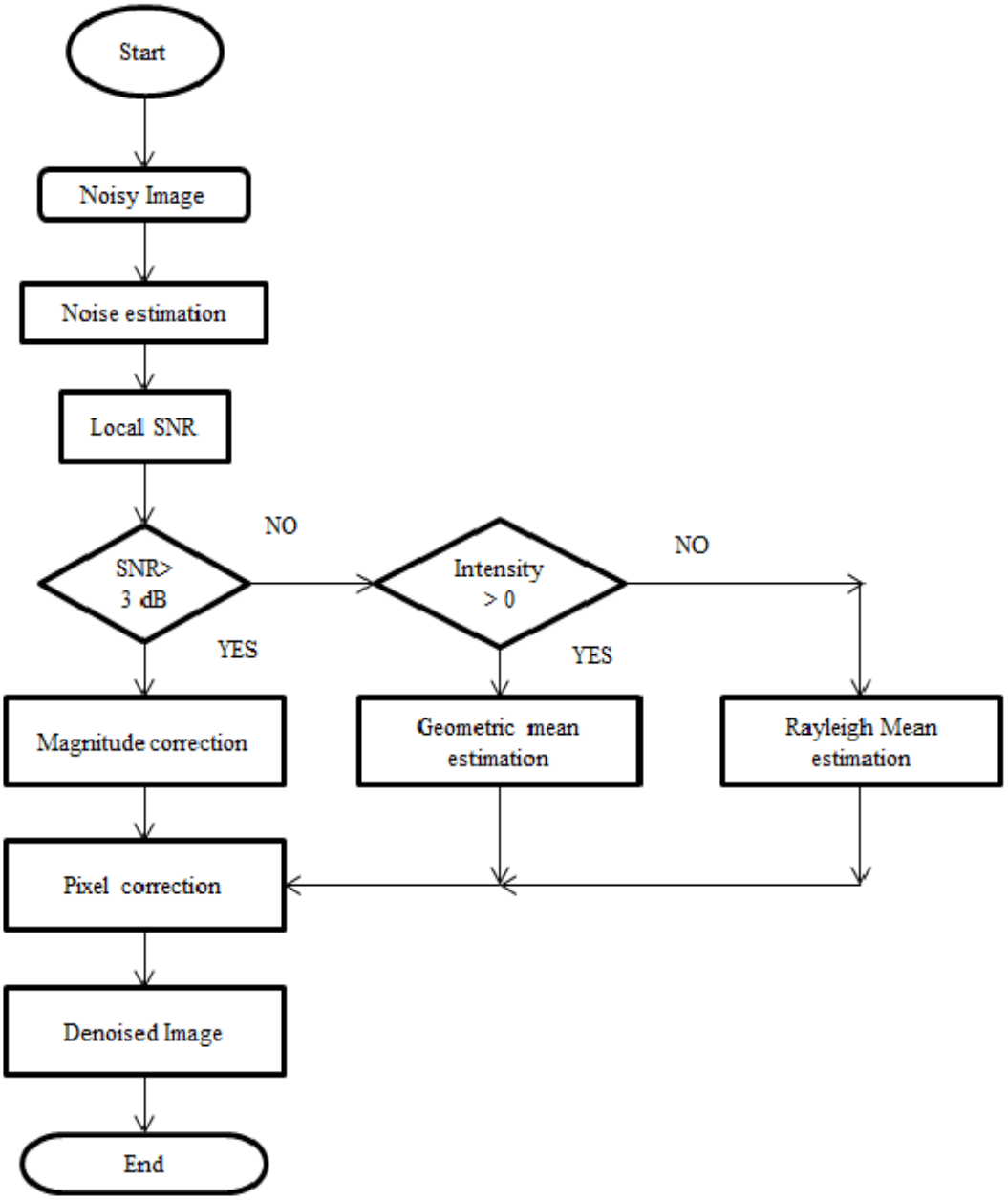

FIGURE 2.8: Flowchart of the proposed denoising method

In this manner, depending on the local SNR of the region the filter adapts itself and performs denoising using the local statistics of the neighbourhood.

2.4.2.2 Results and Simulation Study - II

The proposed filtering technique has been implemented on both synthetic and magnitude MRI images. A phantom cartilage has been used as the synthetic image for the simulation study. In the synthetic image Rician noise is artificially introduced using Eq. (2.1) and a random function generator in MATLAB. The magnitude MRI images used

for this denoising study are obtained using 'TE 13 RF Fast FatSat' imaging sequence in a 1.5 Tesla scanner. These MRI images are a part of a dataset containing 62 slices of the articular cartilage. All the MRI images are 512 x 512 pixel resolution with TR=43, TE=13 and flip angle of 50. Since these MRI images are already corrupted by noise due to the image acquisition process, no artificial noise has been introduced in them. The program code for the proposed denoising technique has been written in MATLAB version R2012A in windows 7.

The phantom cartilage image used for the simulation study has been subjected to increasing levels of noise σ, to observe the result for different levels of noise. A standard deviation value of noise σ is provided to the random function generator which introduces these values into the image as noise using Eq. (2.1). For this study we have used different values of standard deviation of noise μ. At each denoising procedure the value of noise is then estimated from the background of the image using Eq. (2.21). A 3 x 3 square mask has been used for performing adaptive filtering in the image. A larger mask can help in obtaining faster simulation but can cause blurring of the image, if not careful. This mask computes the local mean intensity of the region to perform adaptive filtering. The mean intensity value is used with the estimated variance of noise obtained from the background, to determine the local SNR of the region using Eq. (2.40). For high intensity regions, the mean intensity of the observed sample is assumed to be closely similar to the actual signal intensity.

The computed SNR for such a region should be higher than 3 dB. The noisy pixel intensity is then corrected using Eq. (2.6) and the median value of the sample. The mean intensity of the sample for regions with lower SNR is further evaluated by the filtering process. For regions with the mean intensity value less than one; the region within the mask is assumed to be the zero intensity background region of the image. In these regions the pixel intensity is corrected by using the mean estimation value μ for a Rayleigh distribution using Eq. (2.4). The variance value used to compute this pixel intensity is same as the estimated variance of noise obtained from the background of the image. If the mean intensity of the local sample is other than zero we perform geometric mean filtering to estimate true intensity values for such regions. These regions, too display Rayleigh distribution and as such one can still implement Rayleigh filtering for denoising. Rayleigh denoising for these regions can be achieved with help of median filters, Lee filter, Frost filter etc. and depends on the requirement of the user (Yin et al., 1996). In the proposed method we have implemented a geometric mean filter for these regions, as it is found to be more optimal for signal dependent noise (Pitas and Venetsanopoulos,

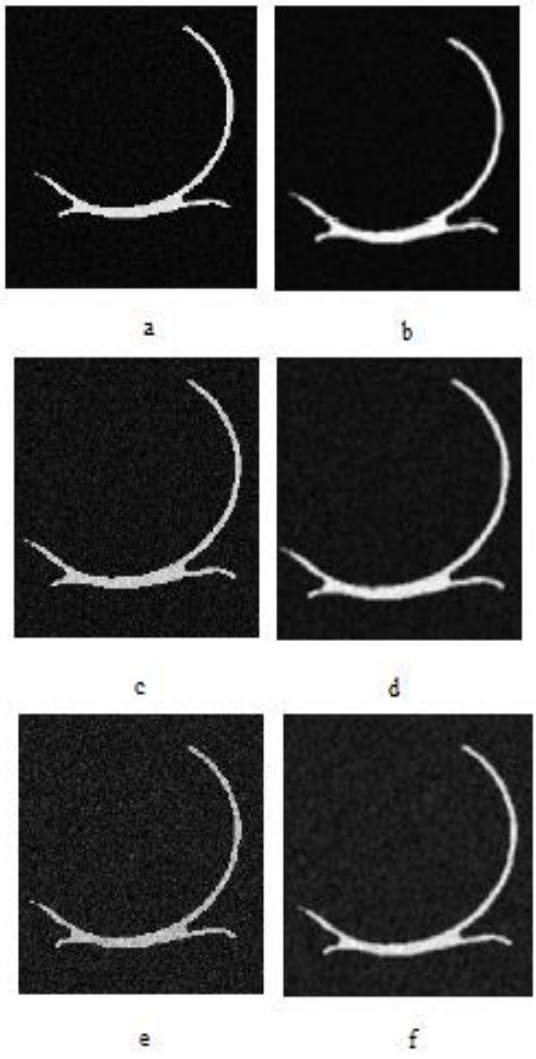

FIGURE 2.9: a) Phantom image with variance of noise 10, b) denoised phantom image for a, c) Phantom image with variance of noise 20, d) denoised phantom image for c, e) Phantom image with variance of noise 30, f) denoised phantom image for image noise 30

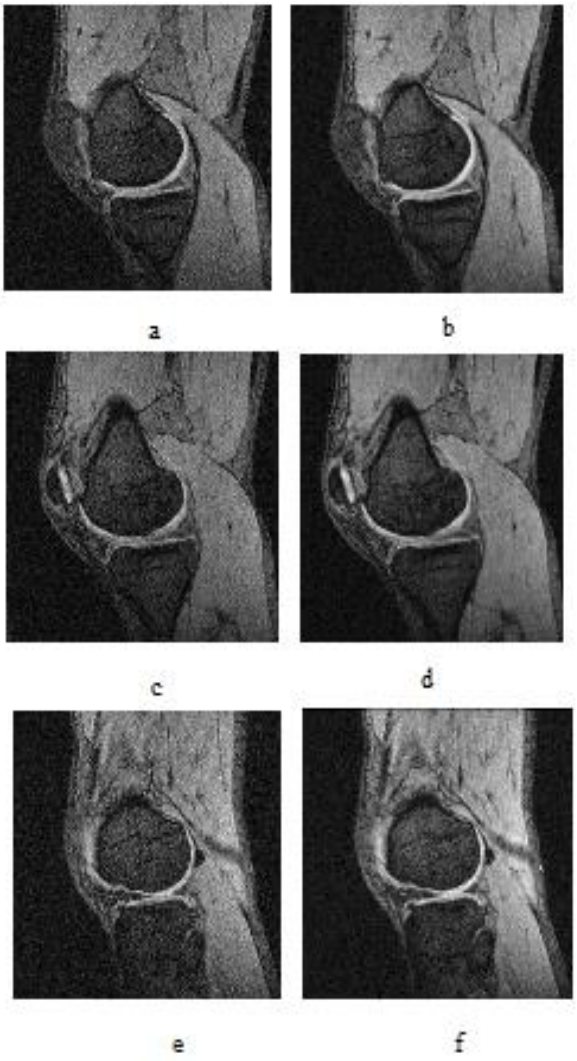

FIGURE 2.10: a) Observed image slice MRIM0016, b) Denoised image slice MRIM0016, c) Observed image slice MRIM0020, d) Denoised image slice MRIM0020, e) Observed image slice MRIM0050 f) Denoised image slice MRIM0050

1986). The centre pixel of the mask is used to replace the noisy pixel in the image.

Fig. (2.9) displays the result of the proposed adaptive filtering technique on the synthetic image. A phantom cartilage with noise variance of 10, 20 and 30 has been used for the simulation study and its corresponding filtered image is shown in Fig. (2.9). To determine the efficiency of the proposed filtering technique, the PSNR, MSSIM and RMSE values for both noisy and denoised image are computed. Tab. 2.2 is used to display these image parameters. The PSNR value is used to indicate the improvement in the

TABLE 2.2: Image Parameter for Phantom Image

Image Parameter		**PSNR**	**RMSE**	**MSSIM**
σ **= 10**	Noise	25.1400	14.1105	0.0388
	Denoised	26.1140	12.6137	0.0614
σ **= 20**	Noise	19.1170	28.2288	0.0160
	Denoised	20.9598	22.8324	0.0219
σ **= 30**	Noise	15.5901	42.3680	0.0126
	Denoised	17.6229	33.5271	0.0142

signal information content with respect to noise in the denoised image (Hore and Ziou, 2010). Structural similarity index (SSIM) is used to determine the image information and to verify if the image has been considerably modified due to the denoising process (Wang et al., 2004). The proposed filtering technique has further been implemented of other MRI image slices as shown in Fig. (2.10).

The visual inspection of the denoised images and study of the image quality parameters show that the proposed filtering technique does offer improved denoising. The proposed filtering technique improves the image quality for magnitude MRI images in presence of Rician noise and is also computationally efficient. The method can be significantly improved if a more robust estimation of the local SNR can be achieved. Also the proposed filtering technique finds limitation in its implementation, for images with absence of zero intensity background. A more accurate estimation of the Rician noise σ_n can also help in improving the denoising result.

2.4.3 Signal dependent Rician Noise Denoising using nonlinear filter

Our investigation of the signal dependent behaviour of Rice noise also brought us to homomorphic filters for nonlinear filtering of noise (Arsenault and Denis, 1983). Homomorphic filters are nonlinear filters in the spatial domain (Arsenault and Denis, 1983). They require a transformation function, to separate signal and noise in the image, thus making noise linear and independent of signal (Arsenault and Denis, 1983). Noise in this form is no longer dependent on signal and can be easily filtered from the image with existing denoising procedures (Arsenault and Denis, 1983). Homomorphic filters also require an equivalent inverse transformation function to return the filtered data back to the original equation (Arsenault and Denis, 1983). A similar concept has been developed

to make Rician noise independent of the true signal intensity. Once the noise has been made reasonably independent of the signal function, it undergoes filtering for noise removal and later the filtered data is transformed back into the magnitude equation. This process leads to betters estimation of the true signal intensity and is computationally more efficient.

For this study we propose a nonlinear homomorphic filtering method for Rician noise denoising. Nonlinear filters are more capable in addressing signal dependent behaviour of noise and offer good denoising with better edge preserving capabilities. A nonlinear filter based on homomorphic filter characteristics has been designed to address Rician noise in MR images. The proposed filter has been implemented on synthetic images and MR images of the articular cartilage. The efficiency of the proposed filtering method is verified by computing the PSNR and SSIM index of the image. The proposed nonlinear filter performs good denoising with improvement in the image quality as observed from the PSNR values of the image. It also offers edge preservation and can be used for both structural MRI and soft tissue study effectively.

Noise can only be considered independent of signal, if its probability distribution function is no longer dependent on the signal parameter and it can be written in a linear form (Walkup and Choens, 1974). In general signal dependent noise can be broadly classified into multiplicative noise such as the speckle noise or a signal-modulated additive noise such as film grain noise (Arsenault and Denis, 1983; Walkup and Choens, 1974). Eq. (2.41) represents multiplicative signal dependent noise known as speckle noise which commonly affects ultrasound images (Walkup and Choens, 1974). The additive signal-modulated noise model is a general model developed by John Walkup et.al to represent signal dependent behaviour of noise and is given by Eq. (2.42) (Walkup and Choens, 1974). Where, r is the observed signal, s is the true signal, $f(s)$ is the signal function and n is noise.

$$r = s.n \tag{2.41}$$

$$r = s + k.f(s).n \tag{2.42}$$

Eq. (2.42) is based on the assumption that the noise is stationary with zero mean, uncorrelated with the signal function and represents linear signal dependent noise (Walkup and Choens, 1974). Noise in MRI magnitude equation is also very similar to Eq. (2.42);

where noise is both signal dependent and additive. At the same time Rician noise is also non-linear due to magnitude image formation, using information of real and imaginary components of the signal with respect to noise (Sijbers et al., 1998).

2.4.3.1 Proposed technique for using nonlinear filter

We propose a signal dependent filtering procedure, for Rician noise using magnitude equation given by (Aja-Fernandez et al., 2008). The proposed filter design tries to decouple noise from the true signal function, before filtering for noise removal (Pitas and Venetsanopoulos, 1986). It is then followed by an intuitive filtering process which tries to minimize error due to noise, using mean square estimate process using Wiener filter, on the observed noisy signal. Such a denoising operation tries to maintain the fidelity of the image without introducing any artifacts due to the filtering process and does not cause any considerable change to the original signal function. This filtered data is then used for reconstructing a noise free estimate of the image by using an inverse transformation operation. This denoising process is divided into two stages; the first stage involves transformation of nonlinear magnitude equation to make noise independent of the signal and the second stage involves filtering of the noise followed by an inverse transformation of the filtered signal; together they form a nonlinear homomorphic filter for signal dependent noise (Pitas and Venetsanopoulos, 1986). The process is explained in more detail in the following sub-sections. Fig. (2.11) indicates the flow chart for the proposed filter method.

2.4.3.2 Transformation of Image

Transformation operation is performed on the image to separate noise from the signal (Pitas and Venetsanopoulos, 1986). This transformation operation can involve any mathematical procedure such as square, logarithmic, Laplace transform, Wavelet transform etc. to simplify a nonlinear equation. Such a transformation operation enables existing image enhancement procedures to be implemented on the image (Pitas and Venetsanopoulos, 1986).

A similar transformation function is implemented on the Rice magnitude equation, given by Eq. (2.1). This transformation operation involves taking square of the magnitude equation, followed by a logarithmic operation. The square operation is performed on the magnitude equation so that one can gain access to individual signal and noise components and is shown by Eq. (2.44).

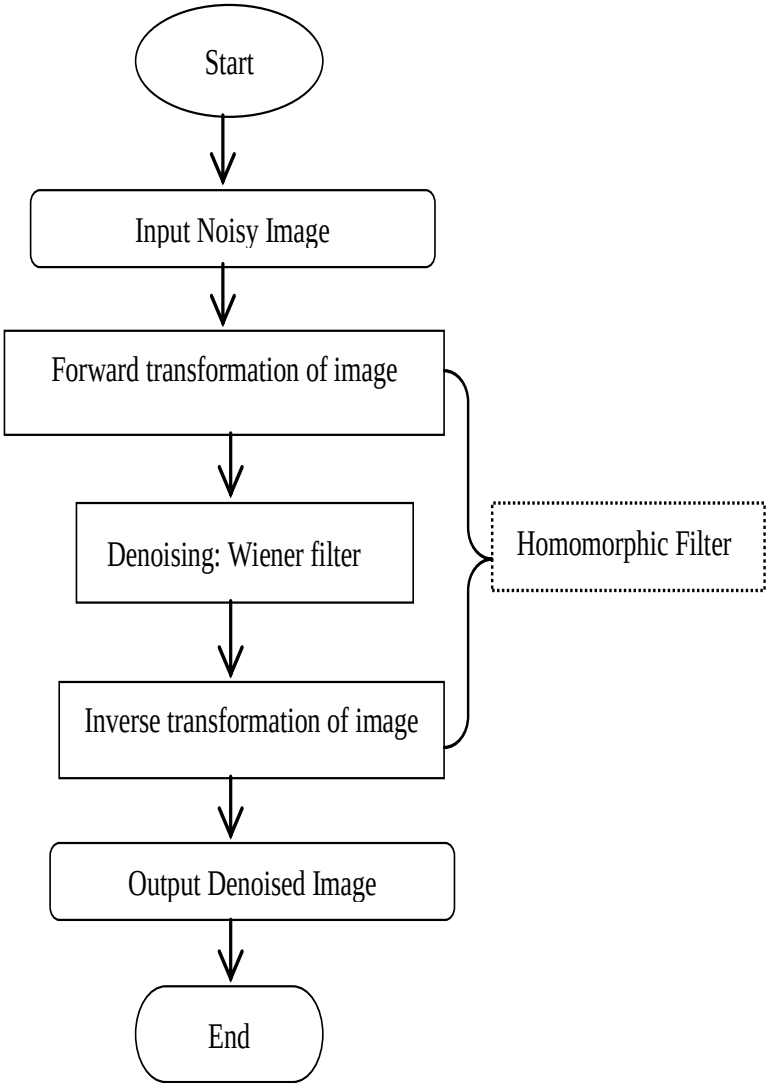

FIGURE 2.11: Flow chart of the denoising procedure

$$M^2 = (A + n_r)^2 + n_i^2 \tag{2.43}$$

$$M^2 = A^2 + 2An_r + n_r^2 + n_i^2 \tag{2.44}$$

Estimation of noise in MR image can be determined from the background pixels using second order moment of the Rice distribution function (Aja-Fernandez et al., 2008).

$$E[M^2] = A^2 + 2\sigma_n^2 \tag{2.45}$$

An estimate of noise variance in the image can then be computed by using Eq. (2.46) (Aja-Fernandez et al., 2008).

$$\hat{\sigma_n^2} = \frac{1}{2N}\sum_{i=1}^{N} M_i^2 \tag{2.46}$$

This variance is assumed by us, to be similar to the sum of the real and imaginary components of Gaussian noise and is subtracted from the magnitude image to reduce the overall effect of noise component in the image as shown in Eq. (2.48).

$$\hat{\sigma_n^2} \cong N^2 \cong n_r^2 + n_i^2 \tag{2.47}$$

$$M^2 - N^2 = A^2 + 2An_r \tag{2.48}$$

Let $M^2 - N^2 = \dot{M}$

$$\dot{M} = A(A + 2n_r) \tag{2.49}$$

In Eq. (2.49), A represents the true signal intensity of the MR image, $\dot{M}$ is the observed data with overall reduced noise variance and n_r is the real component of noise still present in the image. Eq. (2.49) is simplified further by a logarithmic transformation. The logarithmic operation helps to separate the signal and noise component, thus reducing the magnitude equation into a linear form and decoupling noise from the signal (Pitas and Venetsanopoulos, 1986). Eq. (2.50) is further used for the filtering process.

$$log(\dot{M}) = logA + log(A + 2n_r) \tag{2.50}$$

2.4.3.3 Denoising Procedure

Eq. (2.50) can be rewritten as shown below and is similar to additive linear noise present in the image.

$$y = x + n \tag{2.51}$$

where, y is the observed noisy image given by $log(\dot{M})$, x is the desired noise free signal and is equivalent to $logA$ and n is the noise function and represents $log(A+2n_r)$. Wiener

filter is now used for the denoising process, as it is more efficient in removing linear additive noise (Gonzalez et al., 2004). Wiener filter tries to minimize mean square error of the image function by estimating the noise free signal component from the observed signal as shown by Eq. (2.52) (Gonzalez et al., 2004).

$$min(e^2) = [x - \hat{x}]^2 \tag{2.52}$$

Where, x is the desired noise free signal and $\hat{x}$ is the output of the Wiener filter with observed noisy data given by Eq. (2.53) as shown below,

$$\hat{x} = W^T y \tag{2.53}$$

The expectation $E[e]$ of the mean square error output due to Wiener filter can be written as follows (Vaseghi, 2008),

$$E[e^2] = E[x - W^T y] \tag{2.54}$$

$$E[e^2] = E[xx^T] - 2W^T + W^T E[yy^T]W \tag{2.55}$$

$$E[e^2] = R_{xx} - 2W^T r_{xy} + W^T R_{yy} W \tag{2.56}$$

From Eq. (2.56), R_{xx} is the auto-correlation function of desired signal, r_{xy} is the cross-correlation function of desired signal and the observed signal, R_{yy} is the auto-correlation function of observed signal, W represents Wiener filter and E is the expectation operator (Vaseghi, 2008). The optimal solution for Eq. (2.56) exists when the gradient of Eq. (2.56) with respect to filter coefficient is zero (Vaseghi, 2008); thus minimizing error between desired s signal and observed signal r.

$$\frac{\partial}{\partial W} E[e^2] = -2r_{xy} + 2W^T R_{yy} = 0 \tag{2.57}$$

$$W^T R_{yy} = r_{xy} \tag{2.58}$$

$$W_{opt} = \frac{r_{xy}}{R_{yy}} \tag{2.59}$$

Eq. (2.59) represents optimal Wiener filter for linear additive noise (Vaseghi, 2008). For additive noise given by Eq. (2.42), noise has zero mean and is uncorrelated with signal function. Hence, the cross-spectral density of desired and noisy signal can be replaced with the cross-spectral density of desired signal, such that $r_{xy} = r_{xx}$ (Vaseghi, 2008). Wiener filter in frequency domain is used for purpose of denoising and is given by Eq. (2.60) where P_{xx} is the power spectral density of the desired signal s with respect to power spectral density of observed signal r (Vaseghi, 2008; Lim, 1990). $\hat{x}_{u,v}$ is an estimate of true image data obtained after convolution of Wiener filter W_{opt} with the degraded image in the frequency domain (Vaseghi, 2008). $H(u, v)$ in Eq. (2.60) is the point spread function which accounts for image degradation during image acquisition process and is also known as the blur operator of the filter; and $\hat{H}(u, v)$ is complex conjugate of $H(u, v)$ (Vaseghi, 2008; Lim, 1990).

$$W(u, v) = \frac{\hat{H}(u, v) * P_{xx}(u, v)}{|H(u, v)|^2 P_{xx}(u, v) + P_{nn}(u, v)} \tag{2.60}$$

$$\hat{x}(u, v) = W(u, v) * Y(u, v) \tag{2.61}$$

A 5 x 5 Gaussian blur kernel is used as point spread function for the filter, as the source noise in k-space is considered to be Gaussian in nature. Gaussian kernel can be of any size and depends entirely on the end user, although a larger kernel helps in a faster simulation process. Wiener filter too requires a prior knowledge of spectral density of true signal and noise for optimal filtering (Lim, 1990). The power spectral density of Gaussian white noise is a constant flat spectrum (Walkup and Choens, 1974; Lim, 1990) and for the filtering process is estimated from background of the transformed image using Eq. (2.47). The spectral density of true signal in practice is not known, but can be estimated in different ways (Lim, 1990; Banham and Katsaggelos, 1997). For the given filtering process we have used the periodogram of the observed signal as an estimate of the power spectral density of true image (Lim, 1990; Banham and Katsaggelos, 1997). Eq. (2.62) represents power spectral density of the periodogram of the observed image, where F and $\hat{F}$ represent Fourier transform and conjugate of Fourier transform of the observed signal respectively and F^{-1} indicates the inverse Fourier transform (Banham and Katsaggelos, 1997; Mehri et al., 2013).

$$P_{xx} = F^{-1}[F(x) * F(x)] \tag{2.62}$$

The filtered image undergoes inverse transformation to return the image data back to the magnitude equation, with the reduced effect of noise component. For our inverse

transformation we have calculated exponential of the filtered data followed by a square root operation. Eq. (2.63) and Eq. (2.64) indicate inverse transformation of the image data.

$$\hat{M} = exp(\hat{x}) \tag{2.63}$$

$$\hat{A} = \sqrt{\hat{M}} \tag{2.64}$$

The result of the denoising process is shown in Fig. (2.12, 2.13, 2.14). One can also use other filters instead of Wiener filter for denoising depending on the application of the user. If the noise had been multiplicative with the signal intensity it would have been more appropriate to use geometric mean filter which is more useful in denoising signal dependent multiplicative noise (Aja-Fernandez et al., 2008).

2.4.3.4 Result and Simulation Study - III

The above filtering procedure was implemented on MR images of the articular cartilage of the knee and spine image. MR images of the articular cartilage of knee were obtained using T2-weighted fat suppressed imaging sequences. These MR images were obtained from Menzies Research Institute database, Tasmania, Australia, while the image of the spine is a commercially available image obtained from MATLAB toolbox, both of which were used for the purpose of the simulation study. A total of 62 MR image slices of the articular cartilage were used to test the denoising procedure in presence of soft-tissue structure. Primarily histogram, PSNR, MAE and SSIM (Wang et al., 2004) were used to estimate the image quality after the denoising process. Filtered images of the spine and articular cartilage from Fig. (2.12) and Fig. (2.13) respectively, indicate that we have obtained considerable denoising for Rice noise. Also, a visual comparison of the histogram of the true image Fig. (2.12)b and filtered image Fig. (2.13)f of the spine, closely resemble each other indicating adequate denoising.

As predicted, nonlinear filter does not cause excessive blurring of the edges in the image or of the cartilage tissue. The denoising procedure also shows considerable improvement in the contrast levels of the filtered image. The noisy and filtered images for MRI slices 05, 21, 43 and 50 of the articular cartilage dataset are shown in Fig. (2.15). Tab. 2.3 shows a comparison results between the filtered and noisy images of the knee cartilage and spine for the proposed denoising procedure. Both the noisy and filtered images of

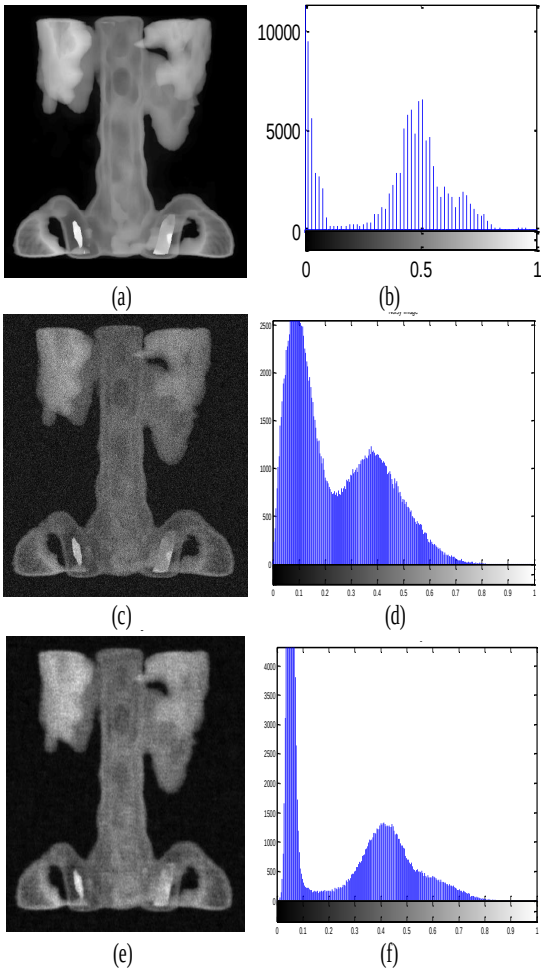

FIGURE 2.12: a) True noise free image of the spine b) histogram plot of true noise free image c) image with standard deviation of noise = 7 d) histogram plot of noisy image e) Denoised image using non-linear filtering and f) histogram plot of filtered image which is very similar to original histogram

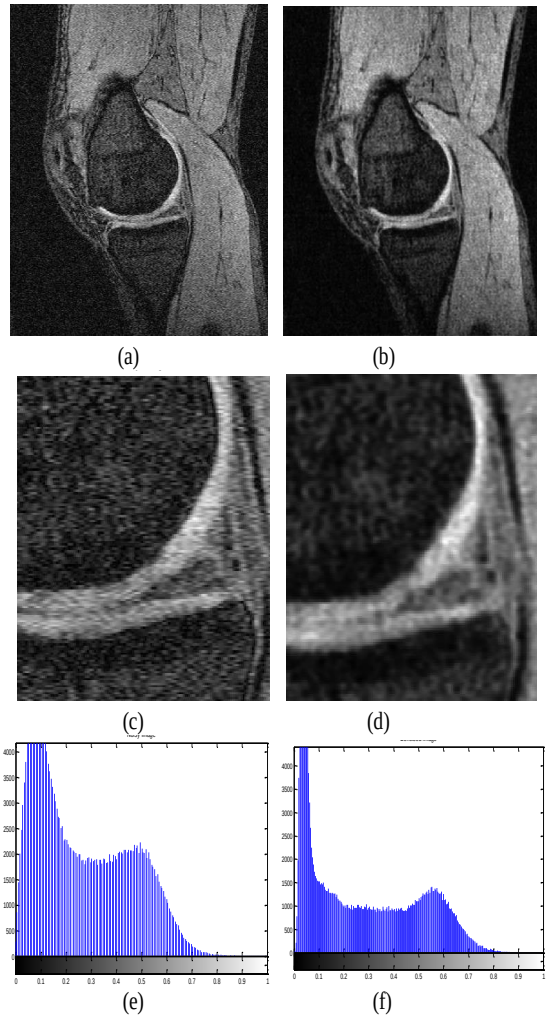

FIGURE 2.13: a) Noisy MRI image of articular cartilage, slice 16 of MRI dataset b) Denoised cartilage image c) magnified image of cartilage tissue d) magnified image of denoised cartilage tissue e) histogram of noisy image and f) histogram of filtered image

the spine have been compared to the true image, for determining PSNR and SSIM index (Wang et al., 2004). The filtered cartilage image has been compared with the observed image, due to absence of true noise free image of the knee. The noise estimated in the knee MRI from the background is of standard deviation 13.54 and that for the spine image is 6.69 using Eq. (2.46).

A plot of PSNR versus standard deviation of noise was also prepared for study of the denoising process at higher values of noise, using the spine image. The original spine

TABLE 2.3: Image Parameters

Images	**Knee σ = 13.54**	**Spine Noisy σ = 6.69**	**Spine filtered**
PSNR	27.1173	29.6466	34.7226
SNR	21.8546	8.8277	23.4107
MSE	126.2842	70.538	21.9191
MAE	8.7230	6.9826	4.0471
SSIM	0.52910	0.3844	0.6201

image was subjected to noise of different standard deviation and a plot of PSNR of the filtered and noisy image was computed for the corresponding standard deviation of noise.

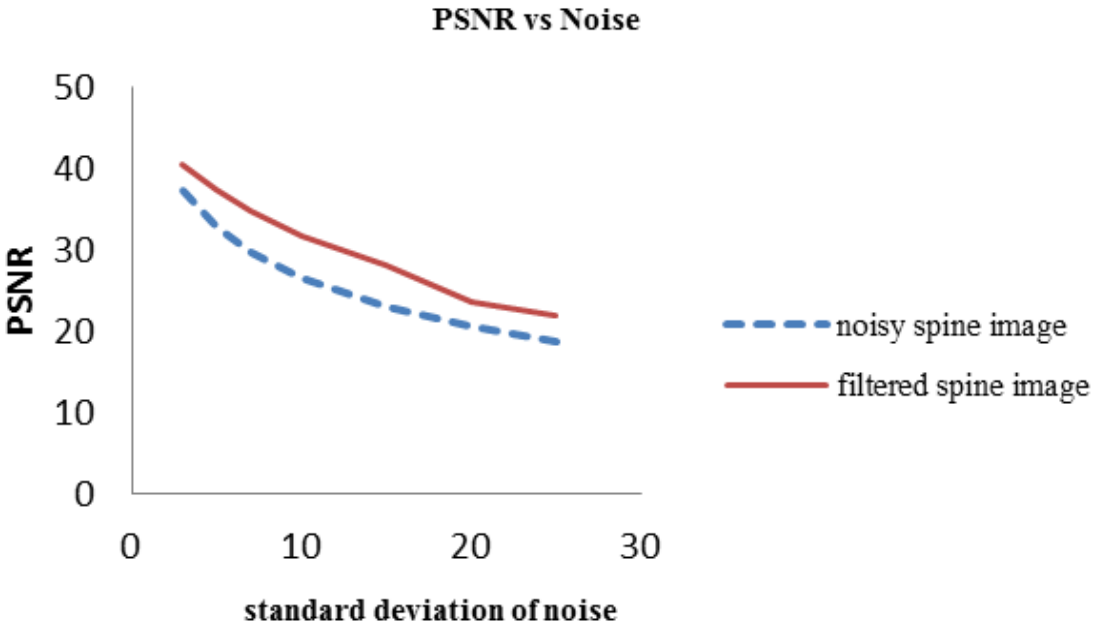

FIGURE 2.14: Plot of PSNR versus standard deviation of noise for spine image

The PSNR value of the filtered image was found to be higher than that of the noisy image and decreased as the standard deviation of noise increased along the horizontal axis as shown in Fig. (2.14).

2.5 Discussion-Rician denoising

In study 1 the proposed method offers better image quality and edge preservation for Rician noise as can also be seen from Fig. (2.6), Fig. (2.7) and Tab. 2.1. In Fig. (2.6) and Fig. (2.7), we can clearly observe the reduction of noise in the background and

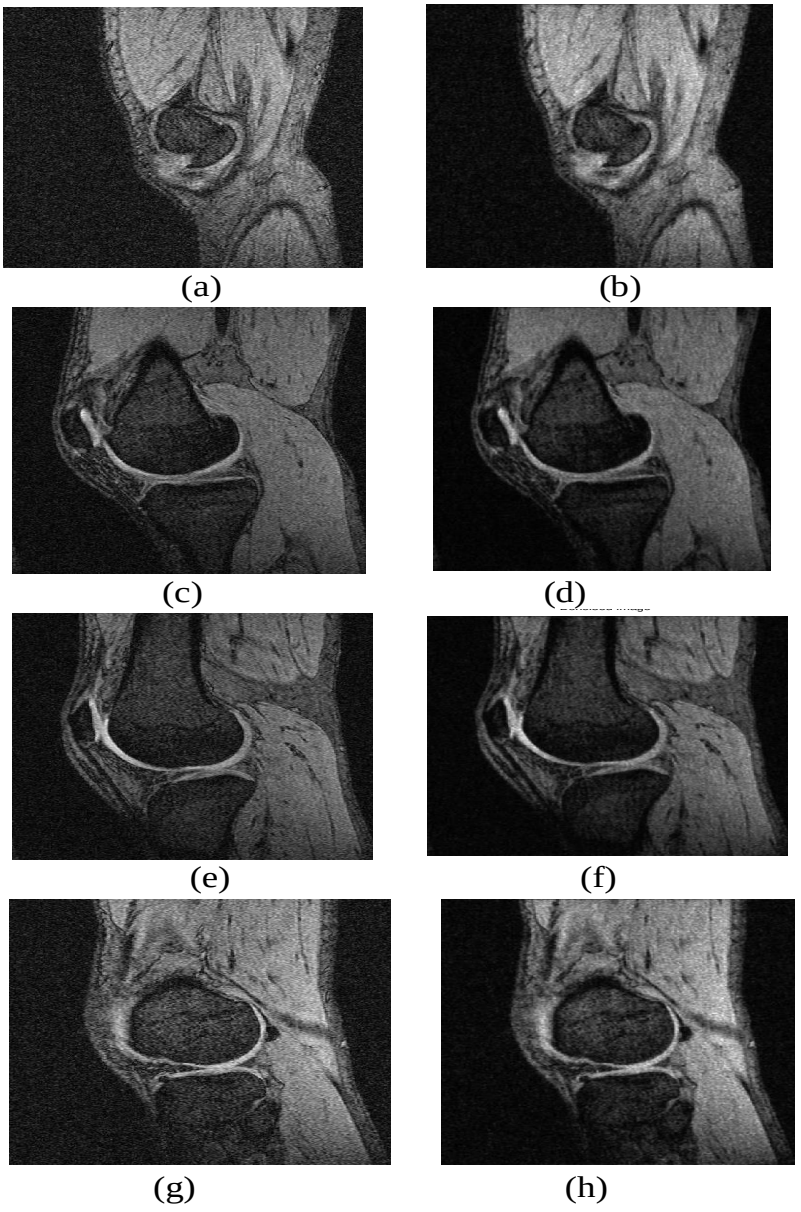

FIGURE 2.15: a) observed image slice 05 and b) denoised image slice 05 c) observed image slice 21 and d) denoised image slice 21 e) observed image slice 43 and f) denoised image slice 43 g) observed image slice 50 and h) denoised images of slice 50 of articular cartilage of the knee

homogeneous tissue regions while there is no blurring of the edges along the cartilage tissue. From Tab. 2.1, we can observe that the proposed method offers improvement in both the signal to noise ratio (SNR) and contrast to noise ratio (CNR) in the denoised images as compared to other existing methods. We can also see improvement in the QILV index thus indicating that the proposed method does not cause any significant changes along the edges and overall structural details of the image. The root mean square error of the image has also significantly reduced after using the proposed denoising method.

It is clear from the simulation process that denoising is the property of the mask used for performing signal estimation and edge detection. Though the circular mask provides us with a more flexible approach in denoising, it also plays a vital role in the edge detection and region selection process. A larger mask can include a much larger sample space, which helps to achieve accuracy and offers better denoising; but it can also be very computationally expensive. A smaller mask can significantly reduce this computation time but may lose on this accuracy as it works with limited number of pixels. An incorrect selection of the mask diameter could still result in excessive blurring of the edge information. Also the nonlocal means estimation is found to be more accurate with a larger mask as compared with a smaller mask; as the sample size used by the mask is larger. With a smaller mask we obtain very limited pixels to compute the nonlocal mean which restricts the ability of the mask to achieve more accurate results. In the proposed method as the mask looks for edges in a neighbourhood and accordingly computes non-local weights every time it is moved across the image, this process can increase the computational cost of the denoising process compared to other methods. But as the proposed method is designed for post-acquisition image enhancement this computational cost may still be considered feasible. In addition more importance is given to estimation of true signal by the denoising method. Computational cost can be brought down by faster processing systems and more advanced algorithms. A proper selection of the diameter of the mask plays a significant role in the optimality of the denoised method.

The variance of noise estimated from the background of the image too plays a significant role in the denoising process. Both the overestimation and underestimation of this noise variance will ultimately lead to incorrect estimation of the denoised signal intensity by the LMMSE method and can affect image quality. In the proposed method, the criterion for edge detection process is based on comparison of regional variance of the two smaller regions across the diagonal. To achieve more robustness in the comparison results we have implemented a Brown-Forsythe test. Such an approach helps to avoid any false

positive or true negatives in the proposed algorithm, as the statistical test is more capable of addressing a non-normal data. But it can also lead to an incorrect edge detection if there are multiple edges in the neighbourhood of the mask, for example a corner. A more efficient way to resolve this issue would be to include the use of additional parameters, such as local mean intensity of the regions for predicting the presence of an edge. Such an operation will further add to the efficiency of the proposed method.

During the study it was observed that the phantom image when subjected to very large standard deviation of noise greater than 10, causes the image to follow a Rayleigh distribution which limits the ability of the proposed filter to perform Rician denoising. Hence, though the proposed method offers improvement in the CNR and QILV ratios it does not show a similar improvement in the SNR ratio of the phantom image as compared to the other methods. This phenomenon has not been observed with the brain image, where there also exist a much larger number of grey levels as compared to the phantom image, which consists of only two grey level values. The proposed method, although definitely improves both the CNR and QILV ratios for the noisy images irrespective of the value of noise in the image. As the proposed method improves the contrast to noise ratio of the image it can further be used for other image enhancement operations such as edge detection, segmentation etc. Noise removal can still be a very difficult task for extremely noisy images irrespective of the denoising process and nature of noise. In such images the original signal content becomes significantly corrupted by noise which causes the signal estimation process to be inaccurate. The future work may include more robust denoising process and extension of the proposed denoising technique for 3D noise removal.

In study 2 for the proposed filtering method the denoising operation is controlled by the localized SNR of the neighbourhood within the image, as it is observed that Rician noise shows a fluctuating distribution pattern for SNR above 3 dB and less than 3 dB. For different types of noise other than Rician such as speckle, salt and pepper, Poisson noise etc. This SNR criterion of 3 db would no longer hold true as it is very specific for Rician distribution only. In this case the filter should use other criterion, specific to the distribution of noise which one desires to remove so that the filter can adapt itself more adequately to this distribution pattern and can perform noise removal more effectively. For example the current filtering algorithm is found to be ineffective for Poisson noise as the SNR criteria for 3 dB does not hold true for the Poisson distribution function. If one uses criterion other than SNR to address various distributions of noise, one might still be able to use the proposed design; but the filtering criteria for the filter has to be redefined. Additional information about the Rician distribution function such as

the higher order moments of the distribution function may also be incorporated in the filtering algorithm to further improve the efficiency of the proposed method.

In study 3, the noise estimation in the proposed filter design has limitations when zero-intensity background is absent in the image. Also, we observe that the proposed transformation function does not make noise completely independent of the signal, which could still lead to insufficient denoising. Future work may include a modified Wiener filter design with a more accurate estimation of true noise and a better nonlinear transformation function to make noise truly independent of the signal function for MRI magnitude equation.

2.6 Conclusion

In study I we have proposed an adaptive Rician denoising procedure with edge preserving capabilities. The objective of the proposed method is to provide sufficient denoising with improved contrast to noise ratio of the image without the loss of edge information. Edge preservation has been achieved by a sophisticated statistical method that performs verification of the null hypothesis of the Brown-Forsythe test for the two independent regions across the diagonal of the circular mask. This method has been tested on magnitude MRI images of the cartilage and synthetic images. We have observed a significant reduction of noise in the image with negligible loss in cartilage tissue due to the edge preservation capability of the filtering method. It also improves the contrast to noise ratio of the cartilage with respect to the surrounding knee structure. The efficiency of the proposed method has been validated, by estimation of the image quality using SNR and CNR index ratios for the denoised MRI images. The proposed method can also be implemented on other magnitude MRI images which are similarly affected by Rician denoising as shown in the simulation study. Future work may include advanced edge detection algorithms for more robust edge detection, a more accurate estimation of noise, improved computational cost and extension of the proposed method for 3D denoising.

In study II we have proposed an adaptive filtering technique for Rician noise removal based on the regional SNR characteristics of the image. The filter computes local SNR and accordingly carries out denoising based on the distribution of noise in the region using local statistics. The proposed filtering technique offers better denoising with improved PSNR and contrast ratio of the image. The proposed method has also been implemented on T2 weighted MR images for various slices. The efficiency of the filtering technique is evaluated by the study of the image quality parameters such as PSNR

and RMSE; which show improvement in the image after the denoising process. The denoising capability of the filtering technique can further be improved by using a more robust estimation of the regional SNR and a more accurate estimation of noise in the image irrespective of the background of the image.

In study III, a nonlinear filter based denoising procedure has been proposed from our observation of the advantages offered by homomorphic filter and Weiner filter. An intuitive reasoning process offered by Wiener filter has been included to deduct the denoising procedure. The simulation results show the efficiency of the proposed method for signal dependent filtering of Rician noise. It can also be observed that the proposed filter helps in better preservation of edge details. As such, it can be used in soft tissue denoising where extreme loss of edge details can be prevented while performing denoising or other image enhancement procedures.

The future research focus can include a more advanced implementation of the filter design using a suitable image transformation to make noise completely independent of the signal and an even more accurate estimation of noise for a more efficient denoising procedure with improved contrast and edge preservation capabilities. Other work may also concentrate on addressing noise for multiple coil signal with a possibility of nonlinear techniques to address this.

Chapter 3

Wavelets for Cartilage Detection

This chapter is an introduction to 3D undecimated wavelet transform and use of wavelet multiresolution analysis for 3D cartilage edge detection in MRI. In this study we have utilized 3D undecimated wavelet transform for cartilage detection due to its non-decimate nature and use of multiresolution for locating fine edge details. The cartilage edge detection have been addressed around previously introduced Rician noise distribution and a separate study indicating edge localization for step edge in image due to Rician noise have been addressed. The proposed method offers a much faster and efficient 3D cartilage detection with optimization in the wavelet domain. In addition this study also proposes a new edge localization factor for step edges in a MRI image subjected to signal dependent Rician noise.

The results of this study have been published in the following

- Aarya I., Jiang D., "Automated 3D articular cartilage detection and optimization using un-decimated wavelets in MRI". Signal, Image and video processing. 2015, 9(1), pp 305-314 (Aarya and Jiang, 2015)
- Aarya I., Jiang D., and Gale T., "Edge localization in MRI for images with signal dependent noise". IET-Electronic Letters. 2015, 51(15), pp 1151-1153 (Aarya et al., 2015)

3.1 Introduction

3.1.1 Wavelets

Fourier transform is the most widely used method for signal analysis and was first discovered by Joseph Fourier (Merry and Steinbuch, 2005). It characterizes signal as infinite

sum of weighted sine and cosine waves which are also multiples of the fundamental frequency (Akay, 1995; Gonzalez et al., 2004). Fourier transform (FT) usually works well if the signal is periodic, but not with transient signals (Akay, 1995). As a result short time Fourier transform (STFT) was proposed in order to address this shortcoming, by dividing the signal over blocks of short duration on which FT was implemented. But STFT depends on the choice of window selected, where a longer window gives better frequency resolution but a poor time resolution.

On the other hand wavelets are oscillatory sinusoids with varying duration (Akay, 1995). Their analysis window can be varied according to frequency with a greater flexibility; shorter for higher frequencies and wider for lower frequencies to analyse all changes within the signal. The primary advantages of wavelet transform is its ability to localize an event not only in frequency but also in the time domain (Akay, 1995). Despite this they still cannot address the Heisenberg criteria of knowing both the frequency and time localization of an event simultaneously (Akay, 1995; Gonzalez et al., 2004). One usually has to trade off knowing either localization in time or frequency domain and not both together.

Wavelet thus have an analogy of working as a mathematical scope whose window can be adjusted depending on the wavelet scale. Generally, for a function to be classified as a wavelet $\psi(t)$ it must satisfy two constraints which are 1) they must decay with respect to time where rate of decay is governed by the selected function as $lim_{\to\infty}|\psi(t)| = 0$ and 2) their integral over time must vanish $\int_{-\infty}^{\infty} \psi(t)dt = 0$ (Akay, 1995). These conditions enable localization and oscillatory function. Note that the integral of scaling function may not always be equal to zero and can be assumed as $\int_{-\infty}^{\infty} \phi(t)dt = 1$.

Wavelet transform analyses signal or function $f(x)$ as a linear combination of expansion functions (Gonzalez et al., 2004)

$$f(x) = \sum_{k} \alpha_k \varphi_k(x) \tag{3.1}$$

where k is an integer index of finite or infinite sum, α_k are real valued expansion coefficients $\varphi_k(x)$ are real valued expansion functions (Gonzalez et al., 2004). The mother wavelet function is often contracted and dilated by changing scale parameter s and moved across the signal with help of t (Merry and Steinbuch, 2005). For a 1D linear signal $f(x)$,

$c_{j_0}(k)$ are usually the approximation coefficients obtained as convolution of signal function $f(x)$ with the scaling function $\varphi_k(x)$ given as, $< f(x), \varphi_{j_0,k}(x) >= \int f(x)\varphi_{j_0,k}(x)dx$. While $d_j(k)$ are normally the wavelet or differential coefficients obtained as convolution of the signal function with wavelet function $\psi_{j,k}(x)$ given as $< f(x), \psi_{j,k}(x) >= \int f(x)\psi_{j,k}(x)dx$. In the following paragraph, Eq. (3.2) indicates the discrete representation of wavelet transform using filter banks.

Discrete wavelet transform (DWT) require filter banks for their faster operation and multiresolution analysis. These filter banks are developed using the refinement equation and are usually low pass and high pass filters (Merry and Steinbuch, 2005). The filter banks used in the forward wavelet transform are often known as analysis filter bank while those used in the inverse wavelet transform are known as synthesis filter banks. 1D discrete wavelet transform is thus given as (Gonzalez et al., 2004),

$$f(n) = \frac{1}{\sqrt{M}} \sum_k W_\varphi(j_0, k)\varphi_{j_0,k}(n) + \frac{1}{\sqrt{M}} \sum_{j=j_0}^{\infty} \sum_k W_\psi(j, k)\psi_{j,k}(n) \tag{3.2}$$

where

$$W_\varphi(j_0, k) = \frac{1}{\sqrt{M}} \sum_n f(n)\varphi_{j_0,k}(n) \tag{3.3}$$

$$W_\psi(j, k) = \frac{1}{\sqrt{M}} \sum_n f(n)\psi_{j,k}(n) \tag{3.4}$$

W_φ and W_ψ are the corresponding scaling and wavelet coefficients obtained by convolution with scaling $\varphi_{j_0,k}$ and wavelet function $\psi_{j,k}$, where scale $j \geq j_0$ and M is the length of the signal. These output coefficients obtained with help of filter bank and are also known as the sub-band details. The scaling coefficients correspond to approximation sub-bands while the wavelet coefficients indicate the details sub-band. In discrete wavelet transform the coefficients are down-sampled during forward decomposition process and up-sampled during inverse reconstruction phase. As long as Shannon's Nyquist criteria is followed the effect of down-sampling does not have any serious consequences as most of the signal information is redundant due to aliasing. In addition these filter banks have to be orthonormal allowing for perfect reconstruction of the signal (Merry and Steinbuch, 2005). The corresponding 2D discrete wavelet transform is thus given as (Gonzalez et al., 2004),

$$f(x,y) = \frac{1}{\sqrt{MN}} \sum_{m} \sum_{n} W_{\varphi}(j_0, m, n)(x, y) + \frac{1}{\sqrt{MN}} \sum_{i=H,V,D} \sum_{j=j_0}^{\infty} \sum_{m} \sum_{n} W_{\psi}^{i}(j, m, n) \psi_{j,m,n}^{i}(x, y) \tag{3.5}$$

where,

$$W_{\varphi}(j_0, m, n) = \frac{1}{\sqrt{MN}} \sum_{x=0}^{M-1} \sum_{y=0}^{N-1} f(x, y) \varphi_{j_0,m,n}(x, y) \tag{3.6}$$

$$W_{\psi}^{i}(j, m, n) = \frac{1}{\sqrt{MN}} \sum_{x=0}^{M-1} \sum_{y=0}^{N-1} f(x, y) \psi_{j_0,m,n}^{i}(x, y) \tag{3.7}$$

and $i = H, V, D$ are the horizontal, vertical and diagonal sub-bands details obtained with the wavelet function and M and N are the dimensions of the 2D signal function.

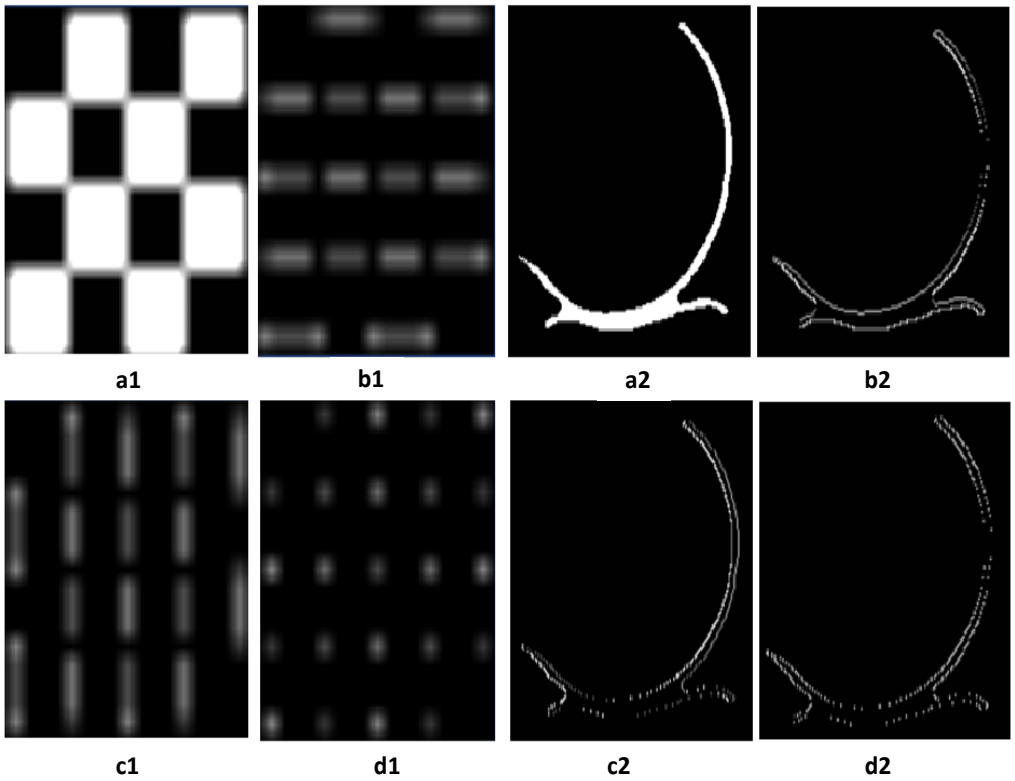

FIGURE 3.1: Demonstration of approximation and detail sub-bands for phantom images with 2D-UWT

As image is a discrete signal, the wavelet transform can be implemented using discrete finite impulse reponse filter (FIR) (Akay, 1995; Gonzalez et al., 2004). For the forward

wavelet transform, the FIR filter for scaling and wavelet functions is given as $h(n)$ and $g(n)$ respectively; while for the inverse wavelet transform the corresponding scaling and wavelet transform is given as $\tilde{h}(n)$ and $\tilde{g}(n)$ respectively (Gonzalez et al., 2004; Starck et al., 2007). These scaling filters are usually low pass filters while the wavelet filters are often high pass filters (Gonzalez et al., 2004). For a fast wavelet transform as the filters are orthonormal and orthogonal to each other they are also known as the quadrature mirror filters (QMF) (Gonzalez et al., 2004). Fig. (3.1) demonstrates scaling and wavelet coefficient obtained using 2D UWT forward transform. As demonstrated by the image, the wavelet coefficients are obtained as high pass filtered image thus providing us with the edge information.

3.1.1.1 Undecimated Wavelet Transform (UWT)

DWT due to its fast operation have found applications in many data analysis operations, but there exists some signal functions which may not benefit from DWT especially its feature of down sampling of data for fast transform. This down sampling may not be able to capture all the crucial events in a signal, especially if it has been removed while being down sampled. In lieu of this, researchers prefer working with CWT which offer the same benefits as DWT but as the name suggests is continuous in nature and does not down sample the signal to be processed. As a result, CWT are relatively slower and generate huge data from the processed signal as they process signal as continuous function of time. In order to resolve this one can work with UWT which offers benefit of both CWT and DWT as it is discrete yet does not down sample the signal function.

Undecimated wavelet transform (UWT) too requires wavelet function $\psi_{j,k}(x, y)$ and scaling function $\varphi_{j,k}(x, y)$ which are scaled and dilated to locate an event in scale space plane $V \in L^2(R)$ as it is moved across the image (Gonzalez et al., 2004). Both scaling and wavelet functions generally consist a set of dilated and scaled functions given as $\varphi_{j,k}(x) = 2^{\frac{j}{2}}\varphi(2^j x - k)$ and $\psi_{j,k}(x) = 2^{\frac{j}{2}}\psi(2^j x - k)$ where j here determines width or scale of the wavelet function along x axis and k here determines the position in scale-space (Gonzalez et al., 2004). Unlike discrete wavelet transform (DWT), the coefficients do not undergo either down sampling or up-sampling, instead the holes are filled using the a' trous algorithm. By changing the scale we can work at different resolutions in an image which also determines the dilations of a wavelet function. This may be used to locate different events in an image. In discrete domain the 1D scaling and wavelet coefficients are given as (Starck et al., 2007),

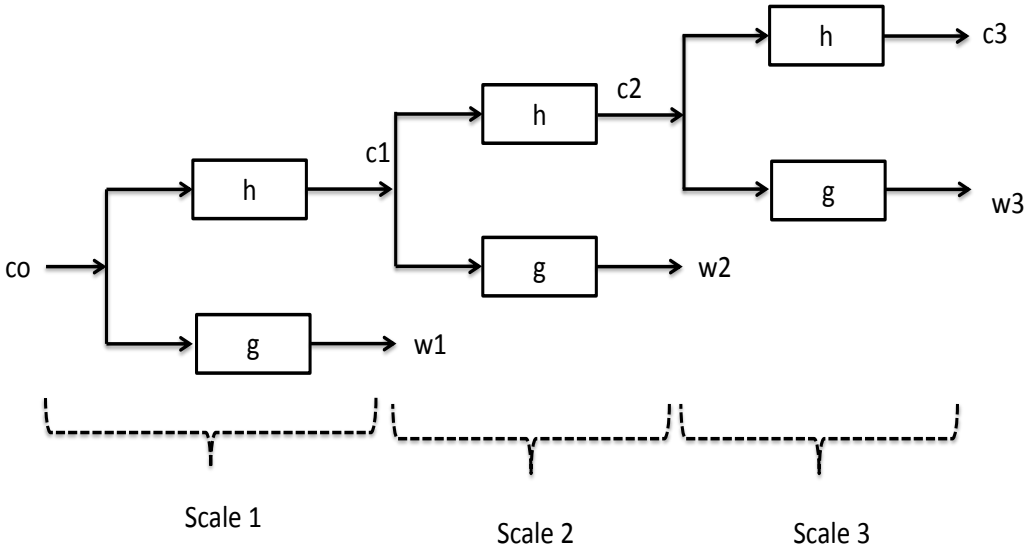

FIGURE 3.2: Block diagram for 1D UWT at three scales

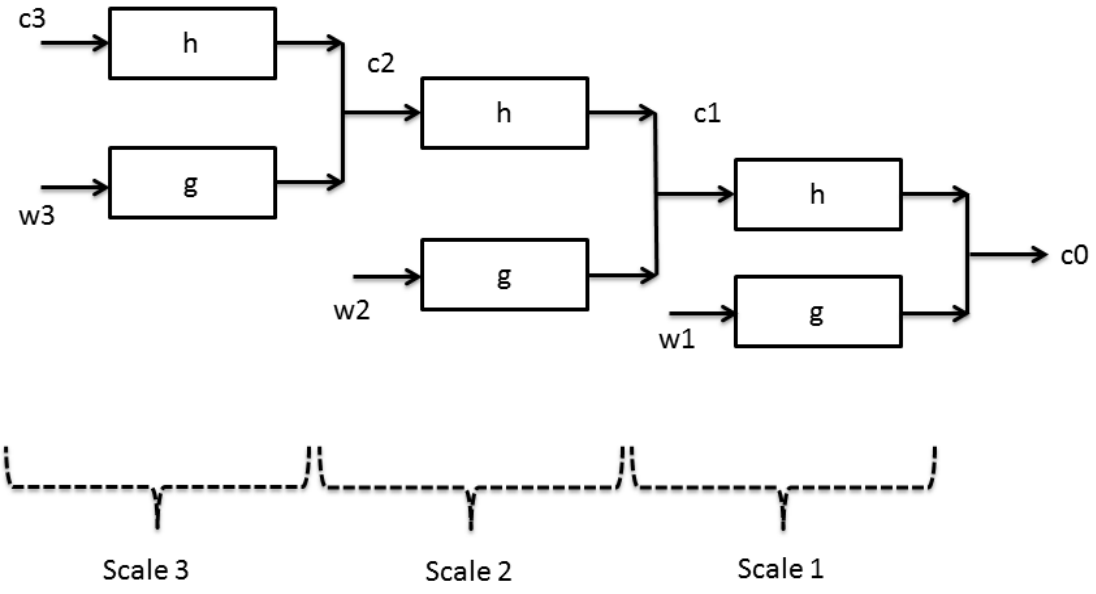

FIGURE 3.3: Block diagram for 1D inverse UWT at three scales

$$c_{j+1}[n] = h_j * c_j = \sum_k h[k]c_j[n + 2^j k] \tag{3.8}$$

$$w_{j+1}[n] = g_j * c_j = \sum_k g[k]c_j[n + 2^j k] \tag{3.9}$$

where c_j and w_j are scaling and wavelet coefficients obtained by wavelet decomposition respectively, k is filter length and n is signal (Starck et al., 2007) . h_j and g_j are discrete low-pass and high-pass wavelet filter banks and represent the scaling $\varphi_{j,k}(x, y)$ and wavelet functions $\psi_{j,k}(x, y)$ respectively. Signal c_j is decomposed into its low and high frequency components using scaling and wavelet functions represented by filter banks h and g respectively. For wavelet multiresolution analysis, coefficients at higher resolution are obtained by further decomposition of scaling coefficients as demonstrated in Fig. (3.2). The corresponding inverse undecimated wavelet transform is given as,

$$c_j[n] = \frac{1}{2}[\tilde{h}_j * c_{j+1}[n] + \tilde{g}_j * w_{j+1}[n]] \tag{3.10}$$

where $\tilde{h}$ and $\tilde{g}$ are orthogonal inverse filter banks. In addition to being orthogonal, wavelet functions are also separable which allows us to convolve the 1D wavelet function along x, y, z axes of the volume to obtain 3D decomposition and reconstruction of the volume (Starck et al., 2007).

Due to the non-decimate operation of UWT we may be left with redundant information which we assume may prove to be useful for structures with limited data content. Though this may not prove to be advantageous in other cases such as those observed with geographical data with the use of CWT. The redundancy content of the UWT is given as $3(J - 1)$ where J is the scale level (Adam and Rădoi,2010; Starck et al., 2007). Like other wavelet functions, UWT too offers us multiresolution property which if properly utilized can help in obtaining cartilage coefficients at various resolution levels. Fig. (3.2) shows block diagram of forward decomposition with 1D UWT at three scales. While Fig. (3.3) displays the inverse wavelet transform

3.1.2 Multiresolution Analysis (MRA)

Let a 1D image function $f(x)$ belonging to square integrable space $L^2(R)$, on decomposition by an orthogonal wavelet basis function form a closed subspace (Mallat and Hwang, 1992). For a given signal function $f(x)$ if the expansion is unique then the expansion set

$\varphi_k(x)$ is called the basis for that class of functions. As a result the subspace of $L^2(R)$ spanned by this function may then be given as,

$$V = \overline{Span_k\{\varphi_k(x)\}} \tag{3.11}$$

where over-bar denotes closure. For a 2D expression the function is scaled and translated as $\varphi_{j,k}(x) = 2^{j/2}\varphi(2^j x - k)$ (Burrus et al., 1998). By choosing an appropriate scaling function $\varphi(x)$ properly; this $\varphi_{j,k}(x)$ can be made to span entire $L^2(R)$. But if we restrict j to $j = j_0$ the resulting expansion set $\varphi_{j_0,k}(x)$ obtained with j_0 is a subset of $\varphi_{j,k}(x)$ that spans entire subspace of $L^2(R)$. Then the two individual sub-spaces may then be denoted as follows, where V_{j_0} is sub-space due to j_0 and V_j is subspace due to j.

$$V_{j_0} = \overline{Span_k\varphi_{j_0,k}(x)} \tag{3.12}$$

$$V_j = \overline{Span_k\varphi_{j,k}(x)} \tag{3.13}$$

By increasing j one increases size of V_j thus allowing functions with smaller variations or finer details to be included in the subspace (Gonzalez et al., 2004). The concept of multiresolution analysis (MRA) considers the sub-spaces to be nested within each other such that,

$$\subset V_{-2} \subset V_{-1} \subset V_0 \subset V_1 \subset V_2 ..... \subset L^2 \tag{3.14}$$

$V_j \subset V_{j+1}\ \forall j \in Z$ with necessary conditions of $V_{-\infty} = \{0\}$ and $V_\infty = L^2(R)$ as $j \to \infty$. Thus implying that low resolution signals may be contained within higher resolution signals (Burrus et al., 1998).

Similarly when using a wavelet function $\psi_{j,k}(x)$ one may obtain a wavelet subspace W_j. This wavelet sub-space also spans the difference between scaling subspace and is given as

$$W_j = \overline{Span_k\psi_{j,k}(x)} \tag{3.15}$$

For MRA the scaling and wavelet subspaces are considered to be nested within each other.

$$V_{j+1} = V_j \oplus W_j \tag{3.16}$$

These subspaces when computed for various wavelet resolutions $j = 0, 1, 2....J$ form a nested subspace function, such that a higher resolution function space may also contain a lower resolution subspace. The corresponding scaling and wavelet function subspace are represented as union of subspaces, given as

$$L^2(R) = V_j \bigoplus W_j \bigoplus W_{j+1}.. \tag{3.17}$$

where V_j is the subspace obtained by scaling function, W_j is the wavelet function subspace over $L^2(R)$ and $\oplus$ represents union function for subspaces as $j \to \infty$ (Gonzalez et al., 2004). This proposition can be extended to a 3D image function $f(x, y, z)$ which may belong to a closed subspace in $L^2(R^3)$.

In addition for multiresolution analysis we require that the scaling $\varphi_{j,k}(x)$ and wavelet functions $\psi_{j,k}(x)$ be orthogonal to each other with integer translates. This orthogonal basis function enables faster computation and allows partitioning of signal energy in the wavelet domain as given by Parseval's theorem, which relates energy of signal $f(x)$ to energy in individual compartments and their wavelet coefficients (Burrus et al., 1998). The discrete multiresolution analysis is then possible with help of recursive scaling and wavelet function popularly known as the refinement equation. This recursive scaling function is given as,

$$\varphi(x) = \sum_n h_\varphi(n)\sqrt{2}\varphi(2x - n) \tag{3.18}$$

$h_\varphi(n)$ coefficients in above recursive equation are called scaling coefficients. h_φ is referred to as scaling vector. And the corresponding wavelet function $\psi(x)$ is given as (Burrus et al., 1998; Gonzalez et al., 2004),

$$\psi(x) = \sum_n h_\psi(n)\sqrt{2}\varphi(2x - n) \tag{3.19}$$

3.1.3 Singularity detection with wavelets

Edges in an image are characterized by changes in intensity across regions commonly observed around the boundaries in the image. These image details may be represented

using singularities and their Lipschitz exponent α. Let $L^2(R)$ denote the Hilbert space with 1D functions given as $f(x)$. In addition also consider a smoothing function $\theta(x)$ whose integral is equal to 1 and converges to infinity at zero. Let the first and second order derivative of this smoothing function be given as $\psi^a(x) = \frac{d\theta(x)}{dx}$ and $\psi^b(x) = \frac{d^2\theta(x)}{dx^2}$ which may also be considered as wavelets as their integral is equal to zero (Mallat and Zhong, 1992).

A wavelet transform thus obtained by convolution of signal function $f(x)$ with wavelet function is given as,

$$W_s^a f(x) = f * \psi^a(x) = f * \frac{d\theta(x)}{dx} \tag{3.20}$$

$$W_s^b f(x) = f * \psi^b(x) = f * \frac{d^2\theta(x)}{dx^2} \tag{3.21}$$

where $W_s^a f(x)$ and $W_s^b f(x)$ are respectively the first and second order derivative of the smoothed signal function. It should also be noted that the zero crossing of $W_s^b f(x)$ correlate with local extrema of $W_s^a f(x)$ which also corresponds with the inflexion points of signal $f * \theta_s(x)$ (Mallat and Zhong, 1992). This detection of zero crossing or local extrema is a commonly used approach for edge detection in an image (Canny, 1986). Note that these are also very similar to the gradients of an image when used with a Laplacian operator.

Similarly one can define wavelet functions for 2D wavelet transform as $\psi^1(x, y)$ and $\psi^2(x, y)$ and their convolution with a 2D signal function $f(x, y) \in L^2(R)$ results in, $W_s^1 f(x, y) = f * \psi^1(x, y)$ and $W_s^2 f(x, y) = f * \psi^2(x, y)$ where (Mallat and Zhong, 1992),

$$\begin{pmatrix} W_s^1 f(x,y) \\ W_s^2 f(x,y) \end{pmatrix} = s \begin{pmatrix} \frac{\partial}{\partial x}(f * \theta_s)(x,y) \\ \frac{\partial}{\partial y}(f * \theta_s)(x,y) \end{pmatrix} = s\overrightarrow{\nabla}(f * \theta_s)(x,y) \tag{3.22}$$

Hence the corresponding edge detection in an image with help of 2D wavelet transform may also be obtained from $W_s^1 f(x, y)$ and $W_s^1 f(x, y)$. As these wavelet transform coefficients are very similar to image gradients they may be used to compute the magnitude, also known as the wavelet transform modulus and angle at each scale s, as given below,

$$M_s f(x, y) = \sqrt{|W_s^1 f(x, y)|^2 + |W_s^2 f(x, y)|^2} \tag{3.23}$$

$$A_s f(x,y) = argument(W_s^1 f(x,y) + iW_s^2 f(x,y)) \tag{3.24}$$

In addition singularities or edges in an image can also be characterized by their Lipschitz exponents. Let n be a positive integer and $n \leq \alpha \leq n+1$. A function $f(x)$ is said to be Lipschitz α at x_0 if and only if there exists two constants A and $h_0 > 0$ and a polynomial of order n, $P_n(x)$ such that for $h < h_0$ (Mallat and Zhong, 1992; Mallat and Hwang, 1992)

$$|f(x_0 + h) - P_n(h)| \leq A|h|^\alpha \tag{3.25}$$

Also function $f(x)$ is uniformly Lipschitz α over the interval $]a,b[$, if and only if there exists a constant A and for any $x_0 \in]a,b[$ and there exists a polynomial P_n of order n. This Lipschitz exponent may then be related to the asymptotic decay of the wavelet transform. Mallat et. al provided two theorems for determining the Lipschitz regularity. Theorem 1 helps in determining the Lipschitz regularity over intervals, but in order to determine regularity over point x_0 for function $f(x)$ one requires the second theorem previously proved by Jaffard which can be given as,

Theorem 2: Let n be a positive integer and $\alpha \leqslant n$. If $f(x)$ is Lipschitz α at x_0, then there exists a constant A such that for all points x in a neighbourhood of x_0 and any scale s (Mallat and Zhong, 1992)

$$|Wf(s,x)| \leqslant A(s^\alpha + |x - x_0|^\alpha) \tag{3.26}$$

Hence in wavelet domain, Lipschitz exponents may evolve across multiple wavelet scales (Mallat and Zhong, 1992). This can be computed using wavelet transform modulus maxima (WTMM) across these wavelet scales. Lipschitz regularity is thus computed by determining the value of α such that As^α approximates decay of $|Wf(s,x)|$. If the edge is smooth we can estimate how smooth it is from its decay using WTMM across wavelet scales. In addition if the modulus maxima of $Wf(sw,x)$ belong to cone of influence (COI) then function $f(x)$ is Lipschitz α at x_0 if there exists constant A and is defined as,

$$|Wf(s,x)| \leq As^\alpha \tag{3.27}$$

To obtain the value of regularity we take log on both sides of the above equation (Mallat and Zhong, 1992)

$$log|Wf(u,s)| \leq log(A) + \alpha log\, s \tag{3.28}$$

You can also obtain the value of regularity by computing the slope of the maxima line (Mallat and Zhong, 1992; Mallat and Hwang, 1992).

As a result by using Lipschitz exponent as numerical descriptor one can reconstruct a close approximation of original signal or singularity from multiscale edges (Mallat and Zhong, 1992). This decay of wavelet transform amplitude across scales is related to the uniform and point-wise Lipschitz regularity of the signal. The following Fig. (3.4) demonstrates the decomposition of singularity across the wavelet domain. Noise in general has the negative Lipschitz exponent. This concept has also been adapted in this study for a global detection of cartilage across wavelet scales.

The motivation of this study, is to make use of 3D wavelet decomposition and multiresolution to look for edge information and their orientations at different resolution levels in an image, for edge detection. By using multiple dimensions we may be able to achieve better understanding of the geometrical connectivity and edge orientation within a 3D volume, which may not be possible with 2D edge detection alone. Wavelets offer better time-frequency localization of an event as compared to other traditional transforms for image analysis and as a result may capture cartilage edge details better. Furthermore in this study edge information is achieved with help of undecimated wavelet multiscale decomposition. By implementing undecimated wavelet transform we avoid discarding coefficients which might be sensitive to cartilage edge at higher resolutions and may be able to contribute in the cartilage detection process. Candidate coefficients representing cartilage details at a given wavelet resolution can be selected using a local threshold for multiscale singularity analysis. In wavelet domain, coefficients relevant to particular singularity event or edge will increase in scale or remain the same at higher resolution levels and will follow a wavelet transform modulus maxima (WTMM) curve. By implementing a global threshold for multiple resolution levels in wavelet domain, we can optimize coefficients selected by local threshold, within this curve for cartilage detection by the proposed method. Such an approach avoids use of operator for cartilage detection. It makes use of 3D orientation information of an edge in addition to the traditional horizontal and vertical details. Also it does not require any a priori information or use of multiple images for cartilage detection. In section 3.3 we describe in detail the proposed cartilage detection method, with performance evaluation and discussion in section 3.4.

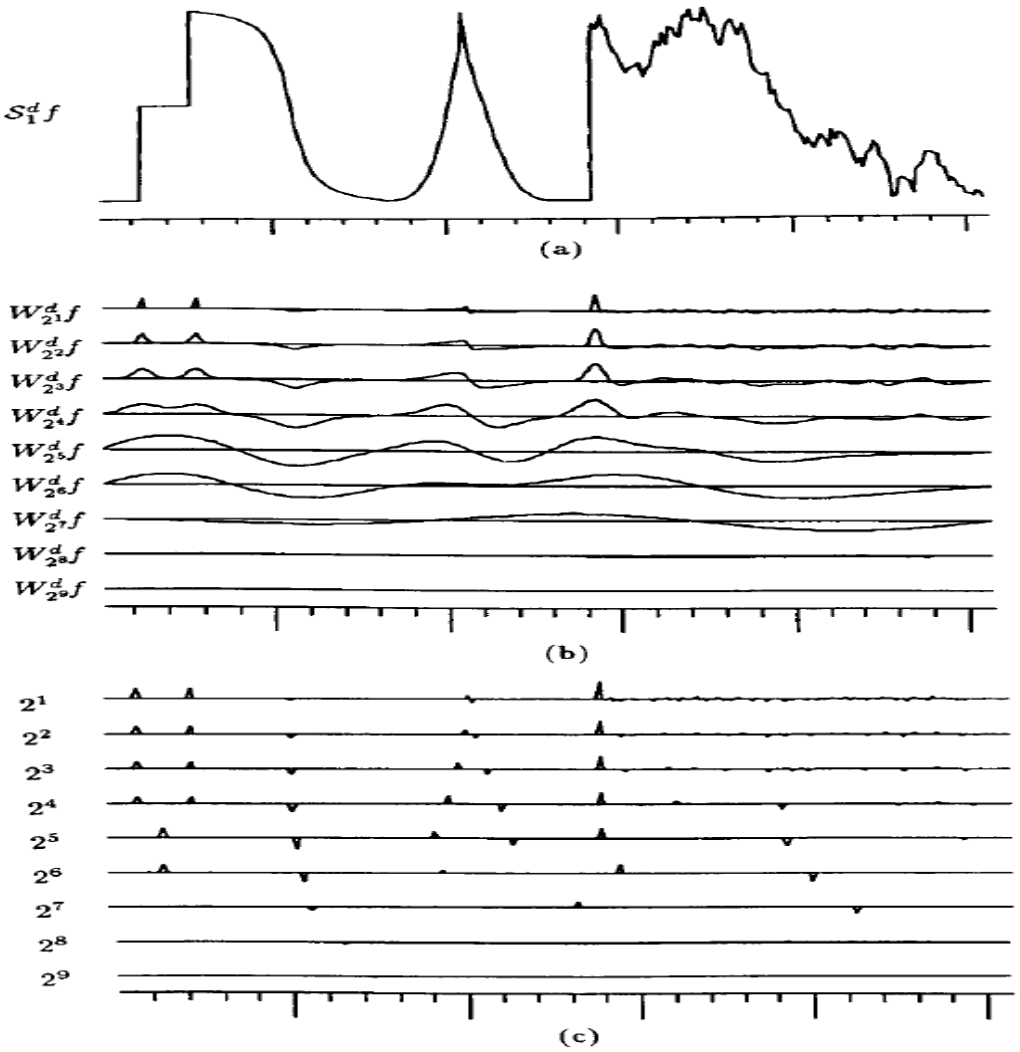

FIGURE 3.4: a) original signal b) DWT of signal c) modulus maxima of decomposed signal. Dirac indicates position and amplitude of modulus maxima (Mallat and Zhong, 1992)

3.2 Related Work

Soft tissue like articular cartilage play a vital role in diagnosis and assessment of medical conditions in modern medicine. The morphological characteristics of articular cartilage such as thickness and volume may often be used as one of the biomarkers for Osteoarthritis (OA) diagnosis (Cicuttini et al., 2002; Kumar et al., 2011). One of the challenges of cartilage detection, is the poor contrast of the cartilage tissue with the surrounding joint structure making it difficult to extract cartilage. This task is made even more difficult due to the limited pixel thickness of the cartilage. Articular cartilage information in healthy people is only 1.5 - 3 mm thick and may be less in patients suffering from OA, making diagnosis even more difficult (Cicuttini et al., 2002). In addition real world

images are often subjected to noise and artefacts during the image acquisition process. This noise if sufficiently large can severely affect the image quality making the image information unreliable.

Current strategies in cartilage detection rely on manual segmentation and semi-automated procedures (Solloway et al., 1997). Manual cartilage detection procedures include an experienced operator to identify boundary of the cartilage tissue which is later used for segmentation and further assessment. Manual procedures can suffer from operator induced errors and consume excessive time. Hence an automated and faster process for improved cartilage detection is desirable for diagnosis and clinical practice. Traditional edge detection and segmentation procedures can be achieved using various strategies such as edge filters, region growing, region split and grow and watershed based segmentation (Pham et al., 2000). Advanced edge detection and segmentation methods include use of semi-automated procedures such as shape prior, active contours and knowledge about bone cartilage interface for an effective cartilage detection (Solloway et al., 1997; Kapur et al., 1998; Hinrichs et al., 2003; Kass et al., 1988). While 'snakes' or active contour initially proposed by Kass et.al. has widely been used, it works on the principle of energy minimizing function and largely relies on the original contour to be closed and placed near the possible region of interest (Kass et al., 1988; Heimann and Meinzer, 2009). Recently active shape models proposed by Cootes et.al. which make use of point distribution model for shape characterization, have also been introduced to offer 3D segmentation of the tissue (Heimann and Meinzer, 2009; Fripp et al., 2005; Baldwin et al., 2010; Fripp et al., 2010). In addition Baldwin et al. propose use of subject-specific information in addition to use of active shape models for efficient cartilage segmentation (Baldwin et al., 2010). The drawback of the active shape models is that they require a-priori information about the tissue structure to be segmented and may utilize use of either atlases or parametrization techniques which makes the process time consuming and complex (Heimann and Meinzer, 2009). Also the effectiveness of this process depends on the choice of shape model algorithm and its ability to address the possible variation for a real world tissue changes (Heimann and Meinzer, 2009). Another approach for cartilage segmentation includes feature learning for the cartilage tissue and is implemented either with neural networks or support vector machines (Prasoon et al., 2013; Zhang et al., 2013; Tamez-Pena et al., 2012). Feature learning methods require dictionary for identifying cartilage and a-priori information. Some of the methods such as the image registration techniques may offer unsupervised and automated segmentation but require use of multiple datasets (Urish et al., 2013). Other methods may include dynamic edge tracing, feature extraction using machine learning, shape description, graph cut based segmentation and neural networks (Withey et al., 2009; Nain et al.,2007; Pastor et al.,

2001; Yin et al., 2010; Unser and Eden, 1989).

Some of the other image processing tools used for segmentation may include b-splines, water-shed segmentation, live wires etc. (Pham et al., 2000; Eckstein et al., 2006;). More advanced methods may include use of radial transformation for segmentation and gradient flow vector for segmentation; these methods try to address the curvature of the cartilage tissue (Ku-Yaw et al., 2009; Jinshan et al., 2006). Tang et. al proposed use of gradient flow vector as opposed to traditional snake based vectors introduced by Kass et. al as a more suitable approach to segment the cartilage as it can be adapt more readily with the curved nature of the cartilage. It also makes use of b-spline to identify the contours of the cartilage prior to segmentation (Jinshan et al., 2006).

3.3 Proposed Multiresolution Edge Detection

Articular cartilage is a thin and curvilinear structure and segmentation of this structure, often depends on the expertise of an operator. In this study, we propose an automated and optimal multiresolution cartilage detection technique using 3D histogram and wavelet multiscale singularity analysis. 3D undecimated wavelet transform is implemented on MRI volume to obtain wavelet coefficients, which are used to determine an adaptive threshold for a given local resolution. Local threshold helps to segment foreground edge details, relevant to cartilage details and is obtained using maximum likelihood estimate of the 3D histogram. Once ideal wavelet coefficients relevant to cartilage for a certain confidence level for intensity of the histogram are selected, we further optimize cartilage detection using wavelet multiresolution singularity. Wavelet singularity helps us to regulate cartilage coefficients obtained at different resolution levels and thus globally optimize cartilage coefficients resulting in enhancement of fine edge details which might be necessary for cartilage diagnosis. The final selected wavelet coefficients are used to compute the inverse wavelet transform of the MRI volume, which is further used to obtain a 3D model of cartilage tissue using the volume rendering process. The proposed method has been tested and validated using MRI and phantom datasets of articular cartilage. Quantitative analysis has been performed using mean square error (MSE), signal to noise ratio (SNR) and volumetric estimation of the datasets for different confidence levels and noise. The proposed method displays reduction in MSE for both denoised and noisy MRI volumes at different standard deviations of noise with overall improvement in SNR. The proposed method demonstrates advantage for soft tissue detection using wavelet transform and multiresolution analysis as observed in the simulation study with MRI datasets. It helps to appropriately segment out tissue in

noisy images with poor contrast and limited structural information.

Let the 3D image function obtained by successive stacking of 2D MRI image slices be given as, $f(x,y,z) = \sum_{x}^{M-1}\sum_{y}^{N-1}\sum_{z}^{K-1} M(x,y,z)$ and $f(x,y,z) \in L^2(R^3)$ square integrable space. $M(x,y)$ is 2D magnitude MR image function where x and y represent co-ordinate positions and z represents slice number. The proposed method performs automated edge detection using coefficients C_ψ obtained by forward decomposition of image volume with un-decimated wavelets. An automated edge detection at local resolution j is performed using adaptive threshold t_L followed with optimization of coefficients at a global scale $\grave{\gamma}$ using wavelet multiresolution analysis as shown in Fig. (3.5).

At each scale we obtain wavelet coefficients which contain the horizontal, vertical and directional edge information. For a 3D volume $f(x,y,z)$ we have horizontal, vertical and directional edge information along the 6 faces of the volumetric cube in addition to corners; and the corresponding histograms for these edge details are used for edge detection by the proposed method at local and global wavelet resolutions.

3.3.1 Local edge detection

The main objective of local edge detection by the proposed method, is to collect all candidate edge details obtained by forward wavelet decomposition at a given resolution level j using an adaptive threshold t_L. In the proposed study this adaptive threshold t_L is determined by using the maximum likelihood estimate (MLE) of wavelet histograms and its intensity distribution P for selected confidence level α_1. An optimal adaptive threshold is defined by its capability to segregate a multimodal distribution without causing inadequate clustering of image data and is simple to compute. Histogram of wavelet coefficients usually follow a mixture-model distribution and are characteristic of grey-level distribution within the image. Depending on the image this distribution may be multimodal; in this study as the coefficients C_ψ are obtained from single coil magnitude MR image the distribution is considered to be Rician in nature.

In single coil magnitude MR image, due to the nature of image reconstruction from raw k-space data, the inherent Gaussian noise in the image data causes the distribution of final image to be non-linear and signal dependent with Rice distribution (Gudbjartsson and Patz, 2005). For the Rician noise affected MR images; at low intensities such as the background, the histogram has a Rayleigh distribution whereas for high intensity region the distribution is more Gaussian, given by Eq. (3.29).

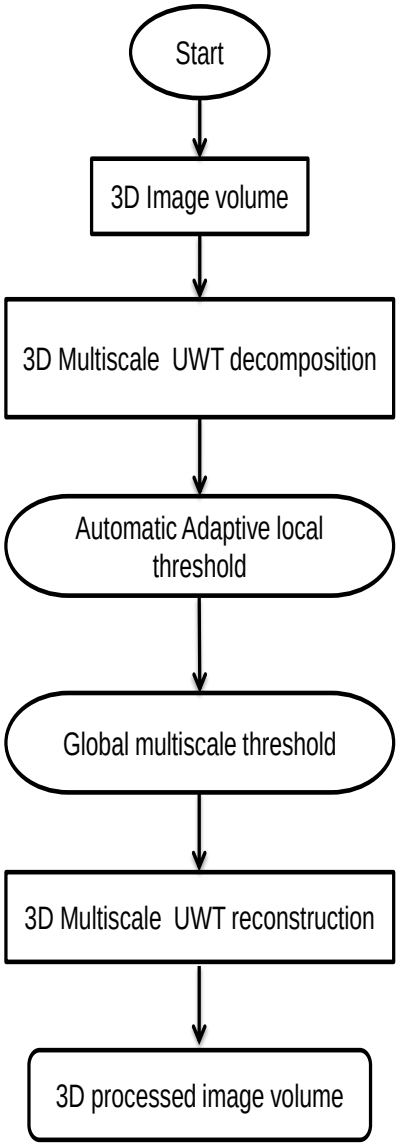

FIGURE 3.5: Proposed method for cartilage edge detection

In this study, for simplicity of analysis we consider the wavelet histogram to follow a bi-modal distribution characterized mainly by low intensity background information and high intensity edge information which may also contain the desired cartilage details. For local edge detection we need to isolate coefficients which are under high intensity Gaussian distribution P_G and can be done using a threshold t_L. By computing the lower i_{GL}, i_{RL} and higher intensity i_{GH}, i_{RH} confidence limits of individual histogram we can compute a single threshold value t_L for the parent histogram, by using linear interpolation.

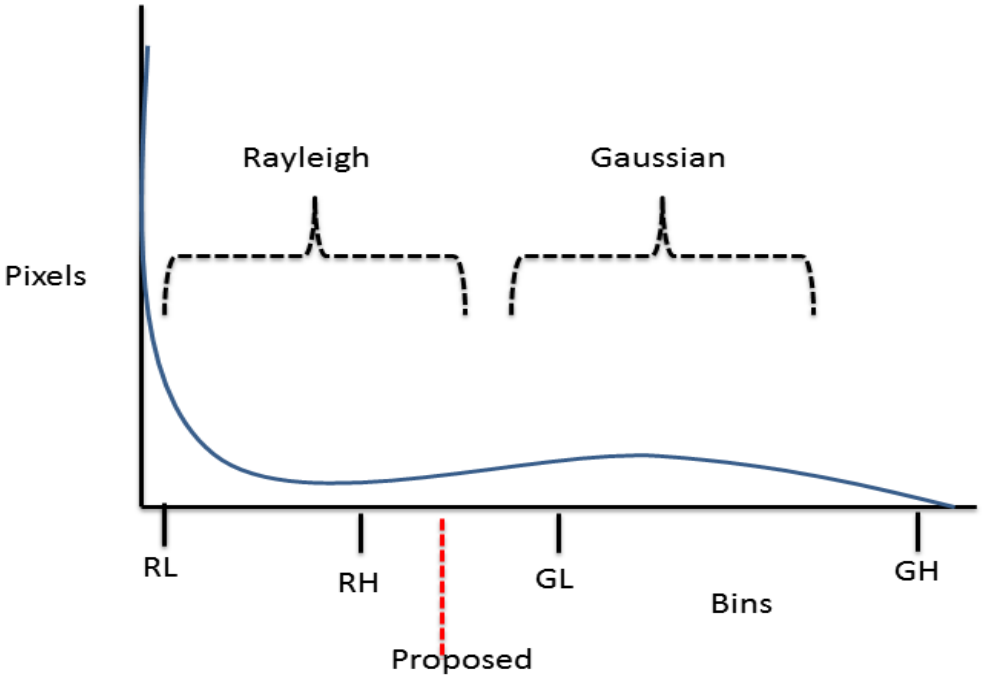

FIGURE 3.6: Proposed threshold estimation using histogram

3.3.1.1 Estimation of intensity interval using MLE

To compute the local threshold value t_L, we first need to determine the MLE and intensity interval of the bimodal histogram. The foreground image details are assumed to have Gaussian distribution P_G and a local threshold value t_L is implemented to isolate wavelet coefficients $\hat{C_{\psi G}}$ belonging to this distribution. The background distribution in the parent bimodal histogram is assumed to be Rayleigh and is given as (Siddiqui, 1964),

$$P_R(C_{\psi_i}|\mu_R, \sigma_R) = \frac{C_{\psi_i}}{\sigma_R^2} e^{-\frac{(C_{\psi_i}^2)}{2\sigma_R^2}} \tag{3.29}$$

where P_R is the probability distribution function, μ_R is the mean of the Rayleigh distribution, σ_R is the variance of the distribution and C_{ψ_i} is an independent wavelet coefficients. The MLE for variance of Rayleigh distribution is given as (Siddiqui, 1964),

$$\hat{\sigma_R}^2 \approx \frac{1}{2N_p} \sum_{i=1}^{N_p} C_{\psi_i}^2 \tag{3.30}$$

where N_p represents number of samples and are the histograms of edge details obtained due to wavelet decomposition for a given resolution. The complete derivation of MLE for Rayleigh is given in appendix A. The confidence interval CI for Rayleigh in terms of

unknown mean intensity, is sampled with respect to normal distribution for large number of samples and follows t-distribution. The intensity interval for background coefficients can then be given as follows (Canavos, 1984),

$$\hat{C_{\psi_R}} - t_{1-\alpha/2}\frac{S_R}{\sqrt{N_p}} \leq \mu_R \leq \hat{C_{\psi_R}} + t_{1-\alpha/2}\frac{S_R}{\sqrt{N_p}} \tag{3.31}$$

where μ_R is true unknown mean for Rayleigh distribution, S_R is sample variance for Rayleigh distribution, $\hat{C_{\psi_R}}$ is estimated Rayleigh mean computed with MLE for Rayleigh distribution given as,

$$\hat{C_{\psi_R}} = \hat{\sigma_R}\sqrt{\frac{\pi}{2}} \tag{3.32}$$

The values of respective $t_{1-\alpha/2}$ can be obtained from t-distribution table with N_p degrees of freedom for a selected confidence level α_1 (Canavos, 1984). Higher confidence level α_1 ensures more area is covered under the given distribution. On solving the above equation we can obtain lower and higher intensity values for histogram of Rayleigh distribution. These confidence limits for intensity are represented as i_{RL} and i_{RH} respectively as shown in Fig. (3.6).

Similarly, the probability distribution of wavelet coefficients for foreground are modelled as Gaussian distribution given as $P_G(C_{\psi_i}|\mu_G, \sigma_G) = \frac{1}{\sqrt{2\pi\sigma_G^2}}e(-\frac{C_{\psi_i}-\mu_G}{2\sigma_G^2})$ where P_G is the probability function, μ_G is the mean of Gaussian distribution, variance of the distribution is given as σ_G^2 and where C_{ψ_i} is the variable of histogram distribution (Forbes et al., 2011). The maximum likelihood estimate in terms of mean for Gaussian distribution is given as (Forbes et al., 2011).

$$\hat{C_{\psi_G}} = \frac{1}{N_p}\sum_{i=1}^{N_p} C_{\psi_i} \tag{3.33}$$

Where N_p is the number of samples and $\hat{C_{\psi_G}}$ is the mean of the samples (Forbes et al., 2011). In order to determine confidence interval for intensity with respect to mean we use the sampling distribution of the given distribution for unknown mean with respect to the normal distribution. This sampling distribution follows a t-distribution with $(N_p - 1)$ degree of freedom and is thus given as follows (Canavos, 1984),

$$t = \frac{\hat{C_{\psi_G}} - \mu_G}{S_G/\sqrt{N_p}} \tag{3.34}$$

where μ_G is the true mean of the normal distribution and S_G is the sample variance. t is symmetric around mean $\hat{C_{\psi_G}}$ and image details relevant to the foreground are likely to lie within this confidence interval of the histogram. The intensity values are once again characterized as higher foreground and lower foreground and are represented as i_{GH} and i_{GL} respectively as shown in Fig. (3.6). Appendix 2 gives the mathematical derivation for MLE of Gaussian distribution and computation of intensity interval.

Algorithm 1: Adaptive Local Edge Detection

Input: Input Image Volume $I_{vol} = f(x, y, z)$

1 Select wavelet family $W = \{\varphi_{j,k}, \psi_{j,k}\}$

2 **for** wavelet scale j=1:J **do**,

3 3D un-decimated forward wavelet decomposition,
$W_j = \psi_{j,k} * I_{vol}$

4 3D histogram for wavelet coefficients H_{W_j}
$H_{W_j} = \text{histogram}(W_j)$

5 Maximum Likelihood Estimation (MLE) for mean for multimodal distribution using H_{W_j},

6 Intensity interval, using 99% confidence level
a. Foreground distribution $i_{gaussian} = [i_{GL} : i_{GH}]$
b. background distribution $i_{rayleigh} = [i_{RL} : i_{RH}]$.

7 Linear interpolation to compute local threshold t_l.

8 Selecting wavelet coefficient under foreground distribution with proposed local threshold t_l.

9 **end for**

Output: Local thresholded wavelet coefficients W_s

3.3.1.2 Local threshold

As the parent histogram is a continuous distribution, a linear interpolation of the estimated intensity values is used to compute threshold t_L. A linear interpolation can be obtained by using the higher intensity limit of the background distribution i_{RH} and its corresponding pixel information b_{RH} with that of the lower intensity limit of foreground distribution i_{GL} and its corresponding pixel information b_{GL} as shown in Fig. (3.6). The estimated local threshold value is given as (Wikipedia),

$$t_L = i_{RH} + (i_{GL} - i_{RH})\frac{b - b_{RH}}{b_{GL} - b_{RH}} \tag{3.35}$$

where t_L is the required local threshold for a given resolution scale s. All the relative pixel information are obtained from the 3D wavelet histogram itself and b can be any user entered value anywhere from within the histogram. The pixel information within each bin act like weights when computing the final threshold value.

The local threshold value t_L is computed from wavelet histograms generated for each scale and thus adapts to the data provided by wavelet coefficients at each scale s. Corresponding histograms are used to separate the foreground edge details using t_L value, which are further used to determine optimum coefficients by implementing multiscale edge detection. Local edge detection by the proposed method can thus be summarized in algorithm 1.

3.3.2 Multiscale edge detection

In wavelet domain the edge or singularity can be represented as mathematical piecewise linear function characterized by its Lipschitz exponent α which evolves across different resolution level for multiresolution analysis. According to Mallat et al. if a 1D function $f(x)$ is Lipschitz α at x_0 with a constant A and some $\epsilon > 0$ for all x in the neighbourhood of x_0 at any scale s; the decay of singularity can be determined by tracing its wavelet transform modulus using the following equation (Mallat and Hwang, 1992; Mallat and Zhong, 1992).

$$|W * f(u, s)| \leq As^{\alpha+1} \tag{3.36}$$

where $W * f(u, s) = w_j$ is the wavelet function given by Eq. (3.8), $f(u, s)$ is the corresponding 1D image function in wavelet domain for different scales s where $s = 2^j$, u is coordinate position for x in wavelet domain and $|Wf(u, s)|$ is the wavelet transform modulus maxima (WTMM) of wavelet coefficients (Mallat and Zhong, 1992). Lipschitz exponent α for a signal is usually positive and its corresponding WTMM may increase or remain the same with change in scale s (Lun et al., 2002). In this study the Lipschitz exponent for step edge signal is taken as $\alpha = 0$ (Lun et al., 2002). Whereas singularity attributed due to noise has negative Lipschitz exponent and is expected to decay across wavelet scales by a factor of $1/2^j$ (Mallat and Zhong, 1992; Lun et al., 2002). This behaviour of singularity in wavelet domain can be used to retain coefficients which correspond to image details while letting go of non-significant details and noisy details.

3.3.2.1 Wavelet interscale ratio

Let the candidate wavelet coefficients representing edge details in wavelet domain obtained by localized thresholding be given as $W * f(u, s)$ which is also known as w_j as shown in Eq. (3.8). A better detection of the cartilage edge may then be attained by investigating the decomposition of the cartilage singularity across multiple scales in wavelet domain. But such a process of tracking coefficients of wavelet transform modulus maxima (WTMM) across wavelet scales can be prone to error (Lun et al., 2002). Also the inverse reconstruction process for WTMM is a very complex procedure which requires projections onto convex sets with no particular unique solution to reconstruct the final processed signal (Mallat and Zhong, 1992; Lun et al., 2002).

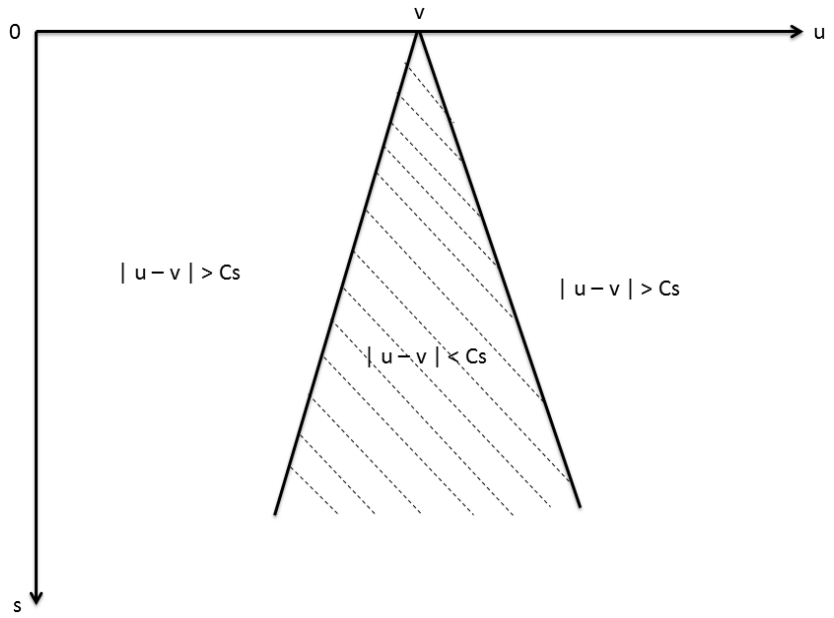

FIGURE 3.7: Cone of influence for wavelet function within wavelet support (Mallat and Hwang, 1992)

To avoid such a complex reconstruction process, D. Lun et al. proposed a more simplistic approach of following wavelet transform modulus sum (WTMS) $N_s f(x)$ for singularity at increasing scales within the cone of influence (COI). COI is a conical scale-space plane (u, s) in wavelet domain which represents set of coefficients belonging to singularity and true x_0 is included in the wavelet function response (Mallat and Hwang, 1992). The wavelet transform modulus sum under COI for point x_0 for 1D function $f(x)$ can then be given as (Mallat and Hwang, 1992; Lun et al., 2002),

$$N_s f(x_0) = \int_{|x-x_0| \leq Ks} |W_s f(x)| dx \leq \acute{A} s^{\alpha+1} \tag{3.37}$$

$$N_s f(x_0) \leq 2A(K + \frac{K^{\alpha+1}}{\alpha+1})s^{\alpha+1} \tag{3.38}$$

where $[-K : K]$ is the support for the mother wavelet, N_s represents the wavelet transform modulus sum and $\acute{A}$ is a constant. As shown in Fig. (3.7), COI of variable u for wavelet transform modulus sum follows a conical trajectory governed by support function of the mother wavelet. Coefficients of the relevant singularity can be safely assumed to lie within this COI region though knowledge of Lipschitz exponent α of true singularity offers a more robust solution for singularity detection (Mallat and Hwang, 1992).

In order to retain coefficients corresponding to this COI we follow an inter-scale ratio W_r given by WTMS for a given Lipschitz exponent α for step edge (Lun et al., 2002). The inter-scale ratio W_r for wavelet coefficients of any two subsequent scales for its Lipschitz exponent is given as (Lun et al., 2002),

$$W_r = \frac{N_{s+1} f(x_0)}{N_s f(x_0)} = 2^{\alpha+1} \tag{3.39}$$

And the Lipschitz exponent α for step edge singularity is equal to zero (Lun et al., 2002). Following singularity within COI for wavelet coefficients we can optimize the edge detection process. Once candidate coefficients within the COI have been selected, we can perform a global thresholding $\grave{\gamma}$ to retain coefficients belonging to a particular singularity and these final coefficients will be used for inverse wavelet reconstruction.

3.3.2.2 Rician inter-scale difference

In this study a global edge detection criteria is required to consolidate all the necessary computed wavelet coefficients for the edge detection process. This criteria is used to optimize the coefficients used for the wavelet reconstruction and edge detection process and is given as a global threshold value for wavelet multiple scales. This global threshold $\grave{\gamma}$ is obtained by computing the inter-scale difference of wavelet coefficients at any two consecutive scales $s, s+1$ and accounts for bias introduced due to the inter-scale ratio (Lun et al., 2002). In our proposed method since we assume that the wavelet coefficients have a Rice distribution function $P(M)$ attributed to noise present in the original image and probability distribution of wavelet coefficients is governed by observed signal function; the inter-scale difference using WTMS modelled for image affected by Rician noise is given as follows,

$$\grave{\gamma} = N_{s+1}f(x_0) - N_s f(x_0) \tag{3.40}$$

where $\grave{\gamma}$ is also the proposed global threshold for edge detection system as per lemma 1 and is a function of image variance and not just wavelet coefficients alone. The proof for $\grave{\gamma}$ stated in the following lemma is given in appendix C.

Lemma 1. Wavelet inter-scale difference for image subjected to single coil Rician noise is a function of image variance. $w_{j+1} - w_j = \gamma * Var(I)$

where $\grave{\gamma}$ is the proposed global threshold for edge detection system and is a function of variance σ^2 and wavelet coefficients C_ψ. The value of σ^2 can be obtained by computing variance of noise in the image itself. Only locally thresholded wavelet coefficients which satisfy both the inter-scale ratio W_r criteria and the global threshold $\grave{\gamma}$ for increasing multiresolution levels j were preserved while the rest are discarded (Lun et al., 2002). Algorithm 2 describes the second stage of the edge detection process.

Algorithm 2: Global Multiscale Edge Detection

Input: Local thresholded wavelet coefficients W_s

1 **for** wavelet scale j=1:J **do**,

2 Wavelet magnitude sum for selected coefficients,

$N_s = |W_s f(x)|$

3 Compute inter-scale ratio W_r for any two consecutive scales

$W_r = \frac{N_{s+1}}{N_s}$

4 Compute inter-scale difference using Rician distribution for any two consecutive scales,

$\grave{\gamma} = N_{s+1}$ - $N_s = \sigma^2$

5 Optimizing wavelet coefficient with proposed global threshold.

Retains coefficients which satisfy both conditions W_r and $\grave{\gamma}$.

6 Computing inverse un-decimated wavelet transform.

7 **end for**

Output: Processed Image volume $\hat{I_{vol}}$

To summarize the proposed edge detection process, an initial set of candidate coefficients representing the image details are obtained by using an adaptive local threshold t_L. This local threshold t_L is estimated by computing the intensity distribution level for the bimodal wavelet histogram. The upper and lower intensity limits of the bimodal distribution are used to estimate an optimal threshold value for thresholding of wavelet coefficients at a local resolution level j as given by Eq. (3.35). In addition we know that edge information in wavelet domain will have a global curve across multiple resolution levels in the wavelet domain. This knowledge is used to optimize the selection of wavelet

coefficients across wavelet scales and used to identify and select edge details at various resolution levels. This is achieved by implementing a global threshold $\grave{\gamma}$ estimated using inter-scale ratio W_r and difference using wavelet transform modulus sum N_s. The final computed wavelet coefficients are used for the inverse wavelet reconstruction process. The final processed volume can be used for various image analysis and enhancement studies.

3.4 Performance Evaluation and Discussion

3.4.1 Materials

For this study we have used MRI and phantom datasets of articular cartilage of the knee. 14 MRI datasets obtained from Menzies Institute of Research,Tasmania, Australia have been used. All datasets contain T2 weighted MR images with 512 x 512 x 62 pixels, slice thickness of 1.5 mm and are acquired with 1.5 T MRI machine. Dataset 14 has flip angle of 50 and fat-saturated image sequence while remaining datasets have flip angle of 30. In addition we use three phantom datasets of the articular cartilage representing ideal, noisy and denoised cartilage for a comparative analysis. The phantom cartilage is artificially created using MATLAB R2013b as a binary map of a healthy cartilage tissue (MathWorks, 2013). All the phantom datasets contain 512 x 512 x 25 pixels with slice thickness of 1.0 mm. The denoised datasets are obtained by implementing Rician denoising for the images as given by (Aarya et al., 2014). The denoising algorithm has been written in Matlab R2013b. The algorithm for the proposed automated edge detection method is written in C++ using Visual Studio 2010. Image analysis and volume rendering of the 3D cartilage model is performed using VTK 5.8.0 implemented in visual studio 2010 (Schroeder et al., 2004).

3.4.2 Experimental results

For the simulation study, a 3D volume $f(x, y, z) \in R^3$ is obtained by stacking 2D image slices $M(x, y)$ successively, to obtain a volumetric cube for the wavelet analysis. To obtain a denoised volume the 2D image data slices undergo Rician denoising. 3D undecimated wavelet transform with Haar filter banks has been implemented for wavelet analysis. Haar scaling and wavelet function is shown in Fig. (3.8) a and b respectively. The 1D separable wavelet function in the form of filter banks is convolved along all three axis of the volume to obtain 3D wavelet decomposition (Muraki, 1995). For multiscale decomposition of MRI volume and phantom datasets, forward wavelet transform at two resolution levels are performed. The histogram of wavelet coefficients is modelled as

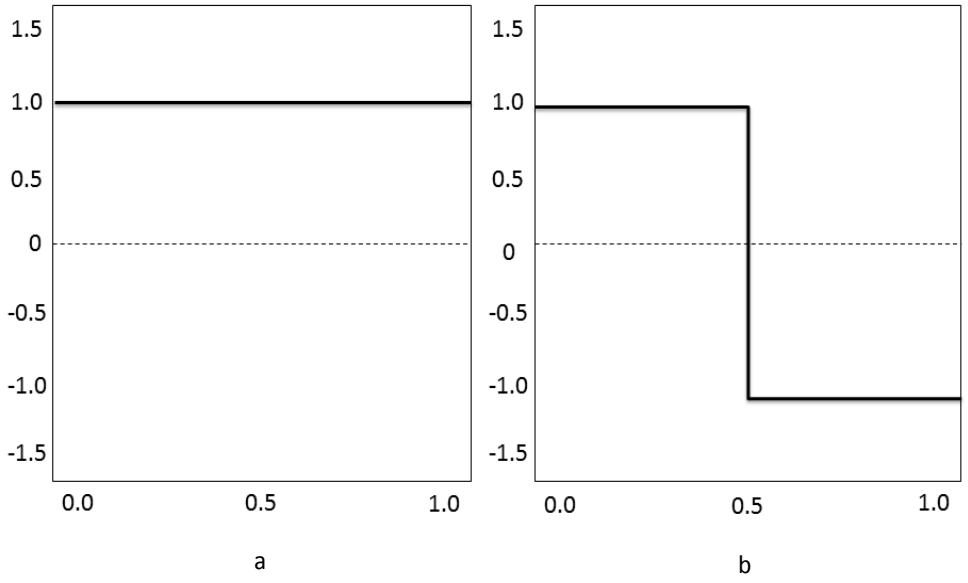

FIGURE 3.8: a) Haar scaling function and b) Haar wavelet function (Gonzalez et al., 2004)

bimodal Rice distribution function. Intensity interval estimation for foreground and background coefficients C_ψ at 99% confidence level α_1 is obtained. Cartilage details present in the foreground are selected using an adaptive local threshold t_L for each scale j in wavelet domain. This local threshold is estimated using linear interpolation for confidence limits of the bimodal distribution. The selected wavelet coefficients at each local scale are subsequently used for multiscale analysis across different wavelet resolutions to obtain global cartilage information for the volume. Global threshold $\grave{\gamma}$ is used to optimize and regulate singularity coefficients across different resolutions using Eq. (3.40) (Lun et al., 2002). The final coefficients obtained from local t_L and global thresholding $\grave{\gamma}$ together represent the cartilage edge information for a given volume. These final selected coefficients are used to obtain inverse wavelet transform as given by Fig. (3.5). The process is repeated for the phantom datasets, which are also used for the quantitative assessment of the proposed method. The efficiency of the proposed method is determined by comparing the signal to noise ratio (SNR), mean square error (MSE) for true and reconstructed volume for different confidence levels and noise.

Fig. (3.9) demonstrates the result of proposed method on phantom cartilage dataset. Fig. (3.9) a and b show original true phantom model and its edge map without any thresholding respectively. Since the original model does not contain any noise or poor contrast we do not use it for thresholding and is shown in Fig. (3.9) c. Fig. (3.9) d, e and f display a noisy phantom model, its edge map with no thresholding and the edge

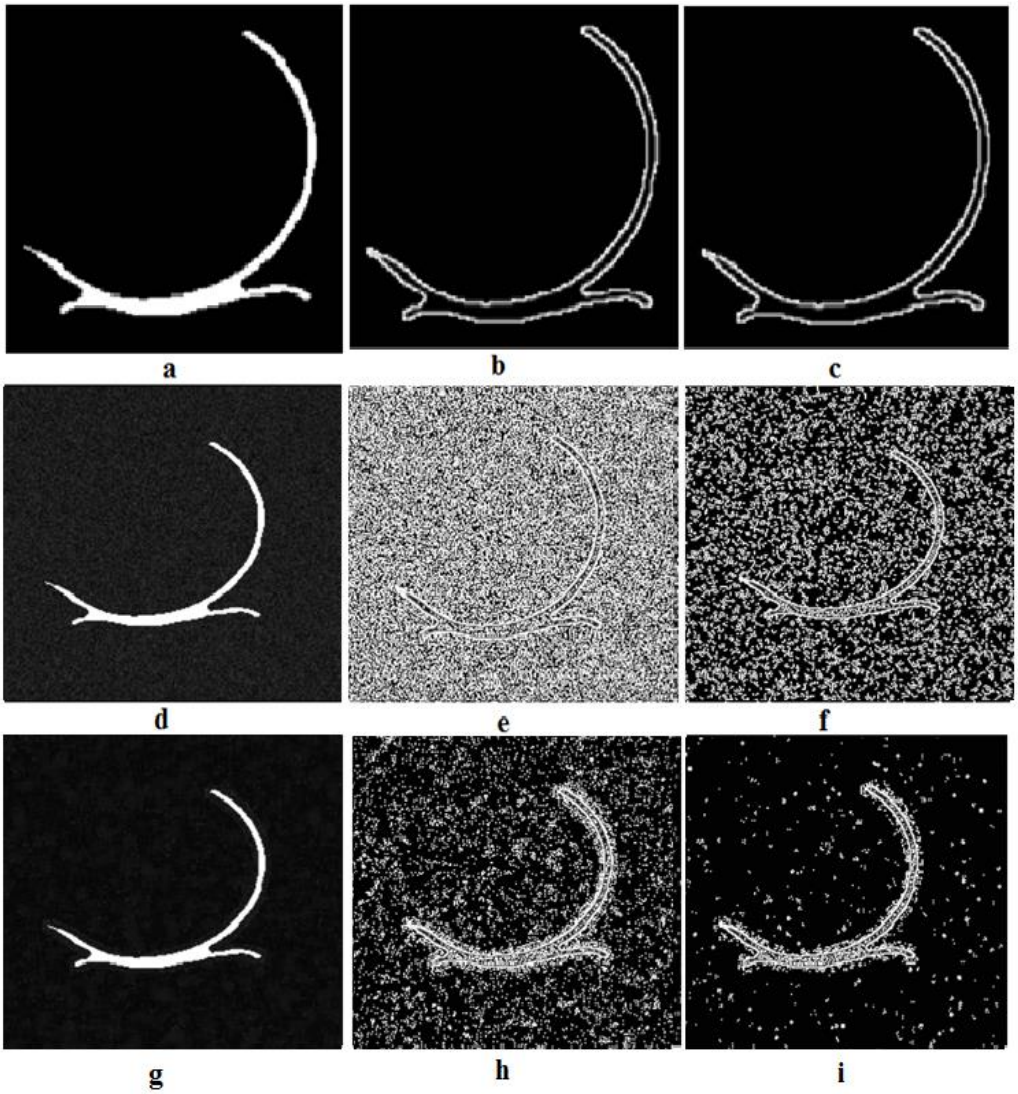

FIGURE 3.9: a. Original phantom cartilage, b. edge model of original phantom cartilage c. edge model of phantom cartilage with proposed method d. original noisy phantom cartilage, e. edge model of noisy phantom cartilage, f. edge model of noisy phantom cartilage with proposed method, g original Rician denoised phantom, h. edge model of denoised phantom cartilage and i edge model of denoised phantom cartilage with proposed method.

model after thresholding with the proposed method respectively. While Fig. (3.9) g, h and i display result for denoised phantom, its edge model without any thresholding and edge model after implementing the proposed method respectively. The noisy phantom for Fig. (3.9) d has been obtained by using the true phantom and subjecting it to Rician noise with standard deviation of 7 while the denoised phantom model shown in Fig. (3.9) g has been obtained by using Rician denoising on the noisy model. Result of the proposed method on MRI dataset is shown in Fig. (3.10). Where Fig. (3.10) display the original MRI volume, its edge profile with no thresholding and thresholding with proposed method respectively. From Fig. (3.9) and Fig. (3.10) one can clearly observe

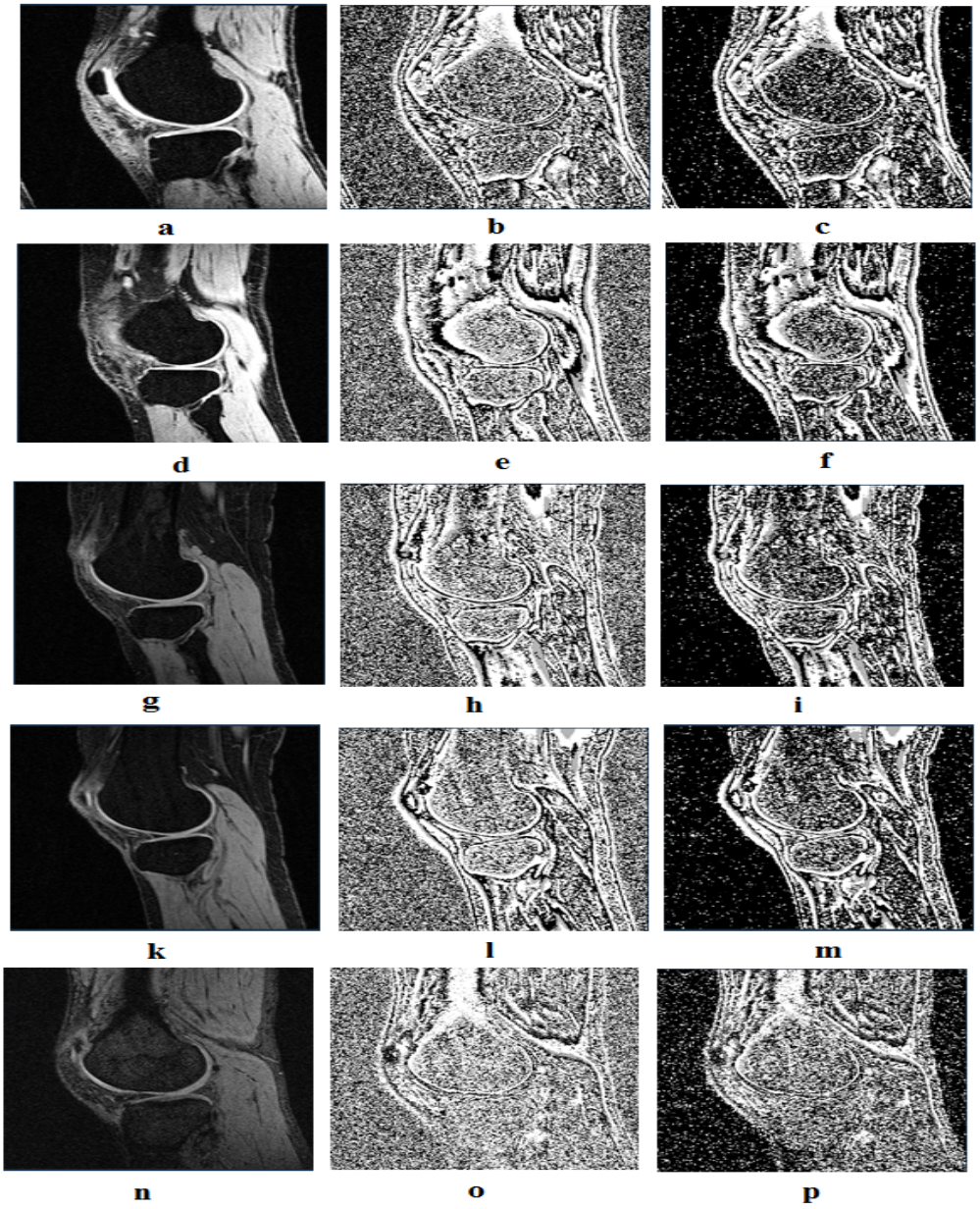

FIGURE 3.10: a. Original cartilage image dataset D1, b. edge model of cartilage dataset D1 c. edge model of cartilage dataset D1 with proposed method, d. original cartilage image dataset D5, e. edge model of cartilage dataset D5 f. edge model of cartilage dataset D5 with proposed method, g. original cartilage image dataset D7, h. edge model of cartilage dataset D7 i. edge model of cartilage dataset D7 with proposed method, k. original cartilage image dataset D9, l. edge model of cartilage dataset D9 m. edge model of cartilage dataset D9 with proposed method, n. original cartilage image dataset D14, o. edge model of cartilage dataset D14 p. edge model of cartilage dataset D14 with proposed method

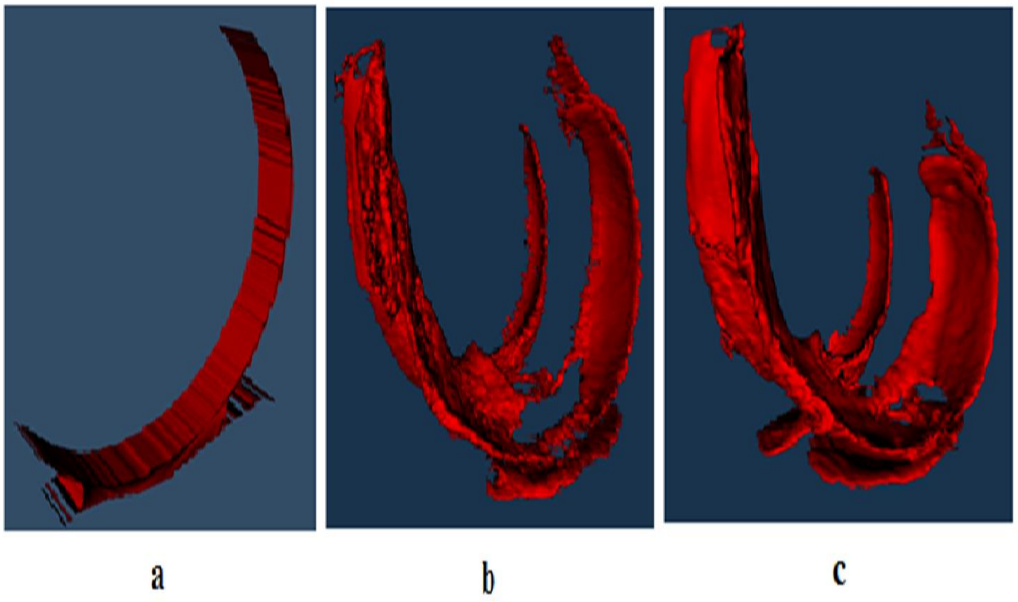

FIGURE 3.11: a. 3D volume rendered phantom cartilage model, b. 3D volume rendered cartilage model for dataset D1 and c. 3D volume rendered cartilage model for dataset D14

reduction of insignificant image details with proposed method. The local threshold t_L values used for the two resolution levels for phantom datasets is given in Tab. 3.1.

Tab. 3.1 also shows results for MSE and SNR for noisy and denoised phantom datasets with proposed method for 99% confidence level α_1. For the quantitative analysis we have selected datasets with standard deviation of noise 3, 5 and 7 and their corresponding denoised image datasets. Values for MSE and SNR for all the datasets are derived with respect to corresponding true phantom. Since the phantom dataset with standard deviation of noise 3, has only two grey scale values, with least amount of noise and relatively less structural content it shows high SNR as compared to other datasets. Volume of the 3D cartilage model obtained with volume rendering process and their corresponding local thresholds for two resolutions for phantom and MRI datasets is given in Tab. 3.1 and Tab. 3.2 respectively. The processed datasets were subsequently used in the volume rendering process for computer visualization of the articular cartilage using VTK 5.8.0. For the volume rendering process the cartilage tissues are extracted and rendered using a contour filter. The generated contour data is converted into a polydata mesh for computer visualization of 3D cartilage. These models provide an interactive way to perform cartilage diagnosis and study. The cartilage models for the true phantom dataset, D14, and D1 are shown in Fig. (3.11) a, b and c respectively.

TABLE 3.1: Image Quality Assessment for Phantom Datasets for confidence level of 99%

Parameter	MSE	SNR	Volume	threshold 1	threshold 2
Noisy std. 3	14.0197	26.5876	36761.8	6.34196	6.63736
Denoised std. 3	2.35529	158.262	37832	6.01353	5.504209
Noisy std. 5	37.3698	9.97467	36711.6	9.13147	9.21692
Denoised std. 5	6.29565	59.2078	37227.1	5.07128	5.59269
Noisy std. 7	69.9989	5.32511	17986	11.8297	11.7615
Denoised std. 7	12.251	30.4262	19149	5.61258	5.95942

3.4.3 Discussion-Cartilage detection

In Fig. (3.9) h the edge profile of the phantom cartilage model which has been denoised for Rician noise still contains effect of noise, which may influence the cartilage extraction process as also previously assumed. Also in Fig. (3.9) f and i both fine and coarse edge details are preserved despite the noise and poor contrast. Thus it can be seen that the thresholds estimated using MLE and inter-scale resolution avoids excessive loss of the image data. From Fig. (3.9) i. It is also worth noting that the new model generated after thresholding with proposed method is sufficiently closer to the true model, which deems our assumption for modelling the wavelet histogram as the noise distribution function to be reasonable enough. Fig. (3.9) and Fig. (3.10) both display improvement in the image data by letting go of insignificant image details contributed either due to noise or artefacts without over thresholding of the data.

Since true noise free data is rare, we make use of a phantom cartilage dataset for emulating structural and noise free behaviour of an ideal cartilage tissue. It is also used as a baseline for the performance evaluation and quantitative assessment of the proposed method. Tab. 3.1 shows this quantitative assessment for datasets with and without noise removal respectively. Confidence limits of the histogram are used to compute the threshold value to separate edge details. The pixel values used for linear interpolation of threshold are obtained from the respective intensity bins of the computed confidence limit. For the user entered pixel information b, given by Eq. (3.35) we enter value zero as it is an unknown pixel information value and also because for highest intensity bin i.e 255 the pixel content is zero.

This enables us to obtain a closest possible threshold value to that of an ideal for thresholding, which in case of binary image would be an intensity value closer or equal to 255. By increasing or decreasing confidence levels α_1 we can control the confidence interval CI for the distribution and hence the local threshold t_L. Selecting higher confidence levels α_1 leads to better accuracy for threshold estimation as selection of coefficients are done with higher probability and covers larger area under the distribution. Lower confidence levels α_1 will result in lower ratio of coefficients used for computing the confidence limit and hence the threshold t_L. Also we observe a relatively larger confidence interval for higher confidence levels like that of 99% and relatively smaller confidence interval for lower confidence levels such as that for 90% percent. In this study we used 99% confidence level α_1 for both real MRI and phantom datasets. If the choice of confidence level α_1 is incorrect you may experience an overlap in the confidence limits for lower Gaussian and higher Rayleigh. Note in this case one can still obtain a threshold value t_L within a reasonable level but which may be less precise. In extreme cases it may so happen that a given sample size of the image may be too small or noisy which can lead to incorrect estimation of the confidence interval, limit or the local threshold itself. In such a scenario where sample is small and corrupted causing incorrect estimation, a reliable threshold value will be difficult and as such it would be more appropriate for the user to perform hard thresholding for separation of coefficient details. In this study as we use large phantom and MRI datasets and due to our selection of un-decimated wavelet transform which does not down-sample our dataset for analysis. Our sample data remains large enough to perform analysis.

In the real world images histogram may have a multimodal distribution with different noise. The user should then consider the image data and noise affecting it and accordingly model the histogram for their application. The proposed cartilage detection and modelling system offers an improvement for cartilage analysis. It can be made completely automated and can also be tailored to address different types of noise affecting the images.

The proposed method offers an automated and optimized detection of articular cartilage using undecimated wavelets. It is able to address signal dependent Rician noise which affects single coil MRI as can be seen from reduction in MSE for both noisy and denoised phantom and MR images. The localized threshold helps to reduce the effect of noise while the global threshold helps in optimizing the wavelet coefficients representing edge details and thus improve the overall SNR of the image volume for different standard deviation of noise as demonstrated in Tab. 3.1. As the proposed method follows cartilage detection globally across multiple wavelet scales and retains edge details only when

they satisfy global criteria; it is said to optimize coefficients across the wavelet domain. Also the proposed method isolates wavelet coefficients representing desired edge details without any significant loss of image data as observed by the volume information. The localized threshold computed for two wavelet resolutions shown in Tab. 3.1 and Tab. 3.2 are similar in nature and support the multiresolution theory which states that lower resolution subspace V_j contains information at higher subspace V_{j+1}. Information from local and multiple wavelet resolutions is used to obtain an automated cartilage detection method without the need of any priori information or atlas. Also it does not require any multiple image datasets or feature learning. As the proposed method uses 3D directional edge information of the cartilage provided by wavelet transform to perform edge detection as against usual 2D edge information, it is able to overcome the under-sampling of image data along the third axis of 3D volume.

TABLE 3.2: Volume Assessment for MRI Datasets for confidence level of 99%

Parameter	**Volume**	**threshold 1**	**threshold 2**	**noise variance**
D1	459940	11.3122	12.5839	10.3580
D2	239858	11.3151	13.5058	11.1703
D3	475158	12.5196	13.6275	11.4068
D4	264243	12.5149	13.59	11.26206
D5	285925	11.3075	12.5385	11.1055
D6	233731	11.3379	13.5578	10.9561
D7	361973	11.3002	12.5173	11.06759
D8	113614	11.293	12.5835	11.1422
D9	291994	11.2899	12.4963	11.1389
D10	33993	11.2706	12.6888	11.0789
D11	419010	11.3299	13.5295	11.2768
D12	406547	11.32223	12.5751	11.16027
D13	214820	11.3249	12.5761	11.12155
D14	597730	16.4464	16.7219	50.1589

3.5 Proposed Edge Localization

While edge detection plays a vital role in medical image processing as it provides important structural details of an object in the image. This process may become challenging

due to the presence of noise in the image. Current edge detection methods are designed for signals with linear additive Gaussian noise and rely on noise removal prior to the edge detection process (Canny, 1986; Ranjbaran et al., 2014). Recent focus has moved towards non-linear filter design for edge detection for signal dependent noise (Oussous et al., 2014; Lopez-Molina et al., 2014). Though these methods offer a good edge detection they seldom take into account the influence of signal dependent noise on edge localization. Real world images, such as those used in MRI may be subjected to non-linear noise. And while there exist several Rician denoising methods, it is not possible to remove noise completely from the image (Rajan et al., 2012; Aarya et al., 2014). Presence of this signal dependent noise can not only affect the edge detection process but also localization of an edge by the filter. Fig. (3.12) shows 1D ideal step edge detection and the influence of additive Gaussian noise and signal dependent Rician noise on the signal. The signal with Rician noise not only demonstrates fluctuation in amplitude of the edge due to presence of noise but also variation in location of zero crossing. In this study we investigate the influence of signal dependent Rician noise and its role in edge localization.

A new edge localization technique for step edges in images with signal dependent Rician noise in MRI is then proposed. Dependent noise can not only affect the detection of true edges in an image but also their position. Inaccurate localization of an edge can lead to insufficient segmentation and reduce the overall accuracy of any edge detection method. The proposed technique uses higher order moments of the noise function to determine the correction factor for localization and thus reduce overall mean square error (MSE) for true edge localization due to noise. The proposed technique offers significant improvement in edge localization for an image as compared to Canny and Sobel methods.

3.5.1 Edge detection process

For this study, edge detection and localization for images with signal dependent noise is structured using an approach inspired by the Canny edge detector. Canny in his investigation proposed three main criteria for ideal edge detection which include 1) effective edge detection, 2) correct localization of the edges and 3) finally inhibition of multiple response for true edges by the detector (Canny, 1986). In order to achieve effective edge detection the filter should generate maxima at true edge positions while good localization is obtained by reducing error between detected and true edge positions thus improving the overall signal to noise ratio. For a step edge detection in 1D magnitude images, let $f(x)$ be a FIR filter with support [-W, W]. The expected step edge response by the FIR for an edge centred at $x = 0$ can thus be given as,

$$E[y_s(x)] = \sum_{t=-W}^{t=+W} A^2(x-t) * f(t) \tag{3.41}$$

where $E[y_s(x)]$ is the expected edge response by filter to a step edge with amplitude equal to $A^2(x)$. Convolution of impulse response filter $f(x)$ for a step edge with the square of the magnitude image function $M^2(x)$ gives us Eq. (3.41) whose response should generate output only in the presence of a local maxima for step edge. The remaining terms of the quadratic equation may contribute to noise and the response of the FIR filter to noise can then be given as,

$$E[y_n(x)] = \sum_{t=-W}^{+W} f(t) * [2A(x-t)n_r(x-t) + N^2(x-t)] \tag{3.42}$$

where $E[y_n(x)]$ is the expected filter response to noise. The signal dependent term $An_r(x)$ in the above expression is governed by noise and may not generate local maxima close to the true edge and hence for higher values of $A(x)$ the response other than local maxima is not considered for step edge detection. If the image is denoised prior to edge detection one can minimize the effect of the $N^2(x)$ term in Eq. (3.42) for the magnitude image equation, given as $M^2(x) = A^2(x) + 2A(x)n_r(x) + N^2(x)$. In a 2D image the edge also has an orientation and is considered normal to the detected edge along x. Thus the detected edge for a 2D signal will have a local maxima given as the magnitude along x and y position, obtained by convolution of a FIR filter along the two directions. Canny demonstrated that the first order Gaussian derivative can be used for step edge detection within an acceptable error rate. For this study too the first order Gaussian derivative is used as the FIR filter for step edge detection for Eq. (3.41). Use of higher order derivative filters would make the filter more susceptible to the noise function and is hence not implemented for step edge detection in this study. The edge detection process should improve the overall signal to noise ratio (SNR) of the image given as $SNR = E[y_s(x,y)]/E[y_n(x,y)]$, which is obtained by improving the signal response to true edges by the FIR filter and minimizing the influence of noise by prior denoising of the image before the edge detection process.

3.5.2 Edge Localization Correction

For a good localization the filter should position the detected edge as close as possible to the true edge centre at $x = 0$ (Canny, 1986). Error in localization may occur due to presence of noise in the image and can be improved by minimizing error between the detected edge and true edge due to noise (Canny, 1986). Proposed edge localization

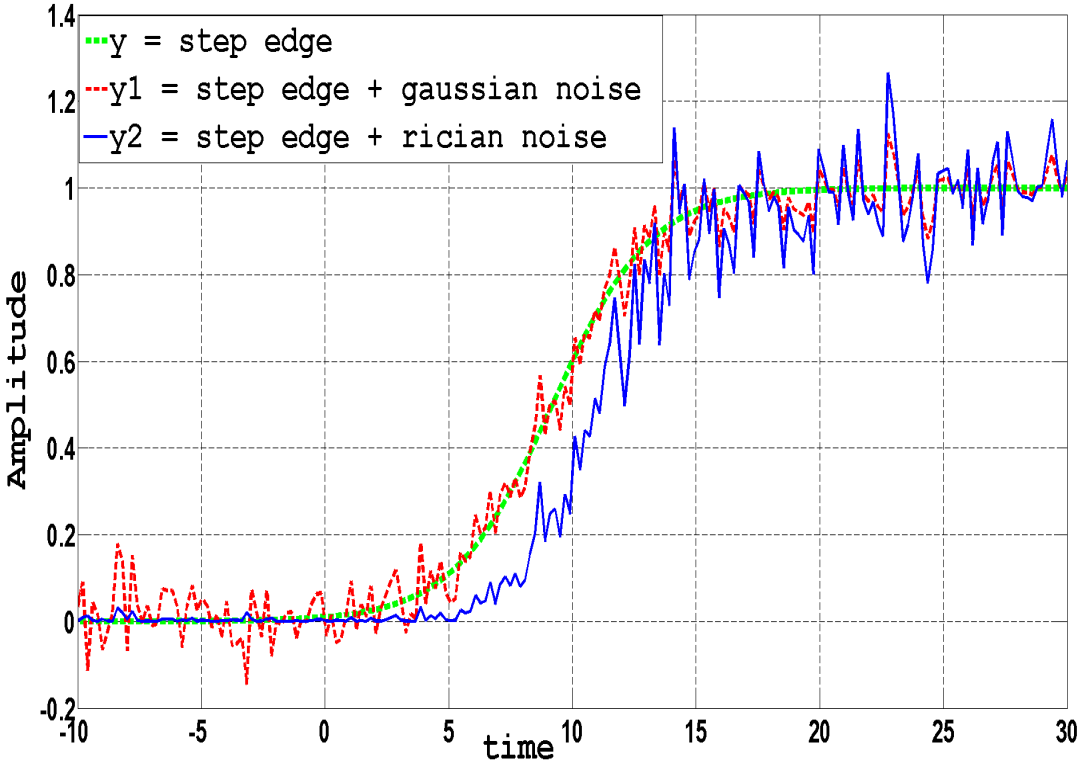

FIGURE 3.12: 1D step edge signal shown in green plot, step edge with additive Gaussian noise indicated by red plot and step edge with Rician noise given by blue plot

attempts to minimize this mean square error (MSE) between detected and true edges due to signal dependent noise. Let the detected edge from a 2D image containing x and y co-ordinate positions be stored as a vector array containing edge l, and $l_{edge} = [l, M^2(x,y)^T]$. For simplicity the edge is investigated for x-component at a fixed y position where edge l is an inflection point across x (Canny, 1986). Let δ be the mean square error (MSE) between detected edge and true edge for filter $f(x)$,

$$\delta = E[(\hat{l} - l)^2] = Var(\hat{l}) \tag{3.43}$$

where $\hat{l}$ is the position of edge detected by filter response to the observed signal $M^2(x)$, l is true edge position by filtering in response to $A^2(x)$. But as noise is dependent on the signal function there exists bias between true and observed signals and including this correction for bias to the δ function gives (Prasad and Rao, 1990),

$$\begin{aligned} \delta &= E[(\hat{l} - l)^2] + (bias(\hat{l}, l))^2 \\ &= E[(\hat{l} - l)^2] + (E[\hat{l}] - l)^2, \end{aligned} \tag{3.44}$$

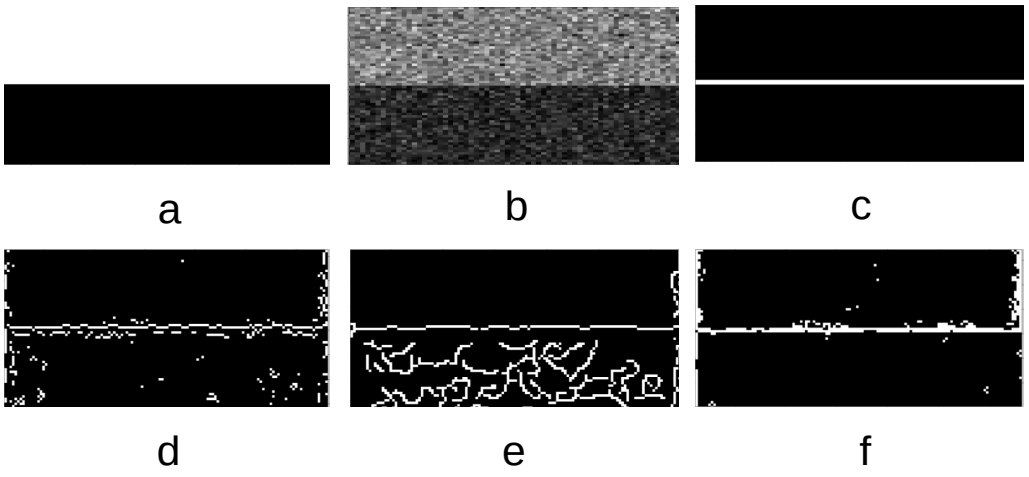

FIGURE 3.13: a) True image for step edge, b) image with Rician noise, c) true edge detection d) edge detection by Sobel filter e) by Canny filter f) by proposed filter

where $E(\hat{l})$ is the expectation of the detected edge obtained by convolution of the FIR filter with the observed magnitude signal function, given as $E[\hat{l}] = E[M^2(x) * f(x)]$. Ideal true edge position then can be given as $l = A^2(x) * f(x)$ where $M^2(x)$ is only a function of $A^2(x)$ in absence of noise. The bias between expected edge position and true position can be obtained from the second order moment of the Rice distribution function where $E[M^2(x,y)] - A^2(x,y) = 2\sigma^2$. Thus mean square error δ is given as,

$$\delta = Var(\hat{l}) + (2\sigma^2)^2 \tag{3.45}$$

where σ^2 is variance of Rician noise obtained from the MR image and $Var(\hat{l})$ can be determined from its covariance matrix as knowledge about true l is seldom known. Hence proposed localization correction for the magnitude image is given as reciprocal of square root of MSE δ

$$localization = 1/\sqrt{\delta} \tag{3.46}$$

The final edge output $E_o[x,y]$ can be obtained as the product of edge response and localization in order to improve overall SNR by filter for true edge detection and to obtain an edge response invariant to spatial scaling (Canny, 1986). The final edge output is thus given as,

$$E_o[x,y] = E[y_s(x,y)] \times \frac{1}{\sqrt{\delta}} \tag{3.47}$$

3.5.3 Simulation results

In order to evaluate the performance of the proposed method we take synthetic image tire.tiff obtained from MATLAB R2013b image processing toolbox. To this image we added Rician noise with standard deviation 20 using Eq.(2.1). Edge detection was performed by convolving a 3 x 3 Sobel edge detector for step edge detection for both horizontal and vertical directions along x and y. Edge response was computed as the magnitude of detected edges along horizontal and vertical directions. Localization factor was used to correct the final edge output by the proposed method using Eq. (3.46) and the final edge output was determined using Eq. (3.47). In addition hysteresis thresholding was performed to remove any non-edge details. The process was also repeated for the denoised image obtained by Rician noise removal using LMMSE method given by S. Aja-Fernandez et.al. for the same noise level (Aja-Fernandez et al., 2008). Pratt's figure of merit (FOM), correlation coefficient (CoC) for edge and mean square error (MSE) were used to monitor the performance of the proposed method. Tab. 3.3 displays the performance parameters for both the noisy and denoised tire images at standard deviation 20 by proposed method as compared to Sobel and Canny edge detectors. In order to demonstrate fluctuation in edge localization we use a 2D phantom image for step edge built in MATLAB with standard deviation of noise 70. This image was Rician denoised prior to edge detection by Sobel, Canny and the proposed method and the resulting output is demonstrated in Fig. (3.13). The proposed method demonstrates better edge location as compared to the output of the other filters. Fig. (3.14) shows the output of the proposed method for true, noisy and denoised tire.tiff images. The study was also repeated for different standard deviations of Rician noise and the performance output is given by Fig. (3.15). In a second simulation study the proposed method was implemented on T2 weighted MR images of articular cartilage of knee. As the real world images already contain noise they were subjected to noise removal prior to the edge detection process. Fig. (3.15) g and Fig. (3.15) h displays the output of the proposed method for the MR images.

From Tab. 3.3 we can observe that the proposed method offers improvement in image parameters for the denoised image, given as I1 as compared to noisy image given as I2. FOM was used to observe the effectiveness of detection of edges while CoC was used to monitor localization of output edges by filters with respect to true edges by the algorithm. The proposed method shows improved performance for Rician denoised images for different noise level as compared to Sobel and Canny edge detectors. Also the proposed method is simple to implement and can be used with existing first order filters for edge detection.

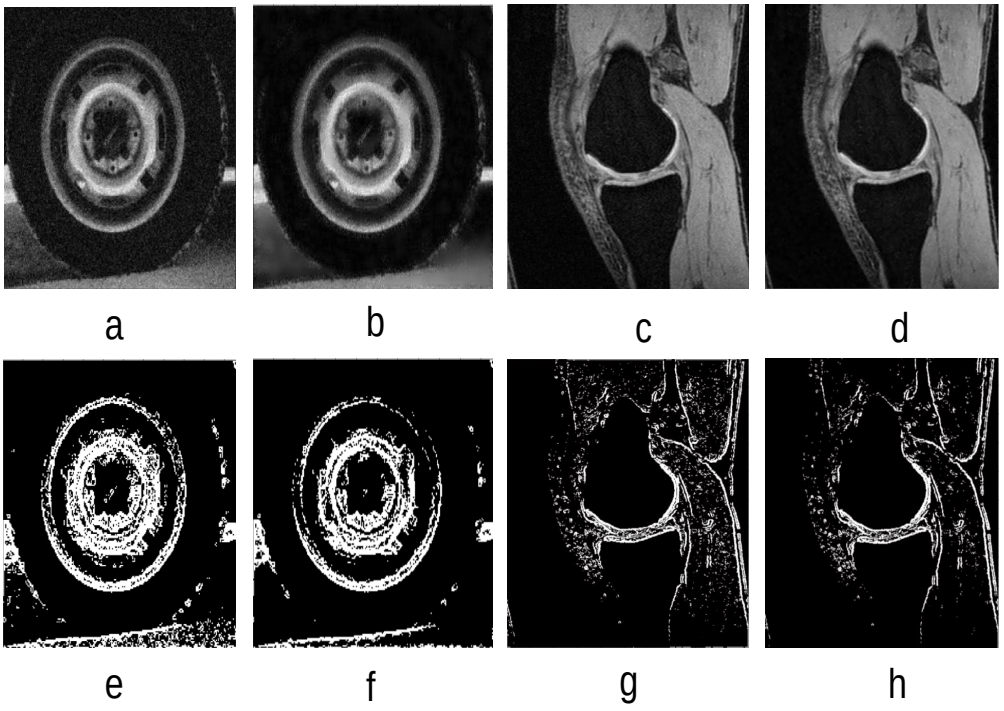

FIGURE 3.14: a) Tire.tiff with Rician noise of standard deviation 20, b) Denoised tire.tiff image, c) Noisy MR image d) Rician denoised MR image e) Edge output with proposed method for noisy tire image, f) Edge output with proposed method for denoised tire image, g) edge output with proposed method for noisy MR image and h) edge output with proposed method for denoised tire image

TABLE 3.3: Image Quality Assessment

Methods	**FOM**		**CoC**		**MSE**	
	I1	**I2**	**I1**	**I2**	**I1**	**I2**
Proposed	0.8387	0.74029	0.6511	0.6012	0.1352	0.171
Sobel	0.3626	0.3587	0.3299	0.321	0.2228	0.2246
Canny	0.5357	0.5686	0.4075	0.3546	0.2008	0.2155

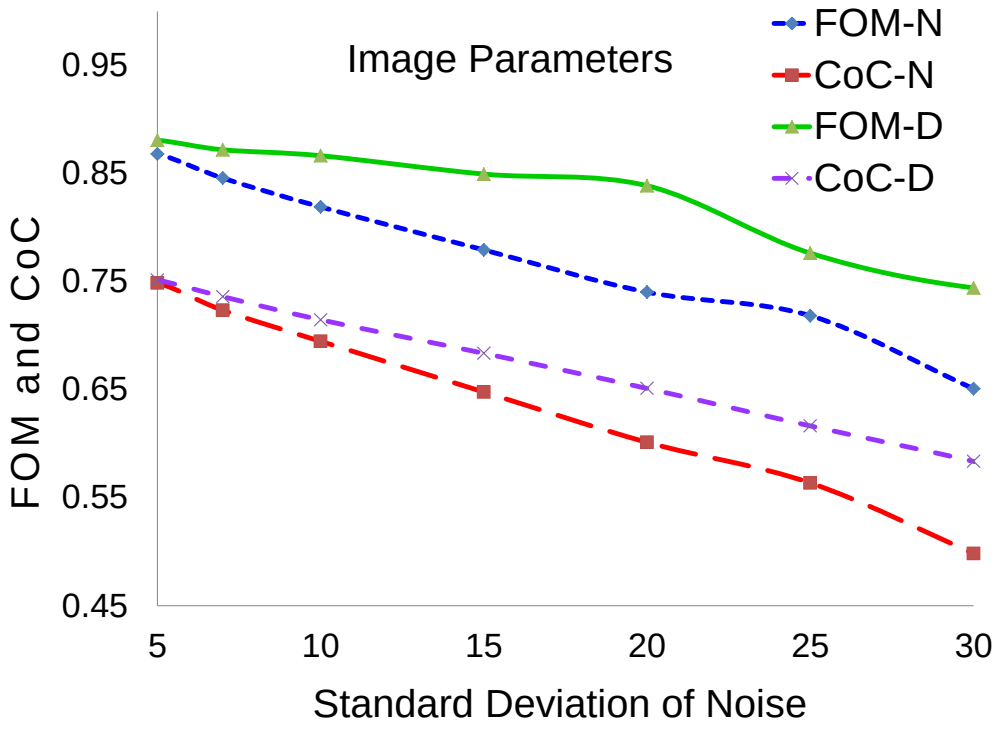

FIGURE 3.15: Image parameters for noisy and denoised images for tire.tiff for different standard deviation of noise; N indicates image with noise and D indicates denoised image

3.5.4 Discussion-edge localization

In this study we have proposed a new edge localization factor for step edges in a MRI image with signal dependent Rician noise. Based on the Rician distribution characteristic the study has identified the effect of noise on step edges and its true position. Using Canny's guidelines for an ideal edge detection process, the proposed study conducts investigation on ability of first order filters to detect edge in an image and its position with respect to true edge for images affected with signal dependent noise.

While some research groups do focus on edge detection for images with non-linear noise. We find that it would be helpful to understand the behaviour of edges in presence of noise as it would help in designing a more efficient filter. We also find that in case of Rician noise, if we sufficiently reduce the effect of noise and obtain image with similar true signal information and edge details, we might be able to use first order filters for step edge detection in these images. We do not have to design a new filter and the existing first order filters will be able to perform a similar function with faster computational operation. In addition as demonstrated by Fig. (3.12) noise may cause the edge position to vary from its true position. Our investigation for Rician noise indicates that this edge

difference may be contributed due to variance of edge localization due to noise. The study computes this value of variance using the second order moments of the Rice distribution function on edge function as demonstrated by Eq. (3.44) and Eq. (3.45). There are other types of non-linear and signal-dependent noise which can affect images. The characteristic distribution function of these noises can then be used to study their effect of edge detection and true location. In addition while most of the edges in an image can be considered as step edges it would be desirable to understand the role of non-linear noise on the types of edges such as a ramp.

3.6 Conclusion

In this chapter we have proposed a new automated articular cartilage detection method using 3D undecimated wavelets. In order to achieve better cartilage detection we use wavelet multiresolution analysis to achieve better segmentation. Wavelet multiresolution allows us to capture edge details for cartilage at different resolution levels. At the same time an adaptive local threshold t_L obtained from the 3D wavelet histogram is used to retain coefficients only relevant to cartilage while discarding the background edge details. Rician distribution function $P(M)$ is used to model the wavelet histogram and selection of appropriate confidence levels for MLE of intensity to retain edge details. 3D assessment of cartilage adds to the directional information and thus gives and overall picture of the cartilage geometry. By implementing undecimated wavelet transform (UWT) we try to retain all the coefficients thus preventing loss of sensitive cartilage information. The proposed method has been validated on phantom and real MRI datasets of the articular cartilage. Experimental results demonstrate better cartilage detection at different standard deviations of noise with reduction in MSE for denoised images. Future work may include use of knowledge of cartilage geometry for a more robust segmentation.

In the second study we have proposed a new edge localization technique for step edges in images affected with signal dependent noise in MRI. The proposed technique offers new correction factor $E_0[x, y]$ for edge localization using the second order moment of the Rice distribution function. It demonstrates improvement for step edge detection in images as compared to both Canny and Sobel edge detectors; as also shown by Pratt's figure of merit (FOM) and correlation coefficient (CoC). In addition proposed method can be implemented using an existing first order filter for step edge detection and offers fast and computationally efficient edge detection for signal dependent non-linear noise. Future work may include analysis of signal dependent noise for different edge profiles other than step edges.

Chapter 4

Wavelet and Riemannian Geometry Descriptor for Cartilage

In this study we have investigated the use of wavelet based geometric descriptor for 3D cartilage shape analysis. The proposed first and second fundamental forms of the Riemannian manifold are used to compute the intrinsic Gaussian curvature of cartilage tissue which is also used as the proposed shape descriptor. Cartilage shape is modelled as a Riemannian manifold and the wavelet functions are used to determine the first and second fundamental forms of this manifold. The proposed descriptor method was later implemented for computation of the curvature of the cartilage shape in the MRI datasets.

4.1 Introduction

OA is primarily characterized as a synovial joint disease which leads to progressive loss of cartilage tissue within these joints. As OA progresses, articular cartilage displays a propensity for shape deformation and subsequent deterioration. Ideally in a real world scenario it would be desirable to have a-priori knowledge about true cartilage shape and its deformation characteristics as the tissue deteriorates. The knowledge about these changes and modification of the cartilage structure may be used for analysing early stage diagnosis of OA. As also previously observed in Tab. 1.1 of chapter 1, the various pathological changes in the cartilage and bone joint structure have already been used to validate the presence of OA and quantify or grade the severity of disease progression. Some of these parameters such as joint space narrowing (JSN) in X-rays or thickness

and volume in MRI can be computed with help of images. In addition these quantitative and semi-quantitative parameters may commonly be known as imaging biomarkers for cartilage tissue and help in quantifying changes within cartilage tissue. Together these parameters, in addition with clinical prognosis may collectively be implemented to grade and classify cartilage tissues for OA.

In recent years we have seen much development in areas of cartilage detection and grading systems for Osteoarthritis. Newer techniques in imaging systems are sought for early diagnosis of cartilage to enable a more reliable and efficient cartilage analysis. The added impetus for such systems is to be able to observe changes in cartilage tissue, in order to monitor disease progression and thus improve the overall understanding of this disease. It may also be helpful in verifying the effectiveness of drugs or medicines used in treatment for Osteoarthritis in patients in the future (Folkesson et al., 2007; Poh et al., 2010; Akhtar et al., 2007). Though biochemical markers are being used to understand patho-physiology of cartilage and may prove helpful in possible prediction of OA. The relation of these biomarkers has yet to be validated clinically in relation to their pathological conditions. The current existing biomarkers are only able to validate presence of OA but are unable to aid prognosis of OA both in individual subjects or large population (Bijlsma et al., 2011).

And although MRI offers clinically safer and better visualization of cartilage tissue; its semi-quantitative analysis may also be hampered by an implicit surface analysis. Quantitative analysis of cartilage tissue in MRI may usually be dependent on the observer or operator using the system thus limiting the scope of the grading system. As a result it is often desirable to offer a more robust scoring system with a reduced operator dependence and inter-patient variations in addition to faster analysis. Also a more reliable and sensitive biomarkers would definitely benefit early OA diagnosis and patient prognosis.

As a result a parameter which is able to quantify cartilage shape changes more globally and yet sensitive to indicate variations would benefit in this situation. In this study we propose the use of 3D cartilage structure to account for shape change during OA and its quantification for OA classification. The 3D geometry of the cartilage structure may thus be able to provide a more clear understanding of the shape and information about tissue degradation during different stages of OA. We are of the opinion that curvature analysis of cartilage shape would thus make it a more promising parameter to quantify and describe changes in the cartilage shape. But the information of true cartilage is seldom known and its shape deformation depends on several factors which may vary

across individuals. This makes it desirable and also difficult to obtain a more invariant descriptor for cartilage tissue that may be able to address shape variations. Once an estimation of the cartilage shape is possible; taking into account its different isometric shape modifications when subjected to mechanical stress it might then be possible to determine a descriptor for this shape and if feasible it may also be able to predict the deformation conditions of the cartilage shape.

4.2 Cartilage Shape descriptor

Shape analysis is often used for statistical evaluation of a geometric shape, matching and for object detection. There exists vast literature on shape analysis for 2D and 3D shapes in image processing and analysis. A descriptor of the shape is often used to perform necessary tasks such as segmentation, classification, shape analysis, retention and object detection (Samir et al., 2006; Bronstein et al., 2005; Mademlis et al., 2009; Kimmel et al., 2000). For shape analysis it is often desirable to obtain a shape descriptor invariant to shape transformation which may be able to account for its different isometries.

Spherical harmonic descriptors or Procrustes analysis work with point cloud and often offer descriptors invariant to shape transformation (Chung et al., 2003). Descriptors which do not change with respect to isometric embedding are usually known as intrinsic shape descriptors (Bronstein et al., 2005). The advantage of this class of descriptors is that they may be applied to deformable objects and a wide group of the real world shapes including those in medical imaging. It also can provide invariant shape information for the 3D shape. The descriptors utilizing Laplace-Beltrami spectrum and heat kernel signatures (HKS) usually fall within this category (Bronstein and Kokkinos, 2010; Chung et al., 2005). The spectrum of Laplace-Beltrami operator is invariant under isometries and is well suited for analysis of non-rigid shapes. HKS is a feature descriptor for deformable shape and relies on eigen-decomposition of heat kernel (Bronstein and Kokkinos, 2010). For every point on the surface, a diagonal of the heat kernel is sampled at a specific time which results in a local signature that can be used for partial matching or symmetry. Volume HKS is similar to HKS but defined over the entire volume and considers Neumann boundary condition over the manifold shape, it is also able to represent 3D transformation more closely (Raviv et al., 2011). Other graph based descriptors such as medial axis or Reeb graph, capture geometric and or topological information but cannot be implemented in a comparative study as the other vector based descriptors (Folkesson et al., 2007).

A shape representation generally depends on the properties of the shape which may be represented as a point cloud, boundary or volume. Furthermore model based methods make use of 3D data which may include feature based, graph based and local feature techniques in their representation. As the name suggests a global based method often represents the global properties of the shape.

Current shape descriptors may usually be obtained by using a set of training image data or a dictionary which may also be used for object recognition (Mademlis et al., 2009). The disadvantage of such a system is that the descriptor has to be trained to account for large and almost all possible variations of a particular shape. It should then be able to identify a particular object from within this large dictionary of shape information. This makes the process extremely time consuming, requires a lot of resources and is computationally expensive. As a result it is often useful to have an invariant descriptor that may be used to identify an object and its different isometric conditions without requiring any additional training. This also reduces the necessity of huge training data sets and speeds up the object recognition process.

In this study we believe that the articular cartilage shape may also benefit from such an intrinsic descriptor with respect to its shape. The objective of using invariant cartilage descriptor is that it may be able to address the different isometric conditions of cartilage topology across vast population scale. These intrinsic properties are invariant under transformation and include surface area, gauss curvature, geodesic distance etc. (Bronstein et al., 2005; Griffin, 1994). Extrinsic properties of the shape are usually dependent on a particular configuration within the surface of the shape and may include either volume, mean curvature or Euclidean distance. The extrinsic descriptor being a more local phenomenon is still sensitive to the topological variations that may occur as cartilage shape varies, during progression of OA. The intrinsic and extrinsic parameter for cartilage shape may thus be used as a more robust biomarker for OA classification and grading.

For this study we focus on a cartilage geometric descriptor using wavelets and Riemannian manifold for the cartilage shape. This descriptor comprises of Gaussian and mean curvature values obtained using the proposed first and second fundamental form of the Riemannian manifold. Such a descriptor may be able to account for the variability across different cartilage shapes for OA analysis and also monitor and compute the different changes across cartilage as a result of deformation. This may prove useful in identifying early stage changes for OA diagnosis. In order achieve this we first have to compute

the Gaussian and mean curvature of the 3D cartilage model. This requires computation of the Riemannian parameters for the cartilage manifold with help of a parametrized function of the 3D shape (Morgan, 1998; Millman and Parker, 1977). Often mapping of shape onto a known arbitrary structure is performed in order to achieve parametrization of the said shape. As cartilage is a more curvilinear it is more appropriate to map it onto a sphere which map be able to take into consideration its curved shape structure. As there is no direct method to parametrize an arbitrary 3D shape, we have considered to work with 3D wavelets which may offer an indirect parametrization with respect to image coordinates in wavelet domain. The wavelet gradients obtained for the cartilage model using the image coordinates may correlate to the shape coordinates on the manifold. By implementing the wavelet gradients for Riemannian tensor computation we might thus be able to obtain the Riemannian metric for the cartilage shape without the need for any complex 3D mapping or transformation. In addition we can reduce the computation time for estimation of Riemannian parameters for 3D shape. Our contribution towards such a 3D shape descriptor will include,

- Wavelet gradients as parametrized gradient information for computation of metric tensor.
- Riemannian-wavelet descriptor for 3D cartilage shape.
- Use of above descriptor for OA analysis and biomarker

More information about Riemannian geometry, use of wavelet and manifolds is given in the following section. Note that there may be some challenges with change of cartilage topology due to complete breakdown and presence of holes as the cartilage tissue degrades in the advanced stages of OA. In this case the nature of the manifold has changed completely and will require more in depth study for this purpose and has not been addressed here. We have already identified certain challenges caused due to cartilage shape and thickness which does not allow us to map this topology directly onto sphere explained in more detail in section 4.8.

4.3 Cartilage Curvature - MRI Imaging Biomarker

Early stage OA may demonstrate changes in cartilage topology while the more advanced stages may be identified with breakdown within the tissue itself. Several research groups have investigated the possibility of use of cartilage curvature as an imaging biomarker for prediction of early stage OA. The commonly employed strategy to use cartilage structure

as a biomarker, is to determine the curvature for cartilage shape and to use it to estimate the smoothness of the tissue and joint congruity (Folkesson et al., 2007). Existing data in literature studies indicate that the global curvature of the cartilage tissue may be associated with joint congruity. This is a measure between curve uniformity between the two corresponding cartilage surfaces and looks at similarity of contacting joint surfaces (Folkesson et al., 2007). Higher congruity may be associated with a healthy joint structure while changes in this measure indicate compromise within the joint structure. In addition a second curvature unit also named as the fine-scale curvature is associated with the smoothness of the cartilage surface. Both the curvature units look at the global and local cartilage surface.

In a study by E. Dam et.al., they have proposed the use of level set function for a fine scale curvature information for cartilage tissue; while coarse scale curvature is obtained using the m-rep model. The level set function for fine scale curvature function is given as (Folkesson et al., 2007),

$$\phi_t = k_M|\nabla\phi| = [\nabla(\frac{\nabla\phi}{|\nabla\phi|})]|\nabla\phi| \tag{4.1}$$

where $\nabla\phi$ is the gradient of the level set representation ϕ with respect to time t and k_M is the mean curvature (Folkesson et al., 2007).

m-rep models are a median means representation of a 3D geometry. The coarse scale curvature information for the cartilage shape is computed using this medial axis model of the segmented cartilage shape. while the coarse curvature information usually represents the global shape information and gives the curvature information of cartilage shape as a whole surface; the fine scale curvature computed using the level set equation is used to obtain information about the surface smoothness. This smoothness of cartilage surface is given as the inverse ratio of the fine scale curvature (Folkesson et al., 2008; Tummala et al., 2011; Tummala and Dam, 2010). In yet another study conducted by Eckstein et.al. the curvature information of cartilage is obtained in-vivo. The approach implemented by this study was to utilize the continuous B-spline surfaces for computation of curvature values. The first and second order derivatives of the B-spline surface were used to compute the cartilage curvature information (Hohe et al., 2002). These curvature values were also used to represent the joint congruity.

There seems to be evidence that curvature information may be used as quantification of cartilage shape to determine the different stage of OA. Coarse scale curvature seems to offer a better prediction of different stages of OA as compared to fine scale curvature

information (Folkesson et al., 2008). In addition curvature results are dependent on the cartilage modelling techniques. And a more efficient OA prediction will require more than one biomarker (Folkesson et al., 2007).

In this study we propose a more robust estimation of the cartilage curvature using the Riemannian manifold. This approach for curvature computation is computationally efficient and faster. Also the intrinsic Gaussian curvature and extrinsic mean curvature computed using Riemannian metric of the manifold is equivalent to the coarse scale curvature and fine scale curvature as mentioned in the above studies.

4.4 Riemannian Geometry

Let surface $S \subset R^3$ represent a smooth Riemannian manifold. Let point on surface be given as $p \in S$. Also let the tangent space of vectors; tangent to S at point p be represented as T_pS. The tangent or position vectors $\mathbf{x}_i$ are then obtained as a partial derivative with respect to u_i which has an orthonormal basis function and is the parametrized coordinate of the shape. The tangent vector $\mathbf{x}_i$ can then be given as (Morgan, 1998; Do Carmo and Do Carmo, 1976),

$$\mathbf{x}_i = \frac{\partial \mathbf{x}}{\partial u_i} = (\frac{\partial x}{\partial u_i}, \frac{\partial y}{\partial u_i}, \frac{\partial z}{\partial u_i}) \tag{4.2}$$

Riemannian metric for surface $S \subset R^3$ can then be given as

$$g_{i,j} = \mathbf{x}_i.\mathbf{x}_j = \frac{\partial x}{\partial u_i}.\frac{\partial x}{\partial u_j} \tag{4.3}$$

The matrix $g = [g_{i,j}]$ is called the first fundamental form or metric (Morgan, 1998). It is an intrinsic quantity and gives length,

$$L = \int ds \Rightarrow \sum g_{i,j}\dot{\xi}_i\dot{\xi}_j \tag{4.4}$$

where ,

$$\sum g_{i,j}\dot{\xi}_i\dot{\xi}_j = 2\,(g_{11}\dot{\xi_1}^2 + 2\,g_{12}\dot{\xi_1}\dot{\xi_2} + g_{22}\dot{\xi_2}^2) \tag{4.5}$$

In addition coefficients g_{11}, g_{12} and g_{22} belong to the first fundamental form I and are also known in literature as E, F and G where $E = \dot{\xi_1}\dot{\xi_1}$, $F = \dot{\xi_1}\dot{\xi_2}$ and $G = \dot{\xi_2}\dot{\xi_2}$. The second

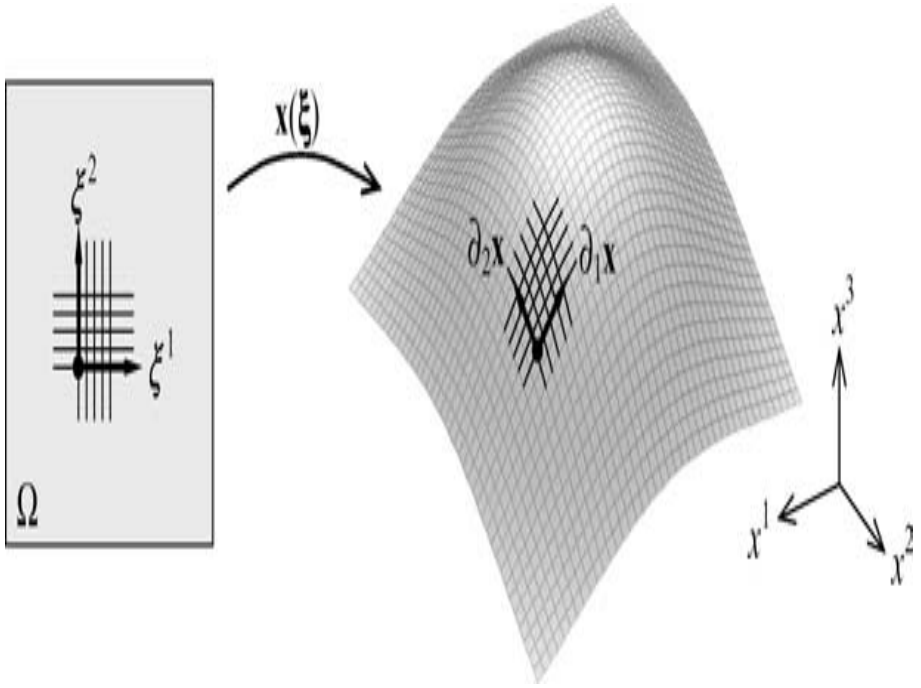

FIGURE 4.1: parametrization of surface on a smooth riemannian manifold (Bronstein et al., 2005)

fundamental form II for point p on surface S is given as,(Morgan, 1998; Do Carmo and Do Carmo, 1976)

$$II = D^2\mathbf{x} = \begin{vmatrix} x_{11} & x_{12} \\ x_{12} & x_{22} \end{vmatrix} \tag{4.6}$$

where $D^2\mathbf{x}$ is known as the bilinear form on tangent space T_pS. The coefficients of the second fundamental form x_{11}, x_{12} and x_{22} with respect to normal n are also known as e, f and g respectively. Together the coefficients of first fundamental form I are used to compute the intrinsic parameter such as Gaussian curvature G for surface S while coefficients of the second fundamental form give us the extrinsic parameters such as mean curvature H.(Morgan, 1998; Do Carmo and Do Carmo, 1976)

Theorema Egregium states that the Gauss curvature of the manifold is an intrinsic quantity and can be determined from within the surface. Principal curvatures k_1 and k_2 measure the amount of curvature of the surface in space. The Gauss curvature K gives us the rate of change of length of the evolving curve while the mean curvature H gives us the rate of change of area of the evolving surface (Morgan, 1998). Maximal normal curvatures k_1 and minimal normal curvature k_2 are called principal curvatures at P (Do Carmo and Do Carmo, 1976).

4.5 Proposed curvature estimation

We model the cartilage surface S_C as a smooth continuous Riemannian manifold where $S_C \subset R^3$. Let P be a point on the surface usually represented as vector $P = [p_1, p_2, p_3, ...]$ and $\xi_{i,j}$ are the local co-ordinates of the shape, where $i, j = 1, 2$. Also points P on the surface S_C of cartilage model are obtained from the original image function I computed after detection and segmentation of cartilage tissue to generate 3D model of the shape. Let the original image volume function be represented as $I_{vol} \in \{x, y, z\}$; where x, y, z-coordinate belong to the original Euclidean co-ordinate system.

In order to compute the Riemannian metric $g_{i,j}$ for the cartilage shape S_C we require the partial derivative information at point P for the shape S_C with respect to local coordinates $\xi_{i,j}$. The partial derivative vectors $P_{i,j}$ belong to the tangent space T_pS and are used to compute the Riemannian metric $g_{i,j}$ for the shape. To compute the Riemannian metric we need to work with vectors in tangent space T_pS; tangent to surface S_C at point p. This tangent space is given by partial derivatives at point P on this surface S_C with respect to $\xi_{i,j}$ as follows (Morgan, 1998).

$$P_{i,j} = \frac{\partial p}{\partial \xi_{i,j}} \tag{4.7}$$

where $\xi_{i,j}$ represent local shape coordinates. Thus Riemannian metric $g_{i,j}$ is the inner product of tangent vectors given as (Morgan, 1998),

$$g_{i,j} = p_i . p_j \tag{4.8}$$

where $i, j = 1, 2$.

To obtain the partial derivative vectors $P_{i,j}$ one needs to parametrize the shape and obtain the differential with respect to local coordinates $\xi_{i,j}$. But not all real world arbitrary shapes can be parametrized or represented with a canonical function; as a result they often have to be mapped or embedded into a known geometry. In this study we utilize wavelet convolution with image function $I_{vol} \in \{x, y, z\}$ to obtain the parametrized representation of cartilage shape S_C. The Euclidean coordinate of shape in the image function $I_{vol} \in \{x, y, z\}$ are encoded in the wavelet coordinates of scale-space s, m, n. As a result we reduce the necessity of specifically obtaining a canonical representation for cartilage shape analysis. To obtain the partial derivative with respect to wavelet function we compute the wavelet gradient with original image function.

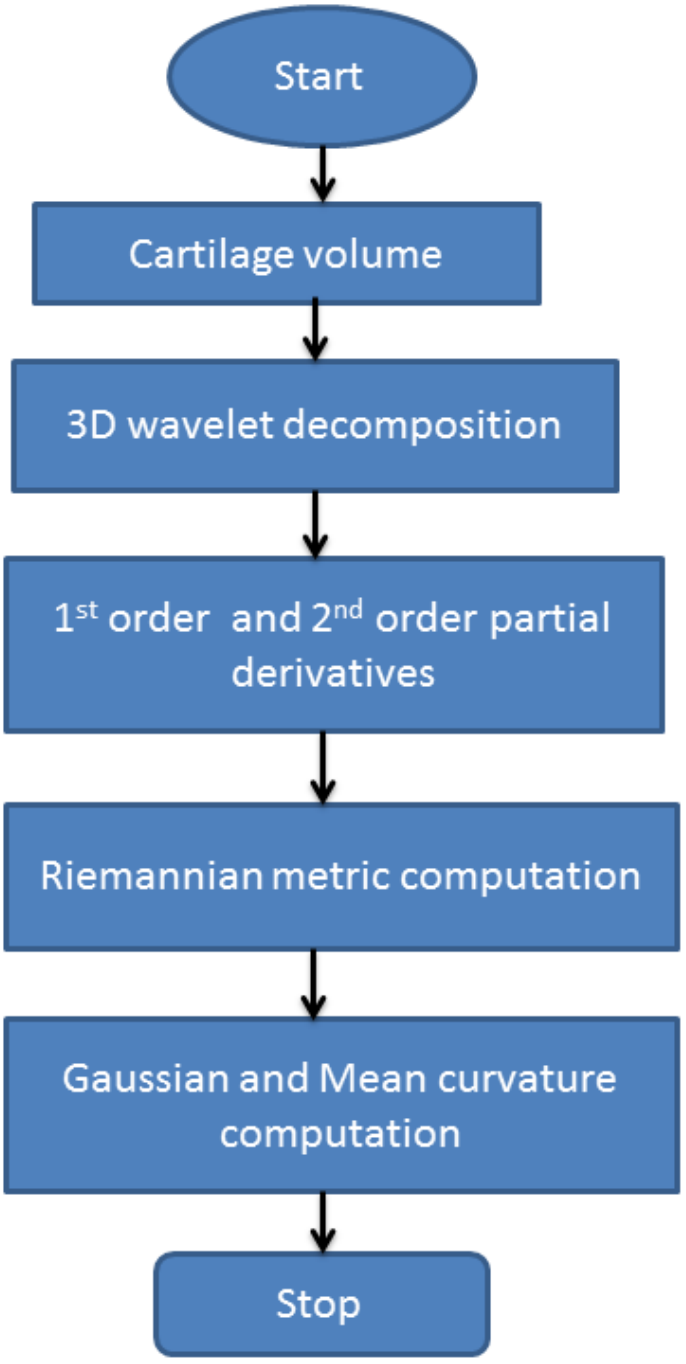

FIGURE 4.2: Algorithm flow chart of the proposed geometric descriptor

Wavelet decomposition $\psi_{j,m,n}$ of image volume I_{vol} is similar to the partial derivatives required for Riemannian metric $g_{i,j}$ computation for descriptor of cartilage surface S_C. The wavelet decomposition function ψ is given as (Gonzalez et al.,

$$\psi_{j,m,n}(x,y) = 2^{j/2}\psi^i(2^j x - m, 2^j y - n) \tag{4.9}$$

The wavelet gradients for 3D image volume I_{vol} can be given as,

$$\begin{aligned} W_p(j,m,n) &= \int I_{vol} * 2^{j/2}\psi(2^j x - m, 2^j y - n)\, dx \\ &= 2^{j/2} \int I_{vol} * \psi(2^j x - m, 2^j y - n)\, dx \\ &\cong 2^{j/2} \frac{\partial p}{\partial \xi_{i,j}} \end{aligned} \tag{4.10}$$

where convolution of wavelet function with image is similar to first and second order partial derivative, j is the decomposition scale, $*$ is convolution function. The partial derivative for surface in terms of wavelet differential function can now be written as

$$WP_{i,j} = W_p(j,m,n) \tag{4.11}$$

where W_{p1}, W_{p2} and W_{p12} are coefficients obtained from first level wavelet decomposition of image volume at $j = 1$ and are first order gradients. While W_{p11} and W_{p22} are wavelet coefficients obtained decomposition of image volume at level $j = 2$ and are second order gradients.

The first fundamental form I and the second fundamental II for the cartilage surface with respect to wavelet coefficients using Riemannian metric $g_{i,j}$ can now be given as,

$$(g^{-1})(D^2 W_p).n = g^{-1} \begin{vmatrix} W_{p11}.n & W_{p12}.n \\ W_{p12}.n & W_{p22}.n \end{vmatrix} \tag{4.12}$$

where n is the normal for surface and is given as,

$$n = \frac{W_{p1} \times W_{p2}}{|W_{p1} \times W_{p2}|} \tag{4.13}$$

The intrinsic Gaussian curvature WG for the cartilage surface S_C can now be computed as,

$$\begin{aligned} WG &= det\ \ g^{-1}(D^2 W_p).n \\ &= \frac{(W_{p11}.n)(W_{p22}.n) - (W_{p12}.n)^2}{W_{p1}^2 W_{p2}^2 - (W_{p1}.W_{p2})^2} \end{aligned} \tag{4.14}$$

While the extrinsic mean curvature WH for the surface S_C can then be given as,

$$\begin{aligned} WH &= trace\ \ g^{-1}(D^2 W_p).n \\ &= \frac{1}{2}\frac{W_{p2}^2 W_{p11} - 2(W_{p1}.W_{p2})W_{p12} + W_{p1}^2 W_{p22}}{W_{p1}^2 W_{p2}^2 - (W_{p1}.W_{p2})^2}.n \end{aligned} \tag{4.15}$$

The proposed Gaussian WG and mean curvature WH can also be used to determine the principal curvatures of the cartilage shape as follows,

$$kw = WH \pm \sqrt{WH^2 - WG} \tag{4.16}$$

where principal curvatures is given as kw.

4.6 Simulation Study & Results

4.6.1 Materials

For this study we have use 7 MRI datasets for proposed curvature descriptor. The MRI datasets are same as those mentioned in section 3.4.1 of chapter 3 and are used to validate the proposed method for curvature computation of the cartilage tissue. All the datasets underwent cartilage detection using 3D undecimated wavelets proposed in chapter 3, section 3.3 prior to shape analysis. The algorithm for cartilage curvature descriptor using wavelet based Riemannian geometry was written in MATLAB R2013b.

4.6.2 Experimental Results

For the computation of the geometric descriptor for cartilage shape, each MRI dataset initially underwent cartilage detection with the proposed local t_L and global thresholds

$\dot{\gamma}$ described in Chapter 3. The segmented volume was reconstructed using the inverse undecimated wavelet transform. This volume was further used to determine the high pass filtered gradients vital for computation of the Riemannian metric $g_{i,j}$ using the wavelet decomposition of the segmented volume.

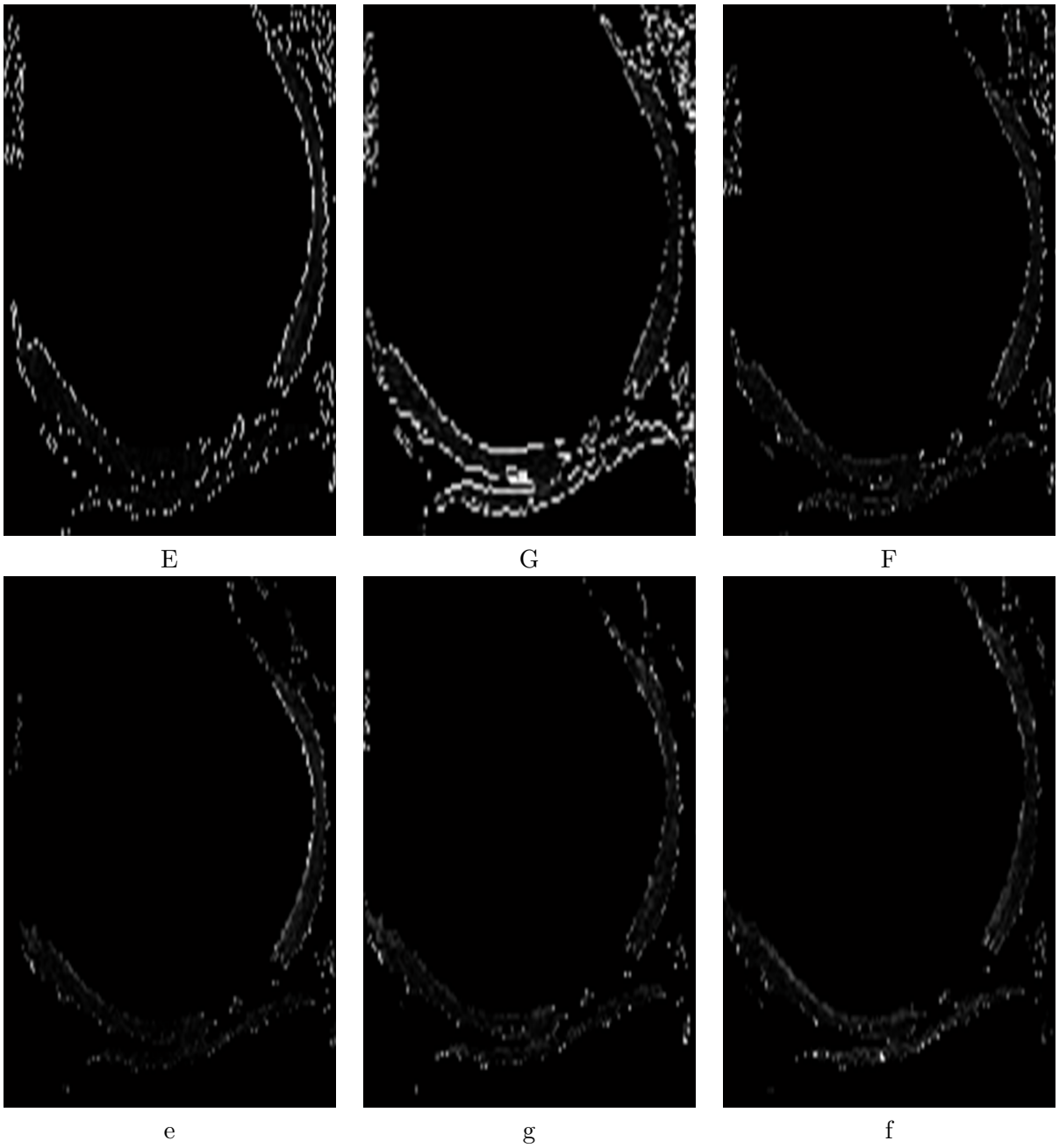

FIGURE 4.3: first fundamental form for cartilage tissue and second fundamental for the cartilage tissue

The wavelet coefficients c_ψ are selected across these two scales. The wavelet coefficients obtained at scale 1 and scale 2 correspond to the gradient information in T_pS for points

a b c

FIGURE 4.4: a) original volume b) cartilage topology 1 and c) cartilage topology 2

across the cartilage surface. The horizontal and vertical coefficients of wavelet decomposition at scale 1 are very similar to the first order gradients for point P across the shape surface S_C. The second order gradients for the surface points is obtained as the second order wavelet decomposition and are given by the gradient information along the horizontal, vertical and diagonal wavelet decomposition. In this study as we have utilized un-decimated wavelet transform which up samples the original signal content as a result, we have resized and normalized the original wavelet coefficients before the Riemannian metric $g_{i,j}$ computation.

The wavelet coefficients of the first and second scale are thus used to compute the first I and second II fundamental form. For the curvature computation using Riemannian metric $g_{i,j}$ we require the first and second fundamental forms of the manifold. The coefficients of first fundamental forms E,G, F are given as the dot product of the horizontal, vertical and diagonal wavelet coefficients W_p. The normal for the 2D shape is obtained using the horizontal and vertical surface gradients as given by Eq.(4.13). Product of the normal n with second order gradients provide us with the elements of the second fundamental form II. The subsequent intrinsic Gaussian curvature WG and extrinsic mean curvature WH for the cartilage surface is then computed using Eq.(4.14) and Eq.(4.15) respectively. Principal curvatures of the shape is computed using Eq.(4.16).

This study is performed only for the femoral cartilage for simplicity of analysis. For computation of the curvature, we select a small region at the base of the femoral cartilage which correlates more closely with the tibial surface used in most of the studies

TABLE 4.1: Riemannian metric computation for different cartilage topologies

Dataset		**Gaussian Curvature**	**Mean Curvature**
D7	original	51.689	43.259
	topology 1	52.708	67.478
	topology 2	59.933	56.495
D11	original	53.894	56.939
	topology 1	54.694	20.954
	topology 2	44.758	48.001

TABLE 4.2: Curvature computation for MRI volume using Riemannian metric

Datasets	**Gaussian curvature**	**Mean Curvature**
D1	41.246	25.262
D2	45.250	47.624
D5	50.664	48.229
D6	41.582	17.563
D12	89.286	53.400

(Folkesson et al., 2007; Tummala and Dam, 2010; Iranpour-Boroujeni et al., 2011). Tibial surface is selected as it is the most weight bearing structure of the cartilage tissue and undergoes degradation earlier as compared to the rest of the surface. In correlation the femoral cartilage at the base surface may also be subjected to high degree of mechanical stress and may be more sensitive to deformation changes.

Fig.(4.3) demonstrates the first I and second fundamental II forms for the cartilage surface of an MRI dataset respectively. While Fig.(4.4) demonstrates the different topologies for cartilage surface. The different cartilage topologies are used to mimic changes in cartilage surface during the initial stages of deformation in OA. While these may not be an accurate depiction, it includes common variations observed in the femoral shape. For this purpose the cartilage geometry is rotated by +/- 10 degrees to mimic variations in the femoral cartilage. These modified cartilage topologies were later used to compute the Riemannian curvature information for the tissue.

The computed values of these Riemannian curvatures for cartilage topologies and MRI datasets are given in Tab. 4.1. and Tab. 4.2 respectively. The objective of the study is to compute the intrinsic and extrinsic curvature value and to determine variations in curvatures. As demonstrated by Tab. 4.1. and 4.2. the Gaussian curvatures WG show very limited fluctuations in their curvature value and may be used as an indicator of the global structure of the cartilage. This is also supported by literature that intrinsic parameters for shape may be more invariant to topological shape change (Griffin, 1994). The mean curvature WH values as indicated by Tab. 4.1. show considerable fluctuations in their values as the cartilage undergoes deformation. This extrinsic local curvature information may be more sensitive to changes in cartilage topology and can be used for study of cartilage deformation (Chung et al., 2003). As compared to Gauss curvature WG values the difference may be not be huge but it is still sensitive to local deformation with the structure. Tab. 4.2 gives us the Gaussian and mean curvature values for other MRI datasets.

4.7 Advantages

The intrinsic curvature or the Gaussian curvature WG is invariant to different topological conditions of the cartilage. It does not require a-priori knowledge about different cartilage conditions and hence is advantageous in shape analysis of cartilage across large population datasets. It helps in determining the global curvature of the cartilage shape which may result in significant changes only if the manifold or cartilage shape has undergone significant changes e.g. complete or partial loss of tissue. This is also demonstrated in a similar study for 3D face recognition, where the intrinsic geodesic distance across the face shape is able to account for variations in expression and illumination for a single individual and used for person identification (Bronstein et al., 2005; Samir et al., 2006).

The extrinsic curvature WH is sensitive to changes in the local topology (Chung et al., 2003; Griffin, 1994). This enables us to investigate local curvature changes during cartilage deformation and may prove vital in understanding OA. Cartilage curvature thus may also be used as an imaging biomarker for OA analysis (Folkesson et al., 2008; Hohe et al., 2002; Tummala et al., 2011).

The advantage of the proposed technique for cartilage curvature computation using Riemannian metric; is that the same wavelet gradient information for cartilage surface may be used to compute both the global and local curvature information. This is not the case with other studies which require different mathematical computation of the shape to

compute these curvature values as also observed from a study conducted by Folkesson et.al. 2008 (Folkesson et al., 2008). In addition it is non-invasive and does not have to be carried out in-vivo; unlike curvature computation by Hohe et.al. in 2002 (Hohe et al., 2002). Once the partial derivative for cartilage surface is obtained it is relatively easier to determine the intrinsic and extrinsic curvature values without the need for any extensive software tool or a large computational study. In addition due to the invariant nature of Gaussian curvature WG we may be able to account for inter-patient variation within the MRI datasets; provided they suffer from similar OA conditions e.g. grade I or grade II. The intra-patient variations may be reduced by utilizing information of both past Gaussian curvature WG and Mean curvature WH information. Together the proposed Riemannian curvature may allow for a faster and quantitative comparison over time as compared to other graph based descriptors for shape. They may also be used collectively for grading and classification of OA and cartilage shape analysis (Barachant et al., 2012; Klassen et al., 2004; Mademlis et al., 2009).

4.8 Discussion

In order to compute the Riemannian metric for a manifold or 3D object, one requires the parametrized function of that shape to compute the first and second fundamental forms. Most of the real world 3D shapes are arbitrary and deformable shapes which present a challenge in obtaining a parametrized representation for that shape. A much simpler solution often implemented is to either map this shape into another parametrized shapes, such as the planar surface. By implementing this operation, one might then be able to determine the Riemannian metric with respect to an already known manifold such as a plane.

One can achieve such a planar mapping by using conformal maps, which will preserve the angular and to a certain extent the textural information of the shape (Haker et al., 2000; Roşca and Antoine, 2009). Although this is an easier choice for most mesh based analysis systems, it may not an ideal choice as the mapping may not always be reversible and there may exist loss of information due to the embedding process. A yet another approach would be to embed this topological mesh into a known geometry such as a sphere or ellipse for which the parametrized representation of the shape already exists (Nain et al., 2007; Roşca and Antoine, 2009). This approach which is garnering much popularity has limitations when it comes to the topology of the original geometry. Not all real world shapes can be embedded into this geometric map; which is also the case for the cartilage tissue. This can be illustrated from the following Fig.(4.5) where although

the cartilage appears to be almost spherical in shape it cannot be parametrized into a spherical map. Though this is not the case for the 3D mesh of the horse as demonstrated by Fig.(4.5). This parametrization of 3D mesh into a sphere requires that the barycentre of the topology be located at the centre of the shape which is not in the case of the cartilage tissue.

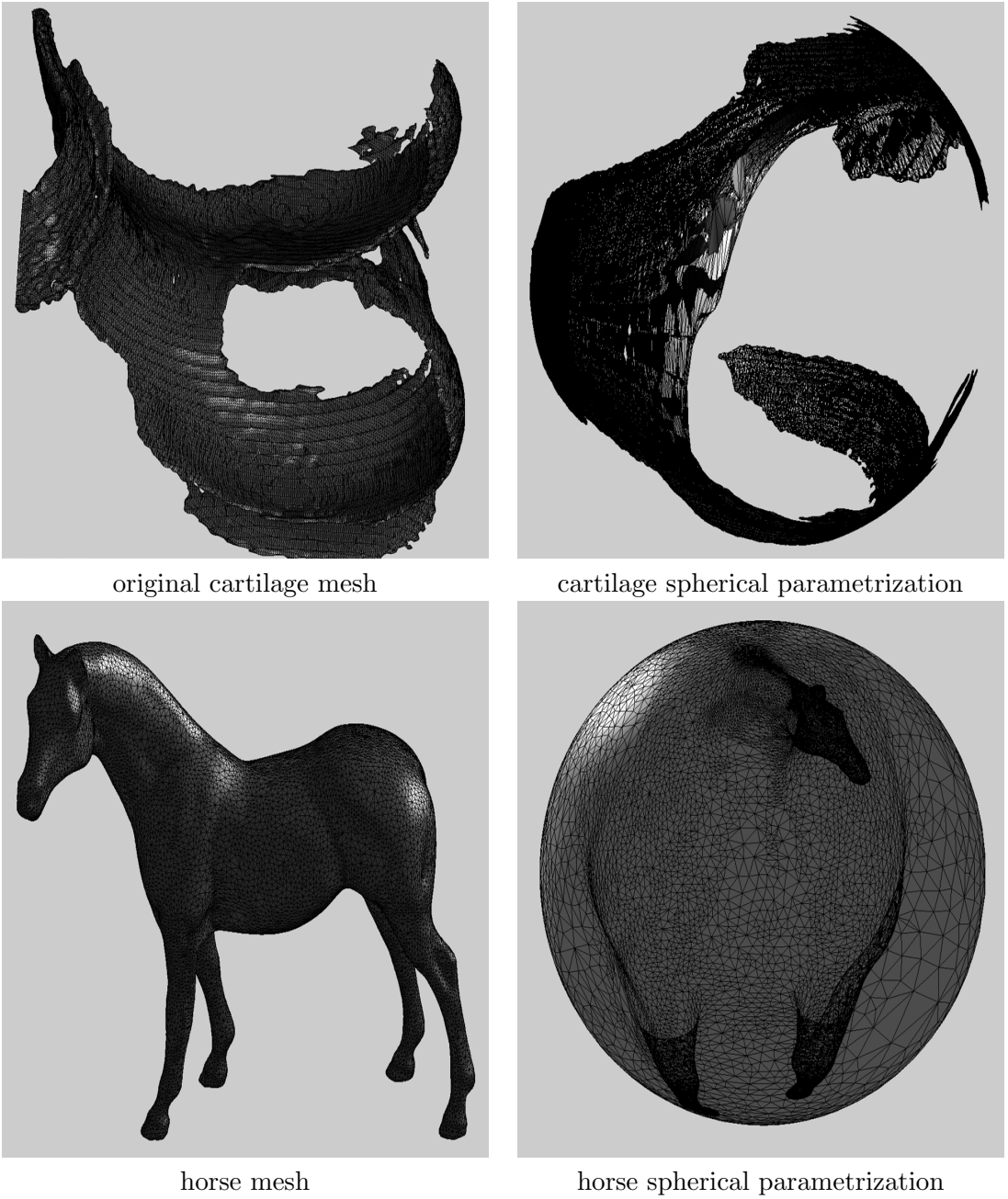

original cartilage mesh | cartilage spherical parametrization

horse mesh | horse spherical parametrization

FIGURE 4.5: original mesh and their corresponding spherical mesh parametrization

In order to resolve this issue we instead treat the wavelet processed image as a parametrized representation of the 3D shape with respect to the wavelet co-ordinates for scale and

space and image function. This approach allows us to overcome the initial challenges of mesh parametrization and at the same time avoids a very complicated process of using mesh neighbourhood to compute the metric tensor for the individual shape as proposed by Moo K Chung (Chung et al., 2003).

The segmented cartilage volume provides the initial co-ordinate position of the shape boundary. The wavelet gradients across this shape surface provide the necessary information to compute the Riemannian metric $g_{i,j}$ for computation of the curvature descriptor for cartilage tissue. The curvature computation with Riemannian metric $g_{i,j}$ enables us to determine the intrinsic and extrinsic information of the cartilage tissue. The intrinsic information being a more topology invariant parameter is used to determine the global information of the cartilage structure. In this study we use this curvature descriptor to identify the severity of the cartilage degradation. A healthy cartilage tissue will present us with a smooth continuous manifold which generates a high curvature values while the severely degraded cartilage tissues will not be a smooth continuous manifold with broken topology and will no longer confound to the curvature values obtained with a healthy tissue.

Gaussian curvature in this study provides us with the global curvature information within the tissue. One can also compute the mean curvature of the cartilage tissue which is a relatively extrinsic quantity of the manifold and provides the local curvature information. This extrinsic quantity is more sensitive to change in curvature topology and may be used to study the local deformation across the cartilage surface as also demonstrated in a study by Moo K Chung for brain surface deformation (Chung et al., 2003). Cartilage deformation for different stages of OA using the mean curvature information has not yet been undertaken in this study and requires further investigation. Although in this study we do compute the mean curvature WH information of the cartilage tissue with respect to global curvature WG information.

The results of the Gaussian WG and mean WH curvature for the cartilage shape with proposed method demonstrate the possibility of implementing a similar strategy for other arbitrary deformable shapes that do not confirm to a conventional mesh topology and parametrization practices.

The proposed shape descriptor is more robust and relatively invariant to changes in the cartilage isometries. It may be able to account for challenges in the intra-patient and

inter-patient analysis as it is an intrinsic descriptor for the cartilage shape though this still has to be rigorously investigated.

4.9 Conclusion

In this chapter we have proposed a new wavelet based Riemannian metric descriptor for computation of intrinsic cartilage curvature WG. The Gaussian curvature WG for cartilage tissue is derived using wavelet based Riemannian metric $g_{i,j}$. The geometric descriptor uses high pass filtered wavelet coefficients c_ψ for computation of the Riemannian metric which are later used to compute the intrinsic curvature for the cartilage surface. The Gauss curvature WG is used as the intrinsic curvature information. A plot of the curvature plot for the different MRI datasets reveals global curvature for different datasets. The proposed geometric descriptor may also be used for other 3D shape objects which do not adhere to conventional 3D mesh analysis practices. Due to the intrinsic nature of curvature it also provides an opportunity to be used as 3D cartilage shape descriptor that may be used for cartilage shape recognition in order to differentiate different stages of OA.

Chapter 5

Software prototype for OA analysis using MRI

In this chapter we introduce a prototype software framework for computer aided analysis (CAD) using MRI images for investigation of knee Osteoarthritis (OA). The proposed software prototype is a wavelet based framework for 3D image analysis of the knee cartilage. This framework implements a 3D un-decimated wavelet multiscale analysis for study of cartilage tissue. In addition a novel 3D multiresolution widget has been developed for visualization of cartilage tissue at different wavelet resolutions. The prototype system implements proposed cartilage detection method mentioned in Chapter 3, which has already been validated with the help of computational experiments on MRI and phantom datasets. It enables the user to interact with the 3D cartilage models and save them for future reference. A closer inspection of the cartilage surface by selection of tissue sub-volume at higher wavelet resolution along with computation of cartilage features and volume at different resolutions is also possible.

5.1 Introduction

Current clinical practices for diagnosis of OA include physical assessment of joints by physicians, patient feedback for pain and use of X-rays or MRI imaging techniques for classification of various stages of disease progression (Theiler et al., 1994; Bijlsma et al., 2011).

While there may have been several computer aided diagnostic (CAD) systems proposed for OA diagnosis (Kauffmann et al., 2003; Akhtar et al., 2007; Mlejnek et al., 2004;

Duryea et al., 2007) their primary focus has been limited to effective segmentation of the knee cartilage and use of thickness map to observe cartilage breakdown which may be used in the assessment of cartilage tissue.

And although there have been several challenges in effective segmentation of cartilage tissue, which may include an automated detection of tissue and its assessment for OA. Improved segmentation techniques using active shape models, atlas based segmentation, graph cuts, kNN classification, support vector machine with kernel based learning, supervised learning and image registration have been proposed for articular cartilage in literature (Folkesson et al., 2007; Kapur et al., 1998; Solloway et al., 1997; Yin et al., 2010; Hinrichs et al., 2003; Prasoon et al., 2013; Tamez-Pena et al., 2012; Zhang et al., 2013; Urish et al., 2013). The segmented cartilage may then be used for grading various stages of OA using a semi-quantitative scoring system (Hunter et al., 2008).

X-rays and its grading systems such as the Kellgren-Lawrence (KL) have remained a gold standard for OA assessment; but detect OA at much later stage where cartilage degradation has already begun. As a result, recent studies have suggested the use of thickness and volume computation of cartilage tissue as semi-quantitative parameters for early stage assessment of OA using MRI (Bijlsma et al., 2011; Crema et al., 2011). Several semi-quantitative scoring systems in MRI have been proposed that focus on size and location of lesions within the cartilaginous and sub-chondral tissue (Hunter et al., 2008; Peterfy et al., 2006). Some of the whole organ scores include the knee osteoarthritis scoring system (KOSS), whole organ MR scoring (WORMS) and Boston-Leeds OA Knee scoring (BLOKS) (Peterfy et al., 2004; Lynch et al., 2010; Felson et al., 2010). And while WORMS and BLOKS offer similar results for several conditions of the cartilage they often split the cartilage tissue area into several sub-regions to compute the thickness and area for these regions (Hunter et al., 2008; Lynch et al., 2010; Felson et al., 2010). Depending on the interrelation of these subregions, the grading system then classifies different stages of OA (Peterfy et al., 2004). As these MRI grading systems require manual division of the cartilage tissue into sub-regions for scoring different stages of OA they are still dependent on operator efficacy (Hunter et al., 2008).

In this study we propose a framework for cartilage analysis which can achieve both cartilage detection and computation of cartilage features such as volume etc. without the need for manual segmentation of cartilage tissue or its surface into subregions. In addition it also offers visualization of the cartilage surface at multiple wavelet resolutions. For this purpose we focus on OA diagnosis, as by being able to visualize cartilage as a whole surface and compute its features such as volume, smoothness etc. to quantify

changes within the structure. As a result we have proposed a novel software framework system for knee cartilage analysis with a new interactive multiresolution widget implemented with help of 3D un-decimated wavelet transform. The proposed system is aimed at OA assessment of the knee cartilage and offers two new features,

- *proposed 3D cartilage detection method*: Use of wavelet analysis for 3D cartilage detection and optimization as mentioned in Chapter 3 section 3.3. This method will provide an improved and robust knee cartilage detection with efficient and faster computational speed required for an interactive assessment of the tissue in real-time.
- *a new multiresolution widget*: A novel user interactive (UI) widget incorporating wavelet multiresolution analysis is developed. It is used to observe cartilage tissue surface for patterns of tissue damage indicating early onset of OA. This new widget uses cartilage models obtained with wavelet analysis for UI analysis of the tissue.

A wavelet multiresolution widget can be utilized for visualization and zooming of cartilage details at different scales (Burrus et al., 1998). This magnification is possible with the help of wavelet filter banks which process and filter out information content depending on the frequency content in a given image (Burrus et al., 1998). Also the proposed framework performs global assessment of the cartilage surface for its analysis and does not require to sub-classify the cartilage surface into several regions for tissue assessment. The structure of this chapter is as follows, in section II we describe in detail the proposed OA analysis system and use of interactive wavelet GUI. This is followed with results and discussion in section III and finally, future work and conclusion.

5.2 Proposed CAD system for OA diagnosis

In this study we have proposed a novel computer aided system for analysis of OA of the knee. The system is designed to perform a user interactive analysis of the 3D surfaces of the articular cartilage of the knee using wavelet multiresolution information. In addition the proposed system aims to achieve analysis of OA using the surface and structural properties of the cartilage tissue. A wavelet based CAD system using 3D un-decimated wavelet transform is utilized for an automated analysis and optimized cartilage detection as also mentioned in Chapter 3 section 3.3. This proposed cartilage detection method offers a more robust and faster segmentation of the cartilage tissue which is crucial for

real time interaction of the tissue. The proposed cartilage detection algorithm has already been validated on MRI and phantom datasets.

In addition as OA diagnosis relies on better inspection of the cartilage surface and structure, we have also proposed a new wavelet based graphical user interface (GUI) that enables the user to display and visualize the 3D structure and surface properties of the cartilage tissue at different wavelet resolutions. This multiscale visualization of the cartilage surface provides us with information about the cartilage shape and volume at different wavelet resolutions for assessment. Also it does not require the tedious task of sub-classification of cartilage surface into several regions for assessment of OA using MRI scoring system.

The primary components of the proposed software framework consists of a) processing unit b) image analysis system which includes 3D wavelet analysis using MRI data, c) a novel multiresolution widget for analysis of cartilage tissue d) and a display unit all of which are described in detail in the following sections. Fig. (5.1) demonstrates the design of the proposed cartilage diagnostic system.

By implementing an object-oriented program structure (OOP) and a parent-child interface within several class functions in the architecture of the proposed software framework, we can choose to perform either specific image processing tasks or only an interactive assessment of the cartilage tissue. The results of the analytical tasks can then be saved for future reference which might be useful for long term clinical evaluation. The system is also designed to allow portability and extension of existing framework for OA analysis. It enables the user to perform a more patient specific diagnosis of the cartilage tissue.

5.2.1 Diagnostic system processing unit

This is the primary body of the proposed software framework as demonstrated by Fig. (5.1). It conducts the necessary image processing operations and visualization tasks related to reading of MRI image data, display of 3D model, wavelet widget interaction and assessment of cartilage tissue.

As the proposed system is designed to be an independent portable unit, free of any paid licensed software we have tried to keep it as much open-source as possible and have implemented it using Microsoft Visual Studio 2010 and visualization tool-kit (VTK) 5.8.0.

For this study, Visual Studio 2010 (VS2010) acts as the desired compiler, enabling us to build and run the dynamic linked libraries(dll) containing vital visualization functions offered by VTK 5.8.0 (Schroeder et al., 2004). This compiler further adds to the extensibility of the proposed system by allowing us to develop wavelet imaging algorithms to carry out the desired imaging and statistical analysis operations. These imaging algorithms are primarily written in C++ which the compiler reads and assimilates with other visualization operations. The individual image processing systems and visualization operations compute the necessary feature of the parent object in this case the cartilage tissue, which may be used either for assessment or 3D visualization of the cartilage structure. The end user can also replace the compiler of their choice for a more autonomous framework, though we haven't tested this scenario.

The proposed software framework consists of the diagnostic system processing unit as the main body of this prototype system while the 3D image analysis and cartilage detection, multiresolution widget, model generation etc. are the sub-systems of this main framework. Each sub-system can still be operated independently of the other as also indicated in Fig. (5.1). Although the main processing system may still be used to control these independent sub-systems to carry out a desired task. The proposed novel multiresolution widget is one such sub-systems controlled by the primary processing unit which adds to the desired interactive nature of cartilage surface visualization and assessment.

User input or feedback is obtained with the help of a mouse controller, which enables the primary processing unit to identify and establish necessary tasks to be carried out. In addition, depending on the mouse input or feedback from the user the 3D model is updated accordingly for corresponding wavelet analysis to be carried out for the model selected. Some of the other aspects of the proposed framework include, reading of the DICOM image files, storage, transfer of 3D wavelet model to the multiresolution widget, 3D wavelet analysis and cartilage feature computation and updating cartilage model based on user feedback. Detailed information on operation of each of these subsystems is given in sections 5.2.2 and 5.2.3 respectively.

The final responsibility of the processing unit is the display of the cartilage model for different wavelet resolutions for visualization on the computer monitor, while the results of cartilage features such as volume and smoothness are indicated on the VS2010 command prompt as also demonstrated by Fig. (5.5). All the necessary operations for data visualization and model generation are conducted by the processing unit using the internal memory of the user's computer and their graphics card. Finally, if the user

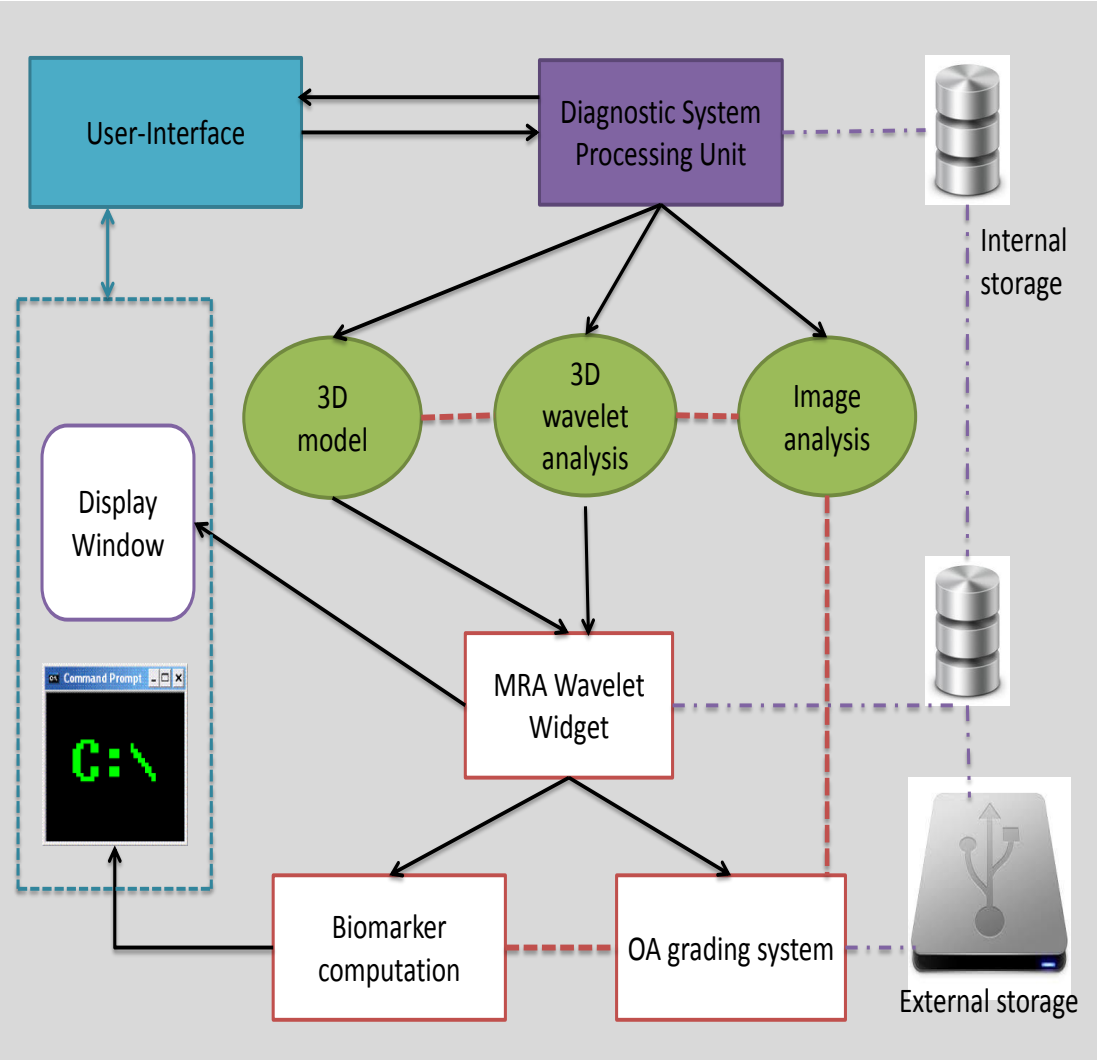

FIGURE 5.1: Proposed system design

requires the output of cartilage feature assessment and the necessary model to be stored as separate file, it can be done by saving the result as an image or VTK object file.

5.2.2 Image and wavelet analysis sub-system

The primary function of this unit is to perform image and wavelet analysis of the MRI image volume for cartilage detection and to provide the processed data to the wavelet GUI. This sub-system largely works with 3D image volumes and performs wavelet analysis on volumetric data. 3D assessment of the MRI volume help compensate for the lack of sampling along the third direction (z-axis) by the MRI machine and helps in improving the thickness estimation of cartilage geometry (Folkesson et al., 2007). Also 3D volume provides complete structural information of the cartilage which might get overlooked when processing 2D images slice by slice. This sub-system is also designed

to carry out other 3D image analysis tasks such as smoothing, thresholding, histogram generation etc. which may support other image processing operations using wavelets. As wavelets offer better 'spatial localization' they are used for the cartilage detection process (Burrus et al., 1998; Starck et al., 2007). The primary tasks of this proposed sub-system is 1) to obtain image spatial and edge details with wavelet decomposition and 2) multiresolution analysis of this wavelet information.

For wavelet analysis, this sub-system decomposes the 3D image volume $I(x, y, z)$ obtained by successive stacking of 2D images slices, read by the DICOM image reader. This 3D image function is given as $I(x, y, z) \in L^2(R^3)$ integrable space (Gonzalez et al., 2004). Low and high frequency components of the image are obtained by volume decomposition using scaling $\varphi_{j,k}(x)$ and wavelet functions respectively $\psi_{j,k}(x)$ (Gonzalez et al., 2004). In the proposed diagnostic system we have used 3D undecimated Haar wavelet transform for cartilage detection. Due to the non-decimate nature of this wavelet transform we retain all coefficients obtained by wavelet decomposition which may prove useful in the cartilage detection process and improve accuracy of diagnosis. The forward and inverse wavelet transform with undecimated wavelets have been previously mentioned in Chapter 3. The values of j are identified by the user to determine the necessary decomposition level and its corresponding inverse operation.

The wavelet decomposition output is further provided for operations such as binary thresholding, matrix transpose etc. necessary to carry out other imaging tasks as required by the cartilage detection process. Adaptive thresholding of wavelet coefficients along with multiscale information are used to perform articular cartilage detection. As the high frequency components contain edge information they are used for localized cartilage detection in the wavelet domain as given in Fig. (5.2). Also the histogram of wavelet coefficients are used to compute the cartilage biomarkers such as the smoothness and entropy for cartilage tissue assessment. Other than wavelet operation, the image analysis system can also carry out standard image processing tasks such as 3D noise removal, image binarization, thresholding, user-defined filtering, geometric data analysis, polydata mesh generation etc. with help of the currently available VTK inbuilt functions for image processing and visualization.

In addition a copy of the wavelet volume is also provided to the widget GUI for visualization at multiple wavelet resolutions. For a wavelet multiresolution analysis, coefficients at higher resolution are obtained by further decomposition of the image volume with scaled and dilated versions of scaling $\varphi_{j,k}(x)$ and wavelet functions $\psi_{j,k}(x)$ (Burrus et al., 1998; Gonzalez et al., 2004). In the wavelet domain the higher subspace information

contains data that is present at the lower subspace (Burrus et al., 1998; Gonzalez et al., 2004).

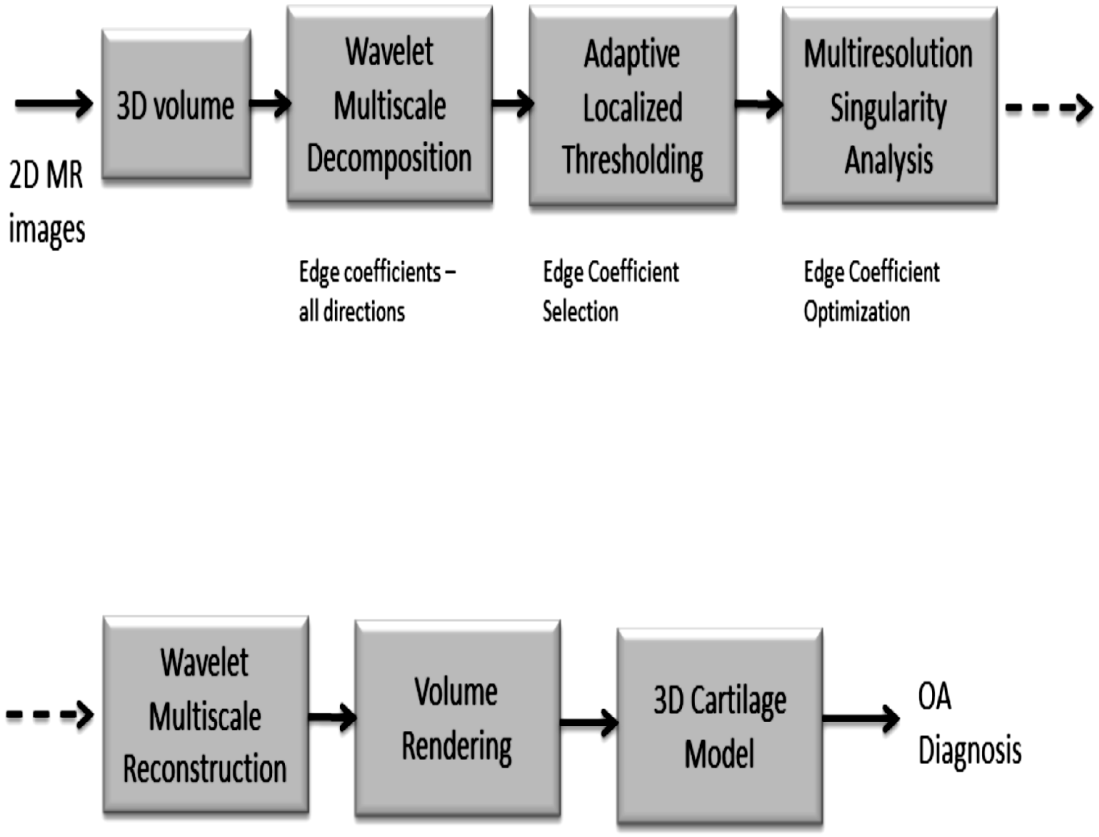

FIGURE 5.2: Wavelet analysis system

The widget uses the output of the image analysis system to display the cartilage volume and update itself on user-interaction. For a faster visualization operation we have restricted the widget GUI to provide only two consecutive wavelet resolutions. As a result once the image analysis system computes the wavelet transform for the user provided input resolution level; it automatically also computes the higher resolution level and provides the information of both the wavelet resolutions to the GUI for display. The image analysis system also uses the same output to determine the smoothness and entropy for cartilage tissue at the two wavelet resolution for assessment.

In addition the 3D volume can be used to generate cartilage models using the volume rendering process inbuilt in VTK 5.8.0. The basic rendering equation can be written as (wikipedia)

$$L_o(x, w_o, \lambda, t) = L_e(x, w_o, \lambda, t) + \int_{\Omega} f_r(x, w_i, w_o, \lambda, t) \\ L_i(x, w_i, \lambda, t)(w_i.\mathbf{n})\ dw_i \tag{5.1}$$

where λ is particular wavelength of light, t is time, x is location space, $\mathbf{n}$ is surface normal at that location, w_o is direction of outgoing light, w_i is the negative direction of incoming light, L_o is total spectral radiance, L_e is emitted spectral radiance, Ω is unit hemisphere containing all possible values of w_i, f_r is bidirectional reflectance distribution function and L_i is incoming spectral radiance (wikipedia). Volume rendering is a computer visualization technique for 3D data and displays 2D projection of discretely sampled 3D data (wikipedia). The volume is considered as extraction of the iso-surface of the volume and rendered as a polygonal mesh. Information content obtained at wavelet decomposition can be used to generate a 3D model of the cartilage tissue for different resolution levels. These models are used to capture changes on the cartilage surface for assessment of the articular cartilage. Then the wavelet information for a given particular level is provided to the multiresolution GUI for an interactive assessment of the geometry of the tissue as shown in Fig. (5.1). If multiple cartilage resolution is required, the user has to enter the wavelet decomposition level and cartilage model for the desired resolution level and higher is generated which is given to the wavelet widget as shown in Fig. (5.3). The wavelet coefficients can also be used to visualize 3D edges of cartilage tissue for a complete assessment or only just the grey scale volumetric data.

5.2.3 Multiresolution Widget

For this study we have developed a novel 3D widget with multi-resolution capability for the purpose of cartilage visualization and diagnosis. This widget has been developed using a parent-child interface using VTK 5.8.0 widget family and additional interface functions written in C++ (Schroeder et al., 2004). Fig. (5.3) displays the widget architecture used by the proposed diagnostic system. The figure on top right indicates the parent widget class function offered by VTK while the figure at the bottom left demonstrates the interaction between the image analysis and wavelet sub-system, user interaction and the proposed widget GUI functions developed for this study. The blue and the dotted arrow in the figure indicate the hierarchy between the parent widget class and proposed wavelet GUI and the translation of mouse events by the parent widget class for the proposed wavelet GUI. Similar to other user interactive (UI) tools, this widget requires two inputs, one provided by the image analysis sub-system and other provided by the user. The user input can be entered as a mouse or keyboard event which

is translated as a execution operation by the event translator which further updates the action of the widget in real time as also shown in Fig. (5.3). Similarly, any update of the model is translated back as an event via a callback mapper and the corresponding change in the model or object is sent back to the image analysis sub-system, which can incorporate any user entered changes if necessary.

One of the primary objectives of the proposed multiresolution widget is to be able to visualize cartilage surface and geometry at multiple wavelet resolutions and perform semi-quantitative assessment of the tissue for the purpose of diagnosis. In order to achieve this, wavelet coefficients obtained during decomposition of a 3D image volume with the help of wavelet function are used to generate the 3D model of the cartilage as given in Fig. (5.3). In addition the cartilage surface is investigated for micro and macro changes such as those mentioned in Tab. 1.1. Also the user may compute the cartilage shape and geometry at different resolution levels and use this information for a further quantitative analysis of the tissue which may prove helpful in prediction of bone and cartilage deformation similar to that given in Tab. 1.2.

In this study the proposed widget displays two models; a higher resolution cartilage model after an interactive selection of primary cartilage surface for a given resolution. To display the higher resolution cartilage models, a second model is reconstructed in yet another UI window, only after a user event has been registered by the widget sub-system. One of the advantages of displaying the second volume in another UI window, is that the user can now interact independently with this volume without affecting the primary model. Such an operation also enables comparison of cartilage tissue at different wavelet resolutions. The user can now independently rotate, zoom in or out or translate the second model. This widget also allows the user a choice to display either a grey scale composite function model of the image or a 3D edge only model of the cartilage at either the given or a higher wavelet resolution level. In order to generate a grey scale model for visualization we use a volume ray casting function already available in the VTK 5.8.0 tool-kit (Schroeder et al., 2004).

An additional feature of the widget sub-system is visualization of the local region also referred to as sub-volume in this study, on the cartilage surface instead of an entire model. In order to display a sub-region of cartilage surface; when the user selects a particular location on the surface of the primary 3D model, the widget sub-system sends the necessary coordinate position to the main diagnostic system processing unit thus indicating the region which the user would like to interact with. The main diagnostic system processing unit will re-compute pixel locations based on co-ordinates of the polygon mesh and generate a sub-volume. In order to hasten the process for real-time visualization, a

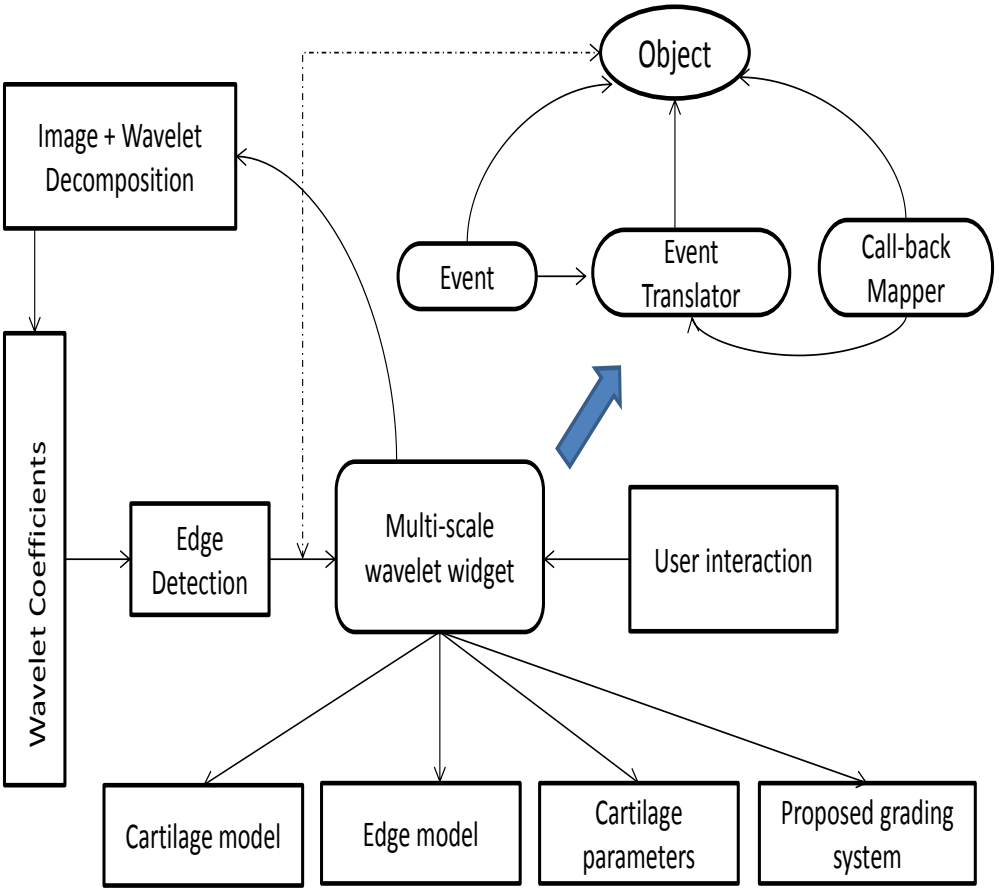

FIGURE 5.3: Multi-scale widget architecture

copy of the primary cartilage volume is already provided to the widget class function by the image analysis sub-system to avoid the entire wavelet reconstruction process. This widget sub-system continues to send information between the primary model and the main system processing unit and accordingly updates the second model. The user can select multiple positions on the original volume and can visualize them as the widget updates itself in real-time in accordance with the new input.

In the current version of the widget GUI, the default resolution for second model is generated at one wavelet resolution higher than the primary model i.e. if the primary model is generated with wavelet coefficients at scale 2 the resolution of the second model of the widget is obtained at scale 3. Also the widget GUI is independent of the image analysis sub-system and can be upgraded to use different computer vision techniques. In addition some of the other miscellaneous tasks carried out by the widget GUI is the computation of the cartilage biomarkers such as smoothness, entropy, and volume (Nixon, 2008; Petrou and García Sevilla, 2006).

Advantages of such a system include improved accuracy, no manual cartilage analysis and hence reduction in operator induced errors with greater computational speed. In addition to 3D wavelet analysis it can also perform regular image processing operations such as denoising, thresholding, binary and morphological analysis. The inverse volume obtained with wavelet reconstruction can be used to generate 3D cartilage models at different wavelet resolutions with volume rendering.

5.3 Results and Discussion

5.3.1 Materials

For this study we have used 14 volumetric datasets of T2-weighted MR images of articular cartilage of the knee. Each volume consists of 512 x 512 x 62 pixels with flip angle of 30, 256 grey levels and slice thickness of 1 mm. A 3D volume is obtained by successive stacking of the 2D image slices. These images were kindly provided by Prof. C. Ding from Menzies's Institute of Research, Tasmania, Australia with prior patient approval. We have also included a phantom cartilage image created in MATLAB R2013b for a comparative study. For the multiresolution widget some of the UI functions have been inherited from parent widget class functions and developed using C++ and VS2010. Cartilage 3D models have been generated using volume rendering process offered by VTK 5.8.0.

5.3.2 Simulation study

A simulation study with MR images and phantom cartilage images has been carried out to test and validate the efficiency of the proposed UI and diagnostic system. A 3D volume is obtained by successive stacking of the 2D image slices for wavelet analysis. In this study we have used a 3D undecimated wavelet transform for cartilage detection as shown in Fig. (5.2).

Depending on the requirement of the user or study, the volume is generated for a specified wavelet resolution. It can be changed at any time on input from the user. Each processed volume with wavelet analysis is used to build a 3D model of the cartilage at that given wavelet resolution. The model is obtained by extracting an iso-surface of specific scalar value and the volume rendered into a polygonal mesh. A similar such cartilage model for two wavelet resolutions at scale $j = 0$ and $j = 1$ for the phantom cartilage and MRI

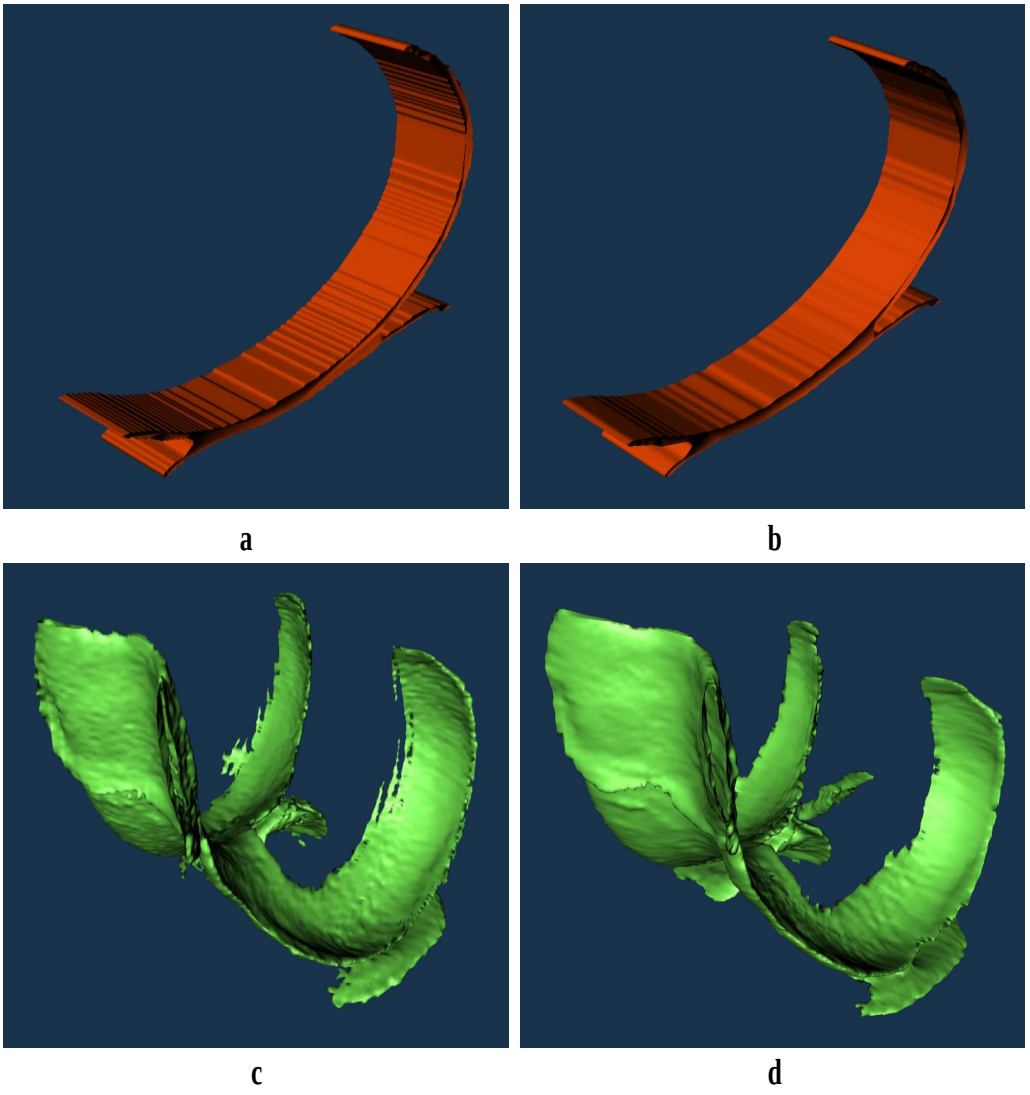

FIGURE 5.4: a & b) Comparison of phantom cartilage surface at two wavelet resolutions, c & d) Comparison of cartilage surface obtained from MRI volume using wavelet decomposition at two resolutions

volume is shown in Fig. (5.4). In Fig. (5.4) b and Fig. (5.4) d one can observe the high resolution cartilage model which is independent of the resolution of the computer screen and is a relatively enhanced version of the prior wavelet resolution level. If there exists any minor deformity or changes on the cartilage surface this will be enhanced by wavelets and can be observed at higher resolution levels. As result one can use high wavelet resolutions to look for any minor changes or alterations which are not visible at current resolution with the naked eye.

In addition cartilage diagnostic parameters such as smoothness, entropy and volume of the cartilage model at multiple wavelet resolutions are given in Table 5.1, where R indicates resolution level. The computed image parameters for texture and smoothness

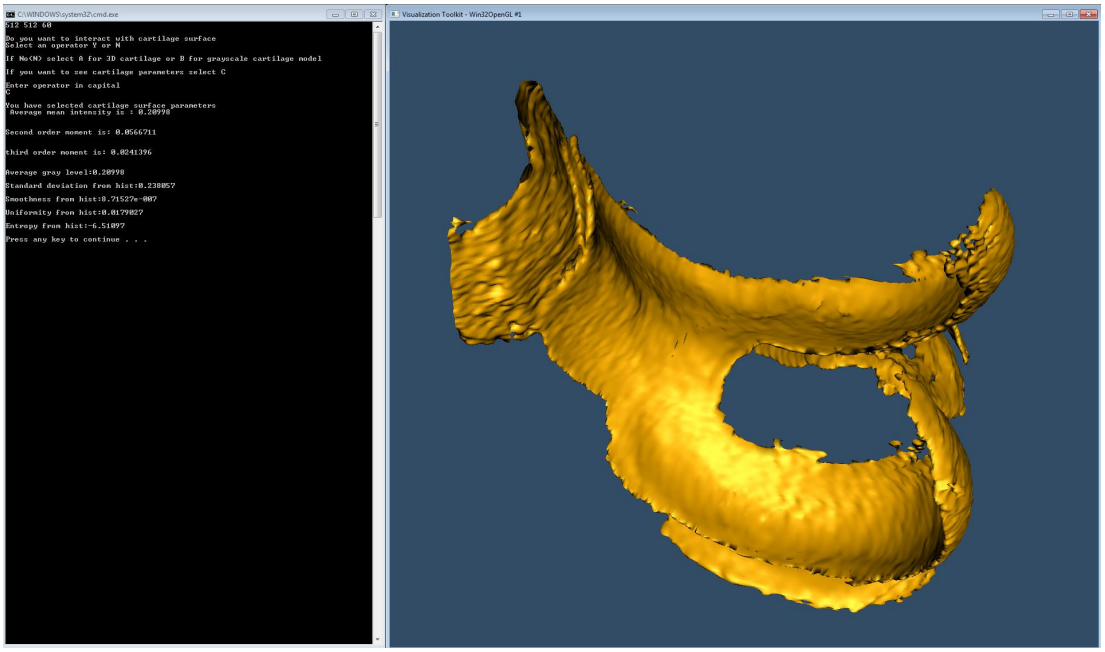

FIGURE 5.5: Software framework displaying cartilage surface parameters with the command prompt as demonstrated on the left and the original cartilage model on the right

of the cartilage surface along with structural information of the cartilage are used by the proposed software framework for cartilage analysis. Furthermore in Table 5.1. we can see that for phantom cartilage we have relatively higher surface smoothness and uniformity at resolution level 2 as compared to wavelet resolution level 1. Also due to the improved signal to noise ratio at higher resolution we can observe significant reduction in entropy as compared with resolution level 1. In the case of the cartilage model obtained from the MRI image we see a lower smoothness and uniformity at higher resolution as compared to lower, this is primarily due to deformity on the cartilage surface which is enhanced at higher resolution as a result of which smoothness is reduced despite improvement in cartilage resolution at higher wavelet scale. Similar changes are also observed in entropy values. Thus cartilage information at higher resolution along with image parameters at current scale together provide more reliable information of the cartilage structure that can aid in early stage diagnosis for OA. Smoothness in this study is normalized between 0 to 1. The higher the smoothness the lower the value and closer it is to zero. Hence, the phantom cartilage displays more smoothness at higher resolution. The MRI cartilage is degraded which contributes to the signal and at higher resolution indicates a more coarser structure as compared to phantom tissue. Uniformity on the other hand is normalized between 0 to 1, but a higher value closer to 1 indicates a more uniform structure as against a lower value. As a result, at higher resolution the phantom cartilage demonstrates more uniformity as compared to MRI cartilage.

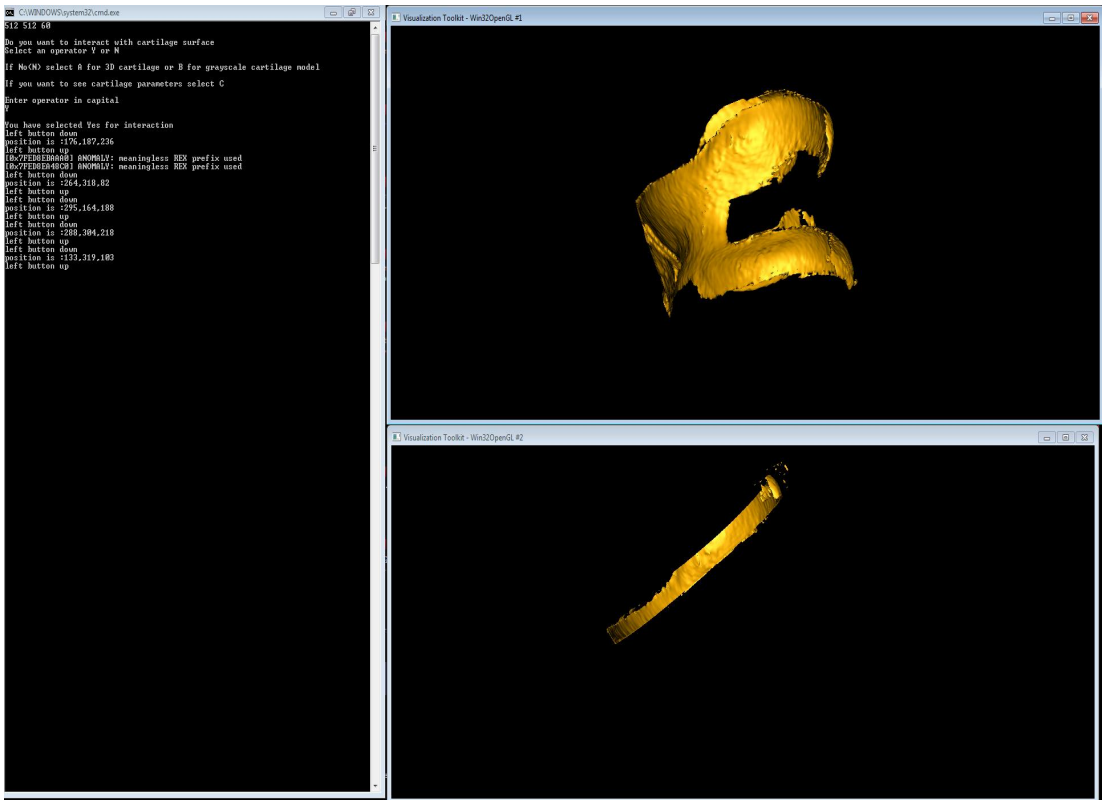

FIGURE 5.6: Software framework a) displaying 3D cartilage surface parameters, b) display of original 3D volume and c) display of sub-volume or local region of cartilage when a location is picked on the cartilage surface shown in b using the mouse pointer

Fig. (5.5) demonstrates the basic functionality of the software framework in displaying cartilage surface and computation of its surface parameters such as smoothness, entropy etc. The proposed framework also has an option to offer simultaneous visualization of 3D cartilage edge or model and its sub-volume. In Fig. (5.6) c we have displayed cartilage sub-volume obtained by selecting position on the cartilage model given in Fig. (5.6) b with help of user input via a computer mouse. As proposed, the framework enables cartilage analysis by selecting or zooming in on the cartilage surface as shown in Fig. (5.6). In addition the proposed framework enables visualization of the cartilage as a grey-scale volume as demonstrated in Fig. (5.7). Currently the multiresolution widget can automatically compute the cartilage parameters without any input by the user which can be used by the proposed grading system. This widget feature can be customized by the user depending on the requirement of their study. At the moment extension of this application is left for future work.

Fig. (5.8) demonstrates a few more UI features where the user can compute the distance between cartilage endpoints and visualize prominent edges on the cartilage surface with help of a glyph. In addition Fig. (5.9) a displays MRI dataset indicating early-intermediate OA with early changes on cartilage surface while Fig. (5.9) b displays a

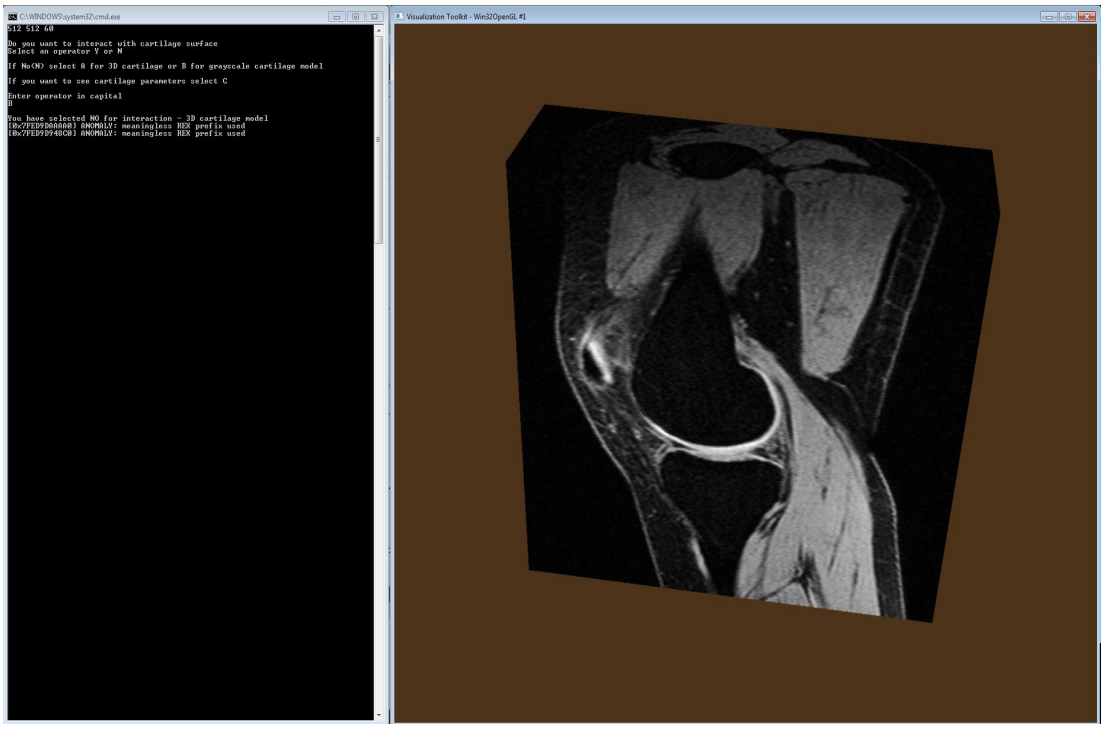

FIGURE 5.7: Software framework displaying MRI volume

TABLE 5.1: Image Parameters for cartilage computed at two wavelet resolutions

Image Parameters	Phantom cartilage		MRI cartilage	
	R1	R2	R1	R2
Volume	39274.7	43531.9	225866	227158
Smoothness	8.799e-8	6.0461e-8	8.3777e-7	9.4497e-7
Uniformity	0.97648	0.97794	0.0196	0.0097
Entropy	-0.1519	-0.1371	-6.7576	-7.3583

dataset demonstrating late OA.

5.3.3 Discussion & Future work

The main challenge that the GUI faces is computation of wavelet decomposition of more than two wavelet resolutions. Wavelet analysis is not a memory efficient operation and as such simultaneous decomposition of volume for more than two resolutions has to be backed up with increase in memory by the computer system. This also increases the visualization burden by the wavelet GUI and may increase the display time for real time visualization by the widget. In addition the widget has to be tested in different

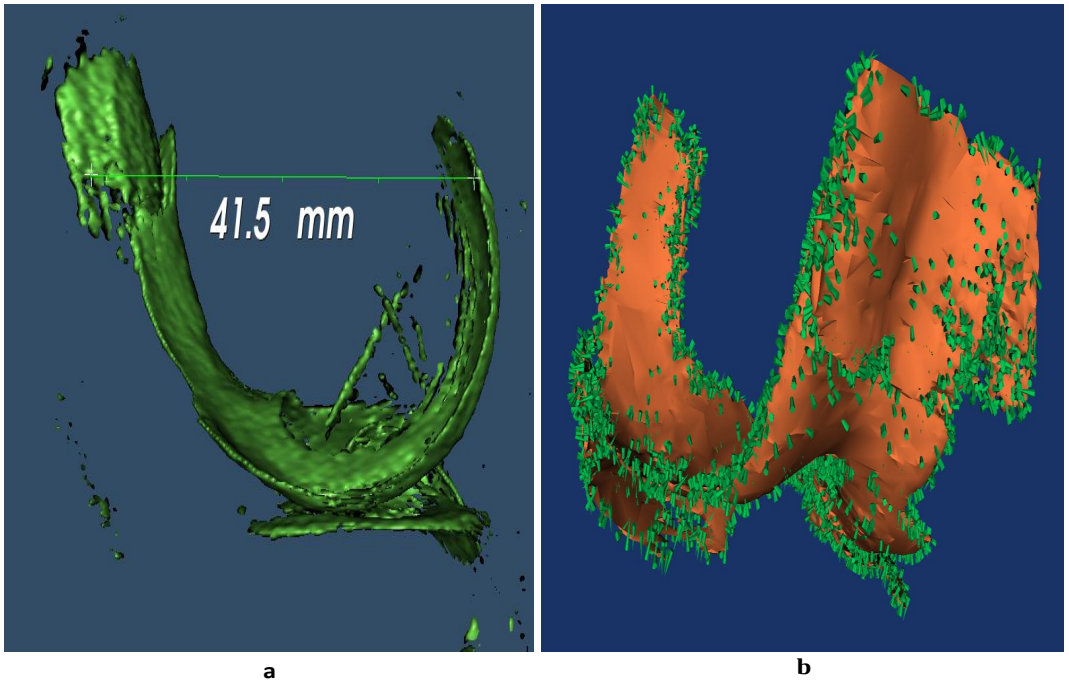

FIGURE 5.8: a) UI distance measurement for cartilage surface and b) Cartilage surface with glyphs representing edge regions

operating environments and other wavelet toolboxes.

One of the primary advantages of the wavelet GUI is its ability to display higher resolution cartilage information and simultaneous visualization of edge or other sub-volumetric information that may contribute towards visual analysis of the cartilage tissue for OA diagnosis. Future work may include assessment the reliability of these parameters as an imaging biomarker for cartilage analysis, and addition of more clinically relevant tissue properties for cartilage assessment. As the grading system and GUI has been programmed using object oriented C++ it allows modification and extensibility of the GUI. Other future work may include the adaptation of this framework to a more user friendly programming language such as Python. The proposed framework may also help in inspiring a specific protocol and parameters required for cartilage analysis and prediction with help of MRI images. And the necessity of an established guidelines for cartilage analysis using MRI. Also one may improve the functionality of GUI by including other computer vision tool-kits.

The proposed diagnostic GUI enables the user to save the 3D cartilage models at multiple resolution as VTK objects and storage of the computed diagnostic parameters, this may

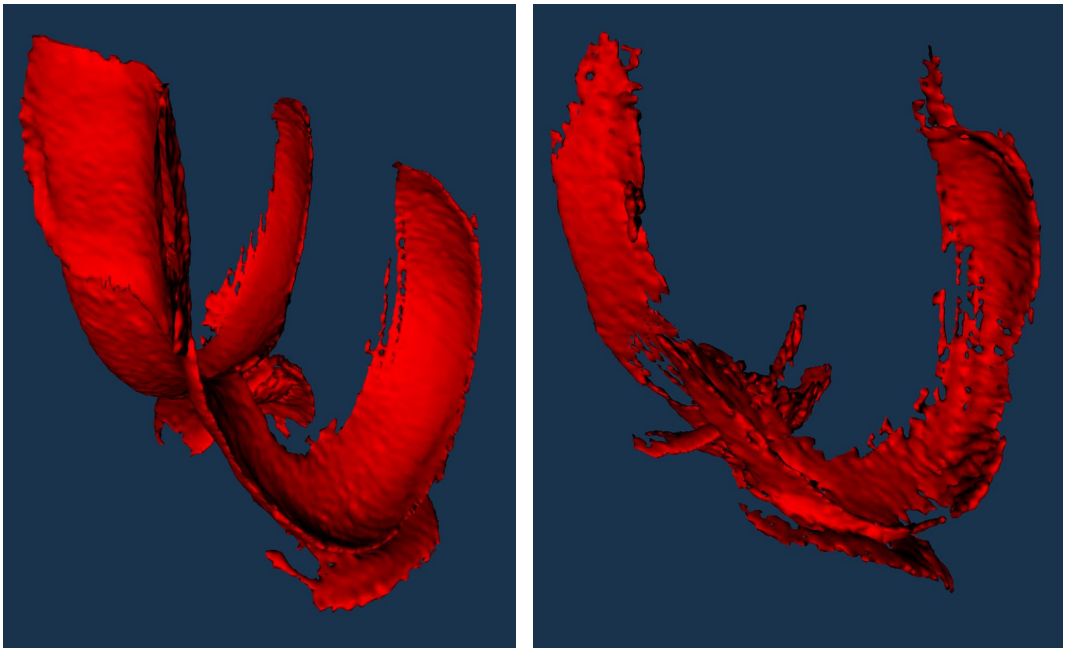

FIGURE 5.9: a) Dataset 1 representing early-intermediate OA and b) Dataset 2 representing late-intermediate OA

prove useful for intra-patient analysis for longitudinal studies and study of treatment methods.

5.4 Conclusion

We have proposed a new framework for diagnosis of articular cartilage for OA. It incorporates use of multiscale analysis of the cartilage tissue using wavelets to compute cartilage tissue parameters with respect to surfaces and surrounding joint structure. 3D models for cartilage are obtained using volume rendering with a visualization tool-kit. The 3D cartilage model is processed for multiple wavelet resolutions and the widget allows interactive visualization of the cartilage surface at these resolutions. It also offers simultaneous visualization of the cartilage edge when the user picks a specific location on the cartilage. The proposed system is able to offer a more comprehensive assessment of the cartilage tissue for different stages of OA. The widget can be extended to other image structures and may have wide applications in the field of diagnosis.

Chapter 6

Conclusion

This chapter is a summary of the research work and its findings. It highlights the contributions of this research study and discusses the challenges encountered in early stage OA analysis using MRI images. In addition it further highlights the possible directions for future work and its final conclusions.

6.1 Summary & Research findings

6.1.1 MRI Denoising

MRI signals are prone to noise and artefacts during the image acquisition process. Usually noise may not be considered as a serious drawback but in case of articular cartilage analysis; presence of noise can significantly impair the accuracy and reliability of the assessment for OA diagnosis.

The noise present in single coil magnitude MRI image is considered to be non-linear Rician noise which not only affects the image quality but also the contrast resolution of the image. Rician noise is dependent on true signal intensities and unlike white noise can affect the original contrast of the image. This may lead to inconsistencies in cartilage detection and may hamper the efficiency and reliability of cartilage analysis. In this study we focused on developing new imaging algorithms which can address this non-linearity of noise and efficiently improve the overall image quality. The study addressed Rician noise in different stages; first by developing an adaptable edge preserving denoising technique and later by analysing the nonlinear nature of noise. Initially a study on a new adaptive filtering technique with edge preserving ability was developed which offered better denoising efficiency and edge preservation as compared to other

existing methods in literature. Later the behaviour of Rician noise across the image was investigated by studying its probability distribution function which resulted in a design of non-linear filter for MRI denoising.

In study 1, we were able to develop an adaptive Rician denoising procedure with edge preserving capabilities which resulted in publication of the first journal paper as previously mentioned in chapter 2. The proposed technique was able to provide sufficient denoising with improved contrast to noise ratio (CNR). As part of the edge preservation process; the proposed denoising method worked with a circular filter which was rotated to naturally align with the edges in the image. A further verification of the null hypothesis H_0 using Brown-Forsythe (BF) test across the two independent regions of the filter was conducted to determine the presence of an edge. A nonlocal selection of weights $w_{i,j}$ depending on the direction of the edge and neighbouring pixels was used to preserve edge details. Signal estimation $A_{i,j}$ with weighted LMMSE was performed as part of the final noise removal stage. The efficiency of the proposed method was validated on both synthetic phantom and MRI images. An improvement in the overall image quality and contrast ratio was observed and further demonstrated by the SNR and CNR index ratios for the image data. The results of this study were published in the journal paper 'Adaptive Rician Denoising with edge preservation for MR images of the articular cartilage'.

Another part of this study investigated the non-linear nature of Rician noise in MRI images. A locally adaptive SNR filtering method was developed addressing this characteristic property of noise. The focus of this investigation was to utilize the regional SNR information to conduct Rician denoising. Since Rician noise demonstrated a fluctuating distribution characteristic with respect to SNR in the image, we considered adopting this feature by the proposed filter for its denoising operation. This method was validated on MRI and synthetic images and demonstrated improvement in the PSNR ratios of the image. The results of this study were published in the conference paper 'Adaptive SNR Filtering Technique for Rician Noise Denoising in MRI' for BMEiCON 2013. In addition as Rician noise is non-linear, an adaptive nonlinear homomorphic method was further developed for denoising. The objective of this study was to investigate if the dependency of noise on true signal information could be isolated to achieve efficient denoising without the requirement of determining the SNR characteristic within the image. While the study did demonstrate improvement in image quality it also demonstrated that it may not be possible to completely isolate true signal information from noise. A more complex and heuristic filtering approach may be required to perform non-linear filtering for Rician noise. The results of this study were published in the second journal paper 'Signal Dependent Rician noise denoising using nonlinear filter'.

6.1.2 3D cartilage detection

OA analysis depends on efficient cartilage detection achieved either manually or through automation. Current practices in cartilage detection include manual or supervised segmentation of the cartilage tissue. This segmentation is often carried out slice by slice on 2D image data and a final assembly of corresponding slices is used to generate a 3D cartilage model. We believe that such an approach of cartilage detection cannot completely account for the thickness and depth estimation along the third dimension (Folkesson et al., 2007). As a result we conducted a study for automated 3D cartilage detection using 3D undecimated wavelet transform.

In the initial stage of this study we carried out 3D cartilage detection that can later be used to generate 3D models of the cartilage tissue. As wavelet transform offers a much better time-space localization of an event in a signal we proposed to use this for a more sensitive cartilage detection. In addition they offer multiresolution (MRA) property which enables to increase the scale j of the signal with reduced window of the wavelet function to capture final details in the signal. For this study we have implemented a 3D Haar undecimated wavelet transform (UWT) for the edge detection process. The proposed cartilage detection method performs edge detection at a local and global wavelet scale j. Local resolution wavelet coefficients C_ψ are considered as a bi-modal distribution where an adaptive threshold t_L is computed using 3D wavelet histogram and MLE of foreground and background distribution function within a pre-determined confidence level α_1 is used to isolate the foreground coefficients from the background. The cartilage edge information is assumed to be present in these foreground wavelet coefficients due to Rician nature of distribution. To further optimize the cartilage detection process, we decompose the MRI image volume I_{vol} into further wavelet resolutions j which are then used to capture cartilage details at higher resolution. The wavelet coefficients C_ψ obtained at various resolution are retained only if they satisfy the wavelet inter-scale ratio N_s and global threshold criteria $\grave{\gamma}$. Thus the proposed method not only carries out 3D cartilage detection but also optimization of the wavelet coefficients in wavelet domain representing the cartilage edge information. Due to our proposition of 3D wavelet decomposition we are able to profile cartilage edge not only along horizontal and vertical direction but also along the diagonal edge information. This provides us with a more complete geometric information of the cartilage structure. The method has been implemented on phantom and MRI datasets of the articular cartilage. Experimental results demonstrate better cartilage detection with reduction in MSE across the MRI volumes. The proposed cartilage detection method and its results were published in our third journal article 'Automated and optimal detection of 3D articular cartilage using

un-decimated wavelets in MRI' as mentioned in chapter 3.

In a latter study, we have also conducted an investigation on the effect of Rician noise on edge localization in an MRI image. Based on our findings we have a proposed a new edge localization factor δ for step edge detection in images with signal dependent noise. Since this study was conducted primarily for MRI image with Rician noise, the edge localization factor δ implements second order moment of the Rice distribution function P. The proposed method demonstrates improvement for step edge detection as also indicated by the Pratts figure of merit (FOM) and correlation coefficient (CoC). The results of this study were published in the fourth journal paper 'Edge localisation in MRI for images with signal dependent noise'. This investigation has been carried out for 2D MRI images and was derived at a much later stage of the initially proposed 3D cartilage detection method, as a result it was not included in cartilage detection method.

6.1.3 Cartilage shape analysis

In order to achieve a more robust descriptor for the cartilage structure, this thesis has conducted a study on the cartilage shape S_C as a Riemannian manifold. As mentioned previously in section 1.1.5 of chapter 1, it is desirable to obtain a more robust descriptor for cartilage shape which may help in observing cartilage shape deformation with less dependence on inter subject variance. This descriptor may be substituted as a MRI imaging biomarker as also pointed out by other studies in literature (Eckstein et al., 2006; Folkesson et al., 2008).

In order to obtain such a robust indicator of the cartilage shape, we have proposed use of geometric shape descriptor using Riemannian metric $g_{i,j}$. For this purpose, the study considered the cartilage shape as a smooth Riemannian manifold and used it to compute the intrinsic and extrinsic Riemannian curvature metric for the cartilage tissue. Wavelet coefficients were used to compute both the intrinsic and extrinsic curvature which are also considered as the local and global curvature information of the cartilage shape. They were further used to determine the mean WH and Gaussian WG curvature values of the cartilage shape. It was proposed to use these geometric descriptors as a new framework for cartilage shape analysis. The advantage of this descriptor is that it may be able to account for variations in cartilage shape across different subjects and may help in investigating the deformation of cartilage over period of time; though this needs to be further validated over long term longitudinal studies. To obtain this descriptor one is required to compute the gradient information for the manifold. In general this task is

usually conducted by a complex process of computing gradients across individual polyhedral mesh data which is not only time consuming but also computationally expensive. To simplify this process we have proposed use of high pass filtered wavelet coefficients which are considered as a parametrized representation of the shape and wavelet function. By selecting suitable wavelet coefficients we are able to compute this Riemannian metric $g_{i,j}$ for cartilage shape S_C more quickly with lesser computations. The study has also revealed that such a strategy may be suitable for smooth manifold for any arbitrary shape but necessitates a further analysis over larger study and datasets.

6.1.4 GUI development

The final part of this study resulted in consolidation of all the imaging algorithms developed during this research project into software prototype framework for 3D cartilage analysis. The proposed prototype system also includes a new wavelet multiresolution widget for interactive visualization of cartilage surface at multiple resolutions. This CAD system is an independent and portable framework that can be installed in any windows operating system and requires Visual Studio 2010 as its compiler while all the imaging methods are available as either C++ or C# algorithms. It also integrates open-source VTK visualization tool-kit as part of this framework. In addition the CAD system can store the 3D cartilage models generated for later reference. It should be noted that this prototype software has yet to evaluated at a clinical level.

6.2 Contributions of this study

- This study has contributed towards improvement in the denoising process for MRI images in presence of signal dependent non-linear Rician noise. The proposed method 'adaptive filtering with edge preservation'; has tried to improve the overall signal content and contrast ratio of the image. This method also tries to retain vital edge information that is an essential part of the cartilage detection process. Both edge preservation and noise removal help in overall improvement of the cartilage estimation and quantification. In addition this thesis project also looks at implementing an adaptive and non-linear denoising filter to reduce the dependency of Rician noise on true signal function with the objective of reducing the overall effect of noise in the image.

- In addition this research study also proposed a new 3D automated and optimized cartilage detection process. This cartilage detection process utilizes multiresolution information obtained in the wavelet domain to detect sensitive cartilage details

that may be difficult to obtain with just 2D image slices. It also proposed a new localization factor for edge detection in MRI images with signal dependent Rician noise.

- The thesis study provided a new geometric based descriptor for cartilage shape analysis. Cartilage shape is modelled as a smooth Riemannian manifold and wavelet based gradients of this manifold are used to compute the Riemannian metric for intrinsic and extrinsic curvature computations. The curvature information is used to observe shape changes for the cartilage tissue. The motivation of developing a geometric based parameter is to offer a more robust analysis of the cartilage tissue with ability is to observe early stage modifications of cartilage curvature.

- The research study also proposed a new software prototype framework for OA analysis using MRI images. The proposed prototype software tool assembles the above mentioned new imaging algorithms for 3D analysis of articular cartilage. It enables cartilage detection and visualization with 3D un-decimated wavelets under this framework. The software tool also contains a 3D multiresolution widget using undecimated wavelets. This widget enables visualization of the cartilage surface at different wavelet resolutions thus providing us with an opportunity to observe any early stage signs of OA progression.

6.3 Future Work

Despite these improvements for 3D cartilage analysis and use of novel imaging algorithms, early stage assessment of OA still remains a challenging task and there exist several areas that need further improvement. The topics mentioned in the following subsections are some of the challenges that affect the accuracy and robustness of several medical image analysis systems for OA assessment and can be addressed in future to further improve cartilage assessment for OA.

6.3.1 Noise

The denoising capabilities of the proposed algorithms mentioned in this research study and also in literature are limited by the accuracy of estimated noise variance. MRI denoising can further be improved by offering a more accurate estimation of the Rician

noise variance. Although one has to remember that Rician noise is nonlinear and for a multi-coil systems it follows a chi-square distribution in multi-coil systems. As a result, future denoising approaches may look at a more nonlinear and optimization methods for this purpose. While a substantial improvement may be obtained using non-linear techniques, it must be noted; as also demonstrated by the study on 'Signal Dependent Rician noise denoising using nonlinear filter' that it may not be possible to completely remove the dependence of noise on signal. In addition this research study also investigated the impact of noise on edge information and carried out this investigation using step edge. It may be worth while to investigate the effect of signal dependent noise on edges other than step edge such as ramp etc.

6.3.2 Resolution

MRI imaging still suffers from under-sampling along the third direction. It is essential that this under-sampling issue may be addressed for a more accurate representation of the cartilage thickness and geometry for OA analysis. In addition cartilage structure has a very limited thickness which makes it crucial that the interpolation technique used for its 3D reconstruction and thickness estimation be appropriately addressed. If it is not properly attended to, it may cause inaccuracies in estimation of the original thickness and volume.

6.3.3 Cartilage detection

One of the major challenges of cartilage detection is that of the limited structural content of the cartilage anatomy itself. Cartilage tissue is curvilinear and shares similar contrast resolution as its surrounding joint structure and synovial fluid. In addition it has limited thickness of 1.5-3 mm for people with healthy cartilage tissue which may be substantially lesser for people with Osteoarthritis. Further additional scenarios such as joint swelling and inflammation may further contribute to difficulties in cartilage segmentation and repeatability of cartilage detection process. This anatomical constraint understandably causes increasing challenges in robust cartilage detection as compared to other soft tissues such as the brain or the liver. One may look at new cartilage detection techniques which can address these anatomical limitations to further improve the efficiency of cartilage analysis. In addition for improved cartilage detection it might be desirable to include a priori information of the cartilage geometry for a more robust segmentation.

6.3.4 OA detection framework

Due to challenges in the cartilage detection process and assessment criteria for OA grading, much focus has been restricted towards automated and efficient detection of cartilage tissue and the computation of semi-quantitative parameters such as area, thickness or volume for its grading. New studies will have to focus on the reliability of these parameters for longitudinal studies and long term clinical trials and their use in clinical grading of early stage OA. A more holistic approach of investigating the joint as a whole rather than restricting it to cartilage only for OA assessment would be more beneficial; though this would some what increase the complexity of cartilage analysis. In addition the OA assessment framework would need to be repeatable and accurate for different stages of diagnosis and cartilage degradation. A more unified analysis and cartilage grading process is required so as to obtain cohesion among research studies across different investigating groups around the world. This will enable repetition and further investigation of articular cartilage tissue over a wider and varied population group and resourceful use of data. In addition focus should move towards how cartilage tissue is affected due to OA, not only due to cartilage tissue degradation but also the subsequent changes in joint bio-mechanics and stress with resulting metabolic and physiological modifications; in order to account for the complex nature of knee joint.

6.3.5 Datasets and study

Another possibility of future work may include design of cartilage investigation protocol; at least at the clinical phase, reuse of datasets and implementation of imaging algorithms which offer reproducibility of results, more automation and faster computational efficiency. As the cartilage thins the repeatability of the diagnostic procedures throw yet another challenge towards both the researchers and clinicians alike. A comparison of inter-patient and intra-patient analysis is difficult and is vital for success at any clinical trials. A more complete understanding of the challenges in cartilage imaging and quantitative analysis is required in order to provide a more comprehensive solution.

6.4 Conclusion

This study has investigated the different challenges in medical image analysis for articular cartilage tissue of the knee using MRI images. It has tried to address some of these issues such as noise, cartilage detection and a more robust cartilage descriptor for clinical analysis of cartilage tissue.

MRI images have gained increased popularity for early stage diagnosis of OA due to possibility of imaging cartilage tissue directly with help of MRI. This enables the clinician to directly look at the cartilage tissue and look for signs of cartilage degradation. A quantitative assessment of MRI images for a more reliable and accurate estimation of OA is still at its infancy. In acknowledging the challenges and limitations of cartilage evaluation with MRI images, we have tried to address some of the possible factors that may help to reduce these inaccuracies.

As a result this thesis has focused on a more efficient denoising procedure for single coil MRI images which may be subjected to signal dependent Rician noise. While the proposed techniques may not be able to remove noise completely it has achieved in reducing noise with overall improvement in CNR and SNR ration and enhanced edge preserving capabilities. This edge preserving ability will be able to retain vital cartilage edge details that the radiologist may require in cartilage detection.

A further step involves in a 3D cartilage detection process and visualization. The study considers 3D cartilage detection as a more reliable way to observe the cartilage structure and if necessary compute imaging parameters needed for cartilage evaluation. Current practices of 2D cartilage detection suffer from loss of resolution along the depth which is often used for thickness and volume assessment. A faster and optimized cartilage detection technique is proposed for this purpose. The proposed technique implements a 3D multiresolution based cartilage detection methodology which may be more sensitive to edge details and optimizes this information in the wavelet domain. In addition it improves efficiency in cartilage detection as it does not require an a-priori information and implements directional edge information along the 3D volume. The study also tries to address edge detection in presence of Rician noise and provides with a new edge localization factor for MRI images with signal dependent noise.

The thesis has addressed the need for a more reliable indicator for cartilage tissue degradation. As a result it looks at global and local curvature information of the cartilage tissue. It proposes a new wavelet based Riemannian curvature computation for cartilage structure which may be able to account for changes in cartilage topology as the tissue deforms and degrades.

As a final stage of this project we have implemented the new imaging algorithms for MRI image analysis for OA under software prototype framework which allows individuals to carry out image analysis for knee MRI. The software prototype also consists of a novel

wavelet multiresolution GUI that allows the user to visualize cartilage surface and subvolume at different wavelet resolutions for a closer inspection of the cartilage surface to observe signs of early stage degradation.

We hope that these techniques will help in improving MRI image analysis of knee cartilage and improve the accuracy of cartilage evaluation with imaging parameters.

Appendix A

Rayleigh Intensity Interval Estimation

To compute confidence limits for Rayleigh distribution with N independent observations, we use the unbiased estimator for variance of the distribution. Where $\hat{\sigma}$ is an unbiased estimator for Rayleigh distribution for σ^2 (Siddiqui, 1964). To computed confidence interval for unknown mean μ for confidence level α for Rayleigh distribution, we assume the distribution to be sampled with respect to normal distribution. The ratio of unknown mean with respect to sample mean follows student's t-distribution and the probability of confidence limits is given as,

$$-t_{1-\alpha/2} \leq \frac{\mu_r - \mu}{S/\sqrt{N}} \leq t_{1-\alpha/2} \tag{A.1}$$

$$\mu_r - t_{1-\alpha/2}\frac{S}{\sqrt{N}} \leq \mu \leq \mu_r + t_{1-\alpha/2}\frac{S}{\sqrt{N}} \tag{A.2}$$

where sample mean μ_r is obtained with unbiased estimator $\hat{\sigma}$.

MLE of $\hat{\sigma}^2$ is unbiased estimator and is obtained using probability distribution for Rayleigh distribution is given as (Siddiqui, 1964; Canavos, 1984),

$$P(x|\mu,\sigma) = \frac{x}{\sigma^2}e^{-\frac{(x)^2}{2\sigma^2}} \tag{A.3}$$

where P is the probability function, μ is the mean of the distribution, σ is the variance of the distribution and x is an independent random variable. For N independent sample the likelihood equation for the distribution is given as (Siddiqui, 1964),

$$L(P) = \prod_{i}^{N} [\frac{x}{\sigma^2} e^{-\frac{(x)^2}{2\sigma^2}}] = (\frac{x}{\sigma^2})^N \prod_{i}^{N} e^{-\frac{(x)^2}{2\sigma^2}} \tag{A.4}$$

To obtain a maximum likelihood for the distribution for unknown variance, taking partial derivative with respect to σ^2 of the log-likelihood equation, but for simplicity replacing σ^2 with q

$$\begin{aligned} \frac{\partial}{\partial q}(lnL) &= \frac{-n}{q} - [\sum_{i=1}^{N} x_i^2 - \frac{1}{2q^2}] \\ &= \frac{-n}{q} + \frac{1}{2q^2} \sum_{i=1}^{N} x_i^2 \end{aligned} \tag{A.5}$$

$$\sigma^2 = q = \frac{1}{2N} \sum_{i=1}^{N} x_i^2 \tag{A.6}$$

Is the MLE for Rayleigh distribution with respect to variance.

$$\hat{\sigma^2} = \frac{1}{2N} \sum_{i=1}^{N} x_i^2 \tag{A.7}$$

Rayleigh mean computed using this estimate is given as,

$$\mu_r = \hat{\sigma} \sqrt{\frac{\pi}{2}} \tag{A.8}$$

To compute confidence limits using this estimator, rearranging the terms in the above equation

$$\mu_r \pm t_{1-\alpha/2} (\frac{S}{\sqrt{N}}) \tag{A.9}$$

where $t_{1-\alpha/2}$ can be obtained from the t-distribution table under given confidence level α for $N-1$ degrees of freedom. S is the rayleigh variance estimated from the sample.

Appendix B

Gaussian Intensity Interval Estimation

To compute confidence interval for Gaussian distribution with N independent observations for unknown mean we use sampling for the given distribution from the normal distribution. The sampling distribution follows a t-distribution with $N-1$ degree of freedom and is given as follows (Canavos, 1984),

$$T = \frac{\hat{X} - \mu}{S/\sqrt{N}} \tag{B.1}$$

To compute the confidence limits for μ with confidence coefficient $(1-\alpha)$ we determine the $t_{(1-\alpha/2),(N-1)}$ value from the t-table with respect to $N-1$ degree of freedom as follows (Canavos, 1984),

$$Pr(T \leq -t_{1-\alpha/2}) = \frac{\alpha}{2} \tag{B.2}$$

$$Pr(T \leq t_{1-\alpha/2}) = 1 - \frac{\alpha}{2} \tag{B.3}$$

The confidence limit is given as follows (Canavos, 1984),

$$-t_{1-\alpha/2} \leq \frac{\hat{X} - \mu}{S/\sqrt{N}} \leq t_{1-\alpha/2} \tag{B.4}$$

$$-t_{1-\alpha/2}(\frac{S}{\sqrt{N}}) \leq \hat{X} - \mu \leq t_{1-\alpha/2}\frac{S}{\sqrt{N}} \tag{B.5}$$

$$-\hat{X} - t_{1-\alpha/2}(\frac{S}{\sqrt{N}}) \leq -\mu \leq -\hat{X} + t_{1-\alpha/2}\frac{S}{\sqrt{N}} \tag{B.6}$$

$$\hat{X} - t_{1-\alpha/2}(\frac{S}{\sqrt{N}}) \leq \mu \leq -\hat{X} + t_{1-\alpha/2}\frac{S}{\sqrt{N}} \tag{B.7}$$

where $\hat{X}$ is also the same as the MLE for Gaussian distribution. Probability distribution for Gaussian distribution is given as (Canavos, 1984),

$$P(x|\mu,\sigma) = \frac{1}{\sqrt{2\pi\sigma^2}}e(-\frac{x-\mu}{2\sigma^2}) \tag{B.8}$$

where P is the probability function, μ is the mean of the distribution, variance of the distribution is given as σ^2 and where x is the variable of the distribution. The likelihood equation for the probability distribution with N independent samples is given as follows (Myung, 2003),

$$L(P) = \prod_{i=1}^{N}[\frac{1}{\sqrt{2\pi\sigma^2}}e(-\frac{x_i-\mu}{2\sigma^2})] \tag{B.9}$$

The maximum likelihood estimation of the above equation with respect to mean is given as follows (Myung, 2003),

$$\frac{\partial}{\partial\mu}(lnL) = -\frac{1}{2\sigma^2}\frac{\partial}{\partial\mu}\sum_{i=1}^{N}(x_i-\mu)^2 \quad = \quad \frac{1}{\sigma^2}\sum_{i=1}^{N}(x_i-\mu)$$

Equating the above equation to zero, we get as follows,

$$\frac{1}{\sigma^2}\sum_{i=1}^{N}(x_i-\mu) = 0 \tag{B.10}$$

$$\mu = \frac{1}{N}\sum_{i=1}^{N}x_i \tag{B.11}$$

Appendix C

Wavelet Interscale Difference

Wavelet coefficients are obtained by convolution of high pass filter on 2D image function $I(x, y)$ (Gonzalez et al., 2004)

$$w_j = \frac{1}{\sqrt{MN}} \sum_{x=0}^{M-1} \sum_{y=0}^{N-1} I(x, y) * \psi^i_{j,m,n}(x, y), i = \{H, V, D\} \tag{C.1}$$

But image function $I(x, y)$ follows a Rice probability distribution function given as (Gudbjartsson and Patz, 2005)

$$P(I|A, \sigma) = \frac{I}{\sigma^2} exp(-\frac{I^2 + A^2}{2\sigma^2}) I_0 \frac{IA}{\sigma^2} \tag{C.2}$$

where I_0 is zero order bessel function and not to be confused with observed image function I and A is true image intensity function in absence of noise.

Thus wavelet coefficients obtained from the image are assumed to have a Rice distribution function, given as

$$P(w_j|I, \sigma) = \frac{w_j}{\sigma^2} exp(-\frac{w_j^2 + A^2}{2\sigma^2}) I_0 \frac{w_j A}{\sigma^2} \tag{C.3}$$

We know in wavelet domain the modulus of sum of wavelet coefficients can be given as (Lun et al., 2002),

$$N_j I(x_0) = \acute{A} s^{\alpha+1} \approx P(w_j|I, \sigma) \tag{C.4}$$

Ideally the interscale difference between wavelet coefficients at two scale is given as,

$$N_{j+1}I(x_0) - N_jI(x_0) = \gamma \tag{C.5}$$

But since the wavelet coefficeints are governed by Rice probability distribution, the interscale difference is no longer a function of γ alone. Instead interscale difference can now be given as,

$$\begin{aligned}\gamma = \frac{1}{\sigma^2}[w_{j+1}exp(-\frac{w_{j+1}^2 + A^2}{2\sigma^2})I_0\frac{w_{j+1}A}{\sigma^2} - \\ w_jexp(-\frac{w_j^2 + A^2}{2\sigma^2})I_0\frac{w_jA}{\sigma^2}]\end{aligned} \tag{C.6}$$

$$\begin{aligned}\hat{\gamma} = \gamma\sigma^2 = [w_{j+1}exp(-\frac{w_{j+1}^2 + A^2}{2\sigma^2})I_0\frac{w_{j+1}A}{\sigma^2} - \\ w_jexp(-\frac{w_j^2 + A^2}{2\sigma^2})I_0\frac{w_jA}{\sigma^2}]\end{aligned} \tag{C.7}$$

Bibliography

[1] David J Hunter. Pharmacologic therapy for osteoarthritisthe era of disease modification. *Nature Reviews Rheumatology*, 7(1):13–22, 2011.

[2] Andrew I Spitzer. Viscosupplementation for osteoarthritis of the knee - stategies to improve patient outcomes. URL http://www.medscape.org/viewarticle/581343.

[3] Matt Driscoll. X-ray joint space width. URL http://www.mattdriscollmd.com/kneearthritis/.

[4] Johannes WJ Bijlsma, Francis Berenbaum, and Floris PJG Lafeber. Osteoarthritis: an update with relevance for clinical practice. *The Lancet*, 377(9783):2115–2126, 2011.

[5] Hakon Gudbjartsson and Samuel Patz. The rician distribution of noisy mri data. *Magnetic Resonance in Medicine*, 34(6):910–914, 2005.

[6] Stephane Mallat and Sifen Zhong. Characterization of signals from multiscale edges. *IEEE Transactions on pattern analysis and machine intelligence*, 14(7): 710–732, 1992.

[7] Stephane Mallat and Wen Liang Hwang. Singularity detection and processing with wavelets. *Information Theory, IEEE Transactions on*, 38(2):617–643, 1992.

[8] Rafael C Gonzalez, Richard E Woods, and Steven L Eddins. Digital image using matlab processing. *Person Prentice Hall*, pages 183–193, 2004.

[9] Alexander M Bronstein, Michael M Bronstein, and Ron Kimmel. Three-dimensional face recognition. *International Journal of Computer Vision*, 64(1): 5–30, 2005.

[10] Robert Theiler, Peter Ghosh, and Peter Brooks. Clinical, biochemical and imaging methods of assessing osteoarthritis and clinical trials with agents claiming chondromodulatingactivity. *Osteoarthritis and Cartilage*, 2(1):1–23, 1994.

[11] Tonia L. Vincent and Fiona E. Watt. Osteoarthritis. *Medicine*, 38(3):151–156, 2010.

[12] Elsternwick. A problem worth solving. *Arthritis and Osteoporosis*, pages 1–72, 2013.

[13] Mark E Adams and Carla J Wallace. Quantitative imaging of osteoarthritis. In *Seminars in arthritis and rheumatism*, volume 20, pages 26–39. Elsevier, 1991.

[14] D. Kumar, A. F M Hani, A.S. Malik, R. Kamil, R. Razak, and A. Kiflie. Development of a non-invasive diagnostic tool for early detection of knee osteoarhritis. In *National Postgraduate Conference (NPC), 2011*, pages 1–6, 2011. doi: 10.1109/NatPC.2011.6136338.

[15] Michel D Crema, Frank W Roemer, Monica D Marra, Deborah Burstein, Garry E Gold, Felix Eckstein, Thomas Baum, Timothy J Mosher, John A Carrino, and Ali Guermazi. Articular cartilage in the knee: current mr imaging techniques and applications in clinical practice and research. *Radiographics*, 31(1):37–61, 2011.

[16] Robert Theiler, Peter Ghosh, and Peter Brooks. Clinical, biochemical and imaging methods of assessing osteoarthritis and clinical trials with agents claiming chondromodulating activity. *Osteoarthritis and Cartilage*, 2(1):1–23, 1994.

[17] Changhai Ding, Flavia Cicuttini, and Graeme Jones. How important is mri for detecting early osteoarthritis? *Nature Clinical Practice Rheumatology*, 4(1):4–5, 2007.

[18] Felix Eckstein, Deborah Burstein, and Thomas M Link. Quantitative mri of cartilage and bone: degenerative changes in osteoarthritis. *NMR in Biomedicine*, 19 (7):822–854, 2006.

[19] Garry E Gold, Christina A Chen, Seungbum Koo, Brian A Hargreaves, and Neal K Bangerter. Recent advances in mri of articular cartilage. *AJR. American journal of roentgenology*, 193(3):628, 2009.

[20] Ali Guermazi, Frank W Roemer, Deborah Burstein, and Daichi Hayashi. Why radiography should no longer be considered a surrogate outcome measure for longitudinal assessment of cartilage in knee osteoarthritis. *Arthritis Res Ther*, 13(6): 247, 2011.

[21] DJ Hunter, W Zhang, PG Conaghan, K Hirko, L Menashe, WM Reichmann, and E Losina. Responsiveness and reliability of mri in knee osteoarthritis: a meta-analysis of published evidence. *Osteoarthritis and Cartilage*, 19(5):589–605, 2011.

[22] David J Hunter, Grace H Lo, D Gale, Andrew J Grainger, Ali Guermazi, and Philip G Conaghan. The reliability of a new scoring system for knee osteoarthritis mri and the validity of bone marrow lesion assessment: Bloks (boston–leeds osteoarthritis knee score). *Annals of the rheumatic diseases*, 67(2):206–211, 2008.

[23] Jan Sijbers, AJ Den Dekker, Johan Van Audekerke, Marleen Verhoye, and Dirk Van Dyck. Estimation of the noise in magnitude mr images. *Magnetic Resonance Imaging*, 16(1):87–90, 1998.

[24] Dzung L Pham, Chenyang Xu, and Jerry L Prince. Current methods in medical image segmentation 1. *Annual review of biomedical engineering*, 2(1):315–337, 2000.

[25] Jenny Folkesson, Erik B Dam, Ole Fogh Olsen, Paola C Pettersen, and Claus Christiansen. Segmenting articular cartilage automatically using a voxel classification approach. *Medical Imaging, IEEE Transactions on*, 26(1):106–115, 2007.

[26] Jenny Folkesson, Erik B Dam, Ole F Olsen, Morten A Karsdal, Paola C Pettersen, and Claus Christiansen. Automatic quantification of local and global articular cartilage surface curvature: biomarkers for osteoarthritis? *Magnetic resonance in medicine*, 59(6):1340–1346, 2008.

[27] Sudhakar Tummala and Erik B Dam. Surface smoothness: cartilage biomarkers for knee oa beyond the radiologist. In *SPIE Medical Imaging*, pages 762323–762323. International Society for Optics and Photonics, 2010.

[28] Isshaa Aarya, Danchi Jiang, and Timothy Gale. Adaptive rician denoising with edge preservation for mr images of the articular cartilage. *Computer Methods in Biomechanics and Biomedical Engineering: Imaging & Visualization*, pages 1–10, 2014.

[29] Isshaa Aarya, Dai Jiang, and Timothy Gale. Adaptive snr filtering technique for rician noise denoising in mri. In *Biomedical Engineering International Conference (BMEiCON), 2013 6th*, pages 1–5. IEEE, 2013.

[30] Isshaa Aarya, Danchi Jiang, and Timothy Gale. Signal dependent rician noise denoising using nonlinear filter. *Lecture Notes on Software Engineering*, 1(4):344, 2013.

[31] F. Eckstein, F. Cicuttini, J. P. Raynauld, J. C. Waterton, and C. Peterfy. Magnetic resonance imaging (mri) of articular cartilage in knee osteoarthritis (oa): morphological assessment. *Osteoarthritis and Cartilage*, 14, Supplement 1(0):46–75, 2006.

[32] P. Cashman, R. I. Kitney, M. A. Gariba, and M. E. Carter. Automated techniques for visualization and mapping of articular cartilage in mr images of the osteoarthritic knee: a base technique for the assessment of microdamage and submicro damage. *NanoBioscience, IEEE Transactions on*, 1(1):42–51, 2002.

[33] Jeny Rajan, Jelle Veraart, Johan Van Audekerke, Marleen Verhoye, and Jan Sijbers. Nonlocal maximum likelihood estimation method for denoising multiple-coil magnetic resonance images. *Magnetic Resonance Imaging*, 30:1512–1518, 2012.

[34] J. Rajan, J. Van Audekerke, A. Van der Linden, M. Verhoye, and J. Sijbers. An adaptive non local maximum likelihood estimation method for denoising magnetic resonance images. In *Biomedical Imaging (ISBI), 2012 9th IEEE International Symposium on*, pages 1136–1139, 2012.

[35] Robert D Nowak. Wavelet-based rician noise removal for magnetic resonance imaging. *Image Processing, IEEE Transactions on*, 8(10):1408–1419, 1999.

[36] Jan Sijbers, Arnold J Den Dekker, Paul Scheunders, and Dirk Van Dyck. Maximum-likelihood estimation of rician distribution parameters. *Medical Imaging, IEEE Transactions on*, 17(3):357–361, 1998.

[37] Hoang Vinh Tran and Danchi Jiang. Articular cartilage segmentation in noisy mr images of human knee. In *Biomedical Engineering Conference (CIBEC), 2012 Cairo International*, pages 146–149, 2012.

[38] Antoni Buades, Bartomeu Coll, and J-M Morel. A non-local algorithm for image denoising. In *Computer Vision and Pattern Recognition, 2005. CVPR 2005. IEEE Computer Society Conference on*, volume 2, pages 60–65. IEEE, 2005.

[39] P. Perona and J. Malik. Scale-space and edge detection using anisotropic diffusion. *Pattern Analysis and Machine Intelligence, IEEE Transactions on*, 12(7):629–639, 1990.

[40] Karl Krissian and Santiago Aja-Fernandez. Noise-driven anisotropic diffusion filtering of mri. *Image Processing, IEEE Transactions on*, 18(10):2265–2274, 2009.

[41] S. Aja-Fernandez, C. Alberola-Lopez, and C. F. Westin. Noise and signal estimation in magnitude mri and rician distributed images: A lmmse approach. *Image Processing, IEEE Transactions on*, 17(8):1383–1398, 2008.

[42] P. Coupe, J. V. Manjon, E. Gedamu, D. Arnold, M. Robles, and D. L. Collins. Object-based rician noise estimation for mr images. *NeuroImage*, 47, Supplement 1(0):S81, 2009.

[43] Dimitri Van De Ville and Michel Kocher. Sure-based non-local means. *Signal Processing Letters, IEEE*, 16(11):973–976, 2009.

[44] L. Lauwers, K. Barbe, W. Van Moer, and R. Pintelon. Estimating the parameters of a rice distribution: A bayesian approach. In *Instrumentation and Measurement Technology Conference, 2009. I2MTC '09. IEEE*, pages 114–117, 2009.

[45] Leonid I Rudin, Stanley Osher, and Emad Fatemi. Nonlinear total variation based noise removal algorithms. *Physica D: Nonlinear Phenomena*, 60(1):259–268, 1992.

[46] V. N. Varghees, M. S. Manikandan, and R. Gini. Adaptive mri image denoising using total-variation and local noise estimation. In *Advances in Engineering, Science and Management (ICAESM), 2012 International Conference on*, pages 506–511, 2012.

[47] Jan Sijbers and AJ Den Dekker. Maximum likelihood estimation of signal amplitude and noise variance from mr data. *Magnetic Resonance in Medicine*, 51(3): 586–594, 2004.

[48] Cheng Guan Koay and Peter J. Basser. Analytically exact correction scheme for signal extraction from noisy magnitude mr signals. *Journal of Magnetic Resonance*, 179(2):317–322, 2006.

[49] Lei Jiang and Wenhui Yang. Adaptive magnetic resonance image denoising using mixture model and wavelet shrinkage. *Proc. VIIth Digital Image Comput.: Tech. Appl*, pages 831–838, 2003.

[50] Pierrick Coupe, Jose V Manjon, Montserrat Robles, and D Louis Collins. Adaptive multiresolution non-local means filter for three-dimensional magnetic resonance image denoising. *IET image processing*, 6(5):558–568, 2012.

[51] Karel Bartušek, Jiří Přinosil, and Zdeněk Smékal. Wavelet-based de-noising techniques in mri. *Computer methods and programs in biomedicine*, 104(3):480–488, 2011.

[52] Mehdi Nasri and Hossein Nezamabadi-pour. Image denoising in the wavelet domain using a new adaptive thresholding function. *Neurocomputing*, 72(4):1012–1025, 2009.

[53] Yeqiu Li, Jianming Lu, Ling Wang, and Takakshi Yahagi. Removal of gaussian noise from degraded images in wavelet domain. *Electronics and Communications in Japan*, 91(1):11–18, 2008.

[54] ER Davies. Circularitya new principle underlying the design of accurate edge orientation operators. *Image and Vision Computing*, 2(3):134–142, 1984.

[55] Zhou Dongxiang, Liu Yun-Hui, and Cai Xuanping. An efficient and robust corner detection algorithm. In *Intelligent Control and Automation, 2004. WCICA 2004. Fifth World Congress on*, volume 5, pages 4020–4024 Vol.5, 2004.

[56] L. Liu, D. Zhang, and J. You. Detecting wide lines using isotropic nonlinear filtering. *Image Processing, IEEE Transactions on*, 16(6):1584–1595, 2007.

[57] Morton B Brown and Alan B Forsythe. Robust tests for the equality of variances. *Journal of the American Statistical Association*, 69(346):364–367, 1974.

[58] Jose Vicente Manjon-Herra. Non-local means filter. Mathworks-Matlab central, November 2006. URL http://www.mathworks.com.au/matlabcentral/fileexchange/13176-non-local-means-filter.

[59] Santiago Aja-Fernandez. Lmmse filter for rician mri data. Mathworks-Matlab Central, May 2012. URL http://www.mathworks.com.au/matlabcentral/fileexchange/36741-lmmse-filter-for-rician-mri-data.

[60] Douglas C. Montgomery and George C. Runger. *Applied Statistics and Probability for Engineers*. John Wiley and Sons, third edition, 2006.

[61] Coupe P., Manjo J. V., M. Robles, and D. L. Collins. Adaptive multiresolution non-local means filter for three-dimensional magnetic resonance image denoising. *Image Processing, IET*, 6(5):558–568, 2012.

[62] Ezequiel Lopez-Rubio and Mara Nieves Florentin-Nunez. Kernel regression based feature extraction for 3d mr image denoising. *Medical Image Analysis*, 15(4): 498–513, 2011.

[63] Alain Hore and Djemel Ziou. Image quality metrics: Psnr vs. ssim. In *Pattern Recognition (ICPR), 2010 20th International Conference on*, pages 2366–2369. IEEE, 2010.

[64] Santiago Aja-Fernandez, Raul San Jose Estepar, Carlos Alberola-Lopez, and C-F Westin. Image quality assessment based on local variance. In *Engineering in Medicine and Biology Society, 2006. EMBS'06. 28th Annual International Conference of the IEEE*, pages 4815–4818. IEEE, 2006.

[65] Tuncer C Aysal and Kenneth E Barner. Rayleigh-maximum-likelihood filtering for speckle reduction of ultrasound images. *Medical Imaging, IEEE Transactions on*, 26(5):712–727, 2007.

[66] Lin Yin, Ruikang Yang, Moncef Gabbouj, and Yrjö Neuvo. Weighted median filters: a tutorial. *Circuits and Systems II: Analog and Digital Signal Processing, IEEE Transactions on*, 43(3):157–192, 1996.

[67] Henri H Arsenault and M Denis. Image processing in signal-dependent noise. *Canadian Journal of Physics*, 61(2):309–317, 1983.

[68] Ioannis Pitas and Anastasios N Venetsanopoulos. Nonlinear mean filters in image processing. *Acoustics, Speech and Signal Processing, IEEE Transactions on*, 34 (3):573–584, 1986.

[69] Zhou Wang, Alan C Bovik, Hamid Rahim Sheikh, and Eero P Simoncelli. Image quality assessment: From error visibility to structural similarity. *Image Processing, IEEE Transactions on*, 13(4):600–612, 2004.

[70] John F Walkup and Robert C Choens. Image processing in signal-dependent noise. *Optical Engineering*, 13(3):133258–133258, 1974.

[71] Saeed V Vaseghi. *Advanced digital signal processing and noise reduction*. John Wiley & Sons, 2008.

[72] Jae S Lim. Two-dimensional signal and image processing. *Englewood Cliffs, NJ, Prentice Hall, 1990, 710 p.*, 1, 1990.

[73] Mark R Banham and Aggelos K Katsaggelos. Digital image restoration. *Signal Processing Magazine, IEEE*, 14(2):24–41, 1997.

[74] Maroua Mehri, Petra Gomez-Krämer, Pierre Héroux, and Rémy Mullot. Old document image segmentation using the autocorrelation function and multiresolution analysis. In *IS&T/SPIE Electronic Imaging*, pages 86580K–86580K. International Society for Optics and Photonics, 2013.

[75] Isshaa Aarya and Danchi Jiang. Automated and optimal detection of 3d articular cartilage using undecimated wavelets in mri. *Signal, Image and Video Processing*, 9(1):305–314, 2015.

[76] I Aarya, D Jiang, and T Gale. Edge localisation in mri for images with signal-dependent noise. *Electronics Letters*, 51(15):1151–1153, 2015.

[77] RJE Merry and M Steinbuch. Wavelet theory and applications. *Literature Study, Eindhoven University of Technology, Department of Mechanical Engineering, Control Systems Technology Group*, 2005.

[78] Metin Akay. Wavelets in biomedical engineering. *Annals of biomedical Engineering*, 23(5):531–542, 1995.

[79] J-L Starck, Jalal Fadili, and Fionn Murtagh. The undecimated wavelet decomposition and its reconstruction. *Image Processing, IEEE Transactions on*, 16(2): 297–309, 2007.

[80] Ioana Adam and Emanuel Rădoi. *Complex Wavelet Transform: application to denoising.* Editura Politehnică, 2010.

[81] C Sidney Burrus, Ramesh A Gopinath, Haitao Guo, Jan E Odegard, and Ivan W Selesnick. *Introduction to wavelets and wavelet transforms: a primer*, volume 23. Prentice hall New Jersey, 1998.

[82] John Canny. A computational approach to edge detection. *Pattern Analysis and Machine Intelligence, IEEE Transactions on*, PAMI-8(6):679–698, 1986.

[83] Flavia M Cicuttini, Andrew Forbes, Wang Yuanyuan, Glen Rush, and Stephen L Stuckey. Rate of knee cartilage loss after partial meniscectomy. *The Journal of rheumatology*, 29(9):1954–1956, 2002.

[84] Stuart Solloway, Charles E Hutchinson, John C Waterton, and Christopher J Taylor. The use of active shape models for making thickness measurements of articular cartilage from mr images. *Magnetic Resonance in Medicine*, 37(6):943–952, 1997.

[85] Tina Kapur, P Beardsley, S Gibson, W Grimson, and W Wells. Model-based segmentation of clinical knee mri. In *Proc. IEEE Intl Workshop on Model-Based 3D Image Analysis*, pages 97–106. Citeseer, 1998.

[86] Enrico Hinrichs, Ben Appleton, Brian C Lovell, and Graham John Galloway. Autonomous direct 3d segmentation of articular knee cartilage. In *Australian and New Zealand Intelligent Information Systems*, volume 1, pages 417–420. Queensland University of Technology, 2003.

[87] Michael Kass, Andrew Witkin, and Demetri Terzopoulos. Snakes: Active contour models. *International journal of computer vision*, 1(4):321–331, 1988.

[88] Tobias Heimann and Hans-Peter Meinzer. Statistical shape models for 3d medical image segmentation: A review. *Medical image analysis*, 13(4):543–563, 2009.

[89] Jurgen Fripp, Sebastien Ourselin, Simon Warfield, Andrea Mewes, and Stuart Crozier. Automatic generation of 3d statistical shape models of the knee bones. In *APRS Workshop on Digital Image Computing*, pages 15–21, 2005.

[90] Mark A Baldwin, Joseph E Langenderfer, Paul J Rullkoetter, and Peter J Laz. Development of subject-specific and statistical shape models of the knee using an efficient segmentation and mesh-morphing approach. *computer methods and programs in biomedicine*, 97(3):232–240, 2010.

[91] Jurgen Fripp, Stuart Crozier, Simon K Warfield, and Sébastien Ourselin. Automatic segmentation and quantitative analysis of the articular cartilages from magnetic resonance images of the knee. *Medical Imaging, IEEE Transactions on*, 29(1):55–64, 2010.

[92] Adhish Prasoon, Kersten Petersen, Christian Igel, François Lauze, Erik Dam, and Mads Nielsen. Deep feature learning for knee cartilage segmentation using a triplanar convolutional neural network. In *Medical Image Computing and Computer-Assisted Intervention–MICCAI 2013*, pages 246–253. Springer, 2013.

[93] Kunlei Zhang, Wenmiao Lu, and Pina Marziliano. Automatic knee cartilage segmentation from multi-contrast mr images using support vector machine classification with spatial dependencies. *Magnetic resonance imaging*, 31(10):1731–1743, 2013.

[94] Jose G Tamez-Pena, Joshua Farber, Patricia C Gonzalez, Edward Schreyer, Erika Schneider, and Saara Totterman. Unsupervised segmentation and quantification of anatomical knee features: data from the osteoarthritis initiative. *Biomedical Engineering, IEEE Transactions on*, 59(4):1177–1186, 2012.

[95] Kenneth L Urish, Ashley A Williams, John R Durkin, Constance R Chu, et al. Registration of magnetic resonance image series for knee articular cartilage analysis data from the osteoarthritis initiative. *Cartilage*, 4(1):20–27, 2013.

[96] Daniel J Withey, Witold Pedrycz, and Zoltan J Koles. Dynamic edge tracing: Boundary identification in medical images. *Computer Vision and Image Understanding*, 113(10):1039–1052, 2009.

[97] Delphine Nain, Steven Haker, Aaron Bobick, and Allen Tannenbaum. Multiscale 3-d shape representation and segmentation using spherical wavelets. *Medical Imaging, IEEE Transactions on*, 26(4):598–618, 2007.

[98] Luis Pastor, Angel Rodrıguez, J Miguel Espadero, and Luis Rincón. 3d wavelet-based multiresolution object representation. *Pattern Recognition*, 34(12):2497–2513, 2001.

[99] Yin Yin, Xiangmin Zhang, Rachel Williams, Xiaodong Wu, Donald D Anderson, and Milan Sonka. Logismoslayered optimal graph image segmentation of multiple objects and surfaces: cartilage segmentation in the knee joint. *Medical Imaging, IEEE Transactions on*, 29(12):2023–2037, 2010.

[100] Michael Unser and Murray Eden. Multiresolution feature extraction and selection for texture segmentation. *Pattern Analysis and Machine Intelligence, IEEE Transactions on*, 11(7):717–728, 1989.

[101] Chang Ku-Yaw, Chen Shao-Jer, Chen Lih-Shyang, and Wu Cheng-Jung. Articular cartilage segmentation based on radial transformation. In *Hybrid Intelligent Systems, 2009. HIS '09. Ninth International Conference on*, volume 1, pages 239–242, 2009.

[102] Tang Jinshan, S. Millington, S. T. Acton, J. Crandall, and S. Hurwitz. Surface extraction and thickness measurement of the articular cartilage from mr images using directional gradient vector flow snakes. *Biomedical Engineering, IEEE Transactions on*, 53(5):896–907, 2006.

[103] MM Siddiqui. Statistical inference for rayleigh distributions. *Journal of Research of the National Bureau of Standards, Sec. D*, 68, 1964.

[104] George C Canavos. *Applied Probability and Statistical Methods*. Little, Brown Boston, 1984.

[105] Catherine Forbes, Merran Evans, Nicholas Hastings, and Brian Peacock. *Statistical distributions*. John Wiley & Sons, 2011.

[106] Wikipedia. Linear interpolation. URL https://en.wikipedia.org/wiki/Linear_interpolation.

[107] Daniel Pak-kong Lun, Tai-chiu Hsung, and Yuk-fan Ho. Wavelet singularity detection for image processing. In *Circuits and Systems, 2002. MWSCAS-2002. The 2002 45th Midwest Symposium on*, volume 2, pages II–156. IEEE, 2002.

[108] MathWorks. Matlab r2013b. URL http://au.mathworks.com/products/newproducts/release2013b.html.

[109] Will J Schroeder, Bill Lorensen, and Ken Martin. *The visualization toolkit*. Kitware, 2004.

[110] Shigeru Muraki. Multiscale volume representation by a dog wavelet. *Visualization and Computer Graphics, IEEE Transactions on*, 1(2):109–116, 1995.

[111] John Canny. A computational approach to edge detection. *Pattern Analysis and Machine Intelligence, IEEE Transactions on*, (6):679–698, 1986.

[112] Ali Ranjbaran, Anwar Hasni Abu Hassan, Eng Swee Kheng, and Bahar Ranjbaran. An edge detection based noise removal algorithm. *Computers & Electrical Engineering*, 40(3):769–784, 2014.

[113] M Ait Oussous, N Alaa, and Y Ait Khouya. Anisotropic and nonlinear diffusion applied to image enhancement and edge detection. *International Journal of Computer Applications in Technology*, 49(2):122–133, 2014.

[114] C Lopez-Molina, B De Baets, and H Bustince. A framework for edge detection based on relief functions. *Information Sciences*, 278:127–140, 2014.

[115] Jeny Rajan, Jelle Veraart, Johan Van Audekerke, Marleen Verhoye, and Jan Sijbers. Nonlocal maximum likelihood estimation method for denoising multiple-coil magnetic resonance images. *Magnetic resonance imaging*, 30(10):1512–1518, 2012.

[116] NGN Prasad and JNK Rao. The estimation of the mean squared error of small-area estimators. *Journal of the American statistical association*, 85(409):163–171, 1990.

[117] Chueh Loo Poh, Tong Kuan Chuah, and Kenneth Sheah. Differentiating healthy cartilage and damaged cartilage using magnetic resonance images in a quantitative manner. In *Digital Image Computing: Techniques and Applications (DICTA), 2010 International Conference on*, pages 552–555. IEEE, 2010.

[118] S Akhtar, CL Poh, and RI Kitney. An mri derived articular cartilage visualization framework. *Osteoarthritis and Cartilage*, 15(9):1070–1085, 2007.

[119] Chafik Samir, Anuj Srivastava, and Mohamed Daoudi. Three-dimensional face recognition using shapes of facial curves. *Pattern Analysis and Machine Intelligence, IEEE Transactions on*, 28(11):1858–1863, 2006.

[120] Athanasios Mademlis, Petros Daras, Dimitrios Tzovaras, and Michael G Strintzis. 3d object retrieval using the 3d shape impact descriptor. *Pattern Recognition*, 42 (11):2447–2459, 2009.

[121] Ron Kimmel, Nir A Sochen, and Ravi Malladi. On the geometry of texture. Technical report, DTIC Document, 2000.

[122] Moo K Chung, Keith J Worsley, Steve Robbins, Tomáš Paus, Jonathan Taylor, Jay N Giedd, Judith L Rapoport, and Alan C Evans. Deformation-based surface morphometry applied to gray matter deformation. *NeuroImage*, 18(2):198–213, 2003.

[123] Michael M Bronstein and Iasonas Kokkinos. Scale-invariant heat kernel signatures for non-rigid shape recognition. In *Computer Vision and Pattern Recognition (CVPR), 2010 IEEE Conference on*, pages 1704–1711. IEEE, 2010.

[124] Moo K Chung, Steven M Robbins, Kim M Dalton, Richard J Davidson, Andrew L Alexander, and Alan C Evans. Cortical thickness analysis in autism with heat kernel smoothing. *NeuroImage*, 25(4):1256–1265, 2005.

[125] Dan Raviv, Alexander M Bronstein, Michael M Bronstein, Ron Kimmel, and Nir Sochen. Affine-invariant geodesic geometry of deformable 3d shapes. *Computers & Graphics*, 35(3):692–697, 2011.

[126] Jenny Folkesson, Erik B Dam, Ole F Olsen, and Claus Christiansen. Accuracy evaluation of automatic quantification of the articular cartilage surface curvature from mri. *Academic radiology*, 14(10):1221–1228, 2007.

[127] Lewis D Griffin. The intrinsic geometry of the cerebral cortex. *Journal of Theoretical Biology*, 166(3):261–273, 1994.

[128] Frank Morgan. Riemannian geometry: A beginners guide, ak peters, 1998.

[129] Richard S Millman and George D Parker. *Elements of differential geometry*. 1977.

[130] Sudhakar Tummala, Anne-Christine Bay-Jensen, Morten A Karsdal, and Erik B Dam. Diagnosis of osteoarthritis by cartilage surface smoothness quantified automatically from knee mri. *Cartilage*, 2(1):50–59, 2011.

[131] Jan Hohe, Gerard Ateshian, Maximilian Reiser, Karl-Hans Englmeier, and Felix Eckstein. Surface size, curvature analysis, and assessment of knee joint incongruity with mri in vivo. *Magnetic Resonance in Medicine*, 47(3):554–561, 2002.

[132] Manfredo Perdigao Do Carmo and Manfredo Perdigao Do Carmo. *Differential geometry of curves and surfaces*, volume 2. Prentice-hall Englewood Cliffs, 1976.

[133] T. Iranpour-Boroujeni, A. Watanabe, R. Bashtar, H. Yoshioka, and J. Duryea. Quantification of cartilage loss in local regions of knee joints using semi-automatedsegmentation software: analysis of longitudinal data from the osteoarthritis initiative (oai). *Osteoarthritis and Cartilage*, 19(3):309–314, 2011.

[134] Alexandre Barachant, Stéphane Bonnet, Marco Congedo, and Christian Jutten. Multiclass brain–computer interface classification by riemannian geometry. *Biomedical Engineering, IEEE Transactions on*, 59(4):920–928, 2012.

[135] Eric Klassen, Anuj Srivastava, Washington Mio, and Shantanu H Joshi. Analysis of planar shapes using geodesic paths on shape spaces. *Pattern Analysis and Machine Intelligence, IEEE Transactions on*, 26(3):372–383, 2004.

[136] Steven Haker, Sigurd Angenent, Allen Tannenbaum, Ron Kikinis, Guillermo Sapiro, and Michael Halle. Conformal surface parameterization for texture mapping. *IEEE Transactions on Visualization & Computer Graphics*, (2):181–189, 2000.

[137] Daniela Roşca and Jean-Pierre Antoine. Locally supported orthogonal wavelet bases on the sphere via stereographic projection. *Mathematical Problems in Engineering*, 2009, 2009.

[138] Claude Kauffmann, Pierre Gravel, Benoît Godbout, Alain Gravel, Gilles Beaudoin, Jean-Pierre Raynauld, Johanne Martel-Pelletier, Jean-Pierre Pelletier, Jacques De Guise, et al. Computer-aided method for quantification of cartilage thickness and volume changes using mri: validation study using a synthetic model. *Biomedical Engineering, IEEE Transactions on*, 50(8):978–988, 2003.

[139] Matej Mlejnek, Anna Vilanova, and Meister Eduard Groller. Interactive thickness visualization of articular cartilage. In *Proceedings of the conference on Visualization'04*, pages 521–528. IEEE Computer Society, 2004.

[140] J Duryea, G Neumann, MH Brem, W Koh, F Noorbakhsh, RD Jackson, J Yu, CB Eaton, and P Lang. Novel fast semi-automated software to segment cartilage for knee mr acquisitions. *Osteoarthritis and cartilage*, 15(5):487–492, 2007.

[141] CG Peterfy, G Gold, F Eckstein, Flavia Cicuttini, B Dardzinski, and R Stevens. Mri protocols for whole-organ assessment of the knee in osteoarthritis. *Osteoarthritis and Cartilage*, 14:95–111, 2006.

[142] CG Peterfy, A Guermazi, S Zaim, PFJ Tirman, Y Miaux, D White, M Kothari, Y Lu, K Fye, S Zhao, et al. Whole-organ magnetic resonance imaging score (worms) of the knee in osteoarthritis. *Osteoarthritis and Cartilage*, 12(3):177–190, 2004.

[143] John A Lynch, Frank W Roemer, Michael C Nevitt, David T Felson, Jingbo Niu, Charles B Eaton, and Ali Guermazi. Comparison of bloks and worms scoring systems part i. cross sectional comparison of methods to assess cartilage morphology, meniscal damage and bone marrow lesions on knee mri: data from the osteoarthritis initiative. *Osteoarthritis and Cartilage*, 18(11):1393–1401, 2010.

[144] David T Felson, John Lynch, Ali Guermazi, Frank W Roemer, Jingbo Niu, Tim McAlindon, and Michael C Nevitt. Comparison of bloks and worms scoring systems part ii. longitudinal assessment of knee mris for osteoarthritis and suggested approach based on their performance: data from the osteoarthritis initiative. *Osteoarthritis and Cartilage*, 18(11):1402–1407, 2010.

[145] wikipedia. Rendering equation. URL https://en.wikipedia.org/wiki/Rendering_equation.

[146] Mark Nixon. *Feature extraction & image processing*. Academic Press, 2008.

[147] Maria Petrou and Pedro García Sevilla. *Image processing: dealing with texture*. 2006.

[148] In Jae Myung. Tutorial on maximum likelihood estimation. *Journal of mathematical Psychology*, 47(1):90–100, 2003.